STUDY OF COMBINED STRUCTURE OF GEO-HEAT EXCHANGERS

Thesis submitted for the degree of
Doctor of Philosophy

Mr Sarwo Edhy Sofyan

THE UNIVERSITY
of ADELAIDE

SUB CRUCE LUMEN

School of Mechanical Engineering
The University of Adelaide
Adelaide, SA 5005

June 2018

Executive Summary

A geo heat exchanger (GHE) utilises a pipe configuration, buried in the ground, to harvest geothermal energy at shallow depths. A GHE could be used in heating and cooling systems as the ground temperature is normally higher than the average air temperature in winter and lower in summer. This difference in the temperature can be utilised to improve the efficiency of air conditioning systems (in summer) and heat pumps (in winter).

Two basic arrangements of GHEs are commonly used: vertical and horizontal. Vertical GHEs, which are particularly suitable for confined spaces, generally have a better performance due to stable soil temperature deep down in comparison with the horizontal arrangement. However, their installation cost is relatively high. Meanwhile, the efficiency of horizontal GHEs may benefit from ambient temperature fluctuations and lower installation costs due to the shallow depth of burying of GHEs. However, this arrangement requires a large land area for installation, which may substantially increase the capital cost. In addition, GHEs' performances, especially for vertical ones, may suffer deterioration with an increase in the operation times due to heat or (coldness) accumulation in the soil. In this study, a combined horizontal-vertical GHE arrangement is proposed to synergy the benefits of the two configurations and negate their disadvantages.

The overall aim of this project is to understand the thermo-dynamic performance of GHEs (including the horizontal, vertical and combined GHE) under various loads and weather/soil conditions, in order to optimise their designs and operations by developing validated computational models of the heat exchangers.

Mathematical models for both horizontal and vertical GHEs have been developed which take into account the fluctuations in soil temperature during seasonal changes. The newly developed models are different from the existing models most of which overlooked the seasonal changes in soil temperature. In the new models, the seasonal changes in soil temperature, which are affected by the thermal interaction between the ground and the atmosphere, are incorporated with a help of an internal source term approach. The values of the internal source term depend on geographic locations and soil depths. The finite difference method is used to obtain the numerical solution of the proposed GHE models. The models are validated using experimental data obtained from custom-built rigs. The simulation results show that the new approach, which takes into account the effect of seasonal periodic soil temperature fluctuations on the performance of the GHE, agrees well with experimental data. The validated models are then used to conduct a sensitivity analysis with the aim of investigation of the effect of design

parameters on the performance of the horizontal, vertical and combined GHE. Outcomes of two case studies are presented to demonstrate the benefits of the combined GHE. The first study was conducted to assist with the operation of cooling systems of Terminal 1 building of the Adelaide airport. The second study analysed the efficiency of the combined GHE for an air conditioning system (heat pump) for twenty units of residential houses.

The thesis has been organised into eight chapters. The structure of the thesis is summarised as follows:

Chapter 1-Introduction: This chapter introduces background, gaps identified in GHEs research area, aims and objectives of the study, contributions to the field, and scope and limitations.

Chapter 2-Literature review: This chapter provides a brief description of ground source air conditioning systems (heat pumps), soil thermal characteristics, the review of GHE models and operation modes, and thermodynamic analysis to account the energy savings of the ground source air conditioning systems (heat pumps). The chapter concludes with a summary of the literature review.

Chapter 3-Seasonal soil temperature changes: The chapter elaborates the method used in order to determine the profile of soil temperature at various depths for a specific day in a year. In addition, it summarises a new approach to model the soil temperature fluctuations during seasonal changes on the GHE's performance. In which the seasonal soil temperature changes are expressed as an internal source term and incorporated into the GHE model.

Chapter 4-Horizontal GHE: This chapter presents the developed mathematical model for the horizontal GHE and outcomes of the comparison with experimental data obtained with a reduced scale GHE custom-built rig. It is followed by sensitivity analysis to investigate the technical parameters affecting the performance of the GHE.

Chapter 5-Vertical GHE: The mathematical model that predicts the performance of the vertical GHE is presented in this chapter. An experimental study utilising a scale down experimental rig has been conducted to validate the model. Then, the sensitivity analysis is performed using the validated model to investigate the effect of some design and operational parameters on the vertical GHE's performance including borehole thermal conductivity, borehole depth, fluid flow rate, and types of carries fluids. In addition, the dynamic performance of the GHE under continuous and intermittent loads is also investigated.

Chapter 6-Combined horizontal-vertical GHE: This chapter analyses the performance of a combined horizontal-vertical GHE based on the two separate validated models.

Chapter 7-Case studies: This chapter demonstrates the potential applications of the combined GHEs to assist in the operation of air conditioning systems. These two studies are focused on the analysis of the combined GHE for the Terminal 1 building, Adelaide airport and twenty units of residential buildings.

Chapter 8-Conclusion: This chapter summarises the result of this thesis and discusses the future work.

Declarations

I certify that this work contains no material which has been accepted for the award of any other degree or diploma in my name, in any university or other tertiary institution and, to the best of my knowledge and belief, contains no material previously published or written by another person, except where due reference has been made in the text. In addition, I certify that no part of this work will, in the future, be used in a submission in my name, for any other degree or diploma in any university or other tertiary institution without the prior approval of the University of Adelaide and where applicable, any partner institution responsible for the joint-award of this degree. I give consent to this copy of my thesis when deposited in the University Library, being made available for loan and photocopying, subject to the provisions of the Copyright Act 1968. I acknowledge that copyright of published works contained within this thesis resides with the copyright holder(s) of those works. I also give permission for the digital version of my thesis to be made available on the web, via the University's digital research repository, the Library Search and also through web search engines, unless permission has been granted by the University to restrict access for a period of time.

Sarwo Edhy Sofyan

Acknowledgements

I would like to express my deepest gratitude to my principal supervisor A/Prof. Eric Hu, for his inspiring guidance, and continuous encouragement throughout my research at the University of Adelaide. I am also deeply grateful to my Co. Supervisor, Prof. Andrei Kotousov, for his help, support and suggestions that benefits me a lot.

A special acknowledgment to Mr. Marc Simpson who helped me in setting up the GHE test rig. My special appreciation also to Ms. Alison Jane Hunter for English editing support of my journal papers. Also, I would like to acknowledge Mr. Philip Schmidt, Mr. Derek Franklin, Mr. Billy Constantine and all school of mechanical engineering staffs who helped me a lot during my PhD candidacy.

I further express my gratitude to Dr. Michael Evans, Dr. Maung Myo, Dr. Timothy Lau and Mr. Jiyun Qin and all my colleagues in the Engineering South Building, Room 216, for their support throughout the PhD study.

I would also like to thank the Indonesian government for the opportunity and financial support that allows me to pursue my PhD degree at one of Australia's prestigious universities, the University of Adelaide.

Then I owe many thanks to my family. I am grateful to my father, my mother, and my wife for giving me their deep love, encouragement and support during my study. Without their support, it would be difficult for me to complete my study.

I would like to extend my sincere gratitude to Bambang Setiawan, Fadliadi, and all Acehnese students in Adelaide, South Australia, for their valuable support.

Table of contents

List of Figures

List of Tables

Nomenclature

Symbols

A	Area	m²
A_s	Amplitude of the annual air temperature	K
b	Contact resistance	W/m²K
COP	Coefficient of performance of an ideal refrigeration cycle	-
COP_a	Actual coefficient of performance of the refrigeration system	-
c	Specific heat	J/kgK
D	Bottom depth of the ground layer	m
d	Diameter	m
d_{in}	Inner pipe diameter	m
E	Total energy consumption	kWh
F_o	Fourier number	-
H_s	Soil internal heat source term	W/m³
h	Enthalpy	kJ/kg
h_{as}	Convective heat transfer coefficient of air in contact with the soil surface	W/m²K
h_f	Convective heat transfer coefficient between the working fluid and the inner pipe surface	W/m² K
h_z	Burial depth	m
i, j, k	Indexes in the x, y, and z directions	-
J	Total solar radiation	W/m²
J_{eh}	Effective emission	W/m²
k	Thermal conductivity	W/mK
k_a	Conductive heat transfer coefficient of air	W/mK
k_v	Vegetation coefficient	-
L	Unit length	m
L_s	Shank spacing	m
$\dot{m}$	Mass flow rate	kg/s
N	Number of pipes inside the borehole	-
N_u	Nusselt number	-
P	Perimeter of the soil boundary	m
P_r	Prandtl number of air	-
Q	Heat transfer	J
$\dot{Q}_{in}$	Refrigeration capacity	kW
$\dot{Q}_{out}$	Heat rejection capacity of the condenser	kW
R_b	Effective pipe to borehole thermal resistance	mK/W
R_e	Reynold number	-
R_{nfuu}	Coefficient of thermal interference between the pipe and borehole when no fluid flow is considered	mK/W
R_{nfuv}	Coefficient of thermal interference between the pipe u and the pipe v when no fluid flow is considered	mK/W
R_{p0}	Thermal resistance between the pipe and the borehole wall	mK/W
R_{uu}	Coefficient of thermal interference between the pipe and borehole	mK/W
R_{uv}	Coefficient of thermal interference between the pipe u and the pipe v	mK/W
r	Radius	m
Δr	Finite increment in the radial direction	m
r_g	Radius from centre of the pipe to centre of grout element	m

r_i	Inner radius of the pipe	m
r_o	Outer radius of the pipe	m
r_s	Radius from centre of the pipe to centre of soil element	m
S	Area of contact surface	m^2
SAT	Sol-air temperature	ºC
T	Temperature	K
$T(x, t)$	Ground temperature at a given depth x on calendar day t	ºC
T_a	Ambient air temperature	K
T_{flu}	Fluid temperature in the pipe u	K
T_{flv}	Fluid temperature in the pipe v	K
T_m	Average annual air temperature	ºC
T_{max}	Maximum ambient temperatures in a month	ºC
T_{min}	Minimum ambient temperatures in a month	ºC
ΔT_s	Soil temperature difference in summer and winter	K
ΔT_m	Local site variable for the ground temperature	K
t	Time period	s, h
t_h	Thickness	m
t_0	Phase of air temperature wave	Day
Δt	Time period	s
U_{as}	Overall heat transfer coefficient between soil and ambient air	W/m²K
V	Volume	m^3
v_f	Velocity of the working fluid	m/s
$\dot{W}_c$	Compressor power	kW
$\dot{W}_c/\dot{m}$	Compressor power per unit mass of refrigerant flowing for an actual condition	kJ/kg
$(\dot{W}_c/\dot{m})_s$	Compressor power per unit mass of refrigerant flowing for an ideal condition	kJ/kg
x	Distance in the x direction	m
Δx	Finite increment in the x direction	m
y	Distance in the y direction	m
Z	Soil depth	m
Z_d	Dumping depth	m
z	Distance in the z direction	m
Δz	Finite increment in the z direction	m

Greek symbols

α_g	Grout diffusivity	m²/s
α_0	Overall heat transfer coefficient between soil and air	W/m²K
α_s	Soil diffusivity	m²/s
α_s	Albedo	-
β_0, β_1	Coefficients of the borehole determined based on the geometry of the GHE	-
ε	Longwave emissivity	-
η	Isentropic efficiency	-
μ_a	Dynamic viscosity of air	N s/m²
μ_f	Dynamic viscosity of fluid	N s/m²
ν_a	Wind speed	m/s
ρ	Density	kg/m³
ψ	Courant number	-

Subscripts

b	Borehole
c	Convection
eq	Equivalent
f	Fluid
g	Grout
gr	Ground
i	Inlet
$i1$	Inlet 1
$i2$	Inlet 2
o	Outlet
$o1$	Pipe-out 1
$o2$	Pipe-out 2
p	Pipe
po	Pipe and borehole wall
s	Soil
w	Water
1	State 1
$2s$	State 2s
3	State 3
4	State 4
$4'$	State 4'

Superscripts

t	At the current time step
$t + \Delta t$	At the new time step

CHAPTER 1

INTRODUCTION

1.1 Background

Geo heat exchangers (GHEs) are very attractive from technical and environmental perspectives in heating and cooling applications because of their renewable nature. GHEs use the ground/soil as a heat source or heat sink to harness the (renewable) thermal energy stored in the ground. Typically, the ground temperature is normally higher than the ambient air temperature during the winter and lower during the summer. Thus, the ground is a suitable medium to be used to extract/store the heat during the winter/summer. GHEs are usually coupled with heat pumps and air conditioning systems to provide one of the most energy efficient ways for buildings' heating and cooling. Compared with a typical air-to-air heat pump and air conditioning systems, the application of GHEs can reduce energy consumption from 30% to 50% [1].

A GHE represents a buried-pipe system where the working fluid, e.g. water is circulated inside to exchange the heat with surrounding soil. Generally, there are two configurations of GHEs: horizontal and vertical. The vertical GHE is a pipe system installed in a vertical direction in a borehole. The borehole, which has a typical depth is around 50-150 m [2], is filled with grout materials, e.g. sand, or bentonite, to fit the pipe to the borehole and to improve heat transfer rate of GHE. Usually, it requires more than one GHE to extract (release) the heat from (to) the ground to provide heating (cooling) for buildings. In order to prevent the thermal interference, the spacing between boreholes ranges from 5 to 6 m.

The vertical GHEs are suitable for the confined area or rocky ground surface. They gain the advantage of stable ground temperature below a certain depth and this results in a better efficiency [3, 4]. As a result, less pipe length is required compared with the horizontal GHE. A drawback of this configuration is that the installation cost is relatively high [5]. Typical drilling costs of the vertical GHE vary from 37 to 56 AUD per metre, depending on the ground composition [6, 7]. Another drawback is the performance of the vertical GHE may deteriorate with the increase of the operating period. The condition is sometimes exacerbated, especially when there is an imbalance in heating and cooling loads. For instance, in Australia, residential and commercial buildings require greater cooling than heating [8]. As a result, more heat is released into the ground rather than absorbed from the ground. This heat dissipation would increase the temperature of the soil around the GHE. In the vertical GHE case, the increase of soil temperature is relatively hard to recover due to poor soil thermal conductivity and relatively

deep depth of burying, which hinders the heat transfer rate to and from the atmosphere. The vertical GHEs are classified into three major types based on their arrangements: single U-shaped pipe, double U-shaped pipes, and coaxial pipes [9]. Figure 1.1 shows schematic of the vertical GHEs coupled with an air conditioning system and heat pump. In a cooling operation, the indoor heat (Q) is absorbed by an air conditioning system and released to the ground through a vertical GHE as Q'. The process is the opposite in a heating operation, in which the ground heat (Q) is absorbed by the GHE's fluid. The heat is then released by a heat pump to the room as Q'.
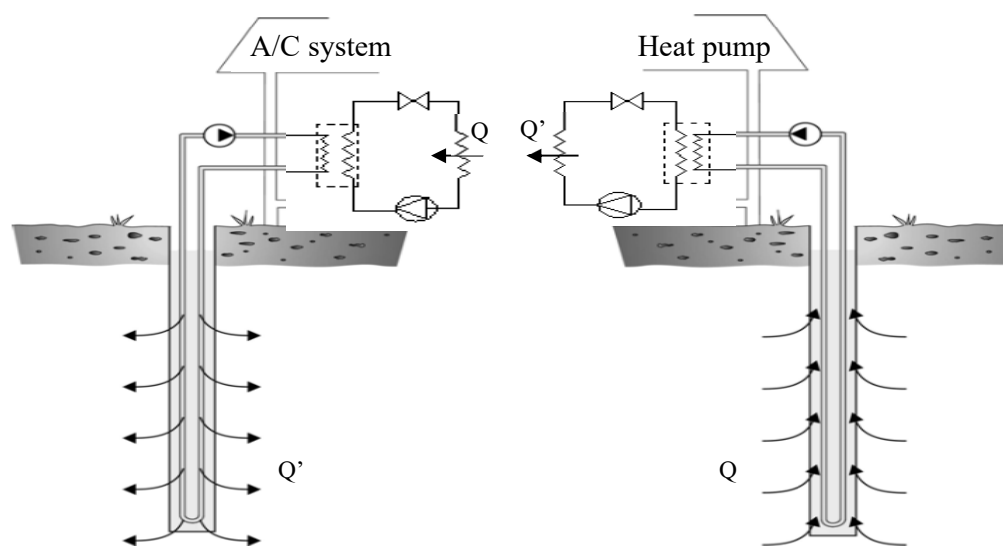
Figure 1.1: Vertical GHEs are coupled with a heat pump and air conditioning system [10]

The horizontal GHEs represent a pipe system, which is embedded in a trench to a typical depth up to 2 m below the ground level. The horizontal GHEs normally require fewer installation costs. For the cooling applications, they can take advantage of storing the heat to the ground at daytime when the ambient temperature is high. The ground then releases the heat to the atmosphere, at nighttime, when ambient temperature drops [11]. This heat transfer mechanism can recover the degradation of the soil temperature around the GHEs and maintain the GHEs' performance for long-term operation. The disadvantage of the horizontal configuration is that it needs a large land area for installation [12]. In addition, the performance of the horizontal GHEs is affected by the weather conditions since they are installed relatively close to the surface [4]. The pipe arrangements are usually in the form of single U-shaped, multiple U-shaped, and slinky coils. Figure 2.1 shows the schematic of a horizontal heat exchanger coupled with a heat pump and used for floor heating.
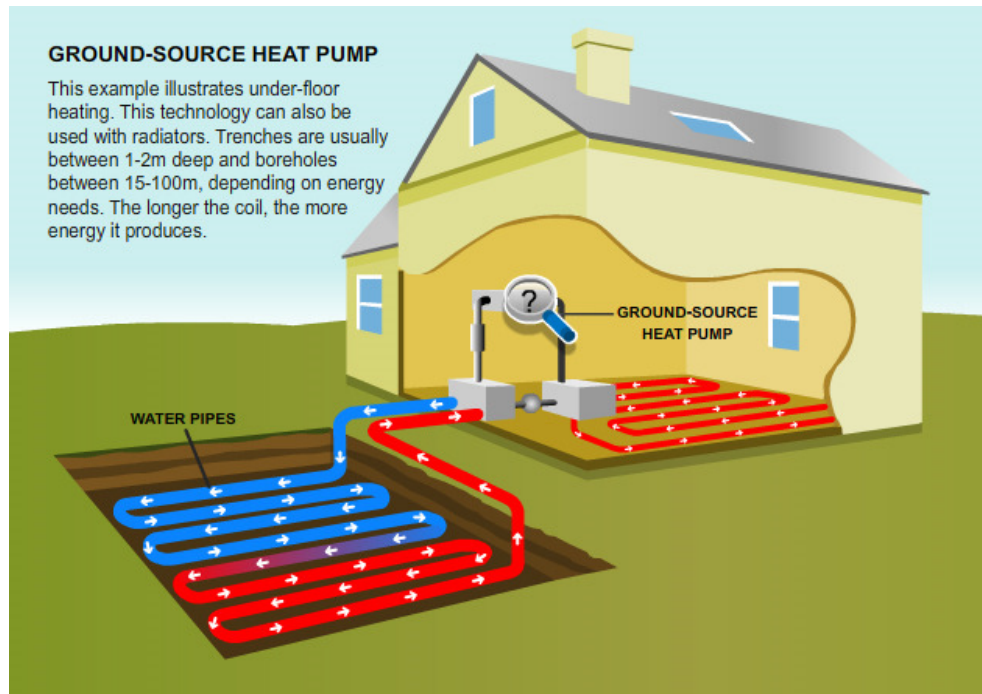
Figure 1.2: A horizontal GHE is coupled with a heat pump system [13]

GHEs can be coupled with air conditioning systems (heat pumps) to provide the cooling (heating as well as hot water supply) for both domestic and commercial buildings. This technology could also be used for the agriculture industry such as greenhouse heating/cooling, drying crops, pasteurising milk, and heating water at fish farms [8]. According to Florides and Kalogirou [14], there have been over 550,000 ground source heat pumps installed worldwide, which 80% of those are domestic. The applications of ground source heat pumps grow rapidly, with an annual increase about 10% [15]. In Australia, 23,000 units have been installed with a total thermal capacity of 275 MW and an annual energy consumption of 370 GWh [15]. Table 1.1 summarises the installed ground source heat pump capacity for developed countries.

Table 1.1: Leading countries using ground source heat pumps [15]

Country	Installed thermal capacity (MW)	Annual energy use (GWh)	Number of GSHP installations
US	6300	6300	600,000
Sweden	2000	8000	200,000
Germany	560	840	40,000
Switzerland	440	660	25,000
Canada	435	300	36,000
Australia	275	370	23,000

Ground source air conditioning systems (heat pumps) are more efficient than conventional cooling (heating) systems, reflected by their high coefficient of performance (COP). For the cooling systems, the COP ranges 10.5-20 for ground source air conditioning systems, and 11-17 for air source air condition systems [16]. For the heating systems, the COP varies 3-5 for

ground source heat pumps (GSHPs), 2.3-3.5 for air source heat pumps (ASHPs), 1 for electric baseboard heaters, 0.78-0.82 for mid-efficiency natural gas furnaces, and 0.88-0.97 for high-efficiency natural gas furnaces [15]. The relatively high COP of ground source air condition systems (heat pumps) renders less operation cost and CO_2 emission. As an example, Tables 1.2 and 1.3 summarise the comparison of economic and CO_2 emissions for several heating systems in selected locations, Canada, respectively [15].

Table 1.2: Economic comparison of several heating systems in selected locations, Canada [15]

Heating systems	Capital cost ($)	Annual heating cost in Alberta ($)	Annual heating cost in Ontario ($)	Annual heating cost in Nova Scotia ($)
GSHPs	9000	601	328	649
ASHPs	4900	813	444	877
Electric baseboard	1550	2257	1231	2432
Mid-efficiency natural gas furnaces	1500	1276	2344	1885
High-efficiency natural gas furnaces	1900	1109	1049	1653

Table 1.3: Comparison of CO_2 emissions for several heating systems in selected locations, Canada [15]

Heating systems	Annual fuel use (kWh)	Alberta		Ontario		Nova Scotia	
		Emission intensity (kg CO_2/kWh)	CO_2 emission (kg)	Emission intensity (kg CO_2/kWh)	CO_2 emission (kg)	Emission intensity (kg CO_2/kWh)	CO_2 emission (kg)
GSHP	6080	1.12	6826	0.188	1143	1.04	6346
ASHP	8214	1.12	9222	0.188	1544	1.04	8573
Electric baseboard	22,280	1.12	25,015	0.188	4188	1.04	23,255
Mid-efficiency natural gas furnaces	28,475	0.19	5410	0.19	5410	0.19	5410
High-efficiency natural gas furnaces	24,655	0.19	4684	0.19	4684	0.19	4684

These tables show that the ground source air conditioning systems and heat pumps are the most efficient cooling and heating system. Their higher investment costs are compensated by a lower operational cost. The ground source air conditioning systems and heat pumps are also environmentally friendly due to their low CO_2 emissions.

1.2 Gaps identified in GHEs research area

Based on the literature review (which will be detailed in Chapter 2) the research gaps identified for GHEs include:

1. There are few studies, which focused on the performance of combined horizontal and vertical GHE under different climate and load conditions.

2. Different operation modes of the combined horizontal and vertical GHE have not been systematically investigated so far.

3. There are limited studies on the evaluation of the performance of GHEs considering seasonal changes in soil temperature. Several existing studies consider the performance of GHEs under constant soil temperature or count the seasonal fluctuation in soil temperature using a complicated approach which can produce large errors. In this study, a new approach is introduced to consider the seasonal changes in soil temperature by incorporating an internal heat source term into the GHE models. This approach was successfully validated with custom-built rigs.

1.3 Aims of the present study
1.3.1 Overall aim

The overall aim of this study is to understand the dynamic performance of GHEs including horizontal, vertical, and combined GHE, under various loading and weather conditions, while the seasonal soil temperature changes have been considered.

1.3.2 Specific objectives

To achieve the aim of the project, several objectives need to be specified. These objectives are to:

1. Develop a conceptual design of a combined horizontal-vertical GHE;
2. Develop a simulation model of combined horizontal-vertical GHE with considering nature soil temperature fluctuations;
3. Validate the developed model by experimental data from custom made rigs;
4. Use the validated model to investigate heat transfer behaviour of the combined horizontal-vertical GHE;
5. Demonstrate the energy saving potential of the GHE by applying the validated model in two case studies, i.e. Terminal 1 building, Adelaide airport and Twenty units of residential buildings development in Adelaide.

1.4 Main contributions to the field

There are two major developments which contribute to knowledge in the field. First, this study presents a new approach to the incorporation of the effect of seasonal changes in soil temperature into the evaluation of GHE's performance. It is different from the existing methods, which either ignore the impact of soil seasonal changes on GHE's performance or consider the seasonal changes in soil temperature by applying a real energy balance to the soil surface boundary. In the new approach, the seasonal changes in soil temperature, which are affected by the thermal interaction between the ground and the atmosphere, are expressed as an internal source term of the soil. The value of the internal source term is derived from the actual or estimated soil temperature profile. The new approach has been proven to be able to increase the accuracy when estimating soil and water temperature (detail see Sections 4.5.3 and 5.5.3). The second major contribution is the introduction of a combined horizontal-vertical GHE arrangement that allows different modes of operation in order to meet demands and thermal loading conditions.

1.5 Scope and limitations

This study has focused on the development model of a combined horizontal-vertical GHE. The model included 1D representation of heat transfer for the heat carrier fluid and pipe, and 2D for the soil domain. This model takes into account the effect of seasonal soil temperature fluctuations by incorporating a proposed internal source term into the GHE model. The model is validated through two separate scaled custom-built experimental rigs of the horizontal and vertical GHE, respectively.

CHAPTER 2

LITERATURE REVIEW

This chapter presents a literature review of recent research on geo heat exchangers (GHEs), their operational strategies, and the energy saving potential. The review is carried out in order to identify some research gaps in order to optimise the GHEs' designs and operations by developing a validated computational model.

This chapter is organised as follows. Section 2.1 presents a brief description of ground source air conditioning systems (heat pumps). Section 2.2 highlights the soil thermal characteristics that significantly influence the thermal behaviour of the GHE. Section 2.3 overviews the recently developed GHE models. Section 2.4 highlights the potential of energy savings of air conditioning systems. Section 2.5 summarises the key findings from the literature review.

2.1 Ground source air conditioning systems and heat pumps

Ground source air conditioning systems (heat pumps) are recognised to be efficient cooling (heating) systems those not only provide high levels of comfort but also offer a significant reduction of electrical energy use. There are three major elements of ground source air conditioning systems (heat pumps) including air conditioning systems (heat pumps), geo heat exchangers, and air distribution systems. During the cooling process, air conditioning systems absorb the indoor heat and transfer it to a heat carrier fluid of geo heat exchangers. Subsequently, the heat is transferred by the geo heat exchangers to the surrounding soil. As a result, the temperature of the heat carrier fluid decreases, in contrast, the temperature of the surrounding soil increases. The cycle is then repeated to provide the cooling for the building. For the heating, the process is vice versa. Figure 2.1 shows a schematic of a ground source air conditioning system [5].
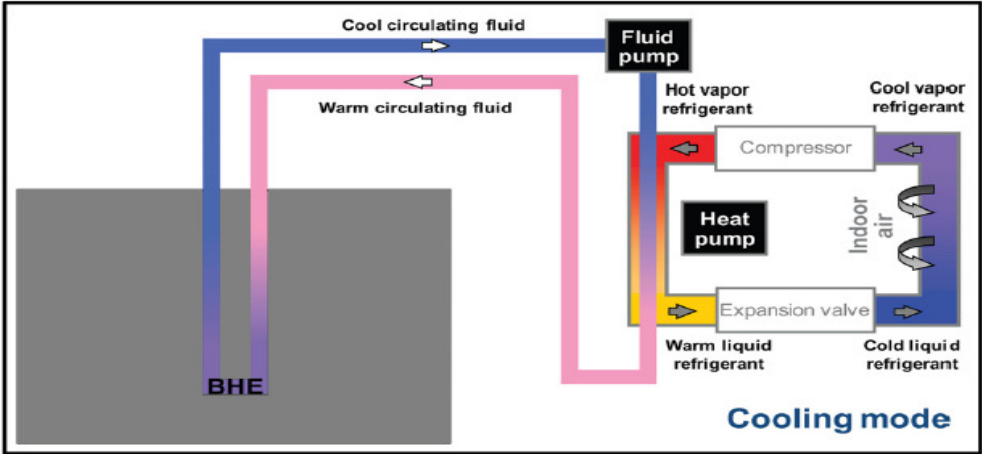
Figure 2.1: Schematic of a ground source air conditioning system [5].

2.2 Soil thermal characteristics

Knowledge of soil thermal characteristics is essential when designing GHEs, as the undisturbed initial soil temperature and soil thermophysical properties such as: thermal conductivity, specific heat, and density, affect significantly the GHEs performance. The soil thermal conductivity is a parameter which determines the capacity of heat transmission inside the soil domain. The soil thermal conductivity is influenced by several factors, including mineral compositions, moisture content, dry density, and temperature [17, 18]. Thermal conductivity for different soil types was reported by a number of researchers. Based on the experimental data, Abu-Hamdeh and Reeder [18] provided the thermal conductivity values for sand, loam, sandy loam and clay loam. They range from 0.58 to 1.94 for sand, from 0.29 to 0.76 for loam, from 0.19 to 1.12 for sandy loam, and from 0.36 to 0.69 W/mK for clay loam. Specific heat is the amount of heat required to change a unit mass of a substance by one degree in temperature. The value of soil specific heat is affected by its density and moisture content [19]. Alnefaie and Abu-Hamdeh reported that the specific heat of loam ranges from 1140 to 2090 J/kgK, while the specific heat of sand ranges from 800 to 1530 J/kgK, at a soil density of 1200 kg/m^3 and moisture contents from 0.01 to 0.2 kg/kg. Al-Khoury [3], presented the thermophysical properties of typical soils summarised in Table 2.1.

Table 2.1: Thermophysical properties of typical soils:

Type of soils	k (W/mK)	ρ(kg/m^3)	c (kJ/kgK)	N
Limestone	1.2-2.15	2300-2500	0.8-0.9	0-0.2
Sandstone	1.8-2.9	2160-2300	0.7-0.8	0.05-0.3
Sand	0.15-4	1280-2150	0.8-1.48	0.2-0.6
Clay	0.15-2.5	1070-1600	0.92-2.2	0.33-0.6

Soil temperature is another parameter that influences the performance of GHEs. There are three main factors affecting the temperature of the soil namely: meteorological, terrain and subsurface characteristics [16,19]. Soil temperature down up to 10 m is influenced by both diurnal and seasonal climate changes. At a deeper region, the soil temperature is almost constant all year around. Figure 2.2 shows the profile of soil temperature at various depths in winter and summer. As illustrated in the figure that the soil temperature changes during winter and summer as the continuous thermal process occurs between the ground surface and the atmosphere. The soil temperature changes significantly in a shallow region and decreases with increasing depth.
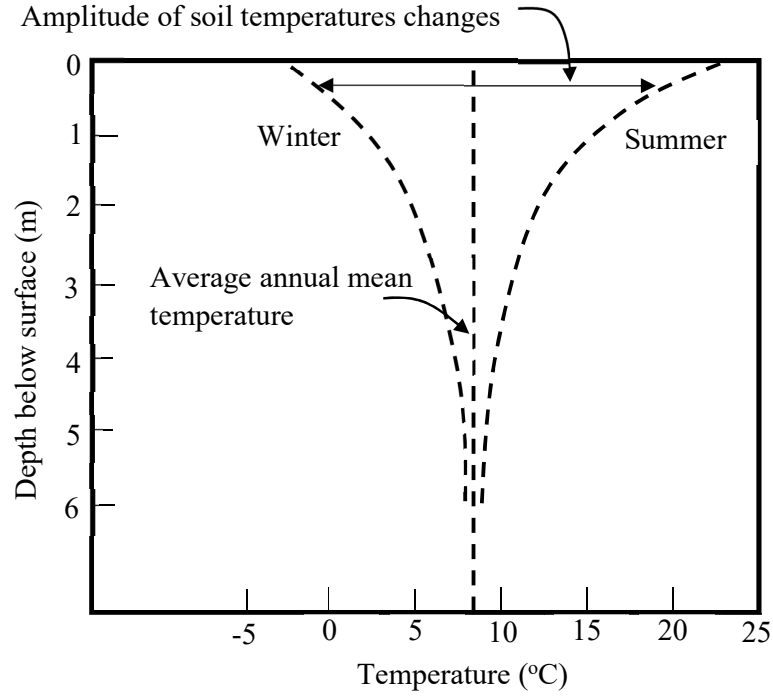
Figure 2.2: Annual dependence of ground temperature on depth

Soil temperature can be obtained from direct measurements or it can be estimated using an analytical model. The soil temperature may be acquired from the Bureau of Meteorology or found in research articles. However, most existing data of soil temperature belong to a specific geographic location and depth. Therefore, the analytical equations may be used in order to estimate the soil temperature at different depths and geographic locations. Baggs [20] presented an analytical model of soil temperature. The model incorporated a variable of vegetation cover to generate a more accurate result. Baggs model is summarised as:

$$T(x,t) = (T_m \pm \Delta T_m) + 1.07 k_v A_s e^{\left(-0.00316x\left(\frac{1}{\alpha}\right)^{0.5}\right)} cos\left[\frac{2\pi}{365}\left(t - t_0 - 0.1834x\left(\frac{1}{\alpha}\right)^{0.5}\right)\right]$$

(2.1)

where $T(x,t)$ is the ground temperature at a given depth x on calendar day t (°C), x is the soil depth (cm), t is the calendar day where 1 January = 1 and so forth, T_m is the average annual air temperature (°C), ΔT_m is the local site variable for the ground temperature (K), k_v is the vegetation coefficient (k_v = 1 for bare ground, k_v = 0.22 for year round full vegetation cover), A_s is the amplitude of the annual air temperature (K), α is the average soil thermal diffusivity (10^{-2} cm^{-2} sec^{-1}), and t_0 is the phase of air temperature wave (day).

2.3 GHE Models

This section presents the previous works related to the modelling of GHEs including the horizontal, vertical, and hybrid GHEs systems.

2.3.1 Horizontal GHE models

Various mathematical models were proposed in the literature to study the thermal behaviour of horizontal GHEs. The models cover different types of the GHEs including the linear [21-35], slinky [36-40], and flat-panel [41-43] configurations.

A 2D model based on the finite difference scheme was developed by Esen et al. [21] to study the thermal regime of a GHE. The model is based on the unsteady heat conduction equation. The computational domain of the model is considered from the pipe's edge to mid span between the pipes as illustrated in Figure 2.3. The adiabatic boundary condition is applied to the sides of the soil domain and the convection heat transfer is considered on the ground surface. This model ignores the effect of the thermal resistance of the pipe. The transient conduction heat transfer in the soil domain is expressed using the following equation:

$$\frac{1}{\alpha}\frac{\partial T(x,y,t)}{\partial t} = \frac{\partial T(x,y,t)}{\partial x^2} + \frac{\partial T(x,y,t)}{\partial y^2} \tag{2.2}$$

where $T(x,y,t)$ is the soil temperature (°C), x is the distance in the horizontal direction (m), y is the distance in the vertical direction (m), α is the soil thermal diffusivity (m²/s), and t is the time step (s).
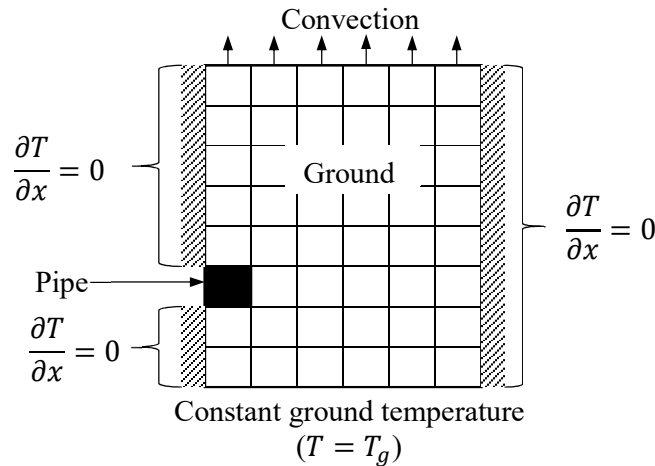
Figure 2.3: Computational domain of the horizontal GHE [21]

A comprehensive mathematical model of horizontal GHE was developed Demir et al. [22]. The model includes all weather effects, including solar radiation, latent and sensible heat transfer, longwave radiation, convection, precipitation and surface cover. The solution of the three-dimensional temperature distribution in the soil domain is obtained by dividing the pipe and soil into small segments. In each soil segment, two-dimensional conduction heat transfer is

considered as represented in Equation 2.2. The finite difference method is used to solve the partial differential equations of heat transfer for the GHE. The model, however, ignores the effect of the pipe thermal resistance. The profile of fluid temperature along the pipe is represented using Equation 2.3 which is illustrated as:

$$T_{fo} = T_s - (T_s - T_{fi})exp\left(\frac{-k_s L}{\dot{m}_f c_f}\right)$$
(2.3)

where T_{fo} is the outlet fluid temperature (°C), T_s is the soil temperature (°C), T_{fi} is the inlet fluid temperature (°C), L is the pipe length (m), k_s is the soil thermal conductivity (W/mK), $\dot{m}_f$ is the fluid mass flow rate (kg/s), c_f is the fluid specific heat (J/kgK).

Rezaei-Bazkiaei et al. [23, 24] proposed a model with an intermediate insulation layer in the soil domain. This insulation layer, called a tire derived aggregate, is introduced to mitigate the effect of climate condition on the soil surface. Rezaei-Bazkiaei et al.'s model is developed based on Demir et al.'s work [22]. The solution of the model is obtained by using both alternating direction implicit and explicit finite difference methods. Figure 2.4 shows the computational domain for Rezaei-Bazkiaei et al.'s model.
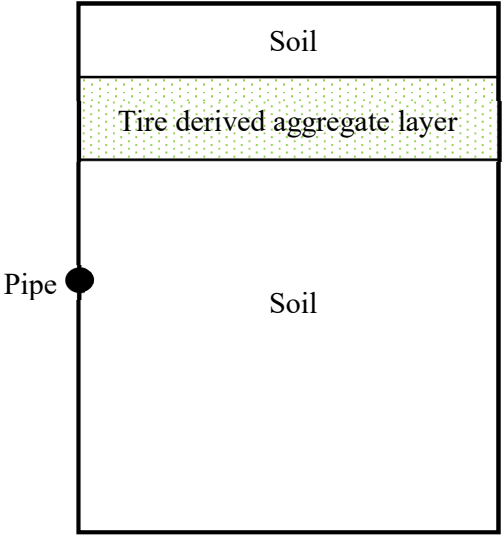
Figure 2.4: Computational domain of the horizontal GHE [23, 24]

A study of the effect of local geological data on GHE's short-term and annual performance was conducted by Han et al. [25] by developing a 3D finite element model. Different boundary conditions are applied in the model. Far-field soil temperature as a function of depth and time is set to the side and bottom boundaries of the soil domain. While on the ground surface, it is only the convective heat transfer counted. The short-term performance of the GHE under linear (with two or four pipes per trench), helical and slinky arrangements is investigated. It is found that the GHE with the linear (with two pipes per trench) and helical arrangements performs

better than others. In addition, it is obtained that the accuracy of the GHE model improves when the measured geological data (e.g. temperature and thermal properties of the soil) is incorporated into the model. While, the annual performance of the GHE is investigated by taking into account various thermal loads of a building (e.g. heating dominant, cooling dominant and balanced). The results reveal that the effect of seasonal variation in soil thermal properties is not significant on the performance of the GHE with a balanced thermal load. It is found that the deterioration of the GHE performance with heating dominant is relatively easier to recover than that with cooling.

Chong et al. [26] suggested a 3D numerical model to study the thermal performance of a horizontal slinky GHE. Different boundary conditions are applied to the soil domain including adiabatic conditions at the lateral boundaries, the constant temperature condition at the bottom boundary and convection at the surface boundary. The thermal performance of the GHE under different loop spacing, loop diameter, soil thermal properties, and intermittent operation was studied. The results reveal that the examined parameters significantly influence the heat extraction rate of the GHE. The thermal performance of the GHE increases as the loop spacing is reduced and the thermal diffusivity of the soil increases. Table 2.2 shows the thermal properties of three different types of soil utilised in this work.

Table 2.2: Soil thermal properties used in the simulation [26]

Soil type	Density (kg/m^3)	Specific heat (kJ/kgK)	Thermal conductivity (W/mK)	Diffusivity (m^2/s)
Loamy sand	1587.32	1.4648	1.24	5.33 x 10^{-7}
Light dry soil	1442	0.8370	0.35	2.90 x 10^{-7}
Wet sand	1440	1.7000	2.6	1.06 x 10^{-6}

Experimental and theoretical study on the single and double loops of slinky horizontal GHEs were presented by Fujii et al. [27]. The experimental study starts with the construction of the single and double loop GHEs. The single loop has a total length of 100 m and occupies nearly 125 m^2 of ground surface area. It is buried at a depth of 1.5 m. The double loops occupy the similar land space as the single loop does. They are buried at depths of 1 m and 2 m for the upper and lower layer, respectively. Each loop has a total length of 100 m. The numerical model is developed by taking a reference to the previously proposed GHE model by Fujii et al. [12]. In the new model, the surface boundary condition is simplified using a sol-air temperature approach for an efficient computation speed. The equation for the sol-air temperature is written as:

$$SAT = T_a + \frac{1}{\alpha_0\big((1 - \alpha_s)J - \varepsilon J_{eh}\big)} \tag{2.4}$$

where SAT is the sol-air temperature (°C), T_a is the ambient temperature (°C), α_0 is the overall heat transfer coefficient between soil and air (W/m²K), α_s is the albedo which is equal to 0.3 for soil, ε is the longwave emissivity, J is the total solar radiation (W/m²), and J_{eh} is the effective emission (W/m²).

Using the model, the optimum burial depth for the double loops of slinky GHE is investigated by varying the depth of the upper loop from 0.5 m to 1.5 m, with the 0.5 m increment, while the lower layer loop is kept at a constant depth of 2 m. The results reveal that the GHE gains the best performance when the upper layer loop is laid to a depth of 1.5 m. In addition, Fujii et al. [26] investigated the effect of circulation direction of the heat carrier fluid of the GHE. The circulation directions of the fluid are varied (1) from the upper to lower layer loop of the GHE, (2) from the lower to upper layer loop of the GHE, and (3) in parallel flow. According to them, the GHE with a flow direction of the heat carrier fluid, from the upper to lower layer loop, yields a better thermal performance. Furthermore, the performance of the GHE installed below different land surfaces, including asphalt pavement, soil, and high reflectance asphalt is investigated. The land surfaces have different reflectance capacity namely, 0.1 for asphalt pavement, 0.3 for soil, and 0.6 for high reflectance asphalt. The results show that the land surface with a higher reflectance capacity is more suitable for a cooling regime. In contrast, the land surface with a lower reflectance capacity is suitable for heating.

An analytical model for both the horizontal and vertical slinky GHE was developed by Xiong et al. [28]. In this model, the analytical ring source solution is applied in order to compute the temperature response of the GHE. The slinky loop GHE is treated as a series of rings, in which, each ring has a uniform heat flux. Figure 2.5 shows a schematic of the simplified slinky heat exchanger.
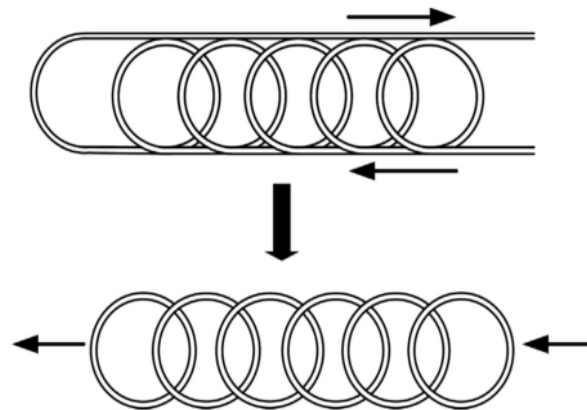
Figure 2.5: A schematic of the simplified slinky GHE [28]

This model assumes that the ground is a semi-infinite medium with homogeneous and isotropic thermal properties. It is also assumed that the heat transfer in the soil domain occurs by conduction only. The thermal solution for the heat exchanger in this model is obtained by using the superposition principle for two heat transfer processes. First, the heat transfer process of the ring source buried in a semi-infinite medium and has a constant temperature. Second, the heat transfer process of a semi-infinite medium that takes into account the effect of seasonal fluctuations in soil temperature.

The seasonal soil temperature variations are computed based on the energy balances, including convection, shortwave radiation, longwave radiation, and evaporation. Figure 2.6 illustrates the schematic of the superposition principle of a slinky GHE.
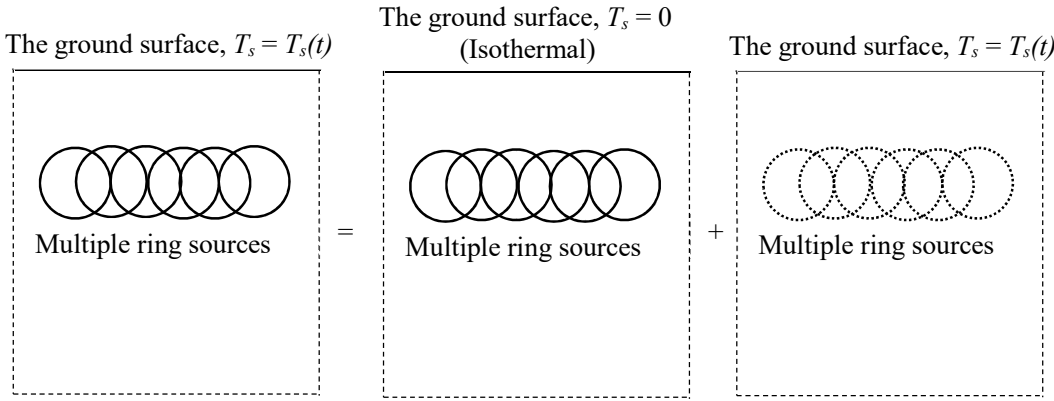
Figure 2.6: The schematic of the superposition principle of a slinky GHE [28]

A 3D finite element model was developed by Go et al. [29] to investigate the effect of rainfall infiltration on the performance of a spiral coil-shaped horizontal GHE. The model simplifies the soil as an isotropic material composed of two different layers. The upper layer, from 0 to 4.5 m, is the unsaturated layer, where the coil is buried to a depth of 1.5 m. While the bottom layer, from 4.5 to 10.5 m, is the saturated layer. In this study, the effect of rainfall infiltration on the thermal properties of the unsaturated soil, including pore water pressure, volumetric water content, the degree of saturation, and thermal conductivity, is investigated. In addition, the duration for the soil to reach fully saturated and desaturated conditions is studied and incorporated into the model. The effect of the groundwater velocity on the thermal performance of the GHE, is also discussed. The results reveal that the rainfall infiltration in the unsaturated soil affects the soil thermal conductivity. As a result, the thermal performance of the GHE is increased.

A 2D explicit finite volume model of a horizontal foundation heat exchanger was developed by Xing et al. [30]. This model considers multiple pipes embedded in the building foundation, in which the cross section of each pipe is represented by a rectangular shape. The computational

domain of the model is discretised using a rectangular mesh. The mesh is fine near the pipe and the earth's surface. It is being coarse gradually at the bottom, left and right sides of the soil domain. Different boundary conditions are applied to the computational domain of the GHE. The convection is applied to the floor and the wall of the basement. The ground surface is subjected to the shortwave and longwave radiation, convection, and evaporation. The adiabatic condition is applied to the lateral and bottom boundaries of the soil domain. The model ignores the effects of snow cover and moisture transport. Lee et al. [31] continued Xing et al.'s work by integrating the model with the building simulation programs and developing a better grid generation technique, which produces better accuracy and simulation efficiency. Figure 2.7 illustrates the cross section of the foundation GHE.
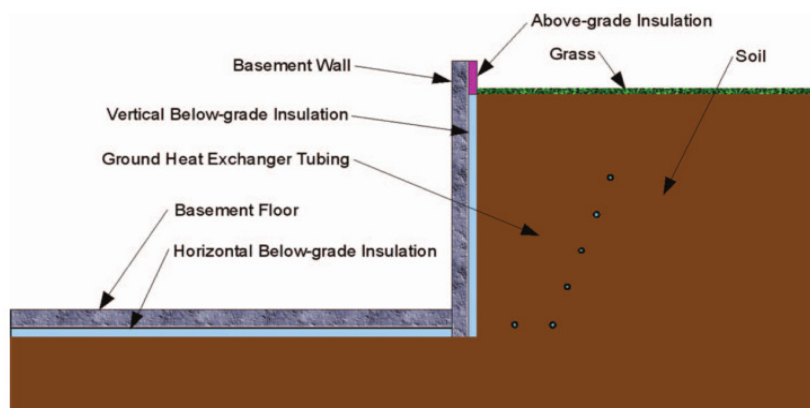
Figure 2.7: Cross section of foundation GHE [30]

A numerical model of a horizontal heat exchanger, installed below the underground parking lot, was developed by Nam et al. [32]. The computational domain of the model is simplified by introducing a symmetry plane as shown in Figure 2.8. The dimensions of the computational domain are 0.3 m wide, 7.65 m deep, and 100 m long. The centre to centre distance between the pipes is set to 0.3 m. The computational domain comprises an epoxy plain concrete layer (0-0.05 m deep), a concrete layer (0.05-0.65 m deep), a soil layer (0.65-7.65 m deep), and a pipe installed at a depth of 0.65 m. The model incorporates several mechanisms of the heat transfer to the ground surface, including the sky radiation, solar radiation, ground surface radiation, evaporation, and convection. On the floor surface of the parking lot, it is merely the convection is considered. While the adiabatic conditions are applied to the right and left sides of the computational domain. The sensitivity analysis is conducted using this model considering different pipe spacing, pipe diameter, and flow rate, temperature of circulating water, burial depth, and operation conditions. Nam et al. conclude that the optimum heat transfer rate with a less installation cost is yielded by the GHE which has an outer diameter of 0.032 m, shank spacing of 0.3 m, flow rate of 9.52 l/min, and buried between the concrete and soil.
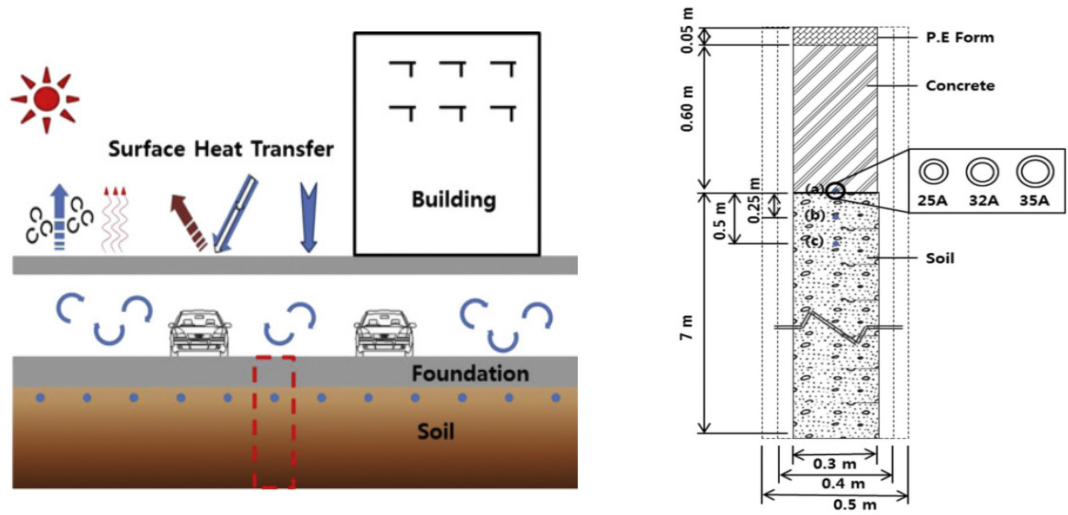
Figure 2.8: Computational domain of the foundation horizontal heat exchanger [32]

An interesting 2D transient model of a horizontal GHE was developed by Wu et al. [6]. Different boundary conditions are applied to the computational domain namely, the adiabatic conditions are applied to the lateral boundaries and the constant temperature condition at the bottom boundary. Then, the thermal performance of the GHE, under various ambient air temperature, soil thermal conductivity, wind speed, and intermittent operation, is investigated. The model ignores the effects of solar radiation and evaporation. The simulation results show that the effect of wind speed does not significantly affect the thermal performance of the GHE.

A 2D finite volume model was proposed by Gan et al. [33], to investigate the transient response of a horizontal GHE operating under freezing and thawing conditions. The model takes into account the changes of soil thermophysical properties that vary with temperature, time, location, and soil constituents. The model considers the effect of dynamic ambient air temperature, however, ignores the effects of radiation and evaporation on the ground surface. The ambient temperature is computed using Equation 2.5. The computational domain of the model is set to have dimensions: 10 m wide and 10 deep. A non-uniform mesh, consists of 720000 quadrilateral cells, is applied to discretise the computational domain. The mesh is fine nearby the pipe and being coarse gradually toward the bottom of the computational domain.

$$T_a = T_{max} - \frac{T_{max} - T_{min}}{2}\left[1 - sin\left(\frac{(t-9)\pi}{12}\right)\right] \qquad (2.5)$$

where T_a is the ambient temperature at any hour of a day (ºC), T_{max} and T_{min} are the maximum and minimum ambient temperatures in a month (ºC), and t is the time period (hour).

The initial soil temperature before the operation of GHE is determined using the following analytical equation:

$$T = T_m - T_{amp}e^{-Z/D}\sin\left((t - t_0)\frac{2\pi}{365} - \frac{Z}{D} - \frac{\pi}{2}\right) \tag{2.6}$$

where T is the initial soil temperature (°C), T_m is the annual mean temperature of soil (°C), T_{amp} is the annual amplitude of surface temperature (°C), t is the time period (day), t_0 is the time lag (day), Z is the soil depth (m), and Z_d is the dumping depth (m).

The dumping depth is calculated as:

$$Z_d = \sqrt{(365/\pi)(86400k/\rho c_s)} \tag{2.7}$$

where Z_d is the dumping depth (m), k is the soil conductivity (W/mK), ρ is the soil density (kg/m³), and c_s is the soil specific heat (J/kgK).

Kupiec et al. [34] suggested a 1D unsteady heat conduction model for a parallel-arrangement horizontal GHE. The model treats the heat exchanger as perfect mixing tanks which are arranged in a number of segments (refer to Figure 2.9). The model considers the temperature changes inside mixing tanks merely occur in a direction parallel to the pipes. The soil domain, where the GHE is buried, is assumed to be a semi-infinite medium. It is composed of upper and lower layers. The topsoil temperature is influenced by the ambient air temperature variations, while the temperature of the bottom layer is assumed to remain constant.
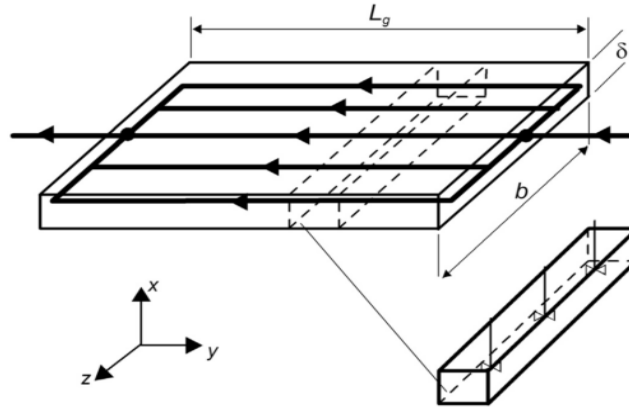
Figure 2.9: The horizontal GHE represented as a cascade of a perfect mixing tank

Rigorous mathematical models for both horizontal and vertical GHEs were proposed by Florides et al. [35]. In these models, the changes of fluid energy inside the control volume are considered as results of thermal diffusion, advection, and heat loss, as represented in Equation 2.9, in rectangular coordinates x, y, z as:

$$\rho_f c_f \frac{\partial T_f}{\partial t} = \rho_f v_f c_f \frac{\partial T_f}{\partial z} + \left[\frac{\partial}{\partial x}\left(-k_f \frac{\partial T_f}{\partial x}\right) + \frac{\partial}{\partial y}\left(-k_f \frac{\partial T_f}{\partial y}\right) + \frac{\partial}{\partial z}\left(-k_f \frac{\partial T_f}{\partial z}\right)\right] + \frac{h_f}{d}(T_f - T_p)$$

$$\tag{2.8}$$

The heat transfer inside the pipe is considered as results of conduction and convection, which is represented as:

$$\rho_p c_p \frac{\partial T_p}{\partial t} = \left[\frac{\partial}{\partial x}\left(-k_p \frac{\partial T_p}{\partial x}\right) + \frac{\partial}{\partial y}\left(-k_p \frac{\partial T_p}{\partial y}\right) + \frac{\partial}{\partial z}\left(-k_p \frac{\partial T_p}{\partial z}\right) \right] + \frac{h_f}{d}\left(T_p - T_f\right) \qquad (2.9)$$

The thermal analysis for the soil domain is based on three-dimensional conduction heat transfer illustrated as:

$$\rho_g c_g \frac{\partial T_g}{\partial t} = \left[\frac{\partial}{\partial x}\left(-k_g \frac{\partial T_g}{\partial x}\right) + \frac{\partial}{\partial y}\left(-k_g \frac{\partial T_g}{\partial y}\right) + \frac{\partial}{\partial z}\left(-k_g \frac{\partial T_g}{\partial z}\right) \right] \qquad (2.10)$$

where ρ is the density (kg/m³), c is the specific heat (J/kgK), T is the temperature (K), t is the time step (s), v_f is the average fluid velocity (m/s), d is the pipe diameter (m), h_f is the convective heat transfer coefficient (W/m²K), and k is the thermal conductivity (W/mK). The subscripts f, p, and g denote the fluid, pipe, and ground, respectively.

The vertical GHE consists of a single U-shaped pipe buried in a multi-layer soil. Each soil layer varies in depths and thermal properties. The horizontal GHE model represents a multi U-shaped pipe buried at a specific depth below the ground surface. Both the horizontal and vertical GHEs are identical in diameter and pipe length. In this model, it is not clear what types of boundary conditions are applied and how the seasonal changes in soil temperature are counted. The performances of both GHEs are compared by taking into account the effect of initial soil temperature, centre to centre distance of the pipes and soil diffusivity. The results show that under the same design conditions, the performance of the vertical GHE is better.

A new analytical transient model of a horizontal GHE was presented by Fontaine et al. [36]. In this model, the heat transfer is analysed based on the relationship between fluid temperature and heat flux variation along a horizontal pipe. It is different from the standard finite line source model, which considers a constant heat flux along the pipe. The new model allows considering the variation of the heat flux along the pipe by dividing the pipe into small segments. The heat flux is assumed constant in each segment. Adiabatic boundary conditions are applied to each side of the soil domain, except for the soil surface, which is imposed a constant temperature of 0 °C. The proposed model has been validated by comparing the resulting soil temperature responses against those generated by a 3D finite element model. The model enables us to predict the profile of soil temperature in directions parallel to the pipe. The simulation results reveal that considering the latent heat effect, caused by the melting of the ice at the soil surface, contributes to an overestimation of the soil temperature. Figure 2.10, shows the geometry of the horizontal GHE utilised in this study.

$T_s = 0^oC$

$q(y)$

T_{fo}

D

T_{fi}

L
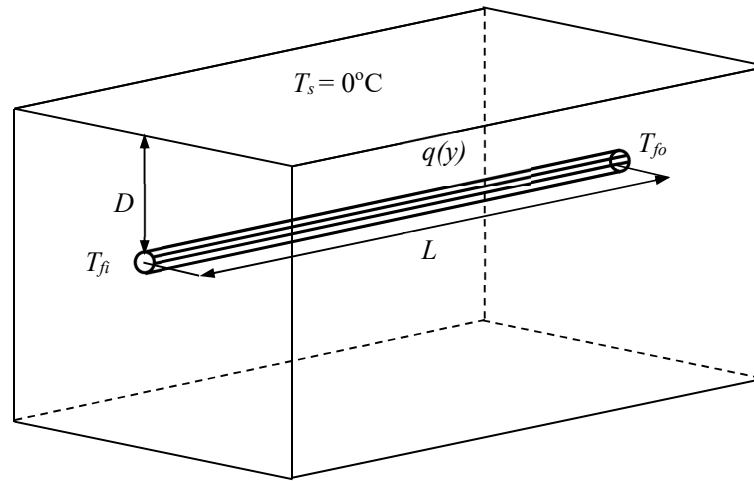
Figure 2.10: Geometry of the horizontal GHE [36]

An equation for assessing the trench length of a horizontal spiral coil heat exchanger was proposed by Kim et al.[37]. It is based on the analytical equation to calculate the borehole length suggested by Kavanaugh and Rafferty [38]. The equation treats the ground as an unsaturated medium subjected to a constant heat from the GHE. In this equation, the thermal resistance of the borehole is replaced with the thermal resistance of the pipe. The effect of ambient conditions on the ground temperature is counted by incorporating the harmonic function of soil temperature into the GHE model. The equation is then verified using the result obtained from the validated CFD simulation model. Kim et al., concludes that the presented design equation is reliable.

Sanaye and Niroomand [39] presented a thermo-economic model of a horizontal ground source heat pump. The thermal modelling of the heat pump is developed based on a thermodynamic analysis in order to specify the length of the evaporator and condenser, mass flow rate of the refrigerant, and compressor power. While the GHE model is developed by considering a six parallel-pipe configuration per trench, as illustrated in Figure 2.11. The configuration is selected to minimise the pressure drop of the heat carrier fluid. The Nelder-Mead and Genetic Algorithm methods are used to generate the solution of the proposed thermo-economic model. The performance of the horizontal ground source heat pump under different climates, soil types, and heat pump capacities is simulated using the model. Sanaye and Niroomand conclude that both the technical and economic performances of the heat pump are affected by the climate and geological conditions. The model ignores the effect of thermal resistance between the pipes. In addition, the technical and economic analysis of the ground source heat pump which considers its dynamic load is yet presented.
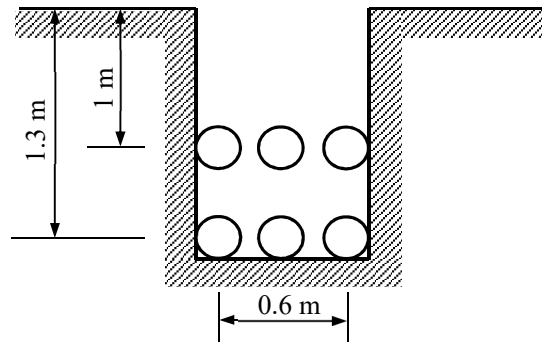
Figure 2.11: Configuration of the horizontal GHE with six pipes per trench [39]

Long-term technical and economic performance of a horizontal ground source heat pump for both heating and cooling applications was investigated by Kayaci and Demir [40]. In this study, the transient performance of the GHE coupled to a heat pump is studied using a validated numerical model. The computational domain of the GHE spans from the centre of the pipe to a distance between the pipe, as the researchers assume the symmetrical heat transfer for both sides of the soil domain. On the ground surface, the convection, evaporation, solar radiation, incident and emitted long wave radiation, are applied. While, the economic analysis is conducted by assessing both the investment and operational costs. Based on both the technical parameters (e.g. pipe length, pipe diameter, pipe spacing, number of parallel pipes, burial depth) and the increase rate in electricity prices, the optimisation parameter is determined.

A new configuration of the horizontal GHE, called the flat-panel ground heat exchanger, was first introduced by Bottarelli et al. [41]. The heat exchanger consists of two horizontal pipes connected in series, as illustrated in Figure 2.12. The pipes are mounted on the top and bottom of a trench filled with encapsulated phase change materials. A 2D finite element model was developed by Bottarelli et al., in order to study the thermal characteristics of the flat-panel ground heat exchanger. The model treats the soil domain as a porous medium. It also considers the effect of groundwater flow that may affect the thermal characteristic of the GHE. The thermal interaction between the ground surface and the atmosphere is counted by applying a transient heat flux condition. The effectiveness of the PCMs, as the backfill material, is compared with the use of the coarse gravel. The results show that the GHE with PCMs as backfill material has a lower performance than that with the coarse gravel. Bottarelli et al. [42] continued their work to investigate the effect of using soil and encapsulated PCMs mixtures as backfill materials. The results show that the GHE with the soil and encapsulated PCMs mixtures have a relatively higher surface temperature than that without the PCMs during winter, and, conversely, lower during summer.
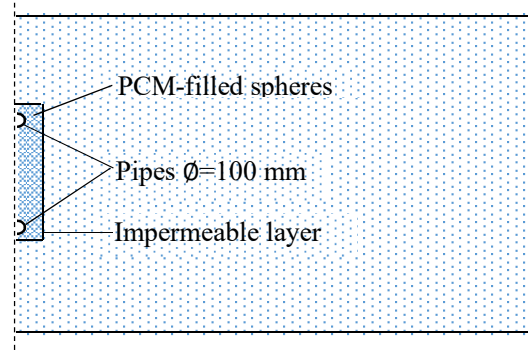
Figure 2.12: Schematic of the flat-panel GHE

Bortoloni et al. [43] developed an analytical line source model to study the thermal performance of the flat-panel GHE. In this study, the flat-panel GHE is treated as an equivalent slinky-coil having the same surface area of heat transfer. The soil domain is assumed as an isotropic medium, in which its surface boundary is determined based on the sinusoidal analytical function of the soil temperature.

A study on the optimisation of the horizontal GHE was presented by Pandey et al. [44] using both the Taguchi method and utility concept. Eight design parameters influencing the optimum length of the GHE including fluid thermal conductivity, fluid specific heat, fluid viscosity, fluid density, fluid mass flow rate, pipe thermal conductivity, pipe diameter, and burial depth are studied. The results reveal that the optimum length of the horizontal GHE is significantly influenced by pipe thermal conductivity and fluid specific heat for the cooling mode, while in the heating mode are the pipe thermal conductivity and diameter.

2.3.2 Vertical GHE models

A number of studies investigating the vertical GHEs' thermal characteristic were presented by several authors. A numerical model based on the finite volume method was proposed by Li et al. [45], to simulate the thermal performance of a borehole heat exchanger (BHE). The model is developed by considering three-dimensional transient heat transfer in the borehole and soil domain. It only half-domain of the GHE is modelled since the heat transfer rate is equal on the symmetry plane (refer to Figure 2.13). An unstructured triangular mesh is used to discrete the cross section domain of the GHE. The size of the mesh cells is finer inside the borehole and being coarse gradually inside the soil domain. This model ignores the effect of groundwater flow and periodic soil temperature fluctuations caused by seasonal changes. The model is validated against the experimental data and it is obtained a significant discrepancy between the theoretical and experimental results, in the first 36 hours of operation of the GHE.
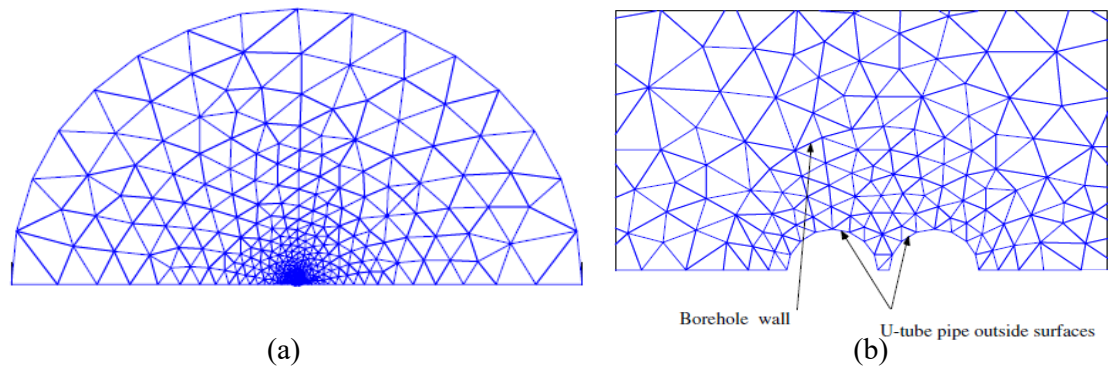
Figure 2.13: (a) The unstructured triangular mesh of the cross section of the BHE, (b) magnification of the mesh of borehole field [45]

The potential application of a bridge pile ground source heat pump used for snow melting system of a bridge deck was studied theoretically by Han and Yu [46]. A 3D single pile heat exchanger model is developed to estimate the heat extraction rate of each GHE in order to satisfy the heating load of the bridge deck, determined based on five atmospheric conditions, namely, air dry bulb temperature, relative humidity, wind velocity, rate of snowfall and apparent sky temperature. In this model, the undisturbed ground temperature is considered as a function of depth and time. While, the ground is assumed to have constant thermal properties. The performance of the ground source heat pump considering various climate conditions and pipe configurations (e.g. U-shaped, W-shaped, and spiral-shaped) is then simulated. The simulation results reveal that the spiral shaped heat exchanger can extract 2-3 times more energy than those of the W and U shaped, respectively. It is found that increasing the fluid velocity from 0.3 to 0.7 m/s can increase the heat extraction rate of the spiral shaped heat exchanger around 20%, while it is no obvious for those the W and U shaped. In addition, the number of pile heat exchangers required to satisfy the heating load of the bridge deck significantly influenced by the climate conditions. The researchers conclude that the pile ground source heat pump for the bridge deck snow removal system is less suitable for the region with large snowfall and low ground temperature. Han and Yu [47] continued their work by incorporating the encapsulated phase change material into the pile. The results reveal, using 3% of phase change material can reduce 25-40% of pile numbers required due to the improvement of the heat extraction generated by the heat exchanger.

A theoretical study to specify the borehole heat exchanger depth was conducted by Chen at al. [48], using an artificial neural network model. In this study, the training and testing data for the artificial neural network model are derived from the previously developed 3D transient model of the BHE. The input parameters of the model consist of the inlet water temperature, fluid flow rate, grout thermal conductivity, soil thermal conductivity, underground water flow and heat

flux. While, the borehole depth is as the output. This model ignores the effects of volumetric heat capacity and soil porosity. Different neuron numbers (varies from 5 to 15) are tried to optimise the BHE model. The simulation results reveal that the minimum error is reached when the number of neurons is 10.

A 3D finite element model was developed by Al-Khoury et al. [49] to simulate the thermal behaviour of a double U-shaped pipe BHE. The model assumes one-dimensional heat transfer inside the borehole and three-dimensional heat transfer in the surrounding soil. The soil is treated as a porous medium. The model also takes into account the effect of the groundwater flow. The seasonal changes of the soil temperature are modelled by assuming a constant temperature across the soil domain, which follows by applying a convective boundary condition on the ground surface. The approach seems over simplified since a range of factors, e.g. evaporation, precipitation and irradiation affect the seasonal soil temperature changes.
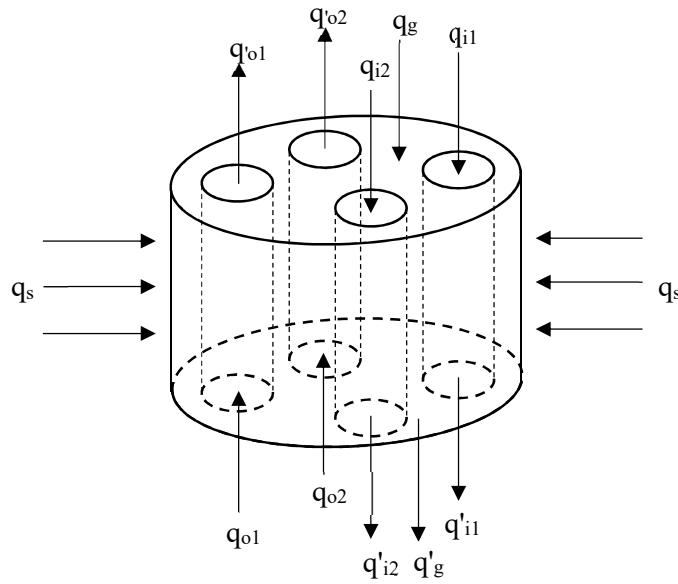
Figure 2.14: Control volume of a double U pipes BHE [49]

Figure 2.14 shows the control volume of a double U pipes BHE consists of two pipes-in (denoted as i1 and i2), two pipe-out (denoted as o1 and o2) and grout (denoted as g). The governing equations for the borehole field are summarised as follows:

For the pipe-in 1:

$$\rho_f c_f \frac{\partial T_{i1}}{\partial t} dV_{i1} - k_f \frac{d^2 T_{i1}}{dz^2} dV_{i1} + \rho c_f v_f \frac{\partial T_{i1}}{\partial t} dV_{i1} = b_{ig1}(T_{i1} - T_g) dS_{ig1} \qquad (2.11)$$

For the pipe-in 2:

$$\rho_f c_f \frac{\partial T_{i2}}{\partial t} dV_{i2} - k_f \frac{d^2 T_{i2}}{dz^2} dV_{i2} + \rho c_f v_f \frac{\partial T_{i2}}{\partial t} dV_{i2} = b_{ig2}(T_{i2} - T_g) dS_{ig2} \qquad (2.12)$$

For the pipe-out 1:

$$\rho_f c_f \frac{\partial T_{o1}}{\partial t} dV_{o1} - k_f \frac{d^2 T_{o1}}{dz^2} dV_{o1} + \rho c_f v_f \frac{\partial T_{o1}}{\partial t} dV_{o1} = b_{og1}(T_{o1} - T_g) dS_{og1} \tag{2.13}$$

For the pipe-out 2:

$$\rho_f c_f \frac{\partial T_{o2}}{\partial t} dV_{o2} - k_f \frac{d^2 T_{o2}}{dz^2} dV_{o2} + \rho c_f v_f \frac{\partial T_{o2}}{\partial t} dV_{o2} = b_{og2}(T_{o2} - T_g) dS_{og2} \tag{2.14}$$

For the grout:

$$\rho_g c_g \frac{\partial T_g}{\partial t} dV_g - k_g \frac{d^2 T_g}{dz^2} dV_g = b_{ig1}(T_g - T_{i1}) dS_{ig1} + b_{ig2}(T_g - T_{i2}) dS_{ig2}$$

$$+ b_{og1}(T_g - T_{o1}) dS_{og1} + b_{og2}(T_g - T_{o2}) dS_{og2} \tag{2.15}$$

For the soil:

$$(\rho c)_{sw} \frac{\partial T_s}{\partial t} + (\rho c)_w \left(v_{wx} \frac{\partial T_s}{\partial x} + v_{wy} \frac{\partial T_s}{\partial y} + v_{wz} \frac{\partial T_s}{\partial z} \right) - k_{swx} \frac{\partial^2 T_s}{\partial x^2} - k_{swy} \frac{\partial^2 T_s}{\partial y^2}$$

$$- k_{swz} \frac{\partial^2 T_s}{\partial z^2} - H = 0 \tag{2.16}$$

where ρ is the density (kg/m³), c is the specific heat (J/kgK), T is the temperature (K), t is the time step (s), V is the partial volume (m³), k is the thermal conductivity (W/mK), v is the velocity, b is the contact resistance (W/m²K), S is the area of contact surface (m²), H is the heat generated (W/m³) and n is the soil porosity. In which subscript r is the refrigerant, $i1$ and $i2$ are the 1st and 2nd pipe-in, respectively, $o1$ and $o2$ are the 1st and 2nd pipe-out, respectively, g is the grout material, s is the soil, w is the groundwater, and x, y, z are the spatial directions.

A 3D implicit finite difference model of a BHE was presented by Lee and Lam [50]. In this model, the computational domain is discretised based on the rectangular coordinate system, as illustrated in Figure 2.15. Several assumptions are made to simplify the thermal analysis of the GHE. The ground is considered as an isotropic and homogeneous material. This model ignores the contact resistance between the borehole and the ground. Also, the constant temperature conditions are applied to the top and bottom boundaries of the soil domain. The heat transfer in the soil domain is represented as:

$$\frac{T_{i,j,m}^{n+1} - T_{i,j,m}^n}{\Delta t} = \left(\frac{q_{x+} + q_{x-} + q_{y+} + q_{y-} + q_{z+} + q_{z-} + qs}{\rho_g c_g \Delta x_j \Delta y_m \Delta z_i} \right) \tag{2.17}$$

where T is the ground temperatures (K), Δt is the time step (s), q is the heat in the control volume of the ground (W/m), qs is the source term (W), ρ is the density (kg/m³), c is the specific heat (J/kgK), Δx, Δy, Δz are the distances in x, y, and z directions, respectively. The superscripts $n+1$ and n denote the new and the previous time steps, respectively. The subscripts i, m and

j denote the indices in x, y, and z directions, respectively, g is the ground, $(+)$ is the downstream direction of the control volume, and $(-)$ is the upstream direction of the control volume.
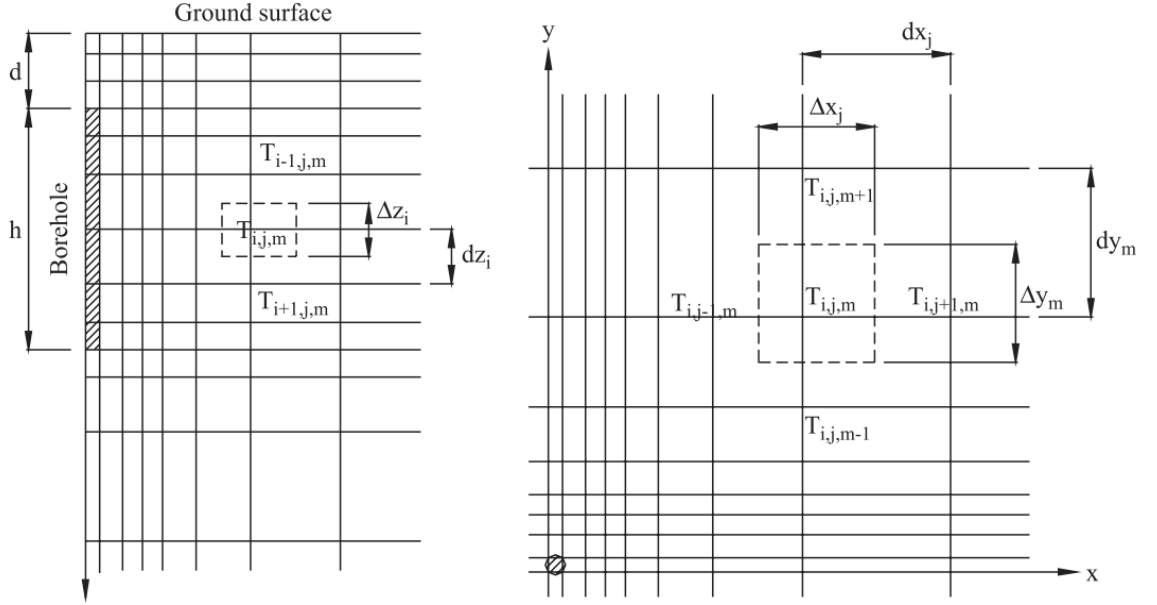
Figure 2.15: Grid and finite difference scheme for the ground around the borehole [50]

The model considers different heat transfer process inside the borehole namely, with/without the fluid flow inside the pipe, refer to Figure 2.16.

The governing equation of the GHE with the fluid flow inside the pipe is given as:

$$(-1)^{m1}\dot{m}_f c_f \frac{dT_{flu}}{dz} = \sum_{v=1}^{u-1} \frac{T_{flu} - T_{flv}}{R_{uv}} + \frac{T_{flu} - T_b}{R_{uu}} + \sum_{v=u+1}^{N} \frac{T_{flu} - T_{flv}}{R_{uv}} \qquad (2.18)$$

While the governing equation of the GHE without the fluid flow inside the pipe is given as:

$$\pi r_{pi}^2 \rho_f c_f \frac{dT_{flu}}{dz} = \sum_{v=1}^{u-1} \frac{T_{flu} - T_{flv}}{R_{nfuv}} + \frac{T_{flu} - T_b}{R_{nfuu}} + \sum_{v=u+1}^{N} \frac{T_{flu} - T_{flv}}{R_{nfuv}} \qquad (2.19)$$

where $\dot{m}_f$ is the fluid mass flow rate (kg/s), ρ_f is the fluid density (kg/m³), c_f is the fluid specific heat (J/kgK), T_{flu} is the fluid temperature in the pipe u (K), z is a distance in the z direction (m), T_{flv} is the fluid temperature in the pipe v (K), R_{uv} is the coefficient of thermal interference between the pipe u and the pipe v (mK/W), R_{uu} is the coefficient of thermal interference between the pipe and borehole (mK/W), T_b is the borehole temperature (K), R_{nfuv} is the coefficient of thermal interference between the pipe u and the pipe v (mK/W) when no fluid flow is considered, R_{nfuu} is the coefficient of thermal interference between the pipe and borehole (mK/W) when no fluid flow is considered, N is the number of pipes inside the borehole, and $m1$ is equal to 1 for downward flowing pipe, 2 for upward flowing pipe.
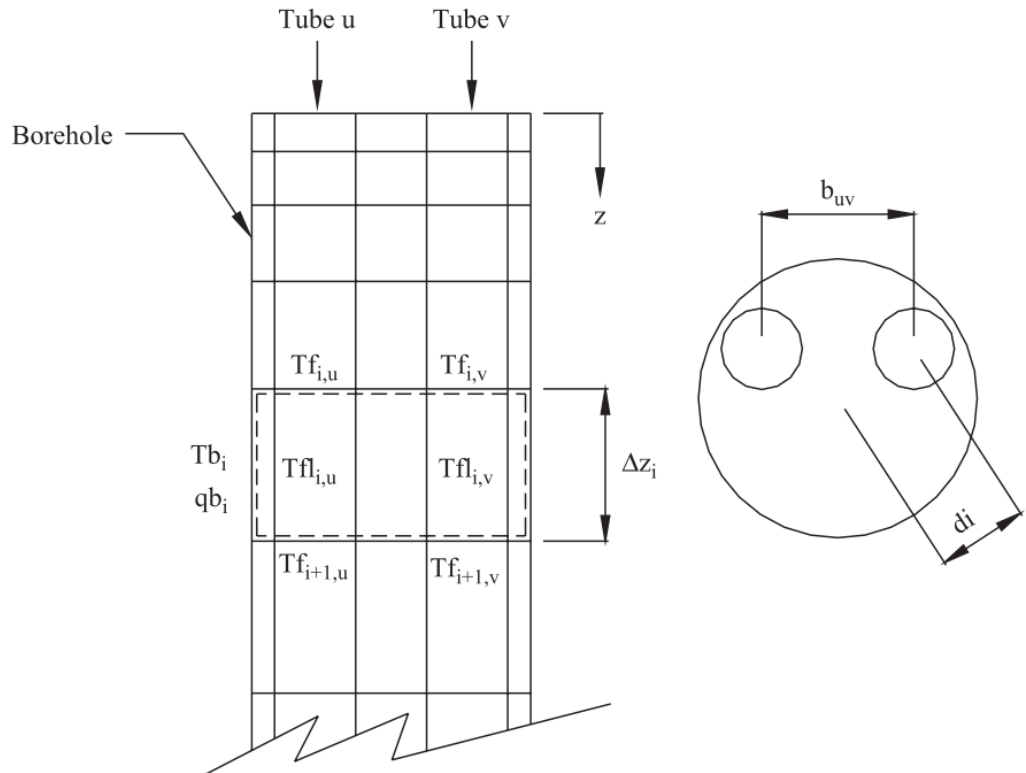
Figure 2.16: Grid scheme inside the borehole field

Lee [51] continued his work by modifying the previously proposed heat exchanger model, in order to consider the effect of multiple soil layers on thermal performance of the BHE. This model ignores the effect of the groundwater flow. The thermal properties of an inhomogeneous ground are determined based on equivalent approaches expressed in Equations 2.20-2.22. Figure 2.17 shows a control volume of an inhomogeneous ground.
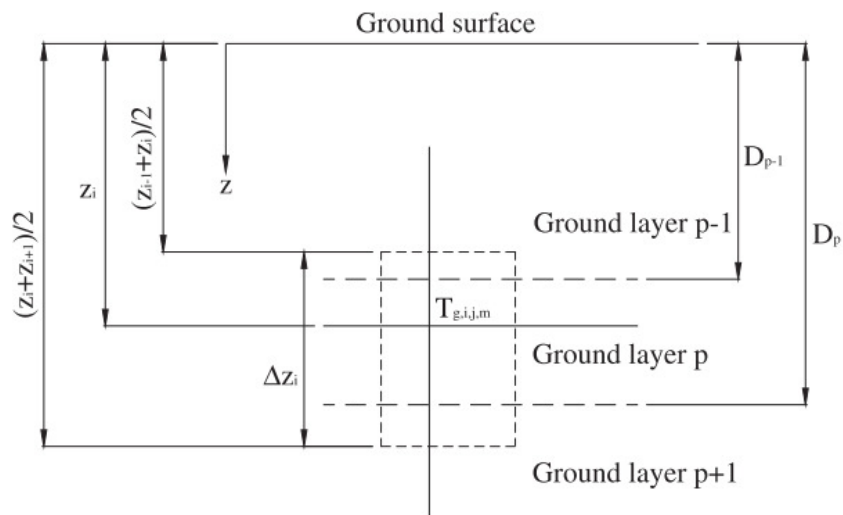
Figure 2.17: A control volume of an inhomogeneous ground [51]

The equivalent thermal conductivity of the ground in the transverse direction is given as:

$$k_{gr,eq,x}$$
$$= \frac{k_{gr,p-1}\left(D_{p-1} - \frac{z_{i-1}+z_i}{2}\right) + k_{gr,p}(D_p - D_{p-1}) + k_{gr,p+1}\left(\frac{z_{i-1}+z_i}{2} + D_p\right)}{\Delta z_i} \qquad (2.20)$$

While the equivalent thermal conductivity of the ground in the vertical direction is given as:

$$k_{gr,eq,z+} = \frac{\Delta z_i}{\frac{D_{p-1}-z_i}{k_{gr,p-1}} + \frac{D_p - D_{p-1}}{k_{gr,p}} + \frac{z_{i+1}-D_p}{k_{gr,p+1}}} \qquad (2.21)$$

The equivalent volumetric heat capacity is determined as:

$$\rho c_{gr,eq}$$
$$= \frac{\rho c_{gr,p-1}\left(D_{p-1} - \frac{z_{i-1}+z_i}{2}\right) + \rho c_{gr,p}(D_p - D_{p-1}) + \rho c_{gr,p+1}\left(\frac{z_{i-1}+z_i}{2} + D_p\right)}{\Delta z_i}$$
$$(2.22)$$

where k is the equivalent thermal conductivity (W/mK), D is the bottom depth of the ground layer (m), Δz is the distance of the grid in the z direction (m), z is the distance from the ground surface to the nodal of a computational domain (m), c is the specific heat (J/kg-K), ρ is the density (kg/m³). The subscripts gr denotes ground, eq means equivalent, x is the transverse direction, z is the vertical direction, i is the index in the z direction, p is the index of the ground layer.

Lee and Lam [52], modified the previously suggested multi-ground-layer BHE model to take into account the effect of the non-uniform groundwater flow in the soil layer. The proposed GHE model is validated against the results generated by the Fluent simulation model. Taking into account the groundwater flow velocity of 10^{-7} m/s, the simulation result reveals a deviation of 0.2 °C in outlet fluid temperature from the Fluent model after ten days of operation.

A 3D numerical model of a BHE was developed by Kim et al. [53] to reduce the computational time and computer memory which are inherent in solving the numerical model. It is developed by applying techniques of domain decomposition as well as state model reduction. In this model, the soil domain is divided into several subzones in both vertical and horizontal directions, as shown in the Figure 2.18. Different time steps are applied to the horizontal subzones. In which, a smaller time step is applied to the innermost subzones and the larger time step for the outwards zones. Using this approach, the computational time is reduced about 30 per cent. In this model, it is not clear how the thermal interaction between the ground surface and atmosphere considered.
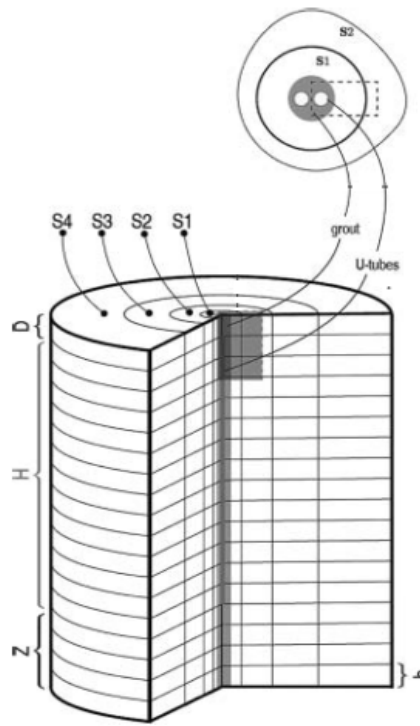
Figure 2.18 Schematic of a BHE with a decomposed soil layer

Rees [54] developed a 2D finite volume model of a BHE focusing on short to medium time scale thermal response. The model considers the transient heat transfer around the pipe system. The pipe is assumed has a constant temperature along its length. The outlet fluid temperature is calculated directly without iterative procedure by using an analogy of evaporating-condensing heat exchanger.

A numerical model for a BHE with a dynamic boundary condition on the outer radius of the soil domain was presented by Wang et al. [55]. The model is developed to deal with the limitations of the adiabatic and constant temperature boundary conditions, as the heat flux or temperature at the far end surface of the soil boundary changes after long-term operation of the GHE. The model is validated against the experimental data and used to simulate the GHE's performance. The simulation results of the GHE model with three different types of boundary condition, including the adiabatic, the constant temperature, and the dynamic condition, are compared. It is observed that utilisation of the constant temperature boundary condition generates a relatively lower temperature of the soil domain. On the contrary, it becomes higher when applying the adiabatic boundary condition. Wang et al., conclude that the newly developed model with dynamic thermal boundary conditions generates more accurate results. In this model, the effect of seasonal soil temperature changes is counted by applying the convection heat transfer on the ground surface.

A study on borehole thermal resistance of a vertical GHE, considering a steady state condition, was presented by Sharqawy et al. [56]. In this study, the effects of geometrical parameters, e.g. the shank spacing and pipe position inside the borehole, are investigated using a 2D numerical model. Based on the simulation results, the best-fit correlation of the effective pipe to borehole thermal resistance is proposed and expressed as:

$$R_b = \frac{1}{2\pi k_g}\left[-1.49\left(\frac{s}{d_B}\right) + 0.656\ ln\left(\frac{d_b}{d_p}\right) + 0.436\right] \tag{2.23}$$

where R_b is the effective pipe to borehole thermal resistance (mK/W), k_g is the grout thermal conductivity (W/mK), s is the shank spacing (m), d_b is the borehole diameter (m), d_p is the pipe diameter (m).

A new design of a vertical GHE which incorporates the longitudinal fins on the inner surface of the pipe was presented by Bouhacina et al. [57]. A 3D Fluent simulation model is developed in order to study the thermal behaviour of the new proposed design of the BHE. In this model, it is assumed that the heat transfer on the ground surface solely occurs by convection. The simulation results reveal that the GHE with the longitudinal fins on its inner surface enhances 7% of the heat transfer capacity in comparison with the conventional design.

Shang et al. [58] investigated the soil thermal regime of a BHE that operates under intermittent mode using a 3D heat transfer model. The model takes into account the effects of moisture and heat transfer in the vertical direction. In addition, the effects of grout material, porosity, thermal conductivity, wind speed and solar radiation on the potential of soil temperature recovery are presented. It is observed that the soil properties have a more significant influence on the BHE's performance than the environmental factors.

A numerical BHE model developed based on an electrical analogy, called capacity resistance model, was developed by De Carli et al. [59]. The model allows simulating the heat flow along the U-shaped pipe to the grout and surrounding soil. The heat dissipation from the borehole to the surrounding soil is considered occurs in a radial direction. In order to take into account the soil temperature distribution in the axial direction, both the BHE and soil domain are divided into a number of segments, in a direction parallel to the borehole. The model disregards the effects of backfill thermal capacity and seasonal soil temperature changes. Figure 2.19 shows the computational domain De Carli et al.'s model.
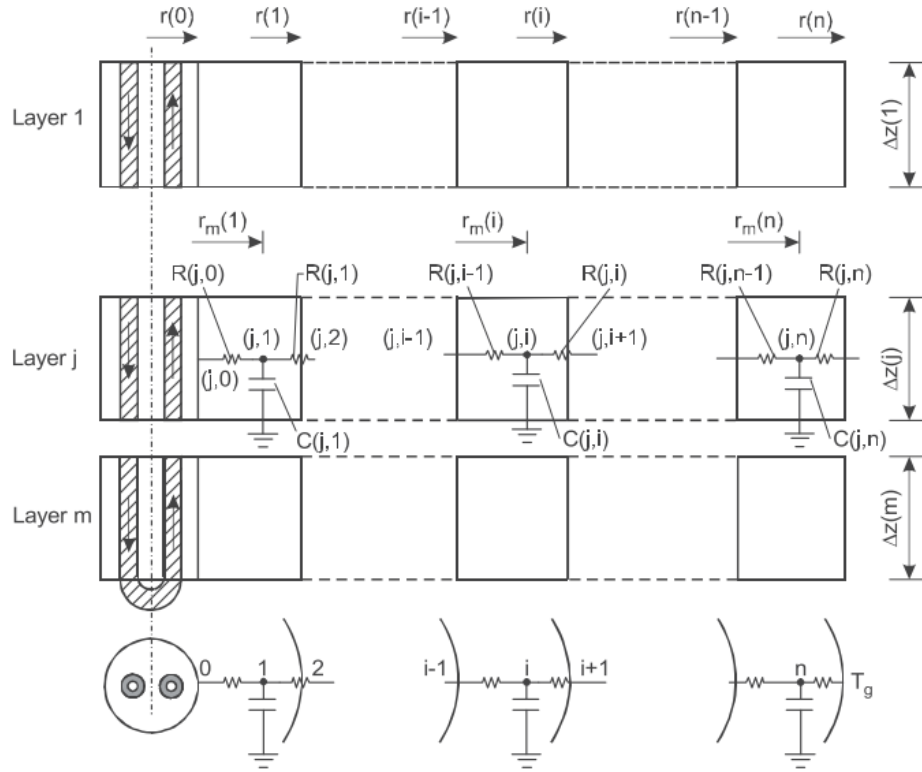
Figure 2.19: Grid scheme for the BHE [59]

De Carli et al.'s model for a vertical GHE is expressed as:

For the heat carrier fluid:

$$\dot{m}_w c_{pw}\left[T_{w,in}(j) - T_{w,out}(j)\right] = 2\pi r_i k \Delta z(j)\left[T_{w,in}(j) - T_{w,out}(j)\right] \qquad (2.24)$$

For the pipe1:

$$\frac{T_{W1}(j) - T_{p,1}(j)}{R_c(j)} + \frac{T_{p,2}(j) - T_{p,1}(j)}{R_{pp}(j)} + \frac{T_0(j) - T_{p,1}(j)}{R_{p0}(j)} = 0 \qquad (2.25)$$

For the pipe 2

$$\frac{T_{W2}(j) - T_{p,2}(j)}{R_c(j)} + \frac{T_{p,1}(j) - T_{p,2}(j)}{R_{pp}(j)} + \frac{T_0(j) - T_{p,2}(j)}{R_{p0}(j)} = 0 \qquad (2.26)$$

For the borehole wall:

$$\frac{T_s(j,1) - T_0(j)}{R_s(j,0)} + \frac{T_{p,1}(j) - T_0(j)}{R_{p0}(j)} + \frac{T_{p,2}(j) - T_0(j)}{R_{p0}(j)} = 0 \qquad (2.27)$$

For the soil:

$$\frac{T_s(j,i-1) - T_s(j,i)}{R_s(j,i-1)} + \frac{T_s(j,i+1) - T_s(j,i)}{R_s(j,i+1)} = C(j,i)\frac{T_s(j,i) - T_{s,-\Delta t}(j,i)}{\Delta t} = 0 \qquad (2.28)$$

where $\dot{m}$ is the mass flow rate (kg/s), c is the specific heat (J/kgK), T is the temperature (K), r is the radius (m), k is the thermal conductivity (W/mK), Δz is a distance in the vertical direction

(m), j is an index in the vertical direction, R is the thermal resistance (mK/W). While the subscript w is the water, p is the pipe, s is the soil, i is internal, c is the convection, po denotes the pipe and borehole wall.

The thermal resistance between the pipe and the borehole wall is expressed as:

$$R_{po} = \left[k_g \beta_0 \left(\frac{r_b}{r_o} \right)^{\beta_1} \right]^{-1} \tag{2.29}$$

where R_{po} is the thermal resistance between the pipe and the borehole wall (mK/W), k_g is the grout thermal conductivity (W/mK), r_b is the borehole radius (m), r_o is the outer radius of the pipe (m), and β_0 and β_1 are the coefficients of the borehole determined based on the geometry of the GHE as illustrated in Figure 2.20.
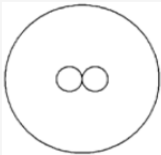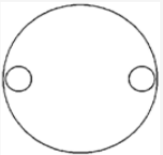
Configuration	(A)	(B)	(C)
β_0	20.10	17.44	21.91
β_1	−0.9447	−0.6052	−0.3796

Figure 2.20: Thermal resistance coefficients of the BHE [59]

Zarrella et al. [60] improved De Carli et al.'s model by incorporating the thermal capacitance of the grout and heat carrier fluid. The model is utilised to investigate the BHE's performance within a short time period.

A capacity resistance model which has an ability to consider the effects of both the axial heat flow and the atmospheric condition has been developed by Zarrella and Pasquier [61]. In this study, the atmospheric condition effect is taken into account by imposing short and long wave radiation, dynamic ambient air temperature, and convective heat transfer on the soil surface.

Experimental and theoretical studies were conducted by Gallero et al. [62] to validate a newly developed BHE model which uses the electrical analogy to count the heat flow within borehole field and g-function method to calculate the thermal flow in the surrounding soil. The model treats the non-homogeneous soil as a homogeneous medium with the average thermal properties gained from the experiment. The U-shape pipe is represented as a single pipe with an equivalent diameter. A constant boundary condition which corresponds to the average vertical ground temperature is imposed on the lateral boundary condition of the soil domain. The variation in heat injection or extraction rates is considered by the use of the superposition principle. The

root mean square and relative errors smaller than 0.2 ℃ and 0.3% for the simulated outlet fluid and borehole temperatures, respectively, were achieved with this model.

A new cylinder source model of a BHE was suggested by Lei et al. [63]. Different from the existing cylinder source models that can only consider a constant load, the new BHE model takes into account the dynamic load based on the actual conditions of heating and cooling. A harmonic technique is used to derive the solution of the composite-cylinder source model. The model ignores the effects of groundwater flow and vertical heat flow in the computational domain. In this study, the single U-shaped pipe is treated as a single pipe with an equivalent diameter. The grout and soil are treated as composite layers which consist of an inner and outer layer, respectively.

An analysis of the thermal response of a BHE considering the effect of the axial heat flow, groundwater flow, and recovery process was presented by Rivera et al. [64] using self-balanced finite line source model. In this model, the heat transfer between the ground surface and atmosphere is counted by applying a constant temperature at the top boundary of soil domain. While the natural geothermal heat flux is considered at the bottom boundary. Rivera et al. [65] presented a finite line source model to observe the thermal response of a BHE. The model considers the effects of the groundwater flow and different types of ground surfaces including sod, bare soil, asphalt and building. The model ignores the effect of variation in the ambient air temperature. The solar radiation is considered by applying a constant temperature value for each type of the ground surface.

 Zhang et al. [66] investigated the technical factors affecting the heat transfer capacity of a BHE by using both the thermal resistance and G function methods. The thermal resistance method is used to calculate the thermal solutions inside the borehole while the G function method is used to estimate the heat transfer rate in surrounding soil. The investigated technical factors include the shank spacing of the U-shaped pipe, grout thermal conductivity, types of circulating fluid, outlet fluid temperature feeding into a heat pump, underground medium, and borehole arrangements.

2.3.3 Hybrid GHE models

The technical challenges associated with GHEs are their performance degradation with an increase in the operation time, which often happens during the heating or cooling seasons. This performance degradation is slow to restore, especially for vertical GHEs. Meanwhile, it can be minimised if the GHEs are run intermittently or with a smaller thermal load, which can be achieved with the proposed GHE system combining both vertical and horizontal arrangements.

To address the performance degradation caused by an imbalance in the heating and cooling loads, a number of researchers have offered hybrid GHE systems and different operation strategies [67].

Hybrid GHE and solar energy systems were suggested by a number of researchers [68-71], to cope with performance deterioration. For example, Dai et al. [68] carried out an experimental study on a solar assisted ground source heat pump system. The system is operated under four different modes: (1) operation of the ground source heat pump only during the daytime while the borehole temperature is recovered naturally during the nighttime; (2) operation of the ground source heat pump only during the daytime and recharging the borehole during the nighttime using the solar energy stored in a solar heat storage water tank; (3) operation of the heat pump during the daytime using the heat source coming from the series operation of a solar-shallow geothermal system (in this scenario, the borehole recovers naturally during the nighttime); (4) operation of the heat pump during the daytime using the heat source coming from the parallel operation of a solar-shallow geothermal system. In the parallel mode, the performance of the heat pump, under three different flow rate ratios of working fluid flowing inside both the solar and shallow geothermal systems, is investigated. The outcomes of this study demonstrate that the hybrid systems can recover the degradation of soil temperature much faster than happens during natural recovery. In addition, the effect of the flow rate ratio in mode 4, has a significant impact on the electricity consumption. The electricity consumption decreases with the increase of the flow rate ratio in the solar heat storage water tank. Furthermore, mode 3 is recommended for use in the coldest months.

Kjellsson et al. [69] analysed the performance of a combined ground source heat pump and solar collector system used to provide indoor heating and hot water for domestic purposes. The outcomes demonstrate that the system works in an optimal regime when the solar energy is utilised to recharge the borehole during winter time and to produce the domestic hot water during summer time.

The performance of a solar assisted ground source heat pump, used for greenhouse heating, was investigated by Ozgener et al. [70] using the exergy analysis method. The exergy analysis is conducted using the measurement data of each component of the solar assisted ground source heat pump. It is found that the highest irreversibility is generated by the greenhouse fan-coil and the exergetic efficiency of the overall system is 67.7%.

Yang et al. [71] presented a theoretical and experimental study on a solar-ground source heat pump system. Four different operation modes are considered (1) a single ground source heat pump mode (the heat pump uses the ground energy solely as the heat source), (2) a combined

operation mode (the heat pump uses shallow geothermal and solar energy as the heat source), (3) a day and night alternate operation mode (the heat pump uses geothermal energy during the night and rainy days, and solar energy during daytime), and (4) a solar U-pipe feeding heat alternate operation mode (the heat pump uses geothermal energy during the night and it turns off during the daytime while the solar energy is injected into the ground through the U-pipe). The experimental COPs of modes 1, 2, 3, 4 are 2.37, 2.69, 2.65 and 2.56, respectively. While the theoretical COPs are found to be 3.48, 3.67, 3.64, and 3.52, respectively, which are quite different from the theoretical values.
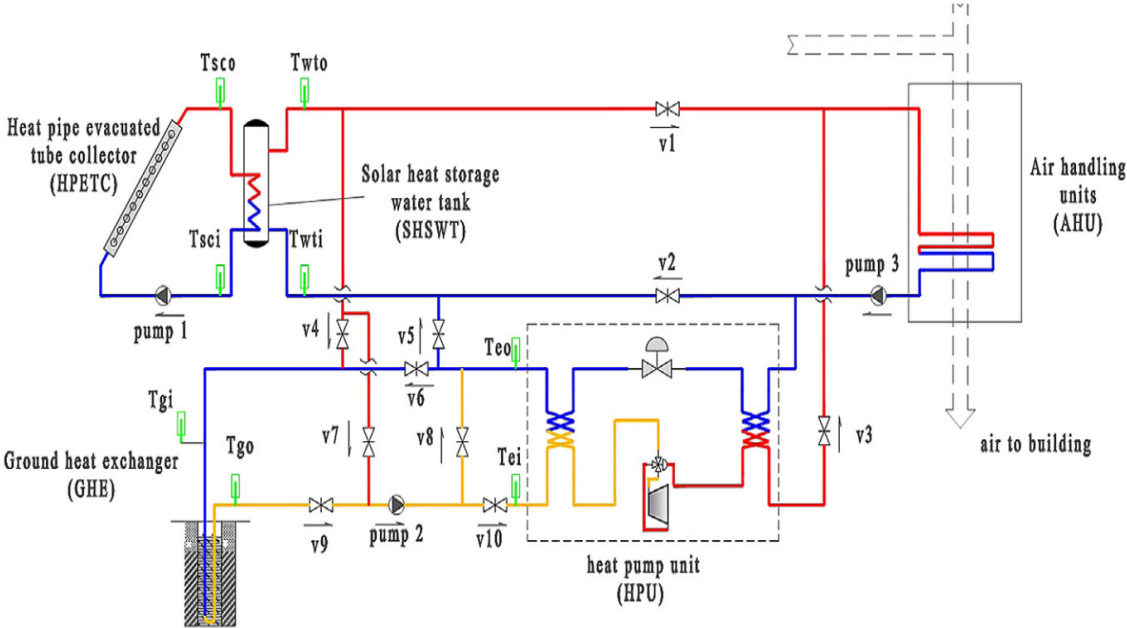
Figure 2.21: Schematic of a hybrid GHE-solar system heat pump [68]

Studies on hybrid ground source heat pump systems with a cooling tower as a supplemental heat rejecter were presented by a number of researchers [64-68]. Park et al. [72] proposed a new parallel system comprising a hybrid ground source heat pump-cooling tower. The new parallel system enables the GHE to be switched off during the recovery period of the soil temperature. The performance of the heat pump is investigated at different flow rates of the fluid in the primary flow loop (the heat pump), GHE, and cooling tower. The results indicate that the parallel system of the ground source heat pump-cooling tower generates 21% higher COP than that generated by the conventional ground source heat pump system.

Man et al. [73] provided the technical and economic analysis of a hybrid cooling tower-ground source heat pump, based on the hourly load of a two-storey residential building located in Hong Kong. The hybrid system in this study not only solves the thermal degradation problem but also reduces the operation and capital costs of the air conditioning system.

A study on the control strategies of a hybrid system of cooling tower-ground source heat pump was presented by Wang et al. [74]. Different control strategies, including the fixed cooling set point, outside air reset, wet bulb reset, and load reset, are examined. The performance of the hybrid system with different control strategies is then compared with the stand-alone system with the vertical GHEs that has a borehole field twice as large as that the hybrid system. The results demonstrated that the stand alone vertical GHEs consume less electrical energy than the hybrid system in the first year of the operation. The performance of the conventional system of vertical GHEs gradually decreases due to an imbalance between heating and cooling load. The second best performance in the first year is yielded by the hybrid GHE system with the fixed setpoint temperature of 26.7 °C. Wang et al., concluded that the hybrid system with different control strategies not only reduce the size borehole field but also offer the energy savings in long-term operation.

Sagia et al. [75] presented a study of a hybrid cooling tower-ground source heat pump. The performance of the hybrid system is assessed by considering different building's glazing properties, fixed temperatures of working fluid feeding into the heat pump, and percentage of the waste heat rejected by the cooling tower. The correlation between the cooling tower capacity and the borehole length is then presented. It is found that the higher the cooling tower capacity, the shorter the borehole length is required. The effect of the pressure drop per packing height of the cooling tower is also investigated. The result reveals that the ratio of pressure drop to the height of packing of the cooling tower is inversely proportional to the increasing the ratio of water flow rate to dry air flow rate.

Fan et al. [76] presented a theoretical design of a hybrid cooling tower-ground source heat pump, which takes into account the effect of borehole distance, borehole depth, and thermal properties of the grout. In this study, the combined operation strategies are introduced. The results show that the lowest energy consumption is obtained when the control strategies of the entering water temperature and wet-bulb temperature differences are combined.

Gang et al. [77] presented a new control strategy by considering either the cooling tower or the vertical GHE as the heat pump's additional heat rejecter. If the cooling tower is treated as the additional heat rejecter, it will run continuously until the fluid temperature at the outlet of the plate heat exchanger (a heat exchanger which is coupled with the GHE) is 2 °C lower than the exit fluid temperature of the cooling tower. Conversely, if the GHE is treated as the additional heat rejecter, it will operate continuously until the temperature of the fluid that exits the cooling tower is 1 °C lower than the temperature of the fluid exiting the plate heat exchanger. The new

control method provides more energy savings than those provided by two frequently used methods (schedule based control and temperature differential based control).
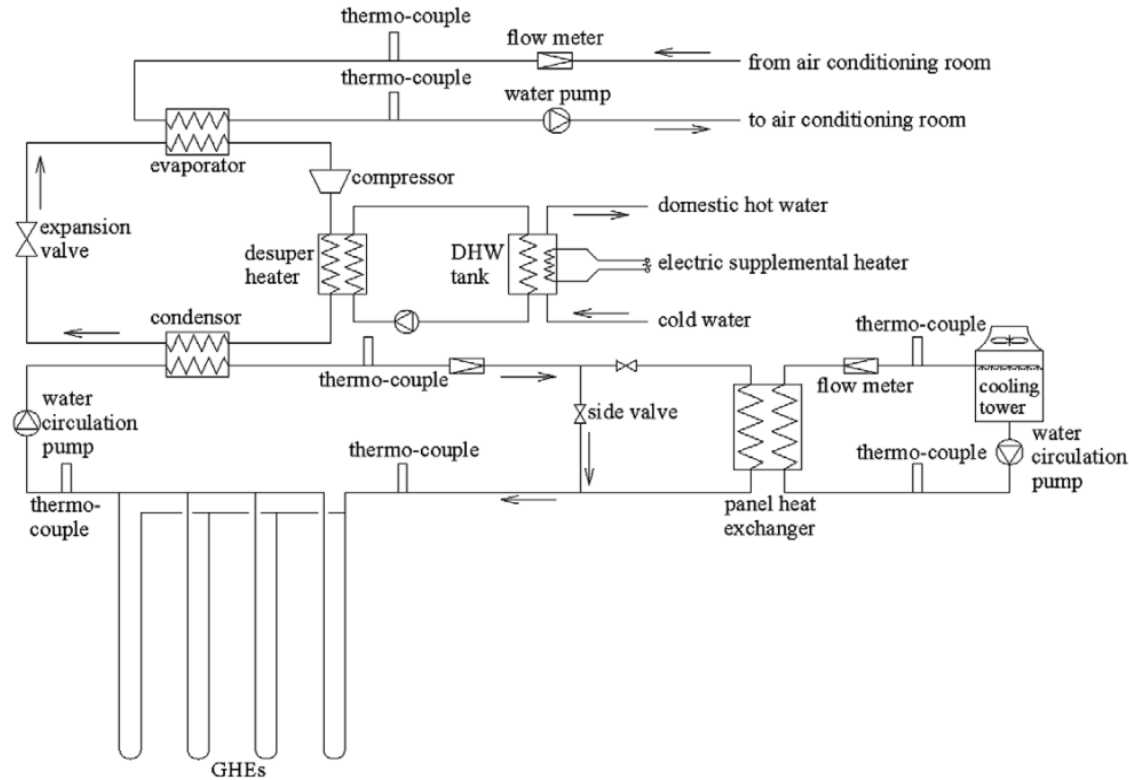
Figure 2.22: Schematic of a hybrid GHE-cooling tower heat pump [73]

Canelli et al. [78] analysed the energy, economic and environmental performances of three different hybrid ground source heat pump systems including (1) a hybrid boiler-chiller-ground source heat pump, (2) a hybrid boiler-chiller-ground source heat pump and fuel cell, and (3) a hybrid boiler-chiller-ground source heat pump and photovoltaic thermal system. The system is optimised to meet the heating and cooling conditions of both residential and commercial buildings, which are in a sharing load. The results indicate that the hybrid system with the fuel cells and the photovoltaic thermal system has a notable advantage in terms of energy savings, operational costs and carbon emission reductions.

A fuzzy logic control strategy was suggested by Putrayudha et al. [79] to optimise the performance of two different systems including (1) a vertical ground source heat pump and (2) a photovoltaic thermal-ground source heat pump system. The results demonstrate that the fuzzy logic control strategy reduces 13.3% and 18.3% of the energy consumption for a vertical ground source heat pump and a hybrid photovoltaic thermal-ground source heat pump system, respectively, in comparison with that yielded by the On-Off operation strategy.

The potential application of the waste heat of a micro gas turbine used to recover the soil temperature around a spiral vertical GHE was studied by Dehghan [80]. The study is divided into two stages. First, the performance of nine existing spiral GHEs is studied experimentally and numerically. The experimental and numerical results are then compared for the validation of the numerical model. In the second stage, the hypothetical study is conducted by introducing sixteen more GHEs, installed around the existing ones (as mentioned in the first stage), to deliver the waste heat of the micro gas turbine to be stored in the ground. Based on the previously validated numerical model, the thermal behaviour of the integrated GHE system is investigated. The simulation result reveals that the heat extraction of the existing GHEs can increase significantly when a system utilising the waste heat of a micro gas turbine is introduced.

A hybrid system of ground source electrical heat pump and ground source absorption heat pump was proposed by Wu et al. [81]. The motivation behind this study was to combine the features of both heat pumps, as the ground source electrical heat pump has a higher energy efficiency in the cooling mode. Conversely, the ground source absorption heat pump has higher energy efficiency in the heating mode. In this study, the effects of supply ratios on thermal imbalance ratio, annual primary energy efficiency, and cost-efficiency characteristics, are investigated.

A theoretical study on a hybrid air source heat compensator-vertical ground source heat pump system was conducted by You et al. [82] using a simulation tool, TRNSYS. Four operation strategies are presented including an air source heat compensator for direct heat compensation, a combined air source heat compensator-ground source heat pump for heat compensation, a combined air source heat compensator-ground source heat pump for space heating, and an air source heat compensator-ground source heat pump for domestic hot water. The results show that the hybrid air source heat compensator-ground source heat pump reduces energy consumption by 23.86% compared with the boiler-split air conditioner system. Also, the operational costs are reduced by 50%.

A hybrid ground source heat pump and air source regeneration system was studied by Allaerts et al. [83]. In this study, the boreholes are classified into two different regions namely, warm and cold regions. These two different regions are proposed to balance the extraction/rejection of heat during heating and cooling periods. In addition, a supplementary dry cooler is used to capture heat/cold during summer/winter to recover the degradation of the soil thermal condition. According to Allaerts et al., the suggested hybrid system can significantly reduce the size of the borehole area by up to 47% in the cost-optimal configuration.

Chiasson et al. [84] developed a model of a slinky pipe pavement heating system. The pavement heating system is normally used as an additional heat rejecter for the borehole heat exchangers (BHEs). This hybrid GHE system is presented to overcome the degradation of the soil thermal conditions around the BHEs, which are operated in a cooling dominated regime. In this study, a two-dimensional finite difference method is utilised to evaluate the transient heat transfer from a pavement heating system. Adiabatic boundary conditions are applied to the lateral and bottom sides of the computational domain. In this study, only two modes of loading of the heat exchanger are considered; (1) the BHEs only, and (2) combined BHEs and pavement heating systems. Chiasson et al.'s model managed to incorporate the temperate climate condition of Tulsa, Oklahoma, USA. However, the performance of the hybrid GHE under general climate conditions has yet to be investigated.

2.4 Energy savings for an air conditioning system coupled with GHEs

In this project, the energy saving of a ground source air conditioning system is assessed by thermodynamic analysis. The energy saving of an air conditioning system will be shown through three parts of the calculation. Firstly, to calculate the energy consumption of a reference cycle air conditioning system. Figure 2.23 shows a T-s diagram for an ideal vapour compression refrigeration.

Figure 2.23: T-s diagram of an ideal vapour compression refrigeration cycle (without underground cooling condenser)

The thermodynamic analysis of the ideal vapour compression refrigeration cycle can be performed by knowing either the temperature or pressure of refrigerant inside the evaporator or condenser [85]. The changes of potential and kinetic energy occur in each component of the vapour compression refrigeration cycle are ignored in this analysis. The cycle begins when the refrigerant enters the evaporator as a two-phase liquid-vapour mixture at state 4 and absorbs the cold region heat as it passes through the evaporator. Due to the heat absorption, the

refrigerant evaporates to saturated vapour, at state 1. The heat transfer process, in the evaporator, occurs in an isobaric condition. The heat transfer rate of the refrigerant in the evaporator [85] is calculated as:

$$\dot{Q}_{in} = \dot{m}(h_1 - h_4) \tag{2.30}$$

where $\dot{Q}_{in}$ is the refrigeration capacity (kW), $\dot{m}$ is the mass flow rate of the refrigerant (kg/s), h_1 is the enthalpy at state 1 (kJ/kg), and h_4 is the enthalpy at state 4 (kJ/kg).

At the compressor, the saturated vapour, in state 1, is compressed to a higher pressure and temperature at state 2s. The compression process inside the compressor is assumed to be adiabatic and reversible. Then, the compressor power is determined as follows:

$$\dot{W}_c = \dot{m}(h_{2s} - h_1) \tag{2.31}$$

where $\dot{W}_c$ is the compressor power (kW), $\dot{m}$ is the mass flow rate of the refrigerant (kg/s), h_{2s} is the enthalpy at state 2s (kJ/kg), and h_1 is the enthalpy at state 1 (kJ/kg).

At the condenser, the refrigerant disposes the heat to a cooler environment at a constant pressure. As a result, the refrigerant condenses and leaves the condenser as a saturated liquid. The heat transfer rate of refrigerant in the condenser [85] is calculated as:

$$\dot{Q}_{out} = \dot{m}(h_{2s} - h_3) \tag{2.32}$$

where $\dot{Q}_{out}$ is the heat rejection capacity of the condenser (kW), $\dot{m}$ is the mass flow rate of the refrigerant (kg/s), h_{2s} is the enthalpy at state 2s (kJ/kg), and h_3 is the enthalpy at state 3 (kJ/kg).

In the expansion valve, the refrigerant expands to the evaporator pressure at state 4 as a two-phase liquid-vapour mixture. The enthalpy at state 4 is considered equivalent to the enthalpy at state 3 [85] written as:

$$h_4 = h_3 \tag{2.33}$$

where h_4 is the enthalpy at state 4 (kJ/kg), and h_3 is the enthalpy at state 3 (kJ/kg).

The COP of an ideal vapour-compression refrigeration cycle [85] is given as:

$$COP = \frac{h_1 - h_4}{h_{2s} - h_1} \tag{2.34}$$

where COP is the coefficient of performance of an ideal refrigeration cycle, and h_1, h_{2s}, h_4 are the enthalpy at points 1, 2s and 4 (kJ/kg), respectively.

The second part is to estimate the energy consumption of an advanced cycle air conditioning system equipped with GHEs. Generally, the thermodynamic analysis of the advanced cycle air

conditioning system is almost the same as that for the reference cycle of the air conditioning system, except for state 3' and 2s (refer to Figure 2.24). For the advanced cycle air conditioning system, it is assumed that the refrigerant leaves the condenser as a subcooled liquid owning to lower temperature of water leaving the GHEs. Assuming that there is no temperature difference between point 3' and 3'', then the enthalpy of the saturated liquid refrigerant at point 3' can be determined. Since the throttling process occurs from point 3' to point 4', then the enthalpy at state 4' is equivalent to the enthalpy at state 3'. The thermodynamic analysis at state 1 is performed the same as that conducted for the cycle of the reference air conditioning system as elaborated in part 1. The enthalpy at state 2s (h_{2s}) is then determined based on the entropy and pressure at state 2s (s_{2s} and P_{2s}). For this cycle, the pressure at point 2s is equal to the saturated pressure of the refrigerant at point 3. Since the process is isentropic from point 1 to point 2s, thus, the entropy at point 2s is equivalent to the entropy of the saturated vapour refrigerant at point 1. The COP of the advanced cycle air conditioning system is then given as:

$$COP = \frac{h_1 - h_4{}'}{h_{2s} - h_1} \qquad (2.35)$$

where COP is the coefficient of performance of an ideal cycle refrigeration system, and h_1, h_{2s}, $h_4{}'$ are the enthalpy at points 1, 2s, and 4' (kJ/kg), respectively.
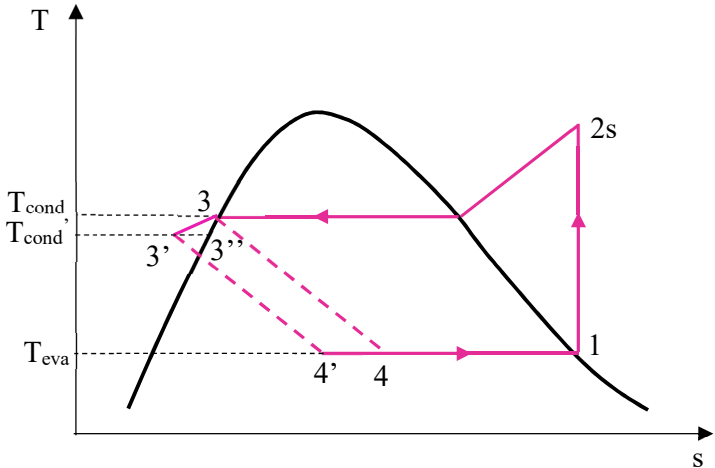
Figure 2.24: T-s diagram of an ideal vapour compression refrigeration cycle (with underground cooling condenser)

The last part is to analyse the energy consumption of an air conditioning system equipped with a variable frequency compressor. The variable frequency compressor air conditioning system offers higher efficiency and more energy savings than the conventional air conditioning system with a fixed speed compressor. It has the ability to speed up and slow down of the refrigerant flow in order to meet heating or cooling load. Figure 2.25 illustrates the T-s diagram of an ideal vapour compression refrigeration cycle of air conditioning system equipped with a variable speed compressor. As an example, two cycles are presented in order to analyse the energy

consumption of the air conditioning system with a variable speed compressor. The cycle (1-2s-3-4) is operated at a higher pressure, while the cycle (1-2s'-3'-4') is run at a lower pressure. The thermodynamic analysis of both cycles is performed using the same procedure as elaborated in part 1. The COP of the second cycle is then calculated as:

$$COP = \frac{h_1 - h_4'}{h_{2s}' - h_1} \qquad (2.36)$$

where COP is the coefficient of performance of an ideal cycle refrigeration system, and h_1, h_2', h_4' are the enthalpy at points 1, 2', and 4' (kJ/kg), respectively.
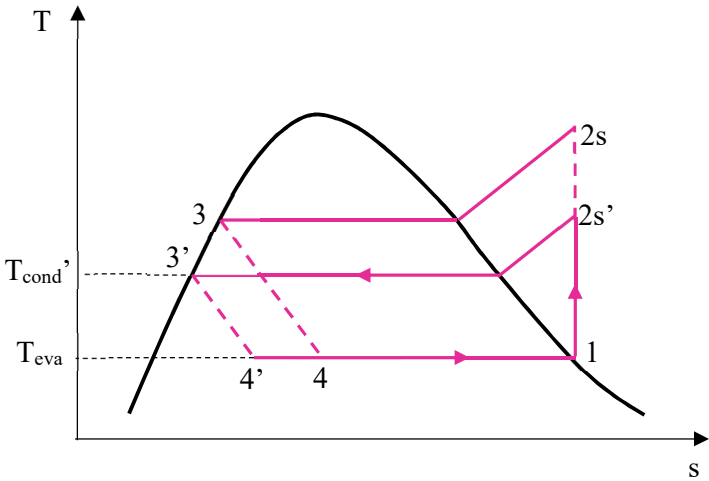
Figure 2.25: T-s diagram of an ideal vapour compression refrigeration cycle with a variable speed compressor.

The actual COP of a refrigeration system, however, cannot be the same as the ideal COP, as the presence of irreversibilities during the adiabatic compression process increase the specific entropy (from compressor inlet to exit). Figure 2.26 shows a T-s diagram of an actual vapour compression refrigeration cycle.
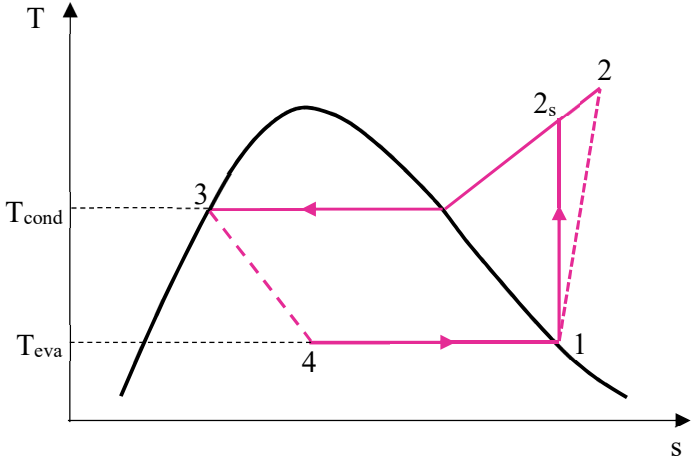
Figure 2.26: T-s diagram of a vapour compression refrigeration cycle with an isentropic efficiency.

41

The isentropic efficiency is given based on the following relationship [85]:

$$\eta = \frac{(\dot{W}_c/\dot{m})_s}{\dot{W}_c/\dot{m}} = \frac{(h_{2s} - h_1)}{(h_2 - h_1)} \tag{2.37}$$

where η is the isentropic efficiency, $(\dot{W}_c/\dot{m})_s$ and $\dot{W}_c/\dot{m}$ are the compressor power per unit mass of refrigerant flowing for an ideal and actual condition, respectively, h_1, h_2, h_{2s} are the enthalpy at points 1, 2, and 2_s, see Figure 2.26.

The actual COP of a refrigeration cycle [85] is given as:

$$COP_a = \frac{h_1 - h_4}{h_2 - h_1} \tag{2.38}$$

where COP_a is the actual COP of the refrigeration cycle, and h_1, h_2, h_4 are the enthalpy at points 1, 2 and 4 (kJ/kg), respectively.

Based on the relationship of the ideal and actual COP and the compressor isentropic efficiency, then the actual COP of a refrigeration cycle can be written as follows:

$$COP_a = COP\eta \tag{2.39}$$

where COP_a is the actual coefficient of performance of the refrigeration system, COP is the ideal coefficient of performance of the refrigeration system, and η is the isentropic efficiency. The power input of an air conditioning system is determined based on the relationship of the actual COP and cooling capacity [85] which is given as:

$$\dot{W}_c = \frac{\dot{Q}_{in}}{COP_a} \tag{2.40}$$

where $\dot{W}_c$ is the power of compressor (kW), $\dot{Q}_{in}$ is the cooling capacity of the air condition system (kW), and COP_a is the actual coefficient of performance of a refrigeration system. The energy consumption of an air conditioning system over a time period Δt is then calculated as:

$$E = \dot{W}_c \, \Delta t \tag{2.41}$$

where E is the total energy consumption (kWh), $\dot{W}_c$ is the compressor power (kW), and Δt is the time step (h).

2.5 Summary

The literature review can be summarised as follows:

1. Ground source air conditioning systems (heat pumps) are efficient cooling (heating) systems that offer high levels of comfort and reductions of electrical energy use.

2. All previous studies indicated that thermophysical properties and temperature of soil are important parameters that determine the efficiency of the GHE.

3. Several authors indicated that the vertical GHE is suitable to be installed in limited land areas such as urban areas. In addition, the vertical GHE has a better efficiency than the horizontal GHE, because the ground temperature 10 m below the surface is relatively stable all year around [1]. However, the installation costs for the vertical GHE is higher than for the horizontal GHE.

4. The computational models reviewed in this chapter demonstrate that the performance of the horizontal GHE is affected by the thermal interaction between the soil and atmosphere. As its efficiency is lower than a vertical GHE, it requires more piping in order to produce the same heat exchange quantity. Also, it needs a relatively larger area for installation. However, the installation cost of the horizontal GHE is almost 50 per cent lower than the vertical GHE in order to produce the same heat exchange quantity.

5. Based on the literature review, it has been demonstrated that the performance of the vertical GHE could decrease following long-term operation due to degradation of thermal conditions around the GHE, particularly when there is an imbalance between the heating and cooling load. This degradation of soil condition around the vertical GHE is relatively difficult to recover since the thermal conductivity of the soil is relatively low.

6. The previous study revealed that the degradation in the horizontal GHE's performance is relatively quick to recover by taking advantage of interaction between soil and atmosphere.

7. As presented in the literature, the combined arrangement of the GHE offers the advantage of relatively lower installation costs and precludes the degradation of its thermal performance compared with the horizontal or vertical arrangements.

8. There is an existing combined horizontal-vertical GHE model as discussed in Section 2.3.3, presented by Chiasson et al. The horizontal GHE is used only as a supplementary heat rejecter of a vertical ground source heat pump. The model was simulated based on conditions in Tulsa, Oklahoma, USA, namely, temperate climate conditions. Therefore, there is a critical need to investigate the performance of combined horizontal-vertical GHEs under diverse climate conditions such as tropical, sub-tropical and temperate. Also, there is a need to understand an optimal operation mode of the GHE under various loading conditions.

9. In related references it was observed that most developed models ignored the effects of seasonal change on soil temperature, especially for the vertical GHE model. There are some models which consider seasonal changes on soil temperatures by considering the real dynamic boundary conditions on soil surfaces such as solar radiation, longwave radiation, convection,

latent and sensible heat transfer, precipitation, and surface cover. However, considering real dynamic conditions on the soil surface renders the models complex and inefficient in computational time. Thus, a new approach, that is relatively simple and efficient in computation time, is required to consider seasonal changes in soil temperatures.

Through a thoroughly literature review, it shows that the aims of the proposed research are well justified.

CHAPTER 3

MODELLING SEASONAL SOIL TEMPERATURE CHANGES

The literature reviewed in Chapter 2 demonstrated that one of the technical parameters that significantly influences of the GHE performance is the seasonal soil temperature changes. A proper approach to consider the effect of fluctuations in soil temperature during the seasonal changes is notable in order to minimise the error generated by the GHE model.

This chapter describes a new approach in order to take into account the effect of seasonal changes in soil temperature by incorporating an internal heat source term into the GHE model. The approach is easy and practical to use. This chapter is organised as follows. Section 3.1 describes the concept of seasonal soil temperature changes modelled by the use of an internal source term. The procedure to determine the soil temperature profile is presented in Section 3.2. Section 3.3 describes the validation of Bagg's equation using Adelaide's soil temperature history. Chapter 3.4 summarises the key finding in this chapter.

3.1 Concept

As it was discussed in the previous chapter the soil temperature around GHEs has a great impact on GHEs' performance. Changes in soil temperatures around GHEs are the result of two factors. First is the result of seasonal changes in soil temperature and the second is rendered by the heat flux released/absorbed by the GHE. For the seasonal soil temperature changes, previously developed models mostly ignored this effect on the GHE performance. Few existing models consider the soil temperature fluctuations during seasonal changes using a complicated method which can result into errors. Therefore, this study proposes a new approach to consider the seasonal changes in soil temperature by using an internal source term. This approach is more practical and simple to use since the internal heat source term is calculated based on soil temperature differences in summer and winter for the different levels of soil. The internal heat source term value normally decreases with increasing depth as the seasonal temperature fluctuation of the soil decreases as the depth increases. For instance, the source term value at a depth of 1 m is higher than that at a depth of 2 m below the surface. The variation in source term values is affected by different amplitudes of soil temperature, at various depths, during winter and summer as illustrated in Figure 3.1. At a depth of more than 16 m below the ground surface, the temperature of the ground is relatively constant [3]. The source term value is positive when the soil gets warmer (August to February in the southern hemisphere),

conversely, negative when the soil gets cooler (February to August). The internal source term H_s at a particular depth is calculated as:

$$H_s = \rho_s c_s \frac{\Delta T_s}{\Delta t}$$

(3.1)

where H_s is the soil internal heat source term (W/m³), ρ_s is the soil density (kg/m³), c_s is the soil specific heat (J/kgK), Δt is the time period (s), and ΔT_s is the soil temperature difference cross Δt (K) at particular depth.
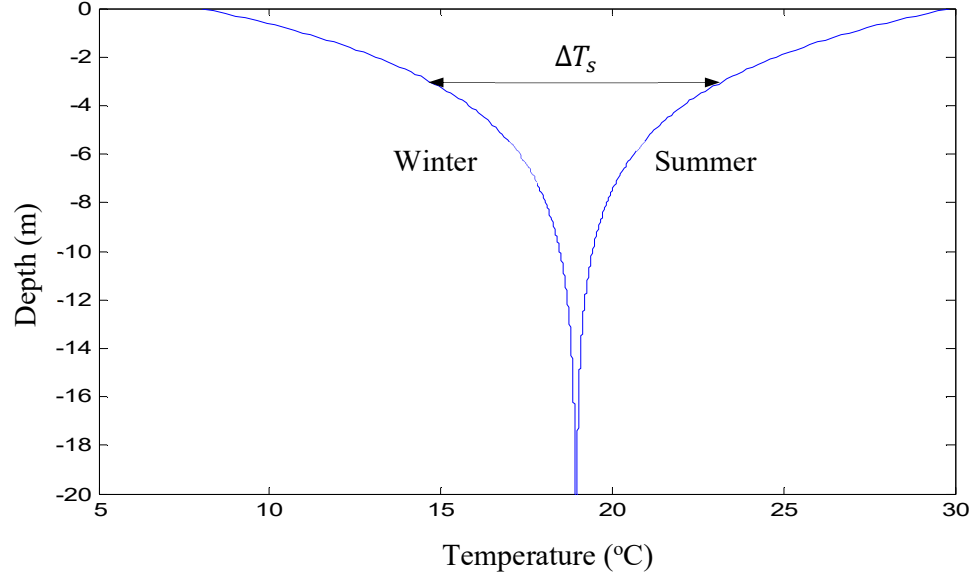
Figure 3.1: Typical profile of soil temperature in summer and winter.

3.2 Determination of soil temperature profile

As defined above, estimation of the soil internal heat source H_s requires knowing the soil temperature profile and its variation at the soil layer over the year. When the actual measurement is not available, Bagg's Equation (Eq. 2.1) would be used to estimate the soil temperature at a specific depth and time [20]. This equation is written as:

$$T(x,t) = (T_m \pm \Delta T_m) + 1.07 k_v A_s e^{\left(-0.00316x\left(\frac{1}{\alpha}\right)^{0.5}\right)} cos\left[\frac{2\pi}{365}\left(t - t_0 - 0.1834x\left(\frac{1}{\alpha}\right)^{0.5}\right)\right]$$

(3.2)

where $T(x,t)$ is the ground temperature at a given depth x on calendar day t (°C), x is the soil depth (cm), t is the calendar day where 1 January = 1 and so forth, T_m is the average annual air temperature (°C), ΔT_m is the local site variable for the ground temperature (K), k_v is the vegetation coefficient ($k_v = 1$ for bare ground, $k_v = 0.22$ for year round full vegetation cover), A_s is the amplitude of the annual air temperature (K), α is the average soil thermal diffusivity (10^{-2} cm² sec⁻¹), and t_0 is the phase of air temperature wave (day).

46

3.3 Validation of Bagg's equation using Adelaide's soil temperature history

The soil type in Adelaide is layered old dune sands, generally compact and normally brown in colour [86]. Due to the exact data of soil thermal properties for the specific location is difficult to obtain, the soil thermal properties are then determined based on the data provided in the literature. Al-Khoury [3], gives a different range of values for the thermal conductivity, density, and specific heat of the sand. They range from 0.15 to 4 W/mK for the thermal conductivity, 1280-2150 kg/m^3 for the density, and 0.8-1.48 kJ/kgK for the specific heat. Taking a conservative approach, the mean values of thermal properties of the sand are summarised in Table 3.1.

Table 3.1: Thermophysical properties of soil in Adelaide

Parameter	Value	Unit
Thermal conductivity	1.3	W/mK
Density	1500	kg/m^3
Specific heat	1.14	kJ/kgK

The soil temperature at a shallow region is affected by both diurnal and seasonal climate changes [3, 39], while it is almost constant at a depth of more than 10 m below the surface [3]. The existing measurement data of soil temperature, in Adelaide, is limited to 1 m depth [87]. Thus, for the purpose of simulation, the profile of periodic soil temperature during seasonal changes is computed using the analytical equation presented by Baggs [20].

The input parameters for Baggs' equation (e.g. average annual air temperature, amplitude of the annual air temperature, phase of air temperature wave) are determined based on the historical climate condition database provided by Australian Bureau of Meteorology. The vegetation coefficient and local site variable for the ground temperature are based on data presented by Baggs [20]. The sand thermal diffusivity is based on the relationship of thermal conductivity, density, and specific heat, which the those values are given in Table 3.1. Table 3.2 summarises the parameters used in the analytical equation of soil temperature.

Table 3.2 Parameters used in the analytical equation of soil temperature

Parameter	Value	Unit
Average annual air temperature (T_m)	16.45	ºC
Amplitude of the annual air temperature (A_s)	11.9	ºC
The local site variable for the ground temperature (ΔT_m)	2.5	ºC
Vegetation coefficient (k_v)	1	-
Soil thermal diffusivity (α)	0.76	10^{-2} cm^{-2} sec^{-1}
Phase of air temperature wave (t_0)	10 (10th January)	Day
The calendar day (t)	18 (18th May)	Day

The estimated soil temperature is validated against the measured soil temperature data (up to 1 m deep) provided by the Bureau of Meteorology, South Australia. Figure 3.2 shows the

comparison of both the estimated and measured soil temperature on May 18th, 2015. It is observed, at a depth of more than 20 cm below the surface, the measured soil temperature is slightly higher than the estimated soil temperature. However, this deviation value is still in tolerated range. While at a shallower region, it is found that the measured soil temperature is lower than the simulated result. This phenomenon could be affected by a diurnal atmospheric condition, which significantly influences the ground surface temperature. Since the surface temperature is sensitive to the diurnal atmospheric condition, the observation time may affect the measurement results. The measured soil temperature used to validate Bagg's model is based on 9:00 am observation data. In a normal condition at 9:00 am, the ground surface receives less solar radiation than during the noon. This could be the reason for discrepancy between the measured and simulated soil temperature at depths up to 20 cm below the ground surface. Overall, the estimated soil temperature is in a good agreement with the experimental data. Then, the Equation 3.2 is used to compute the profile of the soil temperature in both winter and summer as illustrated in Figure 3.3. This figure illustrates the variation of soil temperature at various depths in both summer and winter. It is observed that the soil temperature, at a shallow region, shifts during seasonal changes due to the atmospheric conditions. The changes in soil temperature lags in time than the seasonal ambient air temperature changes. The reason is due to the heat storage capacity of the soil that is much higher than that the ambient air. The soil temperature shifts significantly at the surface. While the changes in soil temperature are more slowly at a deeper region. Due to the atmospheric heat can only penetrate several meters below the surface, the soil temperature is relatively constant deep down 15 m below the surface. It is found that the amplitude of seasonal soil temperature changes varies with depths. It decreases when the depth increases.
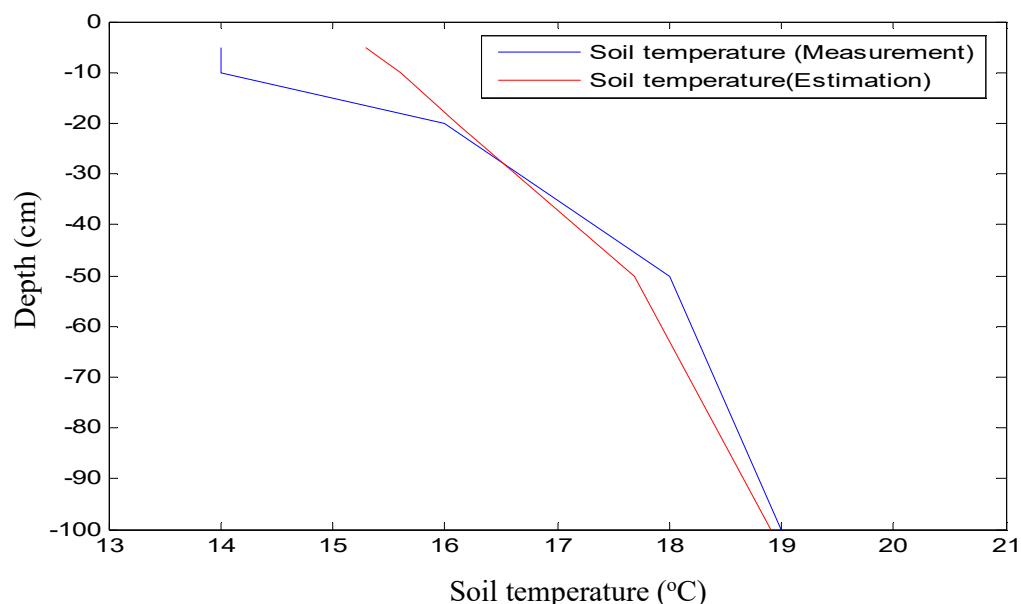
Figure 3.2: Comparison of the estimated and measured soil temperature, on May 18th, 2015.
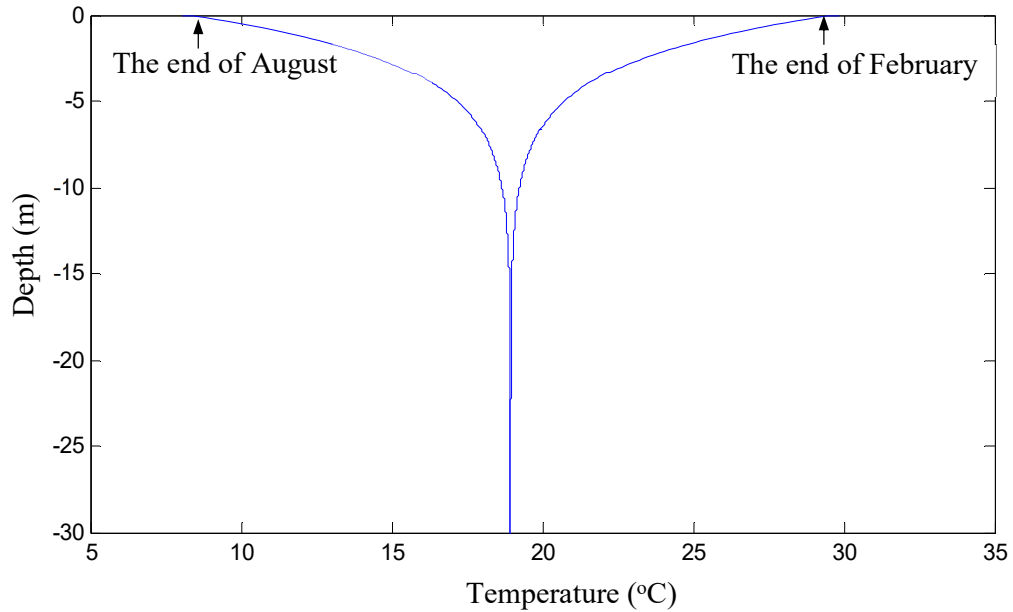
Figure 3.3: Typical soil temperature in Adelaide

Table 3.3 summarises the soil internal heat source term value in Adelaide at different soil depths based on the estimated soil temperature profile shown in Figure 3.3. The value of the internal source term is calculated, based on the soil temperature difference between summer and winter, soil density, soil specific heat, and period of soil temperature changes in Adelaide, using Equation 3.1.

Table 3.3: The value of the internal heat source for each soil layer in Adelaide (Aug-Feb)

Soil layer	Soil temperature difference between summer and winter (°C)	Source term value (W/m³)
1st soil layer (0 -1 m)	15.1	1.64
2nd soil layer (1-2 m)	10.5	1.14
3rd soil layer (2-3 m)	7.3	0.79
4th soil layer (3-4 m)	5.1	0.55
5th soil layer (4-5 m)	3.5	0.38
6th soil layer (5-6 m)	2.4	0.26
7th soil layer (6-7 m)	1.7	0.18
8th soil layer (7-8 m)	1.2	0.13
9th soil layer (8-9 m)	0.8	0.09
10th soil layer (9-10 m)	0.6	0.06
11th soil layer (10-11 m)	0.4	0.04
12th soil layer (11-12 m)	0.3	0.03
13th soil layer (>12 m)	0	0

3.4 Summary

This chapter presents the concept of using the internal heat source term to simulate the seasonal soil temperature changes. The internal source term value depends on the soil temperature

difference between summer and winter. In this study, the soil temperature in Adelaide in both summer and winter is estimated using Baggs' model which has been validated against data provided by Australian Bureau of Meteorology. Overall, the soil temperature generated using Baggs' model agrees well with the data. Based on the amplitude of soil temperature between summer and winter, the internal source term values at various ground depths in Adelaide are derived and tabulated for further use.

CHAPTER 4

HORIZONTAL GEO HEAT EXCHANGER

This chapter presents the horizontal GHE model development. The model incorporates the internal heat source term as described in Chapter 3 in order to consider the effect of seasonal soil temperature changes. This study is conducted in order to understand the effect of seasonal soil temperature changes on the GHE performance through the introduction of the internal heat source term approach to tackle the inherent complexity in the modelling of seasonal soil temperature fluctuations as demonstrated in Chapter 2. In addition, technical parameters affecting the performance of the horizontal GHE are investigated.

This chapter is organised as follows. Section 4.1 overviews the physical model of the horizontal GHE. Section 4.2 presents the development of mathematical model of the horizontal GHE. Section 4.3 describes the input parameters of the horizontal GHE model. Section 4.4 demonstrates the algorithm for the horizontal GHE model. The validation of the horizontal GHE model is presented in Section 4.5. Section 4.6 presents the sensitivity analysis of the horizontal GHE. Section 4.7 summarises the key findings.

4.1 Physical model

The physical model is used to describe the actual arrangement and processes involved in the object to be modelled. A horizontal GHE, as shown in Figure 4.1, is a multi-U-shaped pipe buried in a trench at a specific depth h_z relatively close to the ground surface. It has a total length L, diameter d, wall thickness t_h, and pipe spacing L_s. Initially, the pipe is assumed at soil temperature T_s, before water flows through it. The heat transfer process in the horizontal GHE occurs when the fluid at a temperature T_{fi} enters the GHE which is different from soil temperature T_s and exchanges the heat with the pipe inner surface by convection results in a drop in fluid temperature along the pipe (in summer case). The heat then conducts through the pipe wall to the surrounding soil which then flows to the surface and deep soil. The ground exchanges the heat, at the surface, with the atmosphere through diverse heat transfer mechanisms including reflection, convection, radiation, and evaporation. The heat transfer rate between surface and ambient changes when ambient conditions (e.g. ambient temperature, solar radiation, etc) change.
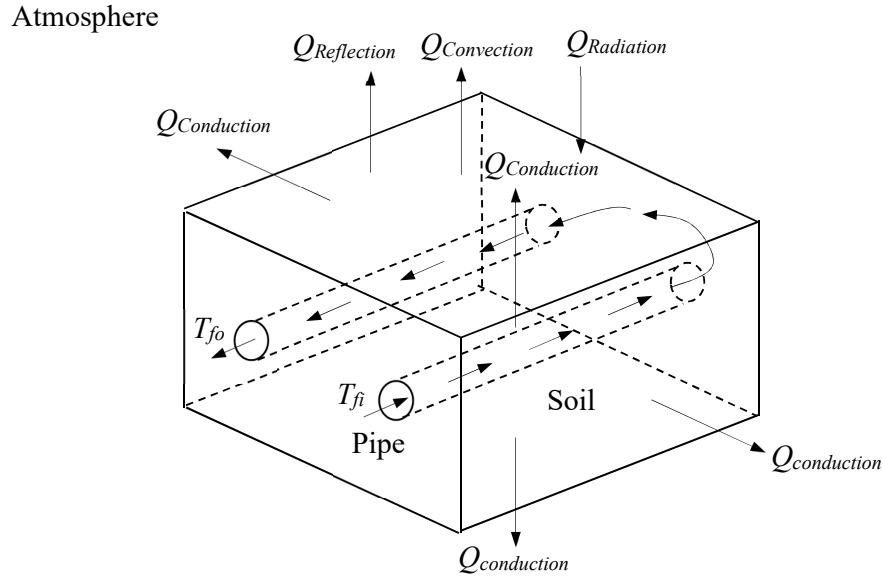
Figure 4.1: Schematic of the horizontal GHE.

4.2 Mathematical model of the horizontal GHE

In this section, the mathematical model of the horizontal GHE is presented. This model is developed by taking a reference on the reviewed horizontal GHE models as discussed in Chapter 2. The developed model considers the transient heat transfer of the working fluid, pipe, and soil. The following assumptions are made for the model:

- The mechanism of heat transfer in the soil domain is pure heat conduction;
- The three-dimensional soil temperature profile is modelled by dividing the soil and pipe into a series of segments. In each segment, the conduction heat transfer in the soil domain is solved in two dimensions;
- Surface's radiative heat transfer is ignored as the model is to be validated with an indoor rig.

The transient temperatures of the working fluid, pipe and soil are evaluated iteratively by using the explicit finite difference method. The governing equations for the fluid, pipe and soil are derived from the equations of energy balance for working fluid, pipe and soil. These equations are given as:

(a) Working fluid

$$c_f \rho_f A \frac{\partial T_f}{\partial t} = \pi d_{in} h_f \left(T_p - T_f \right) - \dot{m}_f c_f \frac{\partial T_f}{\partial z} \tag{4.1}$$

where c_f is the fluid specific heat (J/kgK), ρ_f is the fluid density (kg/m³), A is the cross section area of the pipe (m²), T_f is the fluid temperature (K), t is the time step (s), d_{in} is the inner pipe diameter (m), h_f is the convective heat transfer coefficient between the working fluid and the inner pipe surface (W/m² K), T_p is the pipe temperature (K), $\dot{m}_f$ is the fluid mass flow rate (kg/s), z is the distance in direction parallel to the pipe (m).

(b) Pipe

The governing equation for the pipe is given as:

$$c_p\rho_pV_p\frac{\partial T_p}{\partial t} = Ah_f(T_f - T_p) + \frac{k_sA}{0.5\Delta x}(T_s - T_p) \tag{4.2}$$

where c_p is the pipe specific heat (J/kgK), ρ_p is the pipe density (kg/m³), V_p is the volume of the pipe wall (m³), T_p is the pipe temperature (K), t is the time step (s), A is the heat transfer area of the pipe (m²), h_f is the convective heat transfer coefficient (W/m² K), T_f is the fluid temperature (K), k_s is the soil conductivity (W/mK), Δx is the distance in the x direction (m), and T_s is the soil temperature (K).

(c) Soil

The governing equation for the soil is given as:

$$\frac{1}{\alpha_s}\frac{\partial T_s}{\partial t} = \frac{\partial^2 T_s}{\partial x^2} + \frac{\partial^2 T_s}{\partial y^2} + \frac{H_s}{k_s} \tag{4.3}$$

where α_s is the soil diffusivity (m²/s), T_s is the soil temperature (K), t is the time step (s), H_s is the soil internal heat source term (W/m³), k_s is the soil conductivity (W/mK), x and y are the distances in the x and y directions (m).

The solutions of the differential Equations 4.1-4.3 are obtained by using the explicit finite difference method [88]. Taking into account the symmetry heat transfer, the computational domain of the GHE spreads from the centre of the pipe to the mid span distance between the pipes, as illustrated in Figure 4.2. The soil domain is discretised by using the structured rectangular mesh which has an equal distance in the x and y directions. The discretisation in pipe direction is conducted by dividing both the pipe and soil domain into a series of segment as illustrated in Figure 4.3.
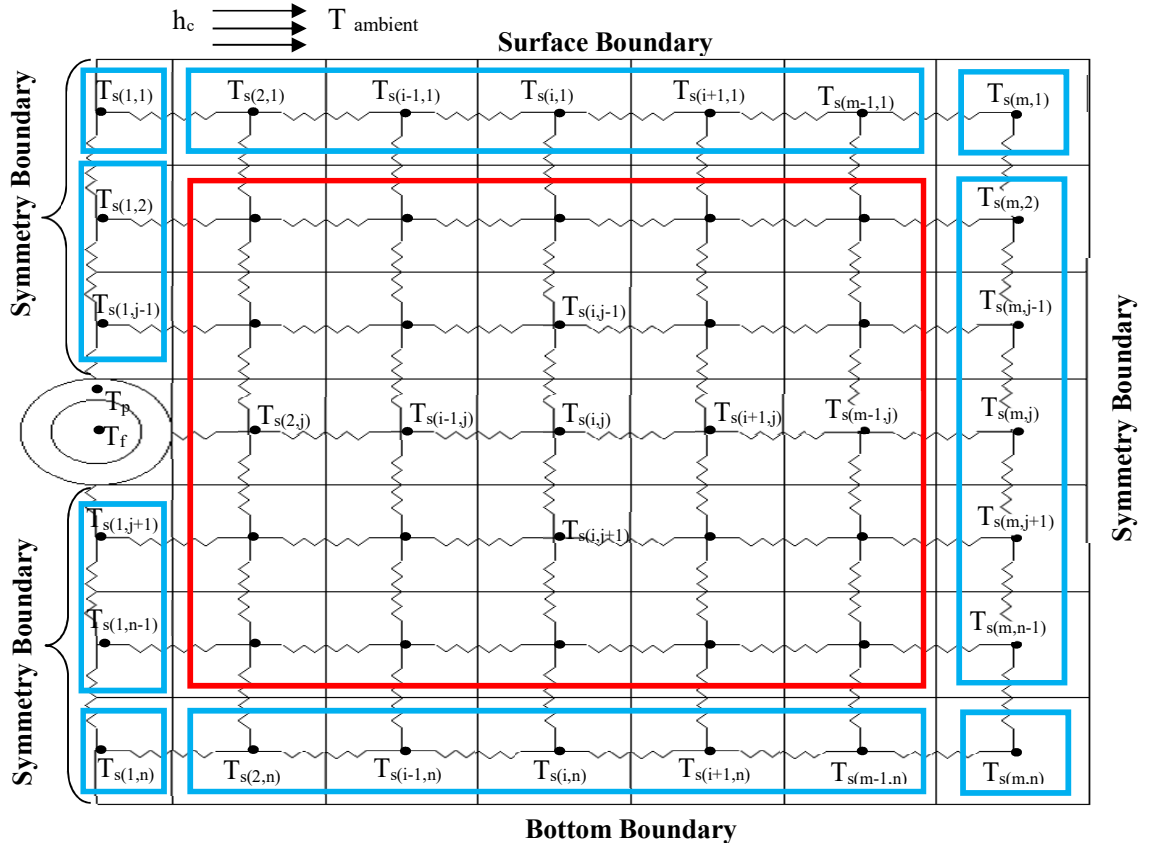
Figure 4.2: Computational domain of the horizontal GHE
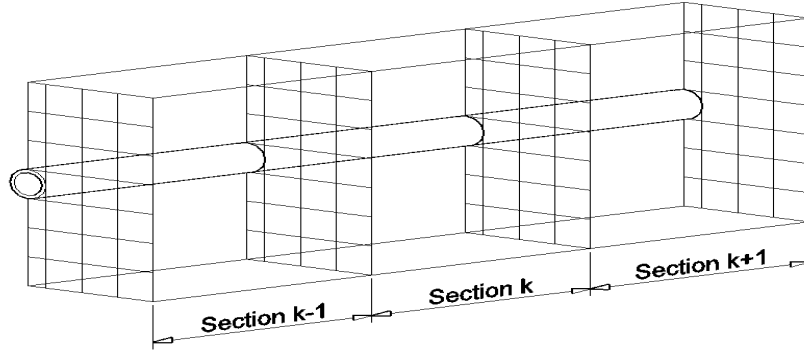
Figure 4.3: Schematic of a horizontal GHE discretization in the pipe direction.

The numerical equations derived from the partial differential equations are given as follows:

(a) Fluid temperature

$$T_{f(k)}^{t+\Delta t} = \frac{\Delta t}{c_f \rho_f A} \left[\pi d_{in} h_f \left(T_{p(k)}^t - T_{f(k)}^t \right) - \dot{m}_f c_f \frac{T_{fo\,(k)}^t - T_{fi\,(k)}^t}{\Delta z} \right] + T_{f(k)}^t \qquad (4.4)$$

where $T_f^{t+\Delta t}$ is the mean temperature of the fluid (K) at the new time step, T_f^t is the mean temperature of the fluid (K) at the current time step, T_{fi}^t and T_{fo}^t are the inlet and outlet temperatures of the fluid at the current time step (K), Δz is the finite increment of the pipe (m),

k is the index in the direction parallel to the pipe. The other parameters are the same as those elaborated in Equation 4.1.

(b) Pipe temperature

$$T_{p(k)}^{t+\Delta t} = \frac{\Delta t}{c_p \rho_p V_p} \left[Ah_f \left(T_{f(k)}^{t+\Delta t} - T_{p(k)}^t \right) + \frac{k_s A}{0.5\Delta x} \left(T_{s(k)}^t - T_{p(k)}^t \right) \right] + T_{p(k)}^t \tag{4.5}$$

where $T_p^{t+\Delta t}$ is the pipe temperature (K) at the new time step, T_p^t is the pipe temperature (K) at the current time step, k is the index in the direction parallel to the pipe. The other parameters are the same as those elaborated in Equation 4.2.

(c) Soil temperature

$$T_{s(i,j)}^{t+\Delta t} = F_o \left(T_{s(i+1,j)}^t + T_{s(i-1,j)}^t + T_{s(i,j+1)}^t + T_{s(i,j-1)}^t + \frac{H_{s(j)}(\Delta x)^2}{k_s} \right) + (1 - 4F_o)T_{s(i,j)}^t$$

$$\tag{4.6}$$

where

$$F_o = \frac{\alpha_s \Delta t}{(\Delta x)^2} \tag{4.7}$$

where $T_s^{t+\Delta t}$ is the soil temperature (K) at the new time step, T_s^t is the soil temperature (K) at the current time step, i and j are indices in the x and y directions, respectively. Other parameters are the same as those elaborated in Equation 4.3.

Different boundary conditions are applied to the computational domain (see Figure 4.2). Convective heat transfer is considered on the soil surface. The other external effects such as radiation, precipitation, evaporation, and vegetation cover, are considered by applying an internal source term value for each soil layer. In addition, the adiabatic condition is applied to both the symmetry and bottom boundaries. The numerical solutions for soil temperatures at the boundaries are given as follows:

➢ The soil temperatures next to the surface (refer to Figure 4.2) are computed as:

a. For i = 1 and j = 1

$$T_{s(1,1)}^{t+\Delta t} = F_o \left(2T_{s(i+1,j)}^t + T_{s(i,j+1)}^t + \frac{U_{as}\Delta x}{k_s} T_a + \frac{H_{s(j)}(\Delta x)^2}{k_s} \right) + \left(1 - \left(3 + \frac{U_{as}\Delta x}{k_s} \right) F_o \right) T_{s(i,j)}^t$$

$$\tag{4.8}$$

b. For i = 2,3,4.....m-1 and j = 1

$$T_{s(i,j)}^{t+\Delta t} = F_o \left(T_{s(i-1,j)}^t + T_{s(i+1,j)}^t + T_{s(i,j+1)}^t + \frac{U_{as}\Delta x}{k_s} T_a + \frac{H_{s(j)}(\Delta x)^2}{k_s} \right) + \left(1 - \left(3 + \frac{U_{as}\Delta x}{k_s} \right) F_o \right) T_{s(i,j)}^t$$

$$\tag{4.9}$$

c. For i = m and j = 1

$$T_{s(m,1)}^{t+\Delta t} = F_o\left(T_{s(i-1,j)}^t + T_{s(i,j+1)}^t + \frac{U_{as}\Delta x}{k_s}T_a + \frac{H_{s(j)}(\Delta x)^2}{k_s}\right) + \left(1 - \left(2 + \frac{U_{as}\Delta x}{k_s}\right)Fo\right)T_{s(i,j)}^t$$

<div align="right">(4.10)</div>

where U_{as} is the overall heat transfer coefficient between soil and ambient air (W/m²K), T_a is the ambient air temperature (K), and other parameters are the same as those elaborated in the Equation 4.6.

➢ The soil temperatures next to the bottom boundary (refer to Figure 4.2) are computed as:

a. For i = 1 and j = n:

$$T_{s(1,n)}^{t+\Delta t} = F_o\left(2T_{s(i+1,j)}^t + T_{s(i,j-1)}^t + \frac{H_{s(j)}(\Delta x)^2}{k_s}\right) + (1 - 3Fo)T_{s(i,j)}^t$$

<div align="right">(4.11)</div>

b. For i = 2,3,4.....m-1 and j = n

$$T_{s(i,j)}^{t+\Delta t} = F_o\left(T_{s(i-1,j)}^t + T_{s(i+1,j)}^t + T_{s(i,j-1)}^t + \frac{H_{s(j)}(\Delta x)^2}{k_s}\right) + (1 - 3Fo)T_{s(i,j)}^t$$

<div align="right">(4.12)</div>

c. For i = m and j = n

$$T_{s(m,n)}^{t+\Delta t} = F_o\left(T_{s(i-1,j)}^t + T_{s(i,j-1)}^t + \frac{H_{s(j)}(\Delta x)^2}{k_s}\right) + (1 - 2Fo)T_{s(i,j)}^t$$

<div align="right">(4.13)</div>

➢ The soil temperatures at the symmetry boundary (refer to Figure 4.2) are computed as:

a. For i = m and j = 2,3,4.....n-1

$$T_{s(i,j)}^{t+\Delta t} = F_o\left(T_{s(i-1,j)}^t + T_{s(i,j+1)}^t + T_{s(i,j-1)}^t + \frac{H_{s(j)}(\Delta x)^2}{k_s}\right) + (1 - 3Fo)T_{s(i,j)}^t$$

<div align="right">(4.14)</div>

b. For i = 1 and j = 2,3,4.....n-1, except for the nodes situated next to the pipe

$$T_{s(i,j)}^{t+\Delta t} = F_o\left(2T_{s(i+1,j)}^t + T_{s(i,j+1)}^t + T_{s(i,j-1)}^t + \frac{H_{s(j)}(\Delta x)^2}{k_s}\right) + (1 - 4Fo)T_{s(i,j)}^t$$

<div align="right">(4.15)</div>

The soil temperatures for those nodes situated next to the pipe (refer to Figure 4.2) are calculated as:

a. Above the pipe:

$$T_{s(i,j)}^{t+\Delta t} = F_o\left(2T_p + 2T_{s(i+1,j)}^t + T_{s(i,j-1)}^t + \frac{H_{s(j)}(\Delta x)^2}{k_s}\right) + (1 - 5F_o)T_{s(i,j)}^t$$

<div align="right">(4.16)</div>

b. Below the pipe:

$$T_{s(i,j)}^{t+\Delta t} = F_o\left(2T_p + 2T_{s(i+1,j)}^t + T_{s(i,j+1)}^t + \frac{H_{s(j)}(\Delta x)^2}{k_s}\right) + (1 - 5F_o)T_{s(i,j)}^t$$

<div align="right">(4.17)</div>

c. Right hand side of the pipe:

$$T_{s(i,j)}^{t+\Delta t} = F_o\left(2T_p + T_{s(i+1,j)}^t + T_{s(i,j+1)}^t + T_{s(i,j-1)}^t + \frac{H_{s(j)}(\Delta x)^2}{k_s}\right) + (1 - 5F_o)T_{s(i,j)}^t$$

<div align="right">(4.18)</div>

The parameters of Equations 4.11-4.18 are the same as elaborated in the Equation 4.6.

Using the explicit finite difference method, the partial differential equations can be solved relatively simply. The unknown nodal temperature at an entity and the new time step are approximated by using the already known temperature values of the adjacent nodes. The explicit method is conditionally stable. To satisfy the stability criterion, the time step Δt must be within the Courant-Friedrichs-Lewy stability condition [89], which is given as follows:

$$|\psi| \leq 1, \qquad \Delta t \leq \frac{\Delta z}{v_f} \tag{4.19}$$

where $\psi = (v_f \Delta t / \Delta z)$ is the Courant number, Δt is the time step (s), Δz is the finite increment of the pipe (m), and v_f is the velocity of the working fluid (m/s).

4.3 Input parameters of the model

In this model, the unknown temperatures of working fluid, pipe, and soil are estimated by using the input parameters summarised as follows:

A. Soil temperature

The initial soil temperatures $(T_{s(i,j)})$ when t = 0 are determined using the analytical soil temperature equation presented by Baggs [20], as Equation 2.1.

B. Soil thermal properties

The thermal properties of the typical soil including thermal conductivity (k_s), density (ρ_s), and specific heat (c_s) are determined based on the existing literature data, as summarised in Chapter 2, Section 2.2. The soil thermal diffusivity (α_s) is then determined as:

$$\alpha_s = \frac{k_s}{\rho_s c_s} \tag{4.20}$$

where k_s is the soil thermal conductivity (W/mK), ρ_s is the soil density (kg/m³) and c_s is the soil specific heat (J/kgK).

C. Soil heat source term

In this model, the soil heat source term $(H_{s(j)})$ at the layer j is introduced to consider soil temperature fluctuations during seasonal changes. The heat source term is calculated by using Equation 3.1, when the soil temperature profile is known either by measurement or estimation using Equation (2.1). For the horizontal GHE, as the pipe buried at the same depth, only one value of heat source term is applied.

$$H_{s(j)} = \rho_s c_s \frac{\Delta T_{s(j)}}{\Delta t} \tag{4.21}$$

where $H_{s(j)}$ is the heat source term (W/m^3) at the layer j, ρ_s is the soil density (kg/m^3), c_s is the soil specific heat (J/kgK), Δt is the time period (s), and $\Delta T_{s(j)}$ is the soil temperature difference in summer and winter (K) at layer j.

D. Convective heat transfer coefficient of air in contact with the soil surface

The convective heat transfer coefficient of air in contact with the soil surface (h_{as}) can be calculated from a relation of turbulent flow over a flat plate. It is given as:

$$h_{as} = \frac{N_u k_a}{L} \tag{4.22}$$

where h_{as} is the convective heat transfer coefficient of air in contact with the soil surface (W/m^{2}K), N_u is the Nusselt number, k_a is the conductive heat transfer coefficient of air (W/mK), L is the unit length (m).

Bahrami [90], presents the average Nusselt number over the flat plate in turbulent region as:

$$N_u = 0.037 R_e^{4/5} P_r^{1/3} \tag{4.23}$$

where N_u is the Nusselt number, R_e is the Reynold number, and P_r is the Prandtl number of air. While the Reynold number is given as:

$$R_e = \frac{\rho_a v_a L}{\mu_a} \tag{4.24}$$

where R_e is the Reynold number, ρ_a is the air density (kg/m^3), v_a is the wind speed (m/s), L is the unit length (m), μ_a is the air dynamic viscosity (N s/m^2).

E. Convective heat transfer coefficient between the working fluid and inner pipe surface

The convective heat transfer coefficient of the working fluid in contact with the inner pipe surface (h_f) is calculated as:

$$h_f = \frac{N_u k_f}{d_i} \tag{4.25}$$

where h_f is the convective heat transfer coefficient between the working fluid and the inner pipe surface (W/m^{2}K), N_u is the Nusselt number, k_f is the conductive heat transfer coefficient of the working fluid (W/mK), d_i is the inner pipe diameter (m).

The Reynold number for the fluid circulated inside the pipe is determined as:

$$R_e = \frac{\rho_f v_f d_i}{\mu_f} \tag{4.26}$$

where R_e is the Reynold number, ρ_f is the fluid density (kg/m^3), v_f is the fluid velocity (m/s), d_i is the inner pipe diameter (m), μ_f is the fluid dynamic viscosity (N s/m^2). In the literature, it is considered that the fluid is in turbulent flow if $R_e > 2000$.

The Nusselt number for laminar flow in circular pipes with constant surface heat flux can be calculated as:

$$N_u = 4.36 \tag{4.27}$$

While for turbulent flow, it is determined based on Dittus-Boelter correlation given as:

$$N_u = 0.023 R_e^{4/5} P_r^n \tag{4.28}$$

where $n = 0.3$ for cooling and $n = 0.4$ for heating [3].

F. Meteorological data

The meteorological data, including ambient air temperature and wind speed, is based on data provided by the local weather bureau.

4.4 Algorithm

A computer program using MATLAB as the programming language has been developed to execute the previously discussed GHE model. The intention of this section is to show the link between the mathematical model and computer programming. The computational procedures for the horizontal GHE are illustrated through a simplified flow chart Figure 4.4.
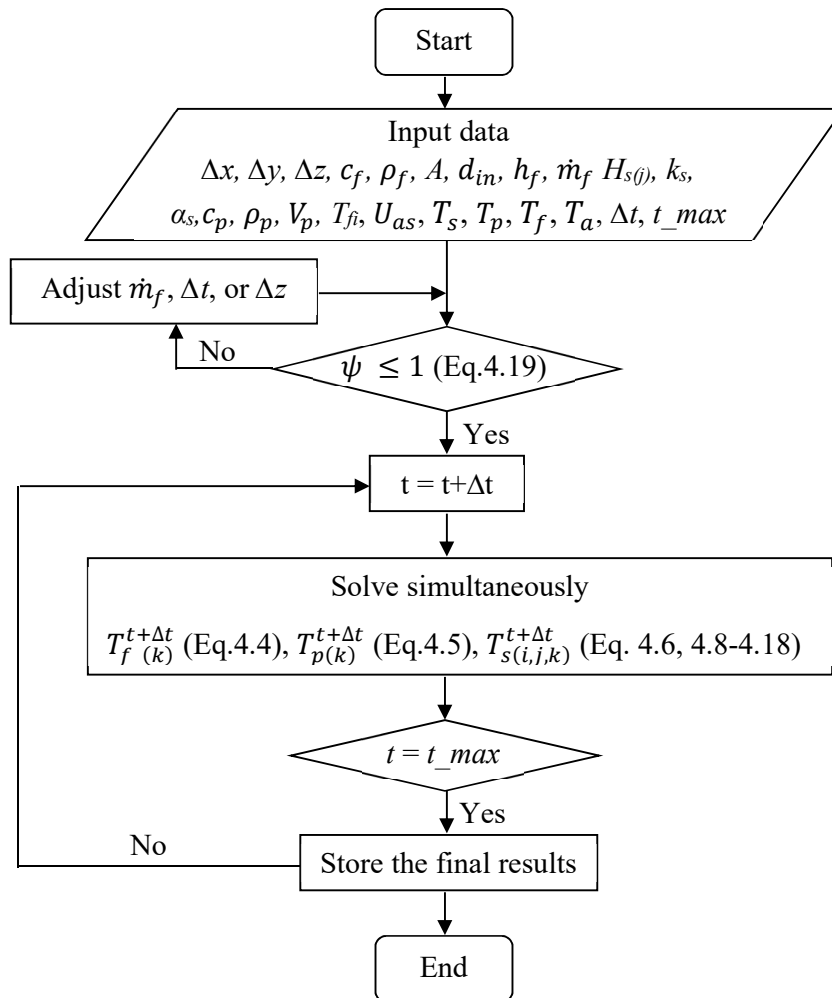
Figure 4.4: Flow chart computational procedure for the horizontal GHE

In order to perform the programming, the input data including the finite increment in the x direction (Δx), the finite increment in the y direction (Δy), the finite increment in the z direction (Δz), fluid specific heat (c_f), fluid density (ρ_f), heat transfer area of the pipe (A), inner pipe diameter (d_{in}), convective heat transfer coefficient of the fluid in contact with the inner pipe surface (h_f), fluid mass flow rate ($\dot{m}_f$), soil source term at the layer j ($H_{s(j)}$), conductive heat transfer coefficient of soil (k_s), soil thermal diffusivity (α_s), specific heat of the pipe (c_p), pipe density (ρ_p), pipe wall volume (V_p), fluid temperature at pipe's inlet (T_{fi}), overall heat transfer coefficient between air and the soil surface (U_{as}), initial soil temperature (T_s), initial pipe temperature (T_p), ambient air temperature (T_a), time step (Δt), maximum simulation time (t_max), are required. The program must satisfy the stability condition, given by Equation 4.19, in order to forward to another step namely, the calculation of the thermal solutions. If the stability condition is not satisfied, it is required to adjust one of the parameters either mass flow rate, time step, or the increment in the z direction. Once the stabilisation condition is met, the simulation is continued where the Equations (4.4-4.6), and (4.8-4.18), are solved simultaneously in order to obtain the thermal solution of the horizontal GHE. The simulation is repeated until the maximum simulation time is attained and then the final results are stored.

4.5 Validation of the horizontal GHE model

4.5.1 Experimental validation

A scale model of GHE was designed and manufactured. The model consists of a single U-shaped pipe laid in a sandy loam-filled box. The box was made of plywood having a thickness of 19 mm reinforced with 70 x 30 mm^2 structural pine. A thick layer of construction lining plastic was used to line the box. The box has dimensions of 14 m long, 1 m wide, and 0.6 m high. A PVC pipe, which has an inner diameter of 0.05 m, a length of 27.5 m, and a centre to centre distance of 0.35 m, was buried at a depth of 0.16 m below the sand surface. The pipe was connected to a water tank where the water is heated to the desired temperature. A hot water pump was used to circulate the hot water through the GHE system. A Solartron Mobrey series 200 rotameter was used to measure the water mass flow rate. A computer connected to a data logger that has ninety two channels of LM 35 temperature sensors was used to record the temperatures of the soil bed and working fluid (water). The temperature sensors were embedded in the soil bed at two different locations along the box, specifically at a distance 1 m and 9.5 m from the inlet/outlet of GHE, at depths of 0.082 m, 0.16 m, 0.238 m, 0.313 m, 0.413 m, and 0.573 m. These temperature sensors were calibrated using water at 20 °C and 50 °C before being located in the sandy loam bed. Forty-five halogen lamps, which have a power of 500 W each, were installed 1 m above the sand bed to simulate solar radiation. The radiation output released

by the halogen lamps were regulated using a lighting dimmer rack which is controlled by Sunlight 2004 software. A radiation meter was used to measure the radiation incident on the sand surface. Figures 4.5 and 4.6 show the schematic of the test rig and the cross section of the sandy loam bed showing the location of thermal sensors, respectively.
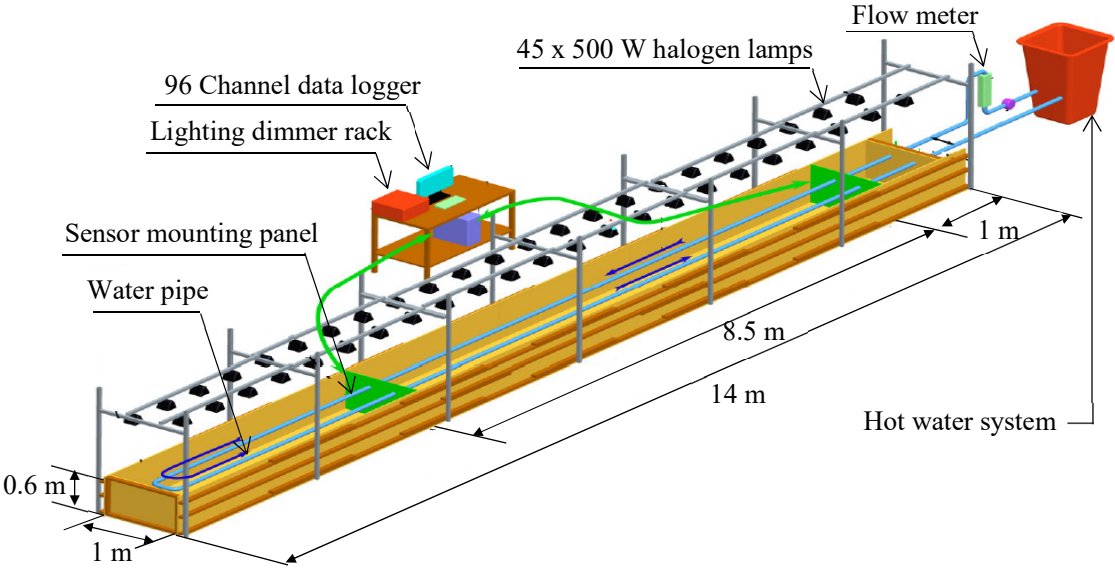
Figure 4.5: Schematic of experimental rig of the horizontal GHE [11]
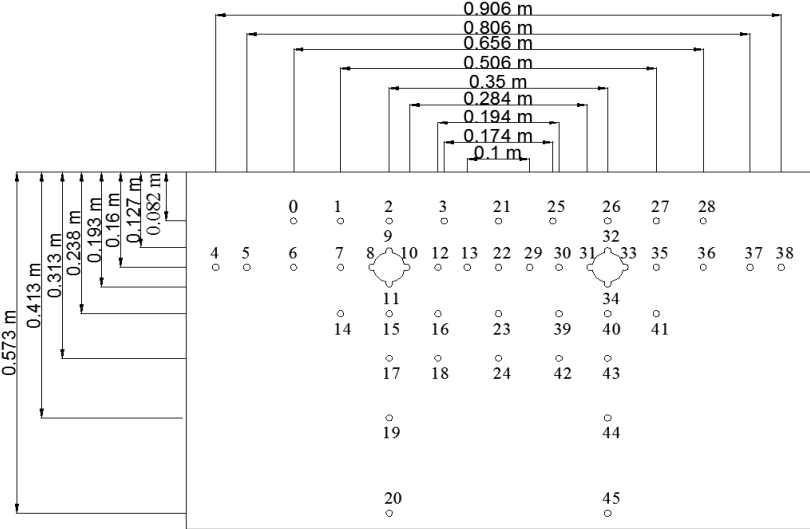
Figure 4.6: Cross section of the sandy loam bed showing the location of thermal sensors [11]

4.5.2 Experimental study

Two sets of experiments were carried out. The first set was conducted to simulate the seasonal changes in soil temperature, in order to acquire the internal heat source term. In this experiment, the changes in soil temperature were rendered by the lamps' radiation exposure and the interaction between the soil surface and the atmosphere while the hot water system was

switched Off. The seasonal soil temperature changes were simulated with 3 hours of light On heating and 10 hours of light Off cooling, without water circulation inside the pipe. These periods were chosen because it is believed that during 3 hours of light On heating, it is sufficient for the heat flux received on the soil surface to penetrate to a certain depth resulting in soil temperature changes. During 10 hours of light Off cooling, it allows the accumulated heat in the soil to dissipate into the atmosphere thereby lowering the soil temperature. Since the pipe in the reduced scale experimental rig was laid quite close to the surface (at a depth of 0.16 m), thus, the periods of 3 hours of light On heating and 10 hours of light Off cooling are considered sufficient. A lighting dimmer rack, controlled by Sunlight 2004 software, was used to regulate the radiation output released by the halogen lamps. It was set to 700 W/m². The changes of the soil temperature during the light On heating and light Off cooling, at six different depths namely, 0.082 m, 0.16 m, 0.238 m, 0.313 m, 0.413 m, and 0.573 m, were recorded using a data logger connected LM 35 temperature sensors, at 1 min intervals. These soil temperature changes were used to determine the amplitudes of soil temperature at various depths which were later used to calculate the value of the internal heat source term. The results were used to create the input values in the simulation. In addition, the ambient indoor air temperature in the laboratory was measured as it contributes to the heat dissipation by natural convection, and it was a parameter in the simulation. The source term value was calculated by using Equation 3.1., which is also presented below.

$$H_{s(j)} = \rho_s c_s \frac{\Delta T_{s(j)}}{\Delta t}$$

where, $H_{s(j)}$ is the soil heat source term (W/m³) at the layer j, ρ_s is the soil density (kg/m³), c_s is the soil specific heat (J/kgK), $\Delta T_{s(j)}$ is the amplitude of soil temperature (K) at the layer j, Δt is the time period (s).

Once values of the soil density, soil specific heat, amplitude of soil temperature, and time period are specified, the value of the internal heat source term can be calculated. The value of the soil density for this calculation was adopted from a report presented by Dally et al. [11]. It is 1777 kg/m³ with an error of ± 5%. The value of the specific heat of sandy loam varies from 800 to 1480 J/kgK [3]. Thus, based on a conservative consideration, it was decided to use a value of 1100 J/kgK for the specific heat of the soil.

In this study, the value of the soil heat source term was calculated, based on the changes of the measured soil temperature at six different depths namely: 0.082 m, 0.16 m, 0.238 m, 0.313 m, 0.413 m, and 0.573 m. As an example, Figure 4.7 shows the profile of mean soil temperature at a depth of 0.16 m during 3 hours of light On heating and 10 hours of light Off cooling. The

profile of mean soil temperature at a depth of 0.16 m is presented because it can properly illustrate the fluctuation of soil temperature during 3 hours of light On heating and 10 hours of light Off cooling due to its relative distance from the surface where the heat flux (radiated from the halogen lamps) is imposed. From Figure 4.7 it can be seen that the changes in the soil temperature can be divided into 4 distinctive periods over the 13 hours, according to the gradients of the changes. Each period refers to a value of the internal heat source term. Tables 4.1a and 4.1b show the calculated values of the internal source term for each soil layer for a certain period of time. In order to increase accuracy, the internal source term at each soil layer was calculated over a short period of time.
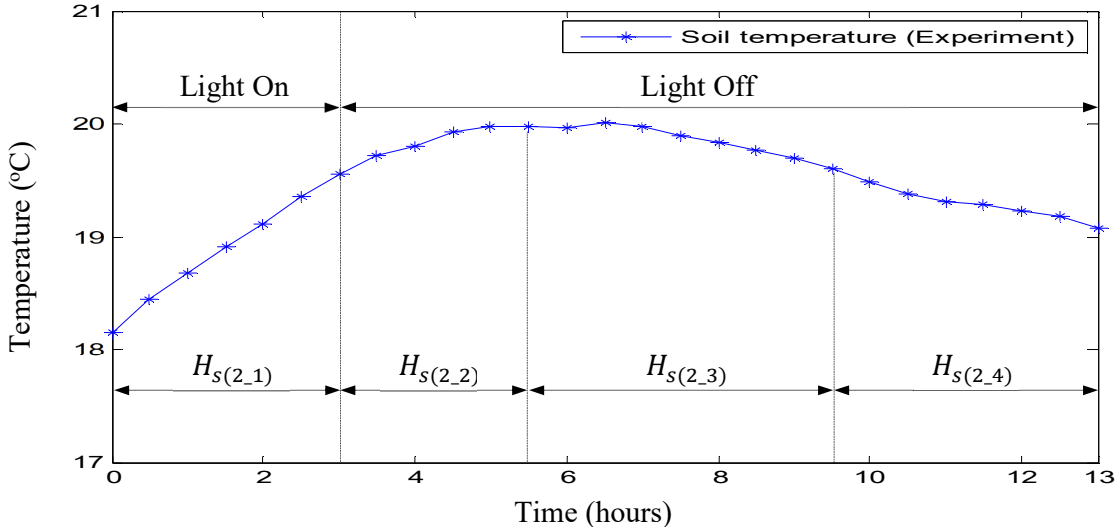
Figure 4.7: Profile of mean soil temperature at a depth of 0.16 m during 3 hours of light On heating and 10 hours of light Off cooling

Table 4.1a: Internal heat source term values

Layer 1 (0-0.082 m)		Layer 2 (0.082-0.16 m)		Layer 3 (0.16-0.238 m)	
Time (hours)	Source term (W/m³)	Time (hours)	Source term (W/m³)	Time (hours)	Source term (W/m³)
0-3	362.5	0-3	254.6	0-3	118.1
3-4	45.2	3-5.5	91.6	3-8	88
4-10.5	-159.8	5.5-9.5	-51.5	8-13	-23.4
10.5-13	-80.1	9.5-13	-80.7		

Table 4.1b: Internal heat source term values

Layer 4 (0.238-0.313 m)		Layer 5 (0.313-0.413 m)		Layer 6 (0.413-0.6 m)	
Time (hours)	Source term (W/m³)	Time (hours)	Source term (W/m³)	Time (hours)	Source term (W/m³)
0-3	69.1	0-3	35.6	0-3	25.3
3-8.5	75.1	3-6	35	3-6.5	14.8
8.5-13	-1	6-8.5	81.4	6.5-13	15.5
		8.5-13	12		

The second set of experiments was conducted to validate the developed model of the horizontal GHE when there was hot water circulating inside the pipe as presented by a number of authors

[21-24] in Section 2.3.1. This experiment was conducted using the same procedure as the experiment 1 with hot water was circulated inside the pipe for the first 3 hours and turned it off for the next 10 hours. The inlet temperature and flow rate were set to 66 °C and 0.66 kg/s, respectively. Figure 4.8 shows the experimental set up of the horizontal GHE. Table 4.2 shows the thermal properties of the GHE materials. The thermal conductivities of the soil, pipe and water used as input in the simulation are based on the values provided in the literature. As discussed in Section 2.2, the thermal conductivity of sandy loam varies from 0.19 to 1.12 W/mK. It was decided to use the average value of 0.5 W/mK for the thermal conductivity of the sandy loam. While, the thermal conductivity of water is based on a reference temperature of 25 °C. The thermal conductivity of PVC pipe varies from 0.13 to 0.15 W/mK [11]. In this study, it was decided to use a value of 0.15 W/mK for the PVC pipe.

Figure 4.8: Photographs of the experimental set up. Sandy loam bed and lamps (left) and water heating system (right)

Table 4.2: Thermal properties of the GHE materials

Thermal properties	Soil	Pipe	Water
Thermal conductivity (W/mK)	0.5	0.15	0.66
Thermal diffusivity (m^2/s)	2.5×10^{-7}	-	-
Specific heat (J/kgK)	1100	1046	4188
Density (kg/m^3)	1777	1400	980

4.5.3 Validation of the horizontal GHE model

The validation of the dynamic model of the horizontal GHE is conducted by comparing the simulated with the measured soil and outlet water temperatures in the 2nd experiment. Figure 4.9 shows the comparison of the measured and simulated soil temperatures, at sensor 2 position (refer to Figure 4.6). The results show that the simulated soil temperature with the source term approach produces a more accurate result than that without the source term. When considering the source term, the model generates a lower relative error than without the source term namely, 1.3% and 2.2% respectively. These results indicate that the new approach is capable to improve the accuracy of the GHE model. Figure 4.10 shows the profile of the outlet fluid temperature. It is observed that the outlet fluid temperature generated by the model with the source term is slightly higher than that without the source term. This tendency is affected by a quick increase

in the soil temperature generated by the model with a source term, as the soil receives both GHE's flux and internal heat source term. It is seen that incorporates the internal heat source term into the horizontal GHE model has improved the accuracy of the soil temperature significantly. In addition, the accuracy of the estimated outlet water temperature has also been improved even though not significant. These findings reveal that considering the soil temperature fluctuations during seasonal changes by introducing an internal heat source term in the GHE model is significant as it would determine the proper size of GHEs. Ignoring the effect of seasonal changes in soil temperature may lead to under sizing the GHEs' length and diminish the heat transfer rate of the GHEs.
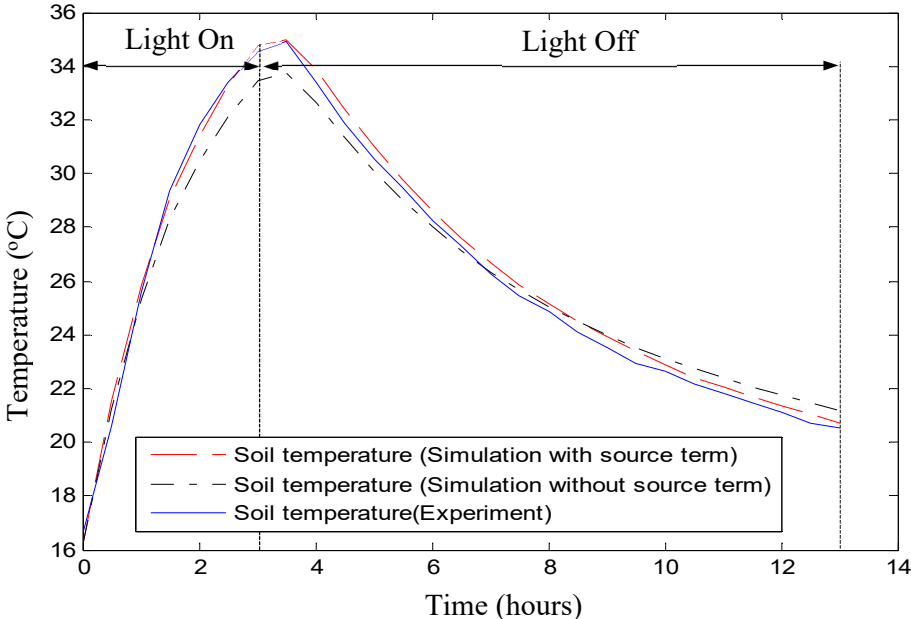
Figure 4.9: Soil temperature at sensor 2 (see Figure 4.6) with water circulated in the first 3 hours
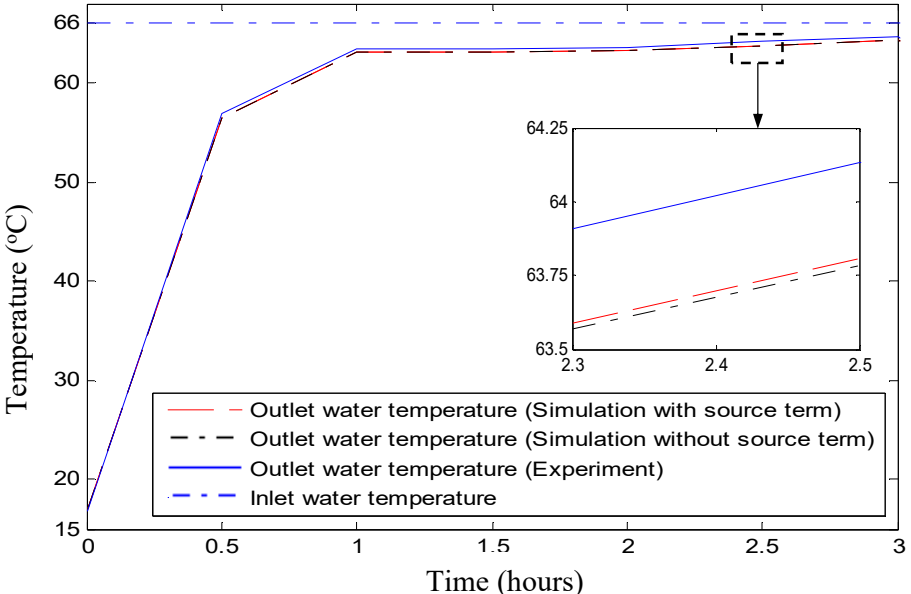
Figure 4.10: Profile of the outlet fluid temperature

65

4.6 Sensitivity analysis of the horizontal GHE

To understand the impacts of some key design and operational parameters (e.g. pipe length, fluid flow rate, inlet fluid temperature, and burial depth) on the horizontal GHE performance, a sensitivity analysis is carried out with the newly developed model, which was validated in the previous section. The reference case used in the sensitivity study based on the soil and weather conditions in Adelaide.

The simulation of the horizontal GHE is conducted by using the reference conditions and thermophysical properties of the GHE materials shown in Tables 4.3-4.4, respectively. As only a single soil layer is considered for the horizontal GHE, its soil source term value is equal to 15.97 W/m^3. The convection heat transfer is counted by taking into account the average ambient air temperature of 29 °C and wind speed of 4.9 m/s [91]. The initial temperature of the pipe, and circulating water is assumed at 20 °C, while the initial soil temperature, at various depths, is calculated using Equation 2.1.

Table 4.3: The reference conditions

Parameters	Value
Pipe length (m)	100
Burial depth (m)	0.25
Pipe inner diameter (m)	0.05
Pipe outer diameter (m)	0.054
Centre distance between pipes (m)	0.35
Inlet fluid temperature (°C)	60
Flow rate (kg/s)	0.5

Table 4.4: Thermal properties of the GHE materials

Thermal properties	Pipe	Water	Soil
Thermal conductivity (W/mK)	0.15	0.66	1.3
Thermal diffusivity (m^2/s)	-	-	7.6×10^{-7}
Specific heat (J/kg.K)	1046	4188	1140
Density (kg/m^3)	1400	980	1500

4.6.1 Pipe length

One of the critical factors affecting the thermal performance of the heat exchanger is the pipe length. In this study, the thermal performance of the horizontal heat exchanger for seven different pipe lengths is investigated. The pipe length is varied from 50 m to 200 m, with an increment of 25 m. Figure 4.11 illustrates the effect of the pipe length on the performance of the GHE at six different periods namely, 1 to 6 hours of operation. It is observed that the outlet fluid temperatures of the horizontal GHE decrease with the increase in pipe length. The longer the pipe means more heat can be transferred to the surrounding soil due to the increase in the area of heat transfer. It shows that the outlet fluid temperatures increase with the increase of the

operation time. This tendency occurs due to the accumulation of heat in the surrounding soil during the operation. The ground temperature around the GHE becomes higher than it was in its initial condition, as the ground absorbs the heat transferred from the circulating fluid. As a result, the amount of the heat transferred to the ground reduces gradually reflected by the rise in outlet fluid temperatures of the GHE. This tendency agrees well with Wu et al.'s findings [6]. Although increasing the pipe length can increase the heat transfer rate, however, the heat transfer rate per pipe length decreases. This tendency occurs because the outlet fluid temperature decreases in a nonlinear trend with the increase in pipe length. For instance, incrementing the pipe length from 50 m to 75 m leads to a drop in the outlet fluid temperature of 0.9 °C. In addition, it drops to 0.8 °C when the pipe length is increased from 175 m to 200 m.
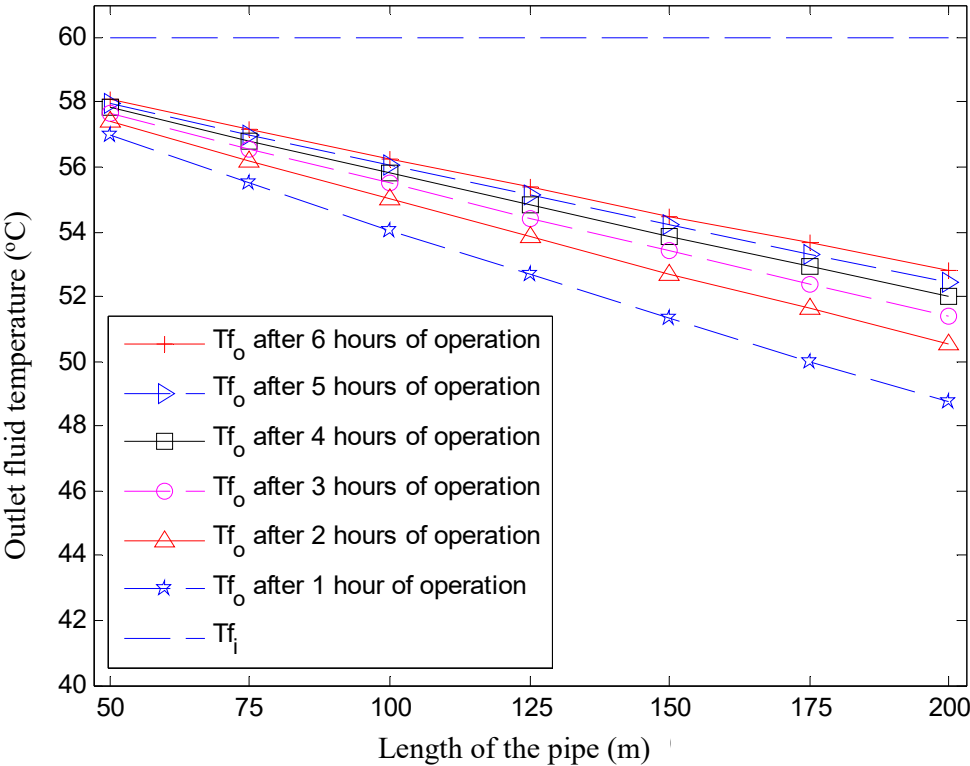
Figure 4.11: The effect of the pipe length on the performance of the GHE
(The inlet fluid temperature = 60 °C, fluid mass flow rate = 0.5 kg/s, burial depth = 0.25 m, initial soil temperature on 1 December).

4.6.2 Flow rate

The fluid flow rate is another factor affecting the performance of the heat exchanger. Figure 4.12 shows the effect of flow rates on the outlet temperatures of the horizontal GHE at six different periods namely, 1 to 6 hours of operation. The flow rate is varied from 0.3 kg/s to 0.7 kg/s, with an increment of 0.1 kg/s. The results reveal that the increase in the fluid flow rate is proportional to the increase in outlet fluid temperature of the GHE. It is observed, at a lower

flow rate, the changes of the outlet fluid temperature over the period of operation are relatively higher. For instance, the difference in the fluid outlet temperature of the GHE with a flow rate of 0.3 kg/s, from 1 to 6 hours of operation, is 3.4 °C. Meanwhile, it is 1.6 °C for a flow rate 0.7 kg/s. This difference is due to the GHE with a higher fluid flow rate releases more heat to the surrounding soil. As a result, the soil temperature around the GHE increases relatively quickly. The degradation in the soil thermal condition affects the heat exchange capacity of the GHE and results in an increased outlet fluid temperature. These results are also confirmed by Nam et al. [32] as discussed in Chapter 2.
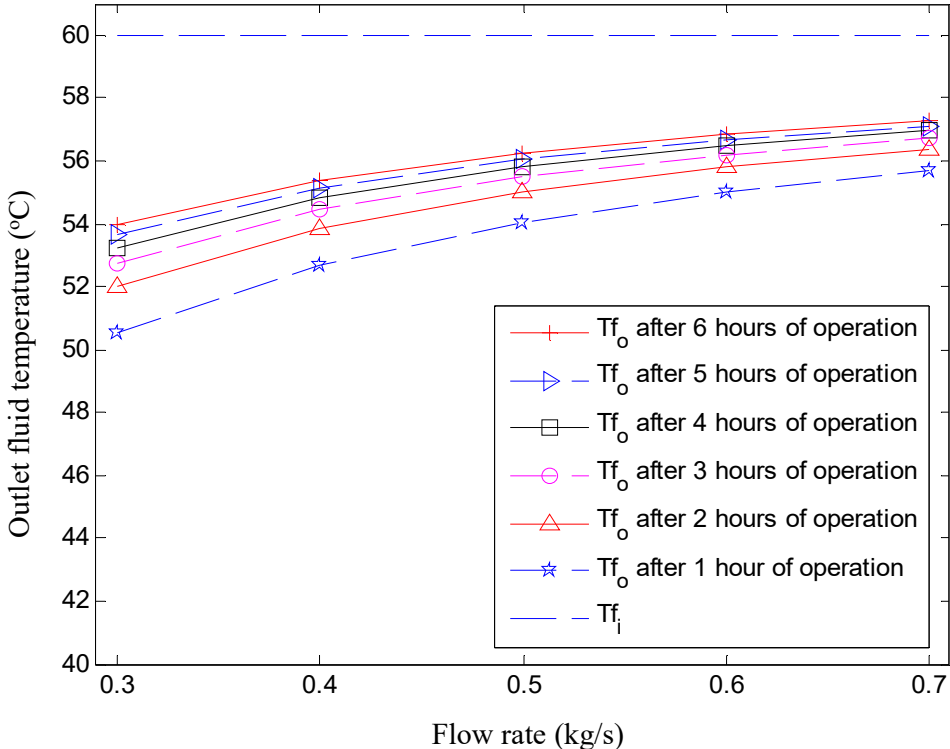
Figure 4.12: The effect of the fluid flow rate on the performance of the GHE
(The inlet fluid temperature = 60 °C, pipe length = 100 m, burial depth = 0.25 m, initial soil temperature on 1 December).

4.6.3 Inlet fluid temperature

The inlet temperature of the GHE may vary, depending on the loading conditions. In this section, the effect of the inlet temperature on the performance of the GHE is presented. Figure 4.13 shows that the outlet fluid temperature is affected by the inlet input temperature and the period of the operation. The temperature difference between the inlet and outlet fluid is higher when the inlet input temperature is higher. The GHE with a higher inlet fluid temperature can release more heat into the ground as the temperature difference between the working fluid and the ground is relatively higher. It is found that the temperature differences between inlet and outlet fluid are 4.2 °C and 7.6 °C, for the GHE with the lowest and the highest inlet fluid

68

temperatures, respectively, after 1 hour of operation. However, these values decrease with the increase of the operation period namely, 2.6 °C and 4.8 °C respectively, after 6 hours of operation.
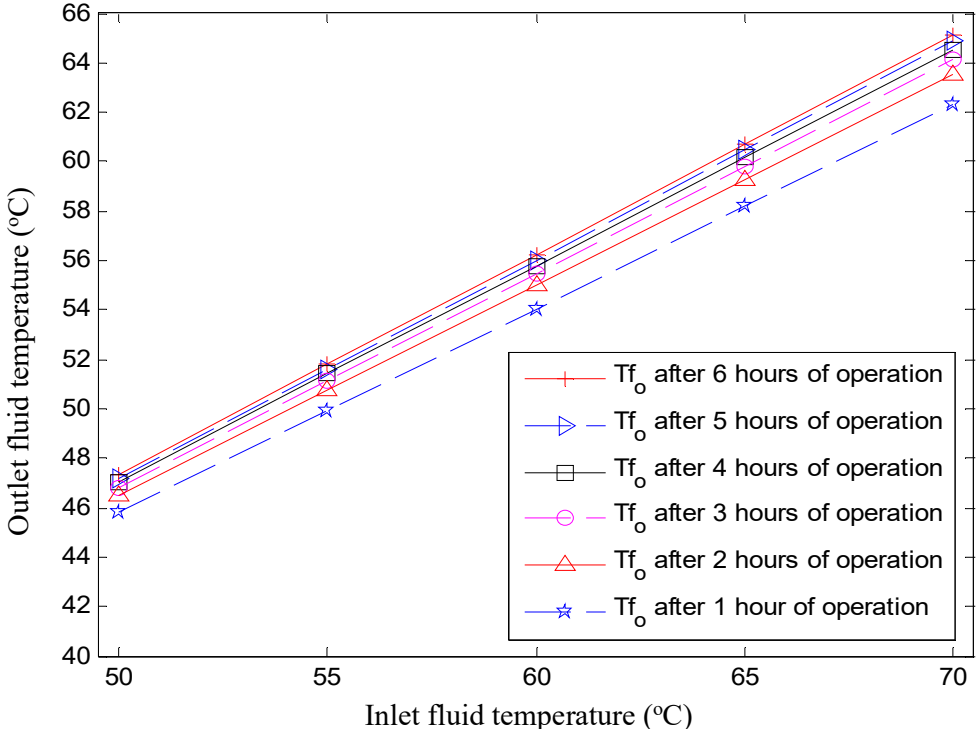
Figure 4.13: The effect of the inlet temperature on the performance of the GHE (The fluid mass flow rate = 0.5 kg/s, pipe length = 100 m, burial depth = 0.25 m, initial soil temperature on 1 December).

4.6.4 Burial depth

The thermal performance of the horizontal heat exchanger at six different burial depths $h_z = 25$ cm, 50 cm, 75 cm, 100 cm, 125 cm, and 150 cm is investigated. Figure 4.14 shows the outlet fluid temperature of the GHE at six different times from 1 to 6 hours of operation. As shown in the figure, the outlet fluid temperature varies with burial depths. The outlet temperature of the GHE is higher when the GHE is installed in a shallow region and decreases with the increase of the burial depth. This phenomenon occurs because the ground temperature at the shallow region, in summer, is higher than deeper layer's soil temperature due to the influence of the atmospheric condition on the ground surface. As a result, it affects the heat transfer capacity of the GHE since the temperature gradient between working fluid and soil varies with depth. It is observed, increasing the burial depth from 0.25 cm to 150 cm results in a drop in the outlet fluid temperature of 0.6 °C after 6 hours of operation. Even though burying the pipe at a shallow region may contribute to a lower thermal performance of the GHE, however, it also may potentially benefit since diverse heat transfer mechanisms take place on the ground surface [33].

The degradation of soil condition during the operation may possibly be recovered relatively quickly since the heat gains/losses take places on the ground surface. For instance, for the cooling purposes when the air conditioning system is in operation, the GHE is heating up the surrounding soil during the daytime when the air conditioning system is on. At nighttime, ambient temperature drops and normally the air conditioning system is turned off, i.e. no water circulated in the GHE. These assist the soil around the horizontal GHE to recover its temperature as it is buried at shallow depths.
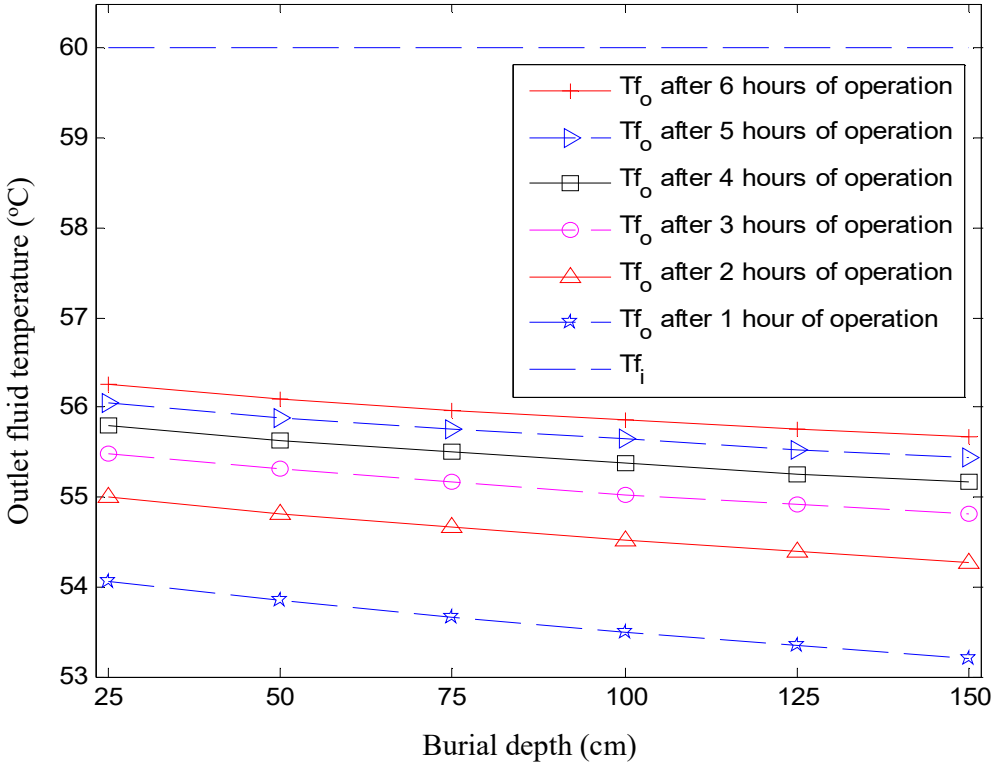
Figure 4.14: The effect of burial depth on the performance of the GHE
(The inlet fluid temperature = 60 °C, fluid mass flow rate = 0.5 kg/s, pipe length = 100 m, initial soil temperature on 1 December).

4.7 Summary

A 2D finite difference numerical model of a horizontal GHE has been developed to study its thermal performance under a transient condition. A new approach to consider the seasonal changes in soil temperature that influences the performance of the horizontal GHE has been introduced and incorporated into the GHE model as an internal heat source term. The theoretical results generated by the model are validated against the measurement data from the experimental study. The results show that incorporating the internal heat source term into the GHE model has improved the accuracy of the soil temperature significantly. The accuracy of estimating of water temperature out of GHE, has also been improved but not significantly. A

sensitivity analysis has been carried out to understand the impacts of some key design and operational parameters (e.g. pipe length, fluid flow rate, inlet fluid temperature, and burial depth) on the horizontal GHE performance. The results show that both the pipe length and the inlet fluid temperature have the significant impact on the GHE performance than the other parameters.

Based on the works on the horizontal GHE, a journal paper entitled "A new approach to modelling of a horizontal geo heat exchanger with an internal source term" has been published in *Applied Energy* and is attached as Appendix I.

CHAPTER 5

VERTICAL GEO HEAT EXCHANGER

This chapter presents the development of the vertical GHE model. The model incorporates the seasonal soil temperature changes by using an internal source term approach as discussed in Chapter 3. The approach is introduced in order to diminish the error generated by the GHE models which mostly ignore the effect of soil temperature fluctuations during seasonal changes as demonstrated in Chapter 2. Incorporating the internal source term into the vertical GHE model also allows us to tackle the complexity in considering the seasonal soil temperature variations due to the complicated heat transfer mechanism on the ground surface as presented in limited numbers of literature.

This chapter is organised as follows. Section 5.1 overviews the physical model of the vertical GHE. Section 5.2 presents the mathematical model development of the vertical GHE. Section 5.3 describes the input parameter for the vertical GHE. Section 5.4 provides the algorithm for the vertical GHE model. The validation of the vertical GHE model is presented in Section 5.5. Section 5.6 presents the sensitivity analysis of the vertical GHE. Section 5.7 summarises the key findings of this chapter.

5.1 Physical Model

A vertical GHE to be modelled, as shown in Figure 5.1, is a single U-shaped pipe which is buried inside a borehole with a diameter d_b and depth z. The pipe has a diameter d, length L, thickness t_h, and shank spacing L_s. The borehole is usually filled with materials which have a relatively higher thermal conductivity than the surrounding soil, in order to enhance the GHE's thermal capacity. The ground environment serves as a huge heat/sink source because it has a relatively stable temperature. The vertical GHE may cross different types of soil layers, at different depths, which have different thermal properties. The heat transfer at the GHE occurs when the working fluid at a temperature T_{fi} and mass flow rate $\dot{m}$ is circulated through the U-shaped pipe by a circulation pump. The heat is transferred by the working fluid to the inner pipe surface by convection. Then, it is transferred through the pipe's wall by conduction. The U-shaped pipe then transfers the heat through the grout to the surrounding soil by conduction. As a result, the temperature of soil would change around the GHE. On the surface of the ground, the convection with air and radiative heat transfer (with sky) occur. In the vertical GHE study, the radiative heat transfer between soil surface and sky is neglected. The vertical GHE is suitable to be installed in the limited land area. It may benefit from the relatively stable ground temperature at a deeper ground depth and may lead to a better performance.
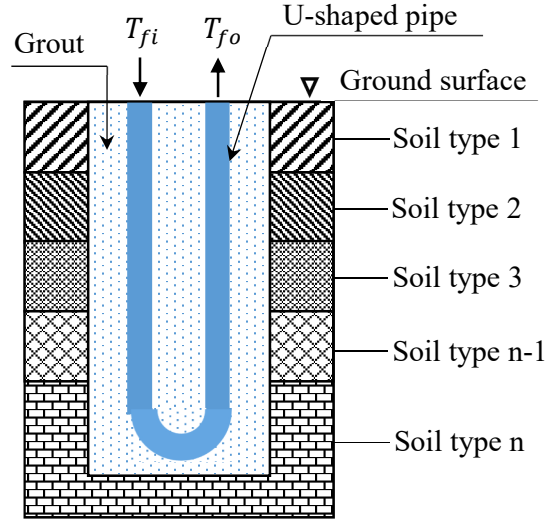
Figure 5.1: Schematic of the vertical GHE

5.2 Mathematical model of the vertical GHE

The mathematical model for the vertical GHE was developed by taking a reference on the existing models as reviewed in Chapter 2, Section 2.3.2. The model considers the transient conditions of the working fluid, pipe, grout, and surrounding soil. The working fluid exchanges the heat with the inner pipe surface by convection. The heat is assumed to flow through the pipe wall by 1D conduction and through the grout and soil by 2D conduction. The governing equations for the vertical GHE model are summarised next:

(a) Working Fluid

The energy balance equation for working fluid is given as:

$$c_f \rho_f A \frac{\partial T_f}{\partial t} = \pi d_{in} h_f (T_p - T_f) - \dot{m}_f c_f \frac{\partial T_f}{\partial z} \tag{5.1}$$

where c_f is the fluid specific heat (J/kgK), ρ_f is the fluid density (kg/m³), A is the cross section area of the pipe (m²), T_f is the fluid temperature (K), t is the time step (s), d_{in} is the internal pipe diameter (m), h_f is the convective heat transfer coefficient of fluid (W/m²K), T_p is the pipe temperature (K), $\dot{m}_f$ is the fluid mass flow rate (kg/s), z is the distance in the direction parallel to the pipe (m).

(b) Pipe

For pipe wall, the energy balance equation is:

$$c_p \rho_p V_p \frac{\partial T_p}{\partial t} = A h_f (T_f - T_p) + \frac{k_g A}{0.5 \Delta r} (T_g - T_p) \tag{5.2}$$

where c_p is the pipe specific heat (J/kgK), ρ_p is the pipe density (kg/m³), V_p is the volume of the pipe wall (m³), T_p is the pipe temperature (K), t is the time step (s), A is the area of the pipe (m²), h_f is the convective heat transfer coefficient of fluid (W/m²K), T_f is the fluid temperature (K), k_g is the grout thermal conductivity (W/mK), Δr is the finite increment in the radial direction (m) and T_g is the grout temperature (K).

(c) Grout

The governing equation for grout is given as:

$$\frac{1}{\alpha_g}\frac{\partial T_g}{\partial t} = \frac{\partial^2 T_g}{\partial r^2} + \frac{1}{r}\frac{\partial T_g}{\partial r} + \frac{\partial^2 T_g}{\partial z^2} \tag{5.3}$$

where α_g is the grout diffusivity (m²/s), T_g is the grout temperature (K), t is the time step (s), r is the radius of grout domain (m), z is the axial distance of the grout domain (m).

(d) Soil

The governing equation for the soil is given as:

$$\frac{1}{\alpha_s}\frac{\partial T_s}{\partial t} = \frac{\partial^2 T_s}{\partial r^2} + \frac{1}{r}\frac{\partial T_s}{\partial r} + \frac{\partial^2 T_s}{\partial z^2} + \frac{H_s}{k_s} \tag{5.4}$$

where α_s is the soil diffusivity (m²/s), T_s is the soil temperature (K), t is the time step (s), r is the radius of soil domain (m), z is the axial distance of soil domain (m), H_s is the soil internal heat source term (W/m³), and k_s is the soil thermal conductivity (W/mK).

In this study, to simplify the geometry of the vertical GHE, the single U-shaped pipe is represented as a single pipe with an equivalent diameter, as illustrated in Figure 5.2 [92]. The equivalent diameter is calculated corresponding to:

$$d_{eq} = \sqrt{2d_p L_s} \tag{5.5}$$

where d_{eq} is the equivalent diameter of the pipe (m), d_p is the pipe diameter (m), L_s is the distance between centres of two legs U-shaped pipe. This approach is valid if $d_p \leq L_s \leq r_b$.
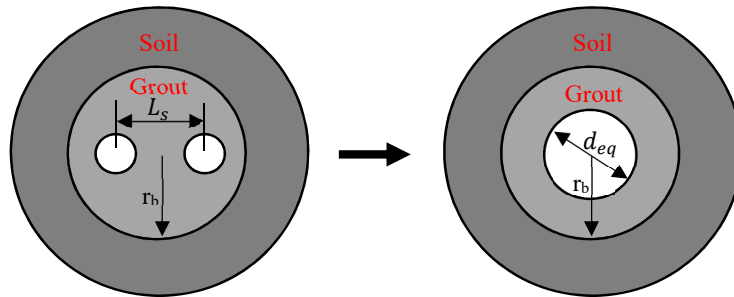
Figure 5.2: A single U-shaped pipe GHE represented as a pipe with the equivalent diameter

Using an explicit finite difference method, the system of differential Equations 5.1-5.4 can be written in the finite difference form, referring to Figure 5.3.

(a) Fluid temperature

$$T_{f(j)}^{t+\Delta t} = \frac{\Delta t}{c_f \rho_f A}\left[\pi d_{in} h_f\left(T_{p(j)}^t - T_{f(j)}^t\right) - \dot{m}_f c_f \frac{T_{fo(j)}^t - T_{fi(j)}^t}{\Delta z}\right] + T_{f(j)}^t \tag{5.6}$$

where $T_f^{t+\Delta t}$ is the mean temperature of the fluid (K) at the new time step, T_f^t is the mean temperature of the fluid (K) at the current time step, T_{fi}^t and T_{fo}^t are the inlet and outlet temperatures of the fluid (K) at the current time step respectively, Δz is the finite increment of the pipe (m), j is the index in the direction parallel to the pipe. The other parameters are the same as those elaborated in Equation 5.1.
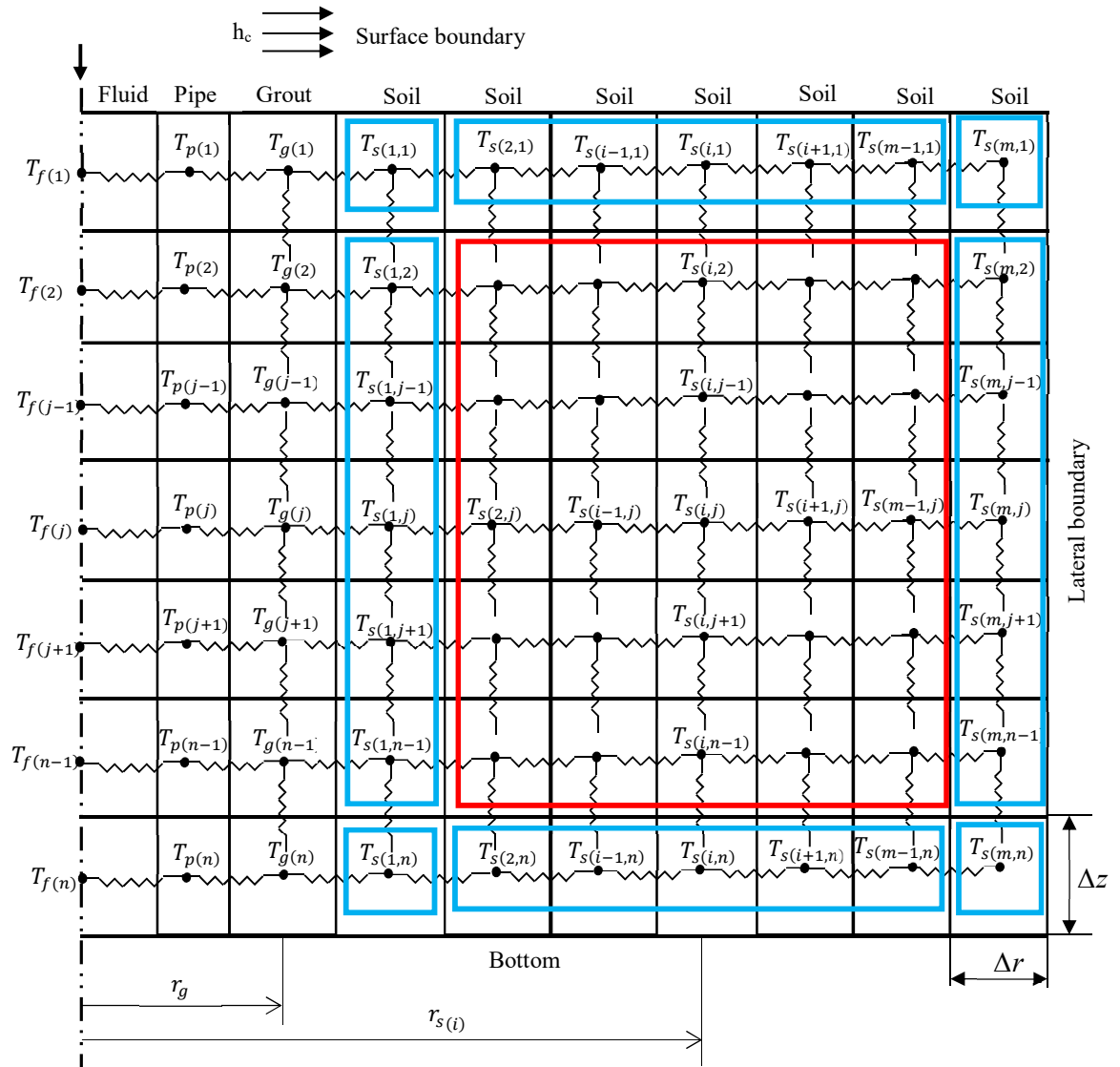
Figure 5.3: Computational domain of the vertical GHE

(b) Pipe temperature

$$T_{p(j)}^{t+\Delta t} = \frac{\Delta t}{c_p \rho_p V_p}\left[Ah_f\left(T_{f(j)}^{t+\Delta t} - T_{p(j)}^t\right) + \frac{k_s A}{0.5\Delta r_g}\left(T_{g(j)}^t - T_{p(j)}^t\right)\right] + T_{p(j)}^t \tag{5.7}$$

where $T_p^{t+\Delta t}$ is the pipe temperature (K) at the new step, T_p^t is the pipe temperature (K) at the current time step, j is the index in the direction parallel to the pipe. The other parameters are the same as those elaborated in Equation 5.2.

(c) Grout temperature

Converting Equation 5.3 into linear equation using finite difference approach, for the internal nodes (j = 2,3,4....n-1) gives:

$$T_{g(i,j)}^{t+\Delta t} = Fo_g\left[2T_p\left(1 - \frac{\Delta r_g}{2r_g}\right) + \frac{T_{s(i,j)}^t}{C_{sg}} + T_{g(i,j+1)}^t + T_{g(i,j-1)}^t\right]$$
$$+ \left[1 - \left[\left(2 - \frac{2\Delta r_g}{2r_g}\right) + \frac{1}{C_{sg}} + 2\right]Fo\right]T_{g(i,j)}^t \tag{5.8}$$

where

$$Fo_g = \frac{\alpha_g \Delta t}{\left(\Delta r_g\right)^2} \tag{5.9}$$

$$C_{sg} = \frac{1/2}{1 + \frac{\Delta r_g}{2r_g}} + \frac{\Delta r_s/\left(2\Delta r_g\right)}{\frac{k_s}{k_g}\left(1 + \frac{\Delta r_g}{2r_g}\right)} \tag{5.10}$$

The solution of the grout temperature next to surface boundary (j = 1) is given as:

$$T_{g(i,j)}^{t+\Delta t} = Fo_g\left[2T_p\left(1 - \frac{\Delta r_g}{2r_g}\right) + \frac{T_{s(i,j)}^t}{C_{sg}} + T_a^t C_{ag} + T_{g(i,j+1)}^t\right]$$
$$+ \left[1 - \left[\left(2 - \frac{2\Delta r_g}{2r_g}\right) + \frac{1}{C_{sg}} + C_{ag} + 1\right]Fo_g\right]T_{g(i,j)}^t \tag{5.11}$$

The solution of the grout temperature next to bottom boundary (j = n) is given as:

$$T_{g(i,j)}^{t+\Delta t} = Fo_g\left[2T_p\left(1 - \frac{\Delta r_g}{2r_g}\right) + \frac{T_{s(i,j)}^t}{C_{sg}} + T_{g(i,j-1)}^t\right]$$
$$+ \left[1 - \left[\left(2 - \frac{2\Delta r_g}{2r_g}\right) + \frac{1}{C_{sg}} + 1\right]Fo_g\right]T_{g(i,j)}^t \tag{5.12}$$

where $T_g^{t+\Delta t}$ and T_g^t are the grout temperatures (K) at the new and current time steps, respectively, Fo_g is the Fourier number, Δr_g and Δr_s are the finite increments (m) in the radial directions of the grout and the soil domains, respectively, r_g is the radius from centre of the pipe to centre of grout element (m), k_g and k_s are the thermal conductivity of grout and soil (W/mK),

respectively, i and j are indices in the radial and axial directions, respectively, and Δt is the time step (s).

(d) Soil temperature

The solution of the soil temperature for the internal nodes is given as:

$$T_{s(i,j)}^{t+\Delta t} = Fo_s \left[\left(1 + \frac{\Delta r_s}{2r_{s(i)}}\right) T_{s(i+1,j)}^t + \left(1 - \frac{\Delta r_s}{2r_{s(i)}}\right) T_{s(i-1,j)}^t + T_{s(i,j+1)}^t + T_{s(i,j-1)}^t \right.$$
$$\left. + \frac{H_{s(j)}(\Delta r_s)^2}{k_s} \right] + (1 - 4Fo)T_{s(i,j)}^t \tag{5.13}$$

where

$$Fo_s = \frac{\alpha_s \Delta t}{(\Delta r_s)^2} \tag{5.14}$$

where $T_s^{t+\Delta t}$ and T_s^t are the soil temperatures (K) at the new and current time steps, respectively, Fo_s is the Fourier number, $H_{s(j)}$ is the internal heat source term (W/m³) at level/layer j, Δr_s is the finite increment in the radial direction of the soil domain (m), r_s is the radius from centre of the pipe to centre of soil element (m), k_s is the soil thermal conductivity (W/mK), i and j are the indices in the radial and axial directions, respectively, and Δt is the time step (s).

Different boundary conditions are applied to the boundary of the soil domain. The convection heat transfer is considered at the ground surface, while the adiabatic condition is applied to the bottom and lateral boundaries of the soil domain. Equations for the soil temperatures at the boundaries are summarised as:

➤ For the top layer of the soil, i.e. $j = 1$ (refer to Figure 5.3), its temperatures:

a. For $i = 1$ and $j = 1$

$$T_{s(1,1)}^{t+\Delta t} = Fo_s \left[\frac{T_{g(i,j)}^t}{C_{gs}} + \left(1 + \frac{\Delta r_s}{2r_{s(i)}}\right) T_{s(i+1,j)}^t + T_a^t C_{as} + T_{s(i,j+1)}^t + \frac{H_{s(j)}(\Delta r_s)^2}{k_s} \right]$$
$$+ \left[1 - \left[\frac{1}{C_{gs}} + \left(1 + \frac{\Delta r_s}{2r_{s(i)}}\right) + C_{as} + 1 \right] Fo_s \right] T_{s(i,j)}^t \tag{5.15}$$

$$C_{gs} = \frac{\Delta r_g / 2\Delta r_s}{\frac{k_g}{k_s}\left(1 - \frac{\Delta r_s}{2r_s(i)}\right)} + \frac{1/2}{1 - \frac{\Delta r_s}{2r_s(i)}} \tag{5.16}$$

$$C_{as} = \frac{\Delta r_s}{k_s/h_{as}} + \frac{\Delta r_s}{2} \tag{5.17}$$

where T_a^t is the ambient temperature (K), C_{gs} is given by Equation 5.16, C_{as} is summarised by Equation 5.17. The other parameters are the same as those elaborated in Equation 5.13.

b. For i = 2,3,4....m-1 and j = 1

$$T_{s(i,j)}^{t+\Delta t} = Fo_s \left[\left(1 - \frac{\Delta r_s}{2r_{s(i)}}\right) T_{s(i-1,j)}^t + \left(1 + \frac{\Delta r_s}{2r_{s(i)}}\right) T_{s(i+1,j)}^t + T_a^t C_{as} + T_{s(i,j+1)}^t \right.$$

$$\left. + \frac{H_{s(j)}(\Delta r_s)^2}{k_s} \right] + \left[1 - \left[\left(1 - \frac{\Delta r_s}{2r_{s(i)}}\right) + \left(1 + \frac{\Delta r_s}{2r_{s(i)}}\right) + C_{as} + 1 \right] Fo_s \right] T_{s(i,j)}^t$$

$$(5.18)$$

c. For i = m and j = 1, assuming adiabatic boundary condition at i = m

$$T_{s(m,1)}^{t+\Delta t} = Fo_s \left[\left(1 - \frac{\Delta r_s}{2r_{s(i)}}\right) T_{s(i-1,j)}^t + T_a^t C_{as} + T_{s(i,j+1)}^t + \frac{H_{s(j)}(\Delta r_s)^2}{k_s} \right]$$

$$+ \left[1 - \left[\left(1 - \frac{\Delta r_s}{2r_{s(i)}}\right) + C_{as} + 1 \right] Fo_s \right] T_{s(i,j)}^t$$

$$(5.19)$$

where the parameters of Equations 5.18-5.19 are the same as elaborated in the Equation 5.13.

➢ The soil temperatures next to bottom boundary (refer to Figure 5.3) are computed as:

a. For i = 1 and j = n

$$T_{s(1,n)}^{t+\Delta t} = Fo_s \left[\frac{T_{g(i,j)}^t}{C_{gs}} + \left(1 + \frac{\Delta r_s}{2r_{s(i)}}\right) T_{s(i+1,j)}^t + T_{s(i,j-1)}^t + \frac{H_{s(j)}(\Delta r_s)^2}{k_s} \right]$$

$$+ \left[1 - \left[\frac{1}{C_{gs}} + \left(1 + \frac{\Delta r_s}{2r_{s(i)}}\right) + 1 \right] Fo_s \right] T_{s(i,j)}^t$$

$$(5.20)$$

b. For i = 2,3,4....m-1 and j = n

$$T_{s(i,j)}^{t+\Delta t} = Fo_s \left[\left(1 - \frac{\Delta r_s}{2r_{s(i)}}\right) T_{s(i-1,j)}^t + \left(1 + \frac{\Delta r_s}{2r_{s(i)}}\right) T_{s(i+1,j)}^t + T_{s(i,j-1)}^t + \frac{H_{s(j)}(\Delta r_s)^2}{k_s} \right]$$

$$+ \left[1 - \left[\left(1 - \frac{\Delta r_s}{2r_{s(i)}}\right) + \left(1 + \frac{\Delta r_s}{2r_{s(i)}}\right) + 1 \right] Fo_s \right] T_{s(i,j)}^t$$

$$(5.21)$$

c. For i = m and j = n

$$T_{s(m,n)}^{t+\Delta t} = Fo_s \left[\left(1 - \frac{\Delta r_s}{2r_{s(i)}}\right) T_{s(i-1,j)}^t + T_{s(i,j-1)}^t + \frac{H_{s(j)}(\Delta r_s)^2}{k_s} \right]$$

$$+ \left[1 - \left[\left(1 - \frac{\Delta r_s}{2r_{s(i)}}\right) + 1 \right] Fo_s \right] T_{s(i,j)}^t$$

$$(5.22)$$

➢ The soil temperatures next to lateral boundary (refer to Figure 5.3) are computed as:

a. For i = 1 and j = 2,3,4….. n-1

$$T_{s(i,j)}^{t+\Delta t} = Fo_s \left[\frac{T_{g(i,j)}^t}{C_{gs}} + \left(1 + \frac{\Delta r_s}{2r_{s(i)}}\right) T_{s(i+1,j)}^t + T_{s(i,j-1)}^t + T_{s(i,j+1)}^t + \frac{H_{s(j)}(\Delta r_s)^2}{k_s} \right]$$

$$+ \left[1 - \left[\frac{1}{C_{gs}} + \left(1 + \frac{\Delta r_s}{2r_{s(i)}}\right) + 2 \right] Fo_s \right] T_{s(i,j)}^t$$

$$(5.23)$$

78

b. For i = m and j = 2,3,4….. n-1

$$T_{s(i,j)}^{t+\Delta t} = Fo_s \left[\left(1 - \frac{\Delta r_s}{2r_{s(i)}} \right) T_{s(i-1,j)}^t + T_{s(i,j-1)}^t + T_{s(i,j+1)}^t + \frac{H_{s(j)}(\Delta r_s)^2}{k_s} \right]$$

$$+ \left[1 - \left[\left(1 - \frac{\Delta r_s}{2r_{s(i)}} \right) + 2 \right] Fo_s \right] T_{s(i,j)}^t \tag{5.24}$$

where the parameters of Equations 5.20-5.24 are the same as elaborated in the Equation 5.13.

To solve the system of Equations (5.1) to (5.4) the explicit method which is conditionally stable is used. Thus, the time step Δt must be within the Courant-Friedrichs-Lewy stability condition [89], which is given as:

$$|\psi| \le 1, \qquad \Delta t \le \frac{\Delta z}{v_f} \tag{5.25}$$

where $\psi = (v_f \Delta t / \Delta z)$ is the Courant number, Δt is the time step (s), Δz is the finite increment of the pipe (m) as shown in Figure 5.3, and v_f is the velocity of the working fluid (m/s).

5.3 Input parameters of the model

In this model, the unknown temperatures of working fluid, pipe, and soil are estimated by using the input parameters summarised as follows:

A. Initial soil temperature
The initial soil temperatures $(T_{s(i,j)})$ when t = 0 at each layer are determined using the analytical soil temperature equation presented by Baggs [20], as Equation 2.1.

B. Soil thermal properties
The thermal properties of the typical soil including thermal conductivity (k_s), density (ρ_s), and specific heat (c_s) are determined based on the existing literature data, as summarised in Chapter 2, Section 2.2. Then, the soil thermal diffusivity (α_s) is determined as:

$$\alpha_s = \frac{k_s}{\rho_s c_s} \tag{5.26}$$

where k_s is the soil thermal conductivity (W/mK), ρ_s is the soil density (kg/m³) and c_s is the soil specific heat (J/kgK).

The typical soil thermal conductivity values as elaborated in the literature review, Section 2.2, is summarised in Table 5.1.

Table 5.1: Typical soil thermal conductivity values [3]

Type of soils	k (W/mK)	ρ(kg/m³)	c (kJ/kgK)
Limestone	1.2-2.15	2300-2500	0.8-0.9
Sandstone	1.8-2.9	2160-2300	0.7-0.8
Sand	0.15-4	1280-2150	0.8-1.48
Clay	0.15-2.5	1070-1600	0.92-2.2
Loam	0.29-0.76	1200-1400	1.14-2.1
Sandy loam	0.19-1.12	1550-1750	0.84 -1.3

C. Soil heat source term

In this model, the soil heat source term ($H_{s(j)}$) is introduced to consider soil temperature fluctuations during seasonal changes. The soil heat source term is calculated by using Equation 3.1. For the vertical GHE model, the heat source term is applied for several soil layers. In which each soil layer has different source term value.

$$H_{s(j)} = \rho_s c_s \frac{\Delta T_{s(j)}}{\Delta t}$$ (5.27)

where $H_{s(j)}$ is the soil heat source term (W/m³) at each layer, ρ_s is the soil density (kg/m³), c_s is the soil specific heat (J/kgK), Δt is the time period (s), and $\Delta T_{s(j)}$ is the soil temperature difference in summer and winter (K) at each soil layer.

D. Convective heat transfer coefficient of air in contact with the soil surface

The convective heat transfer coefficient between air and the soil surface (h_{ca}) can be calculated from a relation of turbulent flow over a flat plate. It is given as:

$$h_{as} = \frac{N_u k_a}{L}$$ (5.28)

where h_{as} is the convective heat transfer coefficient between air and the soil surface (W/m²K), N_u is the Nusselt number, k_a is the conductive heat transfer coefficient of air (W/mK), L is the characteristic dimension of the ground surface for the vertical GHE (m).

According to Lloyd and Moran [93], the characteristic dimension for a circular disk can be calculated as:

$$L = \frac{A}{P}$$ (5.29)

where L is the characteristic dimension of the ground surface for the vertical GHE (m), A is the cross section area of the surface of the soil boundary (m²), P is the perimeter of the soil boundary (m).

Bahrami [90], presents the average Nusselt number over the flat plate in the turbulent region as:

$$N_u = 0.037 R_e^{4/5} P_r^{1/3} \qquad (5.30)$$

where N_{ua} is the Nusselt number, R_e is the Reynold number, and P_r is the Prandtl number of air.

While the Reynold number is given as:

$$R_e = \frac{\rho_a v_a L}{\mu_a} \qquad (5.31)$$

where R_e is the Reynold number, ρ_a is the air density (kg/m³), v_a is the wind speed (m/s), L is the unit length (m), μ_a is the air dynamic viscosity (N s/m²).

E. Convective heat transfer coefficient between the working fluid and the inner pipe surface

The convective heat transfer coefficient of working fluid in contact with the inner pipe surface (h_f) is calculated as:

$$h_f = \frac{N_u k_f}{D_{eq}} \qquad (5.32)$$

where h_f is the convective heat transfer coefficient of fluid in contact with the inner pipe surface (W/m²K), N_u is the Nusselt number, k_f is the conductive heat transfer coefficient of fluid (W/mK), d_{eq} is the equivalent diameter of the pipe (m).

The Reynold number for the fluid circulated inside the pipe is calculated as:

$$R_e = \frac{\rho_f v_f d_{eq}}{\mu_f} \qquad (5.33)$$

where R_e is the Reynold number, ρ_f is the fluid density (kg/m³), v_f is the fluid velocity (m/s), d_{eq} is the equivalent diameter of the pipe (m), μ_f is the fluid dynamic viscosity (N s/m²). In the literature, it is considered that the fluid is in turbulent flow if $R_e > 2000$.

Incropera [94], expresses the Nusselt number for laminar flow in pipes with constant surface heat flux as

$$N_u = 4.36 \qquad (5.34)$$

While for turbulent flow, it can be determined from Dittus-Boelter correlation and it is given as:

$$N_u = 0.023 R_e^{4/5} P_r^n \qquad (5.35)$$

where $n = 0.3$ for cooling and $n = 0.4$ for heating.

F. Meteorological data

The meteorological data, including ambient air temperature and wind speed, is based on data provided by the local weather bureau.

5.4. Algorithm
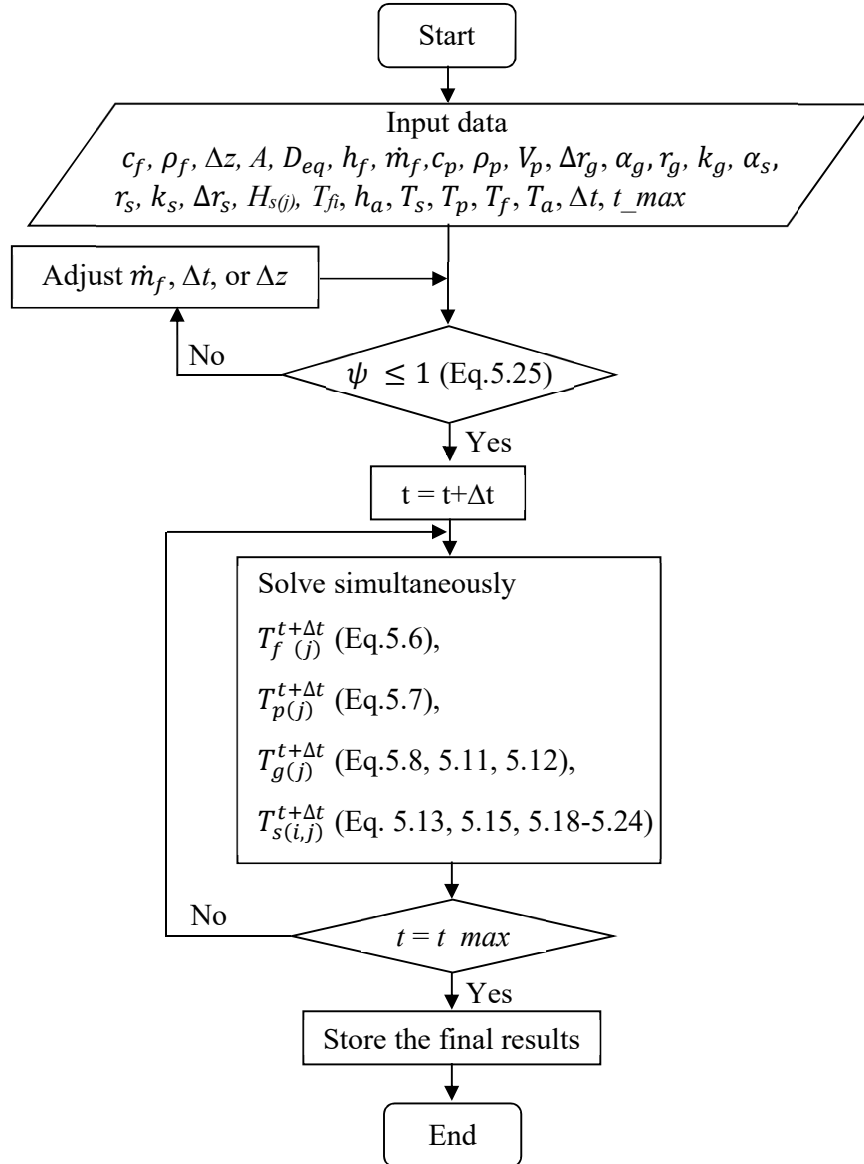
Figure 5.4: Flow chart computational procedure for the vertical GHE

A computer program using MATLAB as the programming language has been developed to execute the previously discussed GHE model. The intention of this section is to show the link between the mathematical model and computer programming. The computational procedures for the vertical GHE are illustrated through a simplified flowchart, Figure 5.4. When the program starts, the input data including the fluid specific heat (c_f), fluid density (ρ_f), finite increment of depth (Δz), heat transfer area of the pipe (A), equivalent pipe diameter (d_{eq}), convective heat transfer coefficient between the working fluid and the inner pipe surface (h_f), fluid mass flow rate ($\dot{m}_f$), pipe specific heat (c_p), pipe density (ρ_p), volume of pipe wall (V_p),

radius increment of grout (Δr_g), grout thermal diffusivity (α_g), radius from the pipe's axis to the centre of grout element (r_g), grout thermal conductivity (k_g), soil thermal diffusivity (α_s), the radius from pipe's axis to the centre of soil element (r_s), soil thermal conductivity (k_s), soil specific heat (α_s), radius increment of soil (Δr_s), soil source term as a depth function ($H_{s(j)}$), inlet fluid temperature (T_{fi}), convective heat transfer coefficient of air in contact with the soil surface (h_{as}), initial soil temperature (T_s), initial pipe temperature (T_p), initial fluid temperature (T_f), ambient temperature (T_a), time step (Δt), maximum simulation time (t_max), are required for the input data in the program.

In order to perform the calculation, the program needs to satisfy the stability condition, as given by Equation 5.25. If the stability criterion is not achieved, one of the following parameters either fluid mass flow rate, time step, or depth increment must be adjusted. Once the stability criterion is achieved, the Equations 5.6-5.8, 5.11-5.13, 5.15, and 5.18-5.24 are solved simultaneously in order to obtain the thermal solutions of the vertical GHE. The calculation is repeated until the maximum simulation time is attained.

5.5 Validation of the vertical GHE model

5.5.1 Experimental validation

A reduced scale experimental rig was constructed to validate the developed vertical GHE model, as shown in Figure 5.5. The scale down GHE system consists of a single U-shaped pipe which has an internal diameter of 0.025 m, an outer diameter of 0.029 m and a leg spacing of 0.064 m. The U-shaped pipe made of PVC was mounted vertically at the centre of a steel drum which has dimensions of 0.845 m high, 0.57 m inner diameter and 0.58 m outer diameter. The steel drum was filled with three different soil layers consisting of sand at the top (0.3 m thick), sandy loam in the middle (0.3 m thick), and loam at the bottom (0.245 m thick), while sand was used as the backfill material of the borehole which has a diameter of 0.15 m (see Figure 5.6). The Earthwool R-2.0 insulation material, which has a thickness of 0.09 m, was used to prevent the heat loss through the drum's side. LM 35 integrated circuit temperature sensors were used to measure the soil temperature, while PT 100 temperature sensors were used to measure both inlet and outlet water temperatures. The LM 35 temperature sensors were distributed at seven locations along the depth of the drum, in which they were mounted from a depth of 0.1 m to a depth of 0.7 m below the soil surface, in 0.1 m increments. They were installed at a distance of 0.125 m, 0.175 m and 0.225 m from the axis of the borehole. Both LM35 and PT 100 temperature sensors were connected to a data acquisition device plugged in a computer. Then, the experimental data was recorded and stored in the computer.

(a)
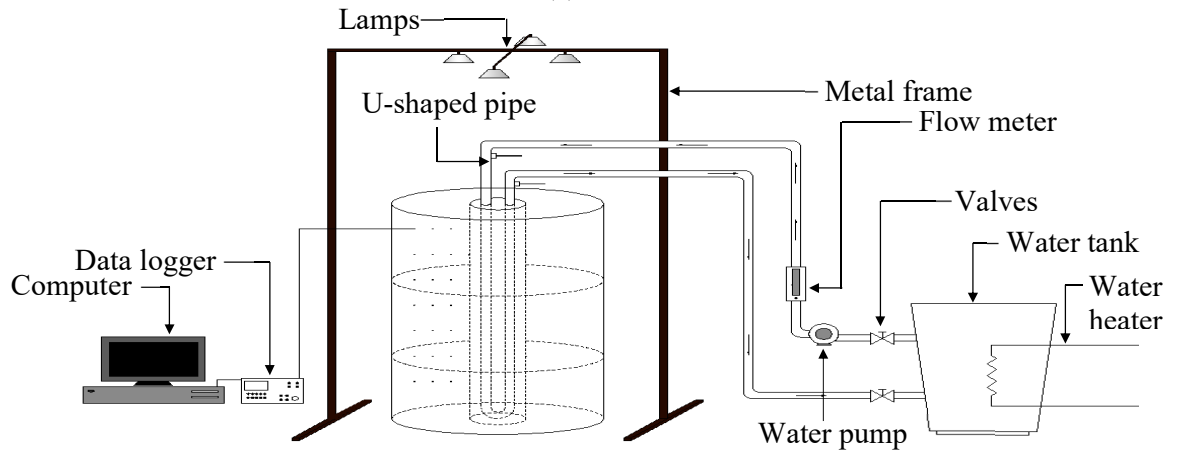
(b)

Figure 5.5: (a) The complete experimental set up (left) and the vertical GHE system (right), (b) Schematic of the vertical GHE rig.
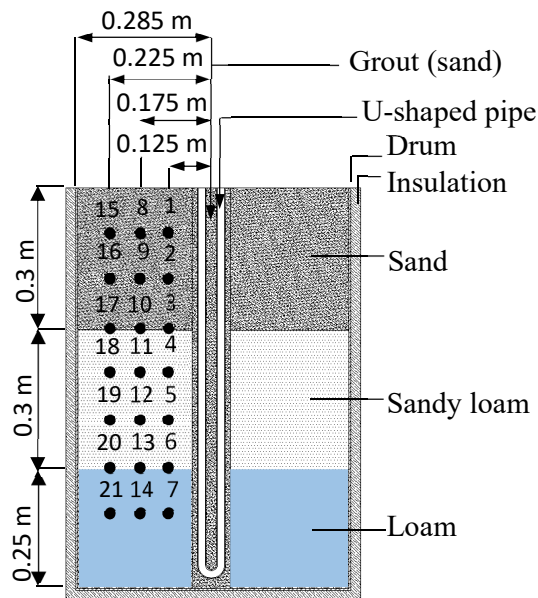
Figure 5.6: Cross section of the vertical GHE showing the location of temperature sensors

5.5.2 Experimental study

Experimental studies were conducted to validate the vertical GHE model. The first study was conducted to simulate the seasonal soil temperature changes in order to obtain the internal

source terms. The changes of soil temperature were driven by both the radiation exposure emitted by the halogen lamps and the interaction of the soil surface and ambient air. In the first experiment, the soil receives only the heat radiated by halogen lamps while the hot water system was turned Off. The (seasonal) changes in soil temperature were simulated by running the experiment with 4 hours of light On and 6 hours of light Off. It is believed that during 4 hours of light On heating is sufficient for the heat flux received on the soil surface of the reduced scale GHE rig to penetrate the shallow region of the soil causing changes in the soil temperature. During the 6 hours of light Off cooling, it allows the accumulated heat in the soil to dissipate into the atmosphere thus lowering the soil temperature. The changes in upper layer soil temperature of the test rig are considered to represent those occur in the in-situ test of the vertical GHE. Thus, these periods are considered sufficient for the scale down experimental rig. The radiation flux on the soil surface, during the light On, was set to 900 W/m². The value of the heat flux was regulated by adjusting the distance of the halogen lamps over the ground surface. The changes in soil temperature during the heating and cooling period were recorded using a data logger connected to a computer. Based on the changes of soil temperature values, the soil's source term values, at different depths of soil, were calculated. Once the source term values have been calculated. They will be incorporated into soil temperature model. As an example, Figure 5.7 shows the profile of mean soil temperature at a depth of 0.2 m during 4 hours of light On heating and 6 hours of light Off cooling based on the measurement results of experiment 1. The profile of soil temperature has been divided into 4 distinctive periods according to the gradient of changes in order to obtain the accurate source term values. Each period refers to a value of the internal heat source term. Tables 5.2.a and 5.2.b show the calculated values of the internal source term for each soil layer for a certain period of time.
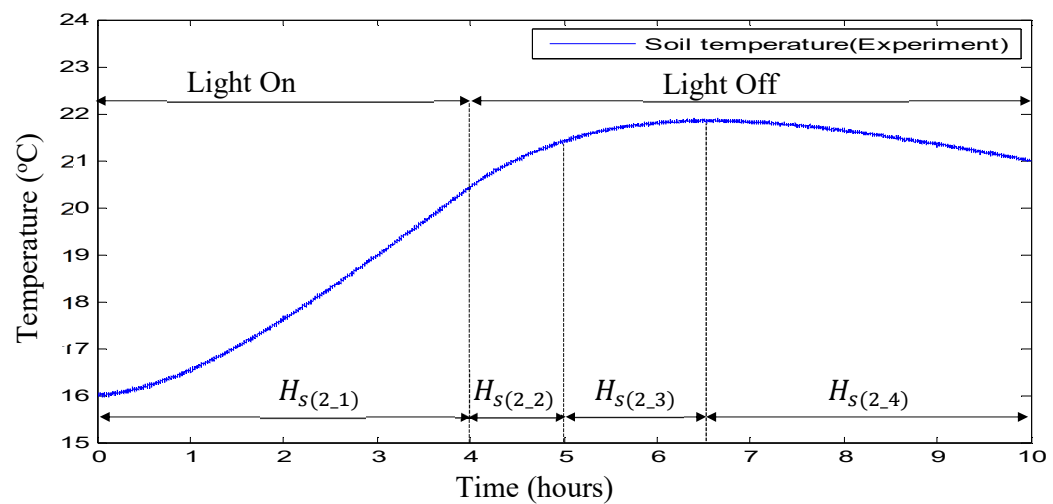
Figure 5.7: Profile of mean soil temperature at a depth of 0.2 m during 4 hours of light On heating and 6 hours of light Off cooling

Table 5.2.a: Values of the heat source term obtained from experimental study

Layer 1 (0-0.1 m)		Layer 2 (0.1-0.2 m)		Layer 3 (0.2-0.3 m)	
Time (hours)	Source term (W/m³)	Time (hours)	Source term (W/m³)	Time (hours)	Source term (W/m³)
0-4	1511.7	0-4	525.8	0-2	62.5
4-10	-549.6	4-5	462.1	2-7	218.1
-	-	5-6.5	142.7	7-10	52.7
-	-	6.5-10	-115	-	-

Table 5.2.b: Values of the heat source term obtained from experimental study

Layer 4 (0.3-0.4 m)		Layer 5 (0.4-0.5 m)		Layer 6 (0.5-0.6 m)		Layer 7 (0.6-0.84 m)	
Time (hours)	Source term (W/m³)	Time (hours)	Source term (W/m³)	Time (hours)	Source term (W/m³)	Time (hours)	Source term (W/m³)
0-3	24.6	0-2	0	0-4	0	0-4	0
3-10	99	2-4	15.9	4.10	23.6	4-10	17.6
-	-	4-10	57.9	-	-	-	-

The second study was conducted to validate the accuracy of the newly developed vertical GHE model. The second experiment was conducted by repeating the procedure of the first experiment as well as switching on the hot water system. In this experiment, the inlet temperature and flow rate of working fluid were set to 60 ºC and 0.5 l/min, respectively. The changes in soil and outlet water temperatures were recorded using data logger connected to a computer. This data was then used to validate the vertical GHE model. Based on the internal heat source term values obtained from the experiment 1 and the input values from the experiment 2, then the performance of the GHE was simulated by using the developed model.

Table 5.3: Thermal properties of the GHE materials

Thermal properties	Grout	Soil layer 1	Soil layer 2	Soil layer 3	Pipe	Water
Thermal conductivity (W/mK)	1.3	1.3	0.37	0.42	0.15	0.66
Specific heat (J/kgK)	1140	1140	1264.7	1650	1046	4188
Density (kg/m³)	1500	1500	1700	1450	1400	980

5.5.3 Validation of the vertical GHE model

The dynamic model of the vertical GHE was validated by comparing the simulated with the measured soil and outlet water temperatures in the 2nd experiment. This procedure has been presented by a number of researchers [45,55,62] in Section 2.3.2. The GHE's performance was simulated by using the source term values and thermophysical properties summarised in Table 5.2 and 5.3 respectively. Two different simulation results (with and without the internal heat source term) are presented and compared with the experimental results, to show the effect of seasonal soil temperature changes on the GHE's performance. Figures 5.8 and 5.9 show the profiles of soil temperatures at depths of 0.2 m and 0.5 m and a radius of 0.125 m, respectively.

These figures show that the soil temperatures increase over the operation time due to absorption of heat of both the GHE and halogen lamps. It is found that incorporating the internal heat source term into the GHE model can significantly improve the accuracy of the simulated soil temperature, especially at a shallower region (see Figure 5.8) where the soil temperature fluctuations during light On/Off (as observed in experiment 1) are significant. On a deeper layer (see Figure 5.9), the effect of the internal heat source term on the simulated soil temperatures is not significant due to the deep soil layer experienced slight temperature changes during the simulation of seasonal changes (experiment 1). It is obtained, the maximum relative errors for the soil temperature generated by the model that incorporates and neglects the internal heat source term are 3.7% and 14%, respectively. Figure 5.10 shows the comparison between the measured and the simulated outlet fluid temperatures. It is observed from the figure that there is a small cyclic variation in the measured inlet water temperature at the beginning operation of the GHE (the experimental data around 54 and 56 °C). This may be due to the noise generated during the measurement which could arise from imperfections in the data acquisition instrument. It is found that incorporating the source term into the GHE model has also increased the accuracy of the outlet fluid temperature even though not significant.
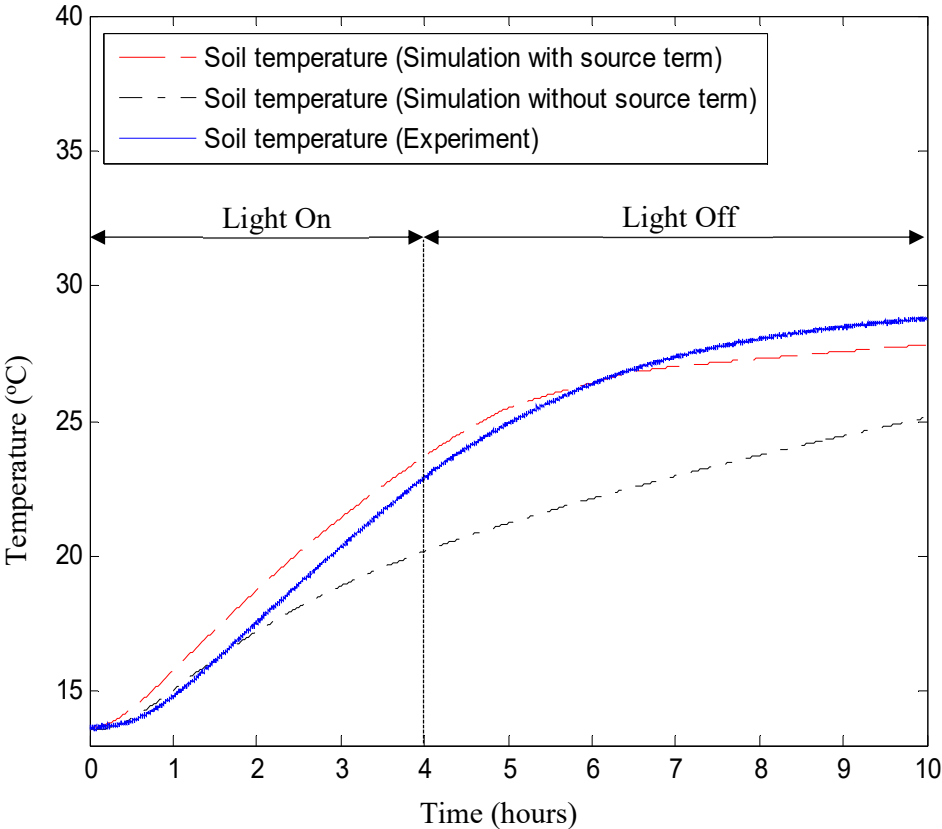
Figure 5.8: Soil temperature at a depth of 0.2 m and a distance of 0.125 m from the borehole axis
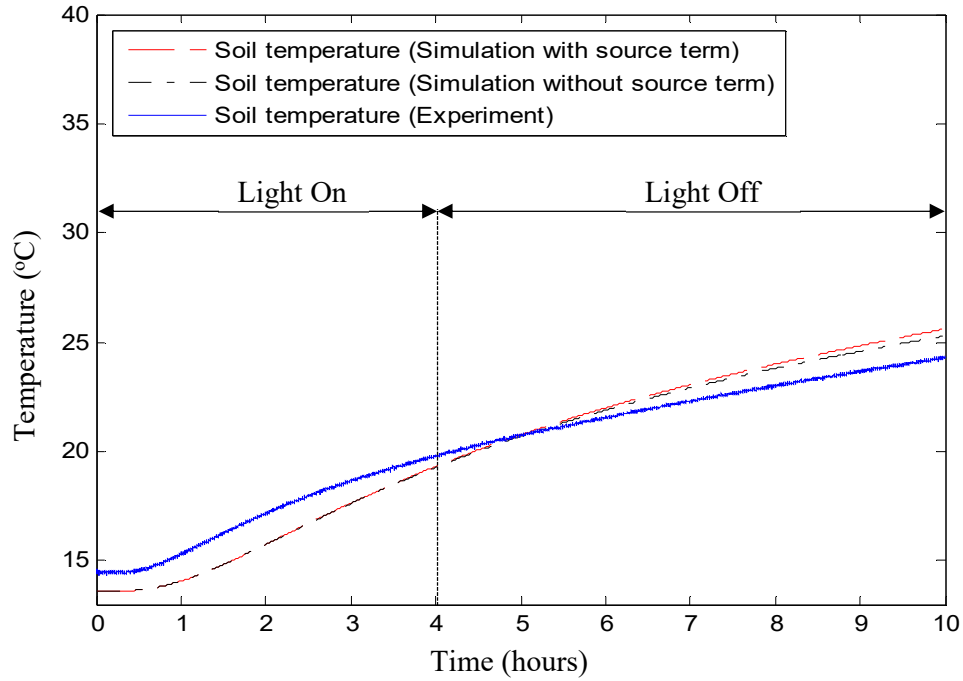
Figure 5.9: Soil temperature at a depth of 0.5 m and a distance of 0.125 m from the borehole axis
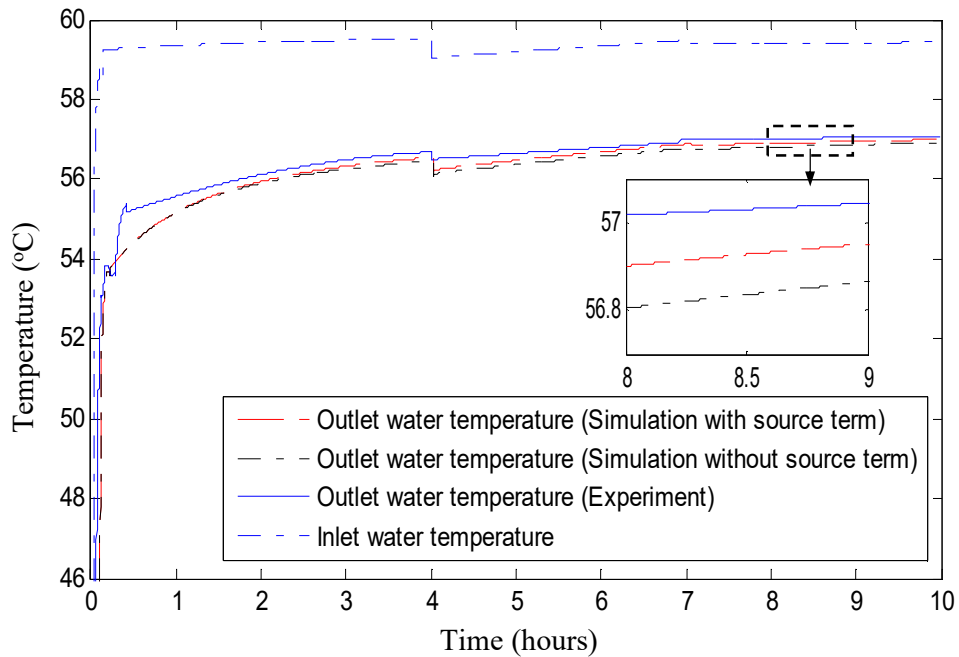
Figure 5.10: Profile of the outlet fluid temperature

5.6 Sensitivity analysis of the vertical GHE

In order to carry out the sensitivity analysis of the vertical GHE, a reference case is set. The GHE has a total depth of 60 m and installed in an area which the geological condition consists of three different soil layers. Each layer has a thickness of 20 m and different thermal properties. At a depth of more than 12 m below the surface, the effect of climate temperature seasonal changes on the soil temperature is insignificant [3]. Thus, the value of the internal heat source

term of such depth is assumed to be zero. Table 5.4 shows the calculated source term values for different depths of soil in Adelaide, Australia. The parameters of reference case are given in Table 5.5.

Table 5.4: The value of the internal heat source for each soil layer in Adelaide (Aug-Feb)

Soil layer	Soil temperature difference between summer and winter (°C)	Source term value (W/m³)
1st soil layer (0-1 m)	15.1	1.64
2nd soil layer (1-2 m)	10.5	1.14
3rd soil layer (2-3 m)	7.3	0.79
4th soil layer (3-4 m)	5.1	0.55
5th soil layer (4-5 m)	3.5	0.38
6th soil layer (5-6 m)	2.4	0.26
7th soil layer (6-7 m)	1.7	0.18
8th soil layer (7-8 m)	1.2	0.13
9th soil layer (8-9 m)	0.8	0.09
10th soil layer (9-10 m)	0.6	0.06
11th soil layer (10-11 m)	0.4	0.04
12th soil layer (11-12 m)	0.3	0.03
13th soil layer (>12 m)	0	0

Table 5.5: The parameters of the reference case

Parameters	Value	Unit	Parameters	Value	Unit
Circulation fluid (water)			*Ground layer 1 (Sand)*		
Inlet water temperature	60	°C	Thermal conductivity	1.3	W/mK
Flow rate	0.3	kg/s	Specific heat	1140	J/kgK
Specific heat	4188	J/kgK	Density	1500	kg/m³
Density	980	kg/m³	Layer thickness	20	m
Pipe (PVC)			*Ground layer 2 (Sandy loam)*		
Inlet diameter	0.04	m	Thermal conductivity	0.37	W/mK
Outlet diameter	0.044	m	Specific heat	1264.7	J/kgK
Centre to centre distance	0.07	m	Density	1700	kg/m³
Specific heat	1046.5	J/kgK	Layer thickness	20	m
Density	1400	kg/m³	*Ground layer 3 (Loam)*		
Borehole			Thermal conductivity	0.42	W/mK
Diameter	0.15	m	Specific heat	1450	J/kgK
Length	60	m	Density	1650	kg/m³
Grout thermal conductivity (Sand)	2	W/mK	Layer thickness	20	m
Specific heat	1140	J/kgK			

The sensitivity analysis is performed by using the developed model. The aim of this analysis is to investigate the effect of some design and operational parameters on the vertical GHE's performance including borehole thermal conductivity, borehole depth, fluid flow rate, and types

of carries fluids. In addition, the dynamic performance of the GHE under continuous and intermittent loads is also investigated.

5.6.1 The effect of borehole thermal conductivity

Figure 5.11 shows the effect of the grout thermal conductivity on the outlet fluid temperature of the vertical GHE over the period of time. In this study, the thermal conductivity of the grout material is varied from 1 to 5 W/mK, with an increment of 1 W/mK. It is observed that the outlet fluid temperature decreases with the increase of grout thermal conductivity. It shows that the use of high thermal conductivity grout results in a decrease in the borehole thermal resistance. As a result, it enhances the heat transfer rate of the GHE. It is found that the decrease in the outlet water temperature is not linear with the increase of the grout thermal conductivity. This tendency is due to the relatively low thermal conductivity value of the surrounding soil which has much a larger domain than the grout [76]. Different types of grout are used to fill the borehole including sand, sand-cement, bentonite, and sand bentonite mixture. The sand bentonite mixture is often used to fill-up the borehole because of its characteristics of water absorption and swelling properties of bentonite crystal [95].
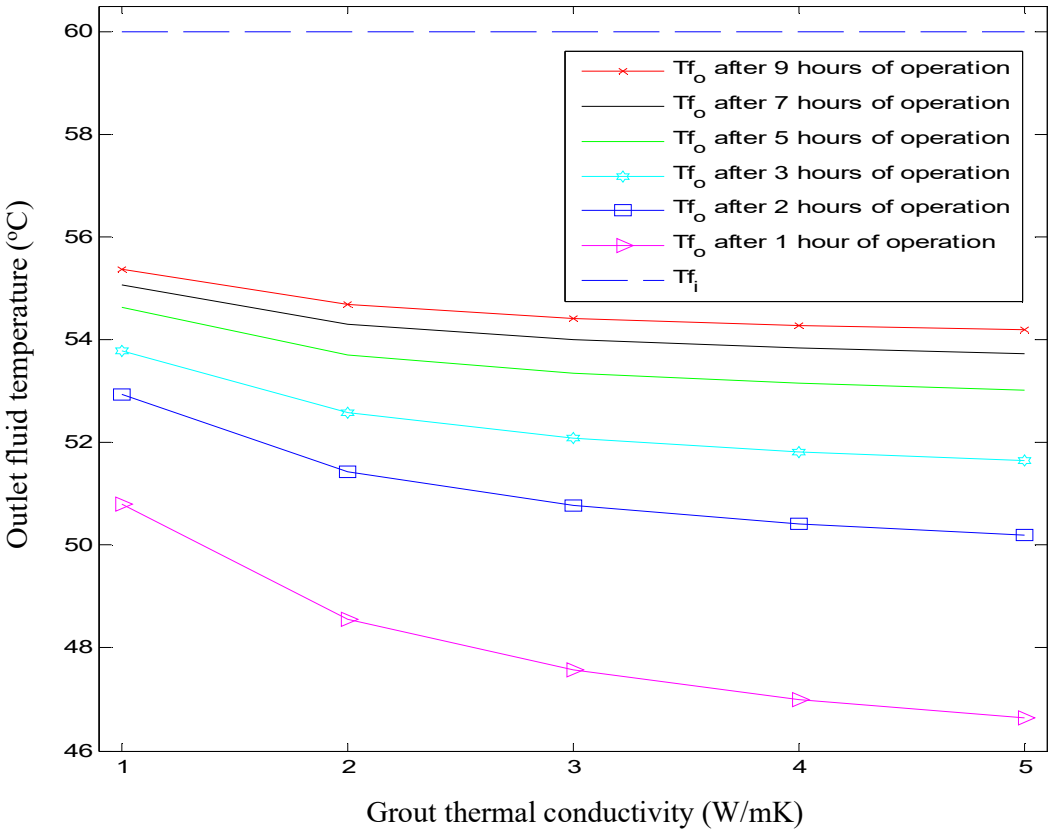
Figure 5.11: Effect of the grout thermal conductivity on the performance of the GHE (The inlet fluid temperature = 60 ℃, fluid mass flow rate = 0.3 kg/s, borehole depth = 60 m, initial soil temperature on 1 December)

5.6.2 The effect of borehole depth

The borehole depth is the main parameter that should be considered since it determines the surface area of the pipe in contact with the circulating fluid and influences the amount of heat transferred from the working fluid to surrounding soil and vice versa. Figure 5.12 shows the effect of the borehole depth on the outlet fluid temperature of the GHE over different periods of time. It is obtained that the deeper of the borehole is, the lower of the fluid temperature can be produced. Increasing the borehole depth means enlarging the heat transfer area of the GHE. As a result, it enhances the heat transfer rate of the GHE. This result is also confirmed by Fan et al. [76] as discussed in Chapter 2. As the GHE is assumed to cross through three different soil layers having the same thickness and different thermophysical properties as given in Table 5.5, the heat transfer rate at each layer simply depends on its thermal conductivity. Since the borehole depth correlates with the drilling cost, thus, the depth of the borehole must be specified thoroughly. It is observed when the operation time increases, the GHE's performance reduces gradually as temperatures of the grout and surrounding soil built up. After 9 hours of operation, it is obtained a temperature difference of 11.6 $^{\circ}$C, in the outlet fluid temperature, between the GHE which has a depth of 60 m and 210 m.
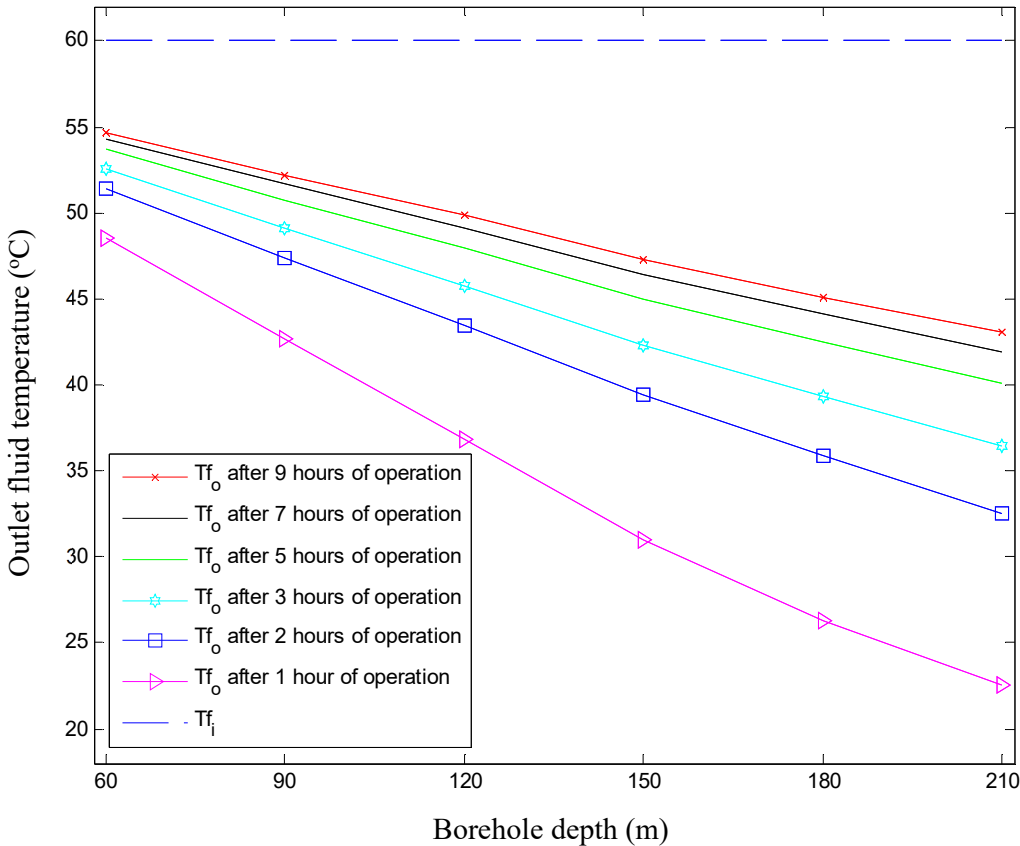
Figure 5.12: Effect of the borehole depth on the performance of the GHE
(The inlet fluid temperature = 60 $^{\circ}$C, fluid mass flow rate = 0.3 kg/s, initial soil temperature on 1 December)

91

5.6.3 The effect of fluid flow rate

The fluid mass flow rate is one of the technical parameters affecting the heat transfer rate of the GHE. Increasing the fluid mass flow rate may increase the convective heat transfer coefficient of the GHE and decrease its thermal resistance. As a result, it increases the heat transfer rate of the GHE. Figure 5.13 shows the variation in the outlet fluid temperature with five different mass flow rates at the inlet of the GHE. It is observed that the outlet fluid temperature, at each mass flow rate, increases with the increase of the operation time. At the lowest flow rate namely, 0.1 kg/s, the outlet fluid temperature of the GHE increases significantly over the period of the time namely, 17.2 °C, from 1 to 9 hours of operation. While at the highest flow rate namely, 0.5 kg/s, the temperature difference over the period of time is relatively small than those at the lower flow rates. This phenomenon can be explained by the fact that, at a higher mass flow rate, the GHE releases more heat into the surrounding soil. As a result, the temperature of the surrounding soil increases relatively quickly due to the accumulation of heat that leads to the GHE's performance degradation.
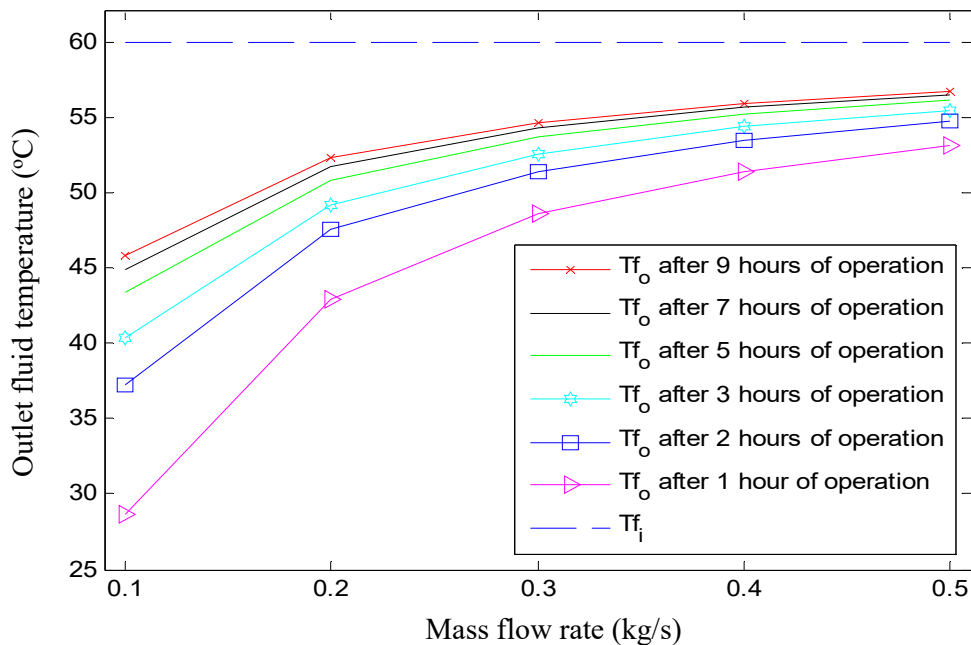
Figure 5.13: Effect of the fluid mass flow rate on the performance of the GHE
(The inlet fluid temperature = 60 °C, borehole depth = 60 m, initial soil temperature on 1 December)

5.6.4 The effect of heat carrier fluid

In this section, the performance of the GHE under different types of heat carrier fluids including pure water and nanofluids, is investigated. The nanofluids are the mixture of the conventional heat transfer fluid and nanoparticles. The metal nanoparticles are usually mixed with water as the base fluid to enhance the thermophysical properties of water. The nanofluids used as

92

working fluids in the simulation are 2%TiO$_2$-water and 3%TiO$_2$-water. Table 5.6 shows the thermophysical properties of working fluids and nano particles. The TiO$_2$ powder is supplied by Fishers Scientific Inc [96].

Table 5.6: Thermophysical properties of working fluids and nano particles [87]

No.	Nanofluid	Thermal conductivity (W/mK)	Viscosity (N s/m^2)	Density (kg/m^3)	Specific heat (kJ/kgK)
1	TiO$_2$ powder	8.4	-	4230	0.17
2	Water	0.641	8.94×10^{-4}	1000	4.197
3	2%TiO$_2$-water	0.646	9.387×10^{-4}	1061.7	4.09
4	3%TiO$_2$-water	0.664	9.610×10^{-4}	1094	4.053

Figure 5.14 shows the effect of the heat carrier fluid on the performance of the GHE. The simulation results reveal that the GHE with the nanofluids as the working fluid produces a relatively lower outlet fluid temperature compared to that using pure water. This phenomenon is influenced by the thermophysical properties of working fluids which determine the heat transfer capacity of the GHE. As illustrated in Figure 5.14, the concentration of the TiO$_2$ particle affects the amount of heat released by the GHE. The higher TiO$_2$ concentration is, the lower outlet fluid temperature can be generated by the GHE.These results are also confirmed by Khedkar et al. [96].
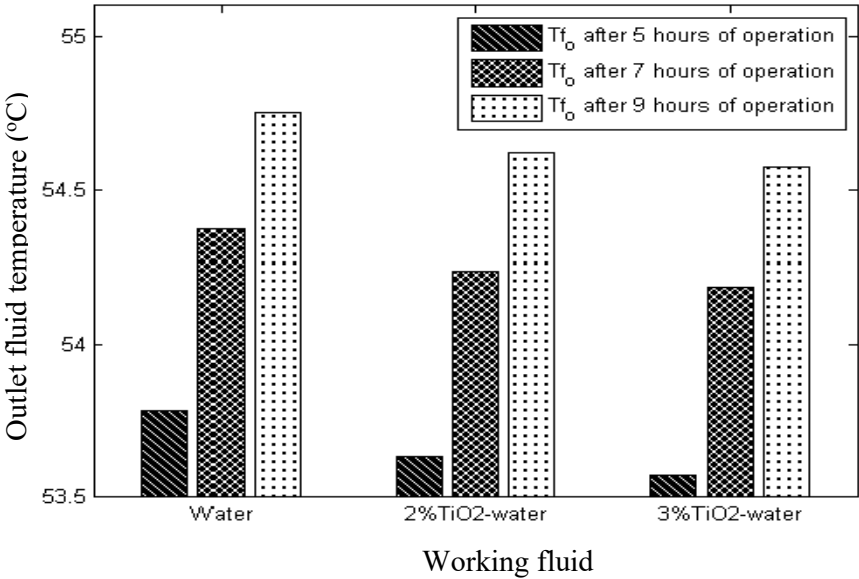
Figure 5.14: Effect of the heat carrier fluid on the performance of the GHE
(The inlet fluid temperature = 60 ºC, fluid mass flow rate = 0.3 kg/s, borehole depth = 60 m, initial soil temperature on 1 December)

5.6.5 The effect of continuous and intermittent operation

Figure 5.15 shows the profile of the outlet fluid temperatures of the GHE operated under different operational strategies including continuous and intermittent modes. During the

operation, water as the heat carrier fluid is circulated inside the U-shaped pipe at a flow rate of 0.3 kg/s and an inlet fluid temperature of 60 °C. The results show that the outlet fluid temperature under the continuous operation mode is higher than that operated under the intermittent mode (8 hours On and 16 hours Off daily). In the continuous operation mode, the heat from circulating fluid is continuously released during the operation which leads to the accumulation of heat in the soil domain. As a result, it deteriorates the performance of the GHE. While in the intermittent mode, the outlet fluid temperature gradually increases during the operation. However, the increase is not as high as that when the GHE is operated continuously. The reason for this phenomenon is because the thermal condition of the surrounding soil is possible to recover when the system is switched off for 16 hours. The intermittent operation strategy of the GHE is possible to be conducted as different cooling or heating load demands during a certain period. For instance, the ground source air conditioning system is usually operated during the day time in summer, and then it is switched off during the nighttime when the ambient air temperature normally drops.
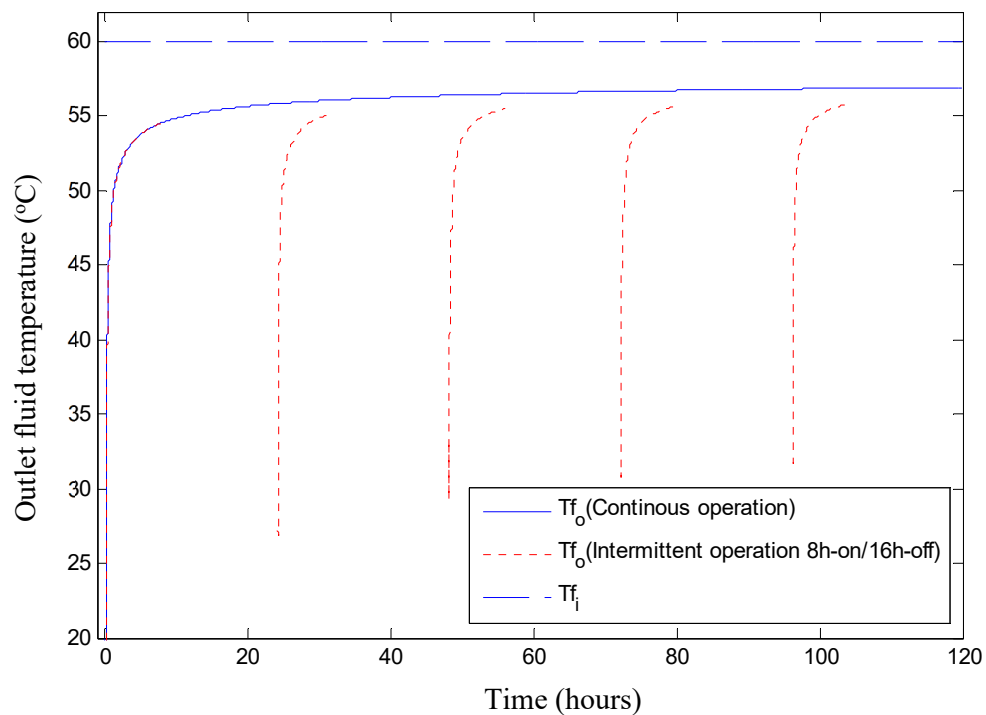
Figure 5.15: The outlet fluid temperature of the GHE under continuous and intermittent modes (The inlet fluid temperature = 60 °C, fluid mass flow rate = 0.3 kg/s, borehole depth = 60 m, initial soil temperature on 1 December)

Figures 5.16-5.18 show the profile of soil temperature, at three different depths, during the continuous and intermittent operations of the GHE. As shown in the figures that the soil temperature is higher when the GHE is in the continuous mode. This phenomenon occurs because, during the continuous operation, the heat is continuously transferred by the GHE to

the soil domain results in accumulation of heat in the surrounding soil. In the intermittent mode, the GHE transfers the heat to the surrounding soil in the daytime only (for 8 hours), while at nighttime the system is switched off, allowing the soil temperature to recover. Figure 5.16 shows the profile of soil temperature, at the 1st soil layer, at a depth of 2 m and a radius of 0.575 m. The result shows that the soil temperature at the 1st soil layer is higher than those at the 2nd and 3rd soil layers (see Figures 5.17 and 5.18), either for the continuous and intermittent modes. The relatively higher soil temperature at the 1st soil layer is due to it receives both the GHE's flux and seasonal soil temperature changes. Since the atmospheric heat could only penetrate the shallow depth of the ground, the middle and bottom layers gain the GHE's flux only. The relatively higher thermal conductivity of the sand (1st layer) than those of sandy loam (2nd layer) and loam (3rd layer) also contributes to the higher soil temperature of the 1st layer as the thermal conductivity determines the transmission of heat in the soil domain. It is observed, the soil temperature at the 2nd layer is slightly higher than that at the 3rd layer (see Figures 5.17 and 5.18). This is due to a slight difference in the thermal conductivity value as well as the heat transfer rate of the GHE that decays along the borehole depth. It is found that the profile of soil temperature at the 1st soil layer slightly fluctuates when the GHE operates in an intermittent mode. This phenomenon, however, does not appear for the other layers. The relatively higher thermal conductivity of sand (1st layer) leads to better soil temperature response.
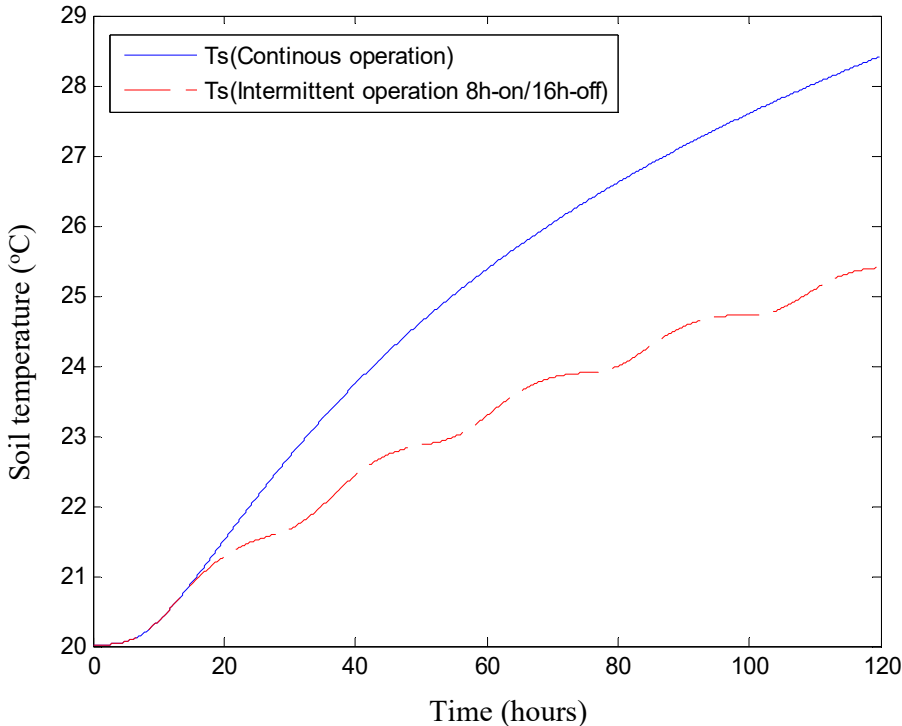
Figure 5.16: Profile of soil temperature at a depth of 2 m and a distance of 0.575 m from the borehole axis under continuous and intermittent modes of the GHE
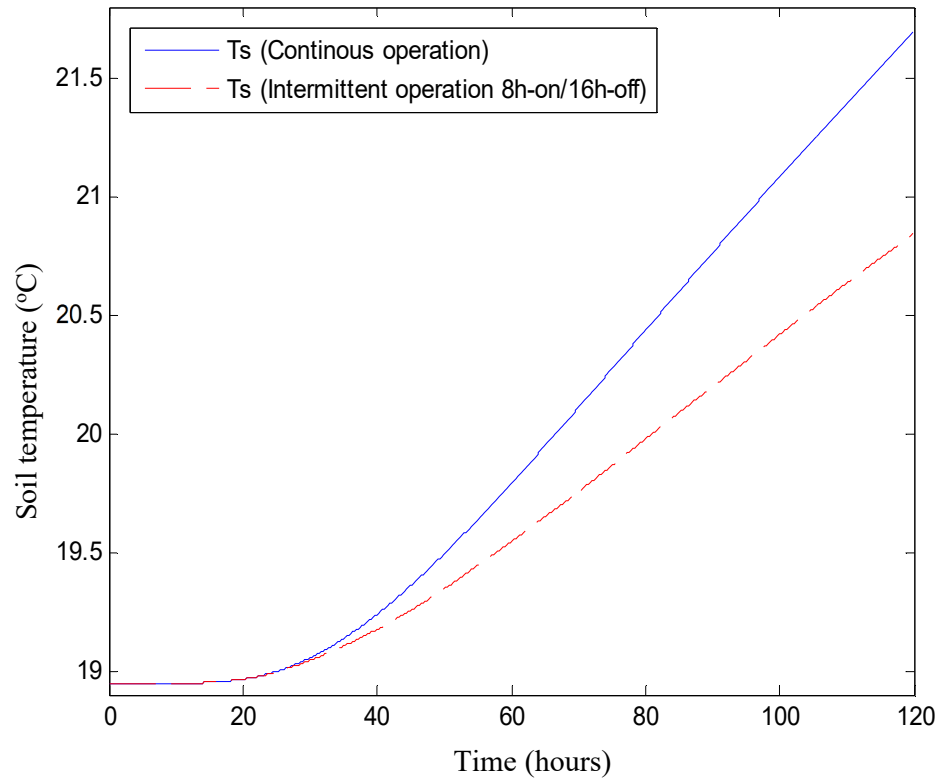
Figure 5.17: Profile of soil temperature at a depth of 25 m and a distance of 0.575 m from the borehole axis under continuous and intermittent modes of the GHE
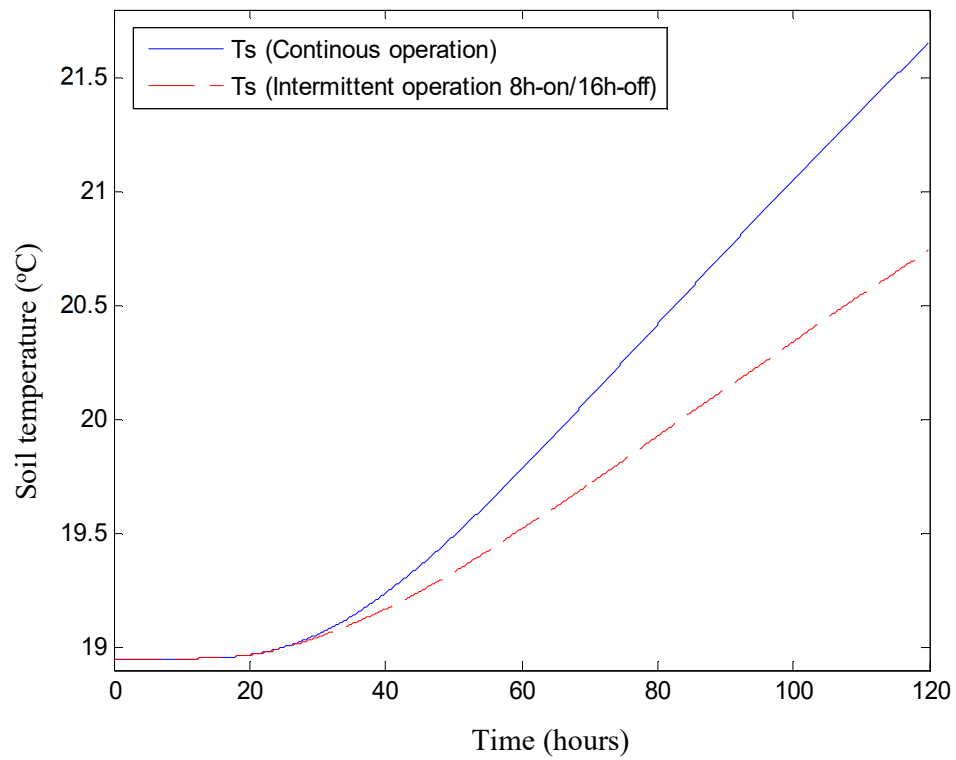
Figure 5.18: Profile of soil temperature at a depth of 45 m and a distance of 0.575 m from the borehole axis under continuous and intermittent modes of the GHE

5.7 Summary

A 2D finite difference numerical model has been developed to study the transient performance of a vertical GHE. A new approach which incorporates an internal heat source term in the GHE model has been introduced to consider the seasonal changes in soil temperature. The model is validated against the experimental data by comparing both the soil and outlet water temperatures. The results reveal that the accuracy of the simulated soil temperature has increased significantly when incorporating the internal heat source term. It is found the maximum relative errors for the simulated soil temperatures with and without the internal heat source term are 3.7% and 14% respectively. In addition, the accuracy of the simulated outlet fluid temperature has also improved when considering the internal heat source term even though not significant. Using the validated model, the effects of some design and operational parameters on the vertical GHE's performance including borehole thermal conductivity, borehole depth, fluid flow rate, types of carries fluids, as well as continuous and intermittent operations, are studied. The simulation results reveal that the borehole depth has the most significant impact on the GHE performance. Increasing the borehole depth can significantly lowering the outlet fluid temperature due to the heat transfer rate of the GHE increases with increasing the heat transfer area. The other parameters, however, are not without significance. Utilizing the grout material with a high thermal conductivity value has increased the heat transfer rate of the GHE reflected by a reduction in outlet fluid temperature. This is due to the borehole thermal resistance decreases when the thermal conductivity of the grout increases. Due to the relatively low thermal conductivity value of the surrounding soil which has much a larger domain than the grout, it is found that the decrease in the outlet water temperature is not linearly with the increase of the grout thermal conductivity. In addition, nanofluids ($2\%TiO_2$-water and $3\%TiO_2$) can be used as the heat carrier fluid due to their thermophysical properties allowing higher heat transfer capacity of the GHE. It is obtained that the amount of heat released by the GHE depends on the concentration of metal particle (TiO_2). The outlet fluid temperature decreases when the concentration of metal particle increases. Besides, the intermittent operation of the GHE allowing the deterioration of the GHE performance to recover when the system off. Thus, increasing the heat transfer rate of the GHE on the next operation day.

CHAPTER 6

COMBINED HORIZONTAL-VERTICAL GEO HEAT EXCHANGER

The hybrid GHE systems (i.e. GHE-solar system, GHE-cooling towers, and GHE-boiler) have been suggested by a number of authors in order to address the soil temperature deterioration due to cold and heat accumulation during heating and cooling operations (see Section 2.3.3). In this chapter, the performance of a combined horizontal-vertical GHE with different operation modes is studied using the mathematical models developed in Chapters 3 and 4, respectively. Chapter 6 is organised as follows. Section 6.1 describes the physical model of the combined horizontal-vertical GHE. Section 6.2 describes the mathematical model of the combined horizontal-vertical GHE. Section 6.3 presents a hypothetical case study of the combined horizontal-vertical GHE. Section 6.4 presents the operation analysis of the combined horizontal-vertical GHE. The key findings are summarised in Section 6.5.

6.1 Physical model

Based on different performance features of the horizontal and vertical GHE, a combined structure horizontal-vertical GHE is proposed, with the thought that it might deal better with various demands and loading conditions. Figure 6.1, shows the schematic of combined horizontal-vertical GHEs coupled with an air conditioning system. Figure 6.2 shows three-dimensional view of combined horizontal-vertical GHEs. The combined GHE system consists of combined horizontal-vertical GHE configuration units. A horizontal-vertical GHE unit consists of a horizontal buried U-shaped pipe (horizontal) and a borehole (vertical) as shown in Figure 6.3. The combined horizontal-vertical GHE can be operated in five different modes through the adjustment of the valves namely: (1) The horizontal GHE only, in which, the working fluid is circulated through the horizontal GHE only, (2) The vertical GHE only, in which, the working fluid is circulated through the vertical GHE only, (3) The horizontal to vertical GHE (the working fluid is circulated from the horizontal to vertical GHE), (4) The vertical to horizontal GHE (the working fluid is circulated from the vertical to horizontal GHE), (5) Splitting the fluid flow through both the horizontal and vertical GHEs concurrently.
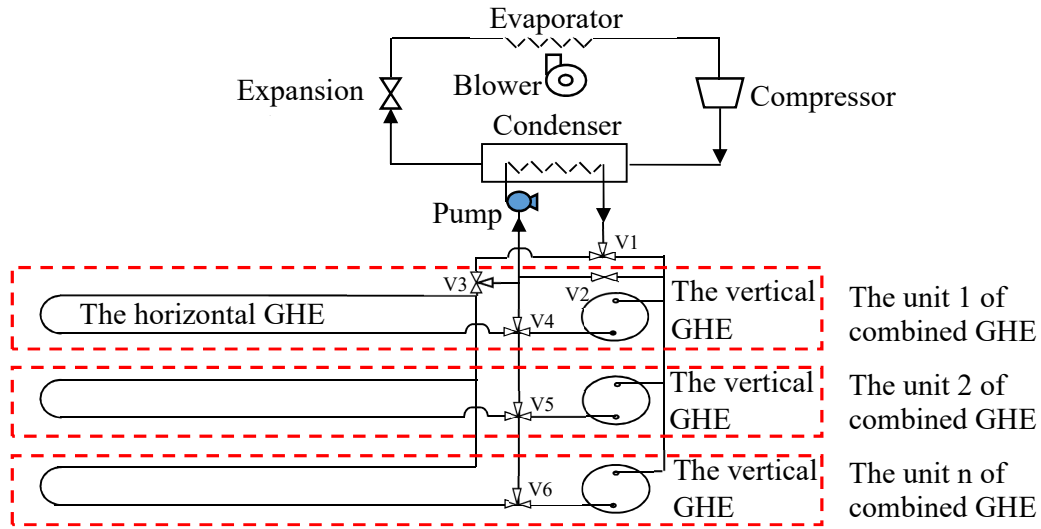
Figure 6.1: Schematic of combined horizontal-vertical GHEs-ground source air conditioning system
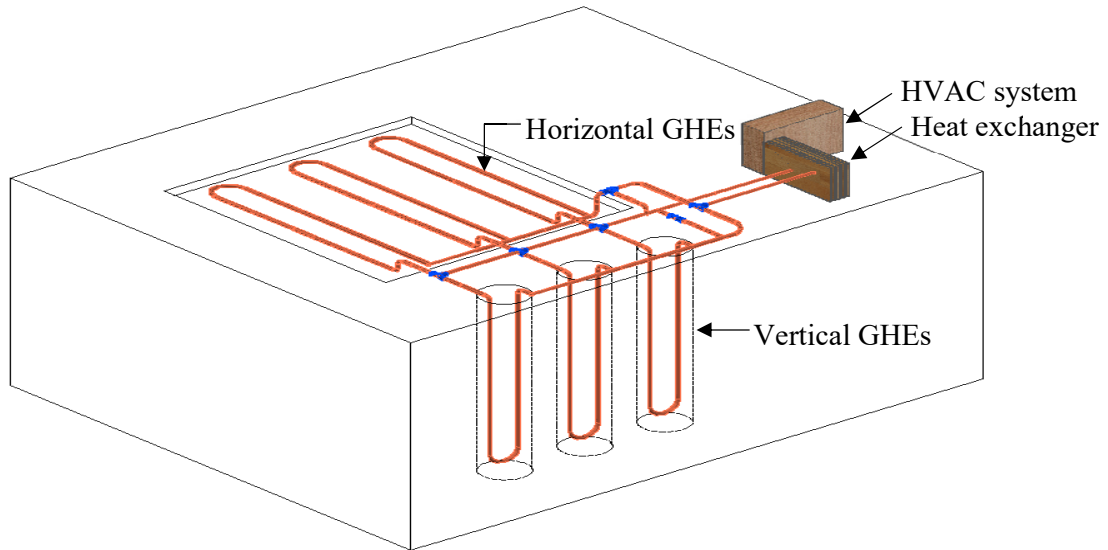
Figure 6.2: Three-dimensional view of a combined horizontal-vertical GHE.

6.2 Combined horizontal-vertical GHE model

The thermal performance of a combined horizontal-vertical GHE is simulated by using combined horizontal and vertical GHE models which are validated separately. In this study, it is assumed that the distance between the horizontal and vertical GHE is relatively far. Thus, the thermal interference between the horizontal and the vertical GHE is regarded insignificant and ignore in the simulation.

6.3 A hypothetical case study

The performance of a combined horizontal-vertical GHE unit has been studied and compared, in all 5 operation modes. In this study, each unit of the combined GHE, as illustrated in Figure

6.3, both the horizontal and vertical part have the same parameters including the pipe length, pipe diameter, and fluid flow rates. The soil domain around the GHE is assumed to be homogeneous and isotropic. Table 6.1 presents the parameters of the reference case used in the simulation to be described next. In this study, the combined GHE is assumed to consist of many combined GHE (C-GHE) units. A C-GHE unit is illustrated in Figure 6.3.
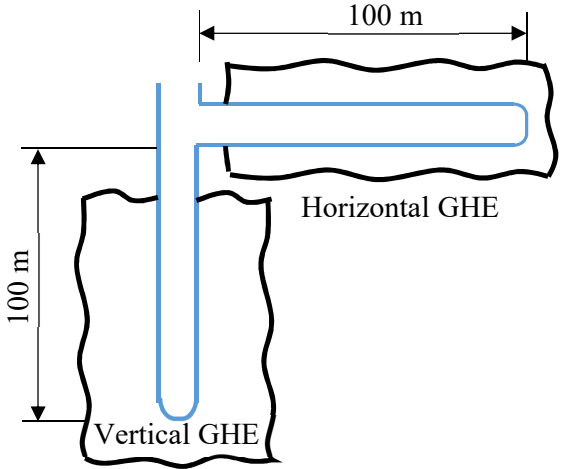
Figure 6.3: Schematic of a combined horizontal-vertical GHE unit.

Table 6.1: The parameters of the reference case

Parameters	Value	Unit	Parameters	Value	Unit
Horizontal GHE			*Circulation fluid (water)*		
Total pipe length	200	m	Inlet water temperature	50	ºC
Burial depth	0.25	m	Flow rate	0.6	kg/s
Pipe internal diameter	0.04	m	Specific heat	4188	J/kg K
Pipe outer diameter	0.044	m	Density	980	kg/m^3
Centre distance between pipes	0.28	m	*Soil type in Adelaide: layered old dune sands [91]*		
Soil domain span in x direction	0.14	m	Thermal conductivity	1.3	W/mK
Soil domain span in y direction	2	m	Specific heat	1140	J/kgK
Vertical GHE			Density	1500	kg/m^3
Total pipe length	200	m	*Soil type in Brisbane: clay [97]*		
Borehole depth	100	m	Thermal conductivity	1.1	W/mK
Borehole diameter	0.15	m	Specific heat	1500	J/kgK
Soil domain diameter	6	m	Density	1300	kg/m^3
Pipe internal diameter	0.04	m	*Grout (vertical GHE)*		
Pipe outer diameter	0.044	m	Thermal conductivity	2	W/mK
Centre distance between pipes	0.07	m	Specific heat	1140	J/kgK
			Density	1500	kg/m^3
			Wind speed (Adelaide)	4.9	m/s
			Wind speed (Brisbane)	3.8	m/s

The initial temperature of the ground is estimated using the analytical Equation 2.1 suggested by Baggs [20] since the existing measurement data of soil temperature in Adelaide and Brisbane is limited to 1 m deep [87]. The input parameters for Baggs's equation are determined based on the data of the climate conditions. The values of the average annual air temperature and the amplitude of the annual air temperature were obtained from the Australian Bureau of Meteorology [98], as shown in Figure 6.4. The local site variable for the ground temperature is based on data given by Baggs [20]. Table 6.2 summarises the parameters used to estimate the soil temperature conditions. Figure 6.5 shows the typical changes of soil temperatures in Adelaide and Brisbane.

Table 6.2: The parameters used to estimate the soil temperature

Parameter	Adelaide	Unit	Brisbane	Unit
Average annual air temperature (T_m)	16.45	°C	25.4	°C
Amplitude of the annual air temperature (A_s)	11.9	°C	11.2	°C
The local site variable for the ground temperature (ΔT_m)	2.5	°C	3	°C
Vegetation coefficient (k_v)	1	-	1	-
Soil thermal diffusivity (α)	0.76	10^{-2} cm^{-2} sec^{-1}	0.55	10^{-2} cm^{-2} sec^{-1}
Phase of air temperature wave (t_0)	10 (10th January)	Day	19(19th January)	Day
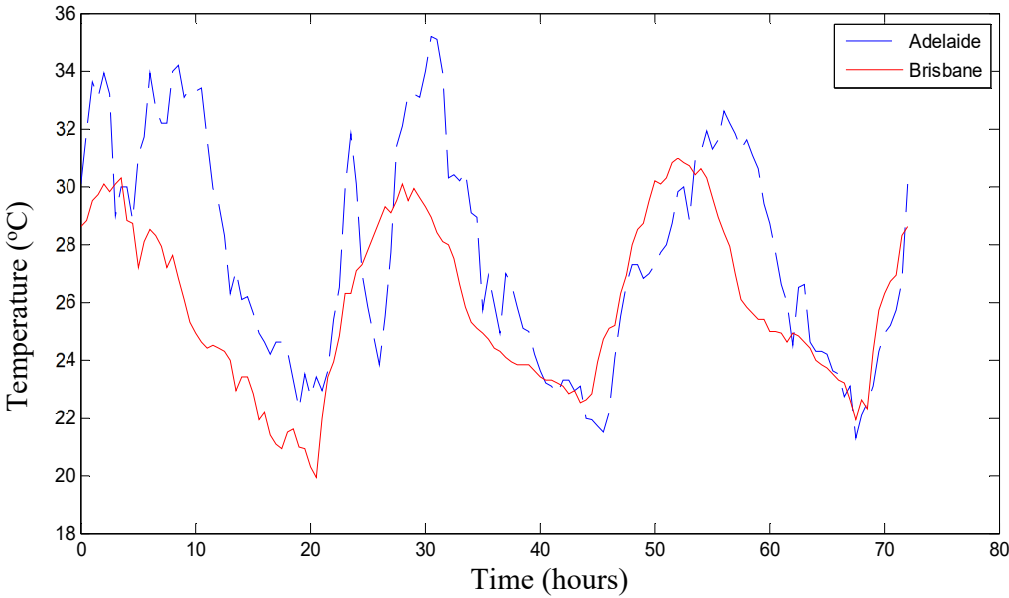
Figure 6.4: An example of ambient temperature in Adelaide and Brisbane in 3 consecutive summer days
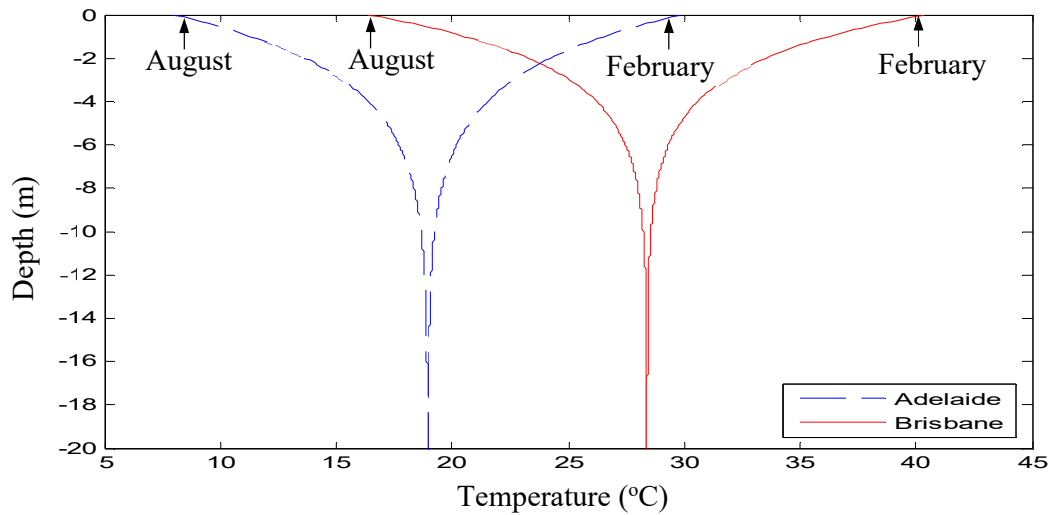
Figure 6.5: Typical soil temperature in Adelaide and Brisbane

The effect of seasonal changes in soil temperature is modelled by incorporating the internal heat source term concept into the GHE model [99]. The value of the internal heat source term varies with the soil depths. It is higher in a shallow region and lower in a deeper zone. At a depth of 12 m below the ground surface, the value of the internal source term is assumed to be zero (this corresponds to the depth at which the effect of the ambient temperature on the soil temperature is negligible). Figure 6.6 shows the absolute value of the internal source term at various depths for two reference locations namely, Adelaide and Brisbane. As shown in Figure 6.6, at the upper layer (0-3.5 m depth), the internal heat source term of the soil in Brisbane is relatively higher than in Adelaide. However, at a deeper layer (soil depth >=3.5 m), the condition is the opposite. This phenomenon could be affected by meteorological, terrain and subsurface conditions. The value of the internal heat source is positive when the ground temperature is warmed (August to February) and conversely negative when the ground temperature is cooled (February to August), as is shown in Figure 6.5.
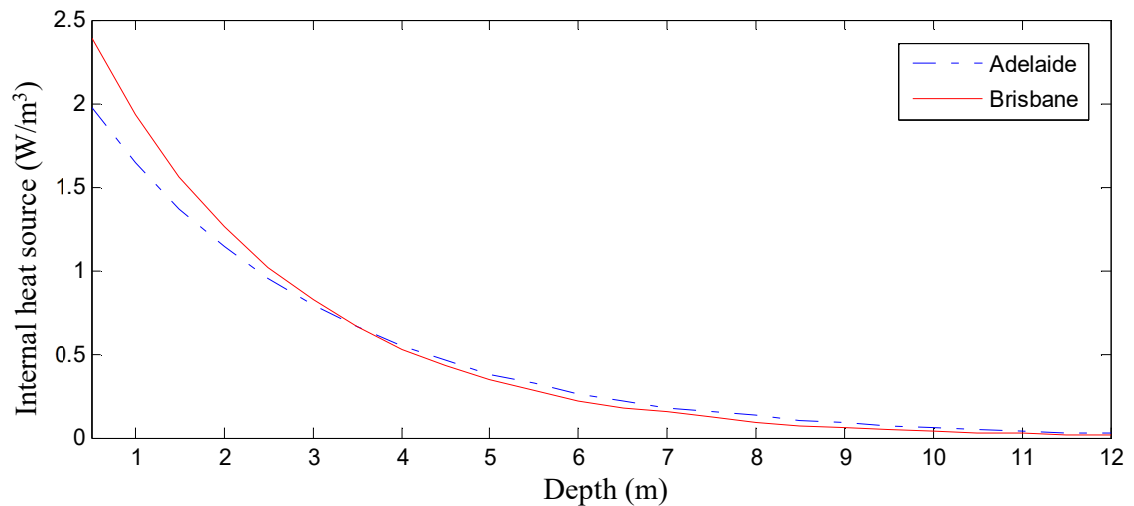
Figure 6.6: The absolute value of the internal heat source at various depths

6.4. Operation analysis of combined horizontal-vertical GHE

This section shows the simulation outcomes of a combined GHE unit subjected to five operational modes, as described above. The performance of the GHE is investigated by taking into account the effects of continuous and intermittent operations, split flow operation mode with different ratios of mass flow rate in the horizontal and vertical GHE, climate conditions and fluid mass flow rates. The amount of energy released by the GHE is calculated in accordance with the following equation:

$$Q = \dot{m}c_p\left(T_{fi} - T_{fo}\right)\Delta t \tag{6.1}$$

where Q is the energy released by the GHE (J), $\dot{m}$ is the fluid mass flow rate (kg/s), c_p is the fluid specific heat (J/kgK), T_{fi} is the inlet fluid temperature (K), T_{fo} is the outlet fluid temperature, Δt is the time (s).

6.4.1 Continuous operation

Figure 6.7 shows the simulation results of the GHE, run in 3 consecutive summer days, with respect to the geological and climate conditions corresponding to Adelaide (South Australia). The amount of energy released by the GHE depends on fluid mass flow rate, fluid specific heat, time period, and the temperature difference of fluid between inlet and outlet as given by Equation (6.1). As an example, Figure 6.8 provides the profile of the fluid temperature generated by operation of the horizontal, vertical, and horizontal to vertical GHE. This figure demonstrates that the outlet fluid temperature increases with the increase in the operation period. The accumulation of heat in the surrounding soil during the operation of the GHE, leads to a reduction in the heat transfer rate. As shown in the figure, the profile of the outlet fluid temperature of the vertical GHE is relatively stable when compared with those generated by the horizontal and series operation modes. This phenomenon occurs because the ambient temperature, which fluctuates diurnally, does not have a significant effect on the performance of the vertical GHE. From Figure 6.7, it follows that the lowest energy is released when operating the horizontal GHE only. The horizontal GHE releases 38% less energy than that released in 3 days by the vertical GHE. The relatively stable temperature of the ground at a deeper layer may enhance the heat transfer capacity of the vertical GHE and leads to better thermal performance [3]. The amount of energy released can be increased by using the combined operation mode of the GHE, including the split flow and series operation modes. It can be seen that the series operation mode, from horizontal to vertical, releases 54% more energy than the vertical mode. While the vertical to horizontal mode rejects 0.5% less energy than the opposite operation mode. It is obtained that the split flow mode, with a ratio of fluid

flow at 50% in the horizontal GHE and 50% in the vertical GHE, releases less energy than the series operation mode. The average heat transfer rate is calculated by dividing the amount of energy released by the operation period. The single arrangement of the horizontal or vertical GHE generates an average heat transfer rate of 6.339 kW and 10.204 kW, respectively. The combined arrangements produce a relatively higher heat transfer rate namely: 15.729 kW, 15.645 kW, and 15.423 kW for operation modes from horizontal to vertical, vertical to horizontal and by splitting the fluid flow, respectively. Therefore, the horizontal or the vertical GHE may be operated when the loading load is relatively low. At peak loads or when heating/cooling demands are relatively high, the combined GHE's operation can have a significant advantage, see Figure 6.7.
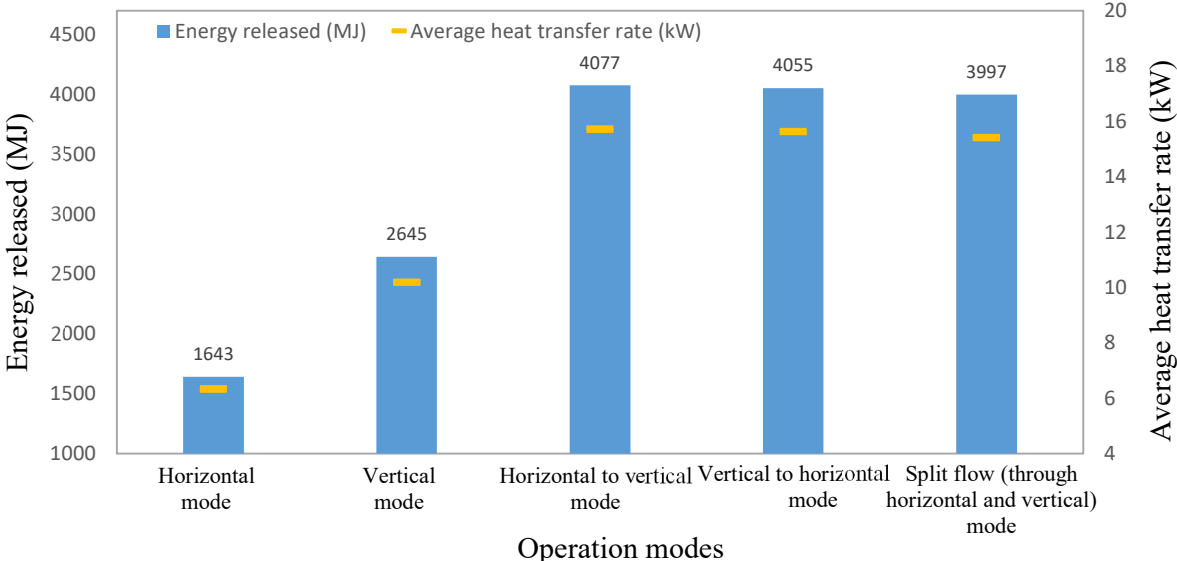
Figure 6.7: Energy released in 3 days (10-12 January) and average heat transfer rate of the GHE under a continuous operation condition (Adelaide case). The inlet fluid temperature = 50 °C, fluid mass flow rate = 0.6 kg/s, length of the horizontal GHE = 200 m, length of the vertical GHE = 200 m.

Figure 6.8: Profile of the outlet fluid temperature of the GHE under different operation modes (Adelaide case).

104

6.4.2. Intermittent operation

The GHE can also be operated in the intermittent condition to cope with cyclic load conditions. Figure 6.9 shows the amount of energy released by the GHE operating intermittently in 3 summer days, see Figures 6.4 and 6.5. The GHE runs for 8 hours (during the working hours) and is Off for 16 hours daily. The results display that during 24 hours of operation, the horizontal GHE releases 41% less energy than the vertical GHE. The combined operation modes of the GHE can increase the amount of energy released, as the contact area, where heat is exchanged with the surrounding soil, increases. It is seen that the series operations can release 40.8% and 39.6% more energy than the vertical mode, for the horizontal to vertical and vice versa modes, respectively. In the split flow mode, the fluid is split to flow with a ratio of 50% in the horizontal GHE and 50% in the vertical GHE. The results demonstrate that the split flow mode releases 2.8% less energy than the horizontal to vertical mode. Even though, the amount of energy released in the intermittent operation regime is less than that generated by the continuous operation due to the total operation period in the intermittent condition is less compared with the continuous condition. However, the average heat transfer rates increase. They are 60.1% for the horizontal mode, 68.5% for the vertical mode, 54% for the horizontal to vertical mode, 53.5% for the vertical to horizontal mode, and 52.6% for the split flow mode. In the intermittent operation condition, the deterioration of the ground temperature during the operation hours is possible to recover during the time when the system is switched off [68]. As a result, it increases the heat transfer rate of the GHE and produces lower outlet fluid temperature over the next day's operation as reflected by an example of fluid temperature generated by the vertical to horizontal mode (see Figure 6.10). This tendency agrees well with Li et al.'s findings [45].
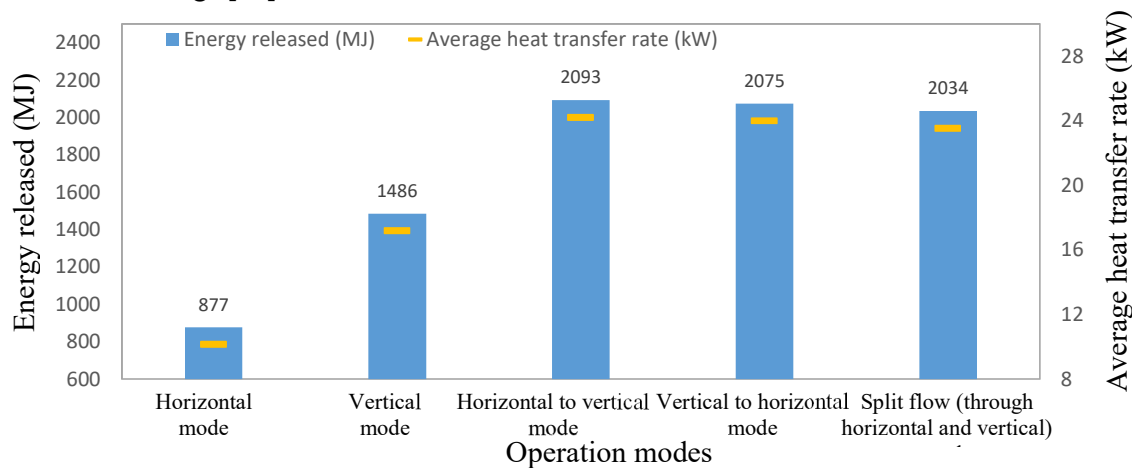
Figure 6.9: Energy released in 3 days (10-12 January) and average heat transfer rate of the GHE under an intermittent operation (Adelaide case). The inlet fluid temperature = 50 °C, fluid mass flow rate = 0.6 kg/s, length of the horizontal GHE = 200 m, and length of the vertical GHE = 200 m.

Figure 6.10: Profile of the outlet fluid temperature of the GHE with the horizontal to vertical mode (Adelaide case).

6.4.3 Split flow operation mode

In this section, the effect of the fluid mass flow rate ratio in the split flow operation mode is investigated. The ratio of the fluid mass flow rate is varied as follows: 30%:70%; 40%:60%; 50%:50%; 60%:40% and 70%:30% for the horizontal and the vertical GHE, respectively. From the current numerical simulations, it has been found that the ratio of fluid mass flow rate in the split flow mode does not significantly affect the amount of energy released by the GHE, as shown in Figure 6.11. As an example, Figure 6.12, presents the outlet fluid temperature of the GHE at three different flow rate ratios, namely: 30%:70%; 50%:50%; and 70%:30% for the horizontal and the vertical GHE, respectively. It is found that the difference in the outlet fluid temperature is relatively small. The highest fluid outlet temperature is yielded by the GHE with a flow rate ratio of 70%:30%. It can be seen that the GHE operated with a flow rate ratio of 70% horizontal and 30% vertical releases the lowest amount of energy across 3 consecutive days of operation, namely, 3% less than the one with a flow rate ratio of 60% horizontal and 40% vertical. The amount of energy released gradually increases with the increase of the ratio of the fluid mass flow rate in the vertical GHE and declines at the ratio of 30% horizontal and 70% vertical GHE namely, 0.7% less than that with a ratio of 40% horizontal and 60% vertical GHE. This tendency is due to a significant reduction in fluid mass flow rate in the horizontal GHE (only 30% of the total fluid flow rate). At a lower mass flow rate, the thermal resistance of the horizontal GHE increases as a reduction in fluid mass flow rate is directly proportional to the decrease in the convective heat transfer coefficient between the working fluid and the inner pipe surface. As a result, it decreases the heat transfer rate of the horizontal GHE. In addition, with 70% of mass flow rate in the vertical GHE, the surrounding soil temperature deteriorates quickly due to heat accumulation, leading to a degradation in heat transfer capacity

of the vertical GHE. From the Figure 6.11, it can be seen that the highest heat transfer rate is produced by the GHE with a ratio of flow rate of 40% horizontal and 60% vertical namely, 15.490 kW.
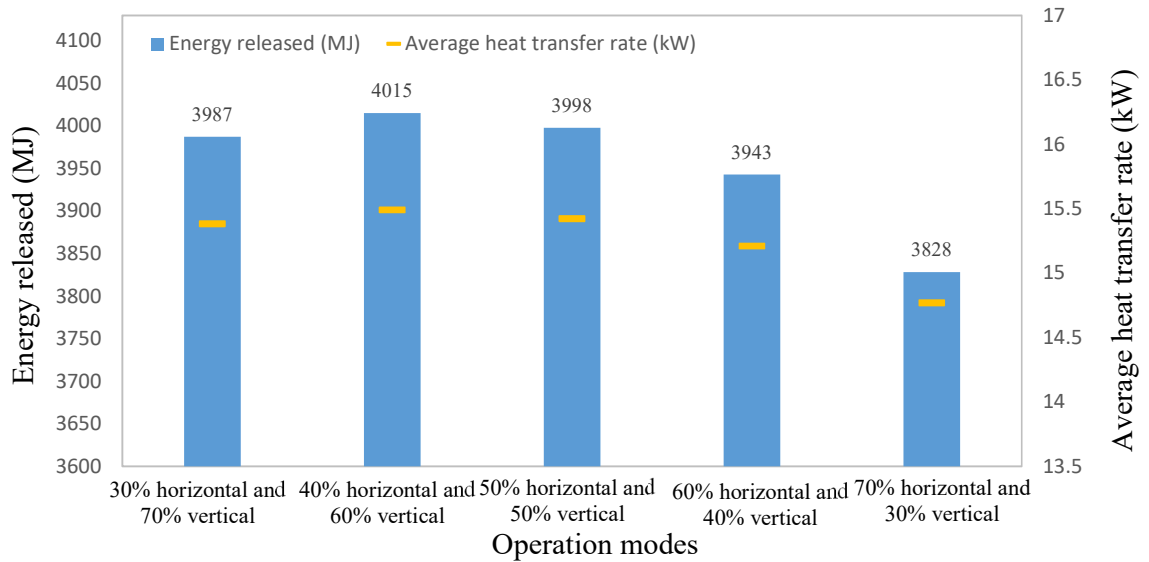
Figure 6.11: Energy released in 3 days (10-12 January) by the GHE with different ratio of mass flow rate (Adelaide case). The inlet fluid temperature = 50 °C, fluid mass flow rate = 0.6 kg/s, length of the horizontal GHE = 200 m, length of the vertical GHE = 200 m.
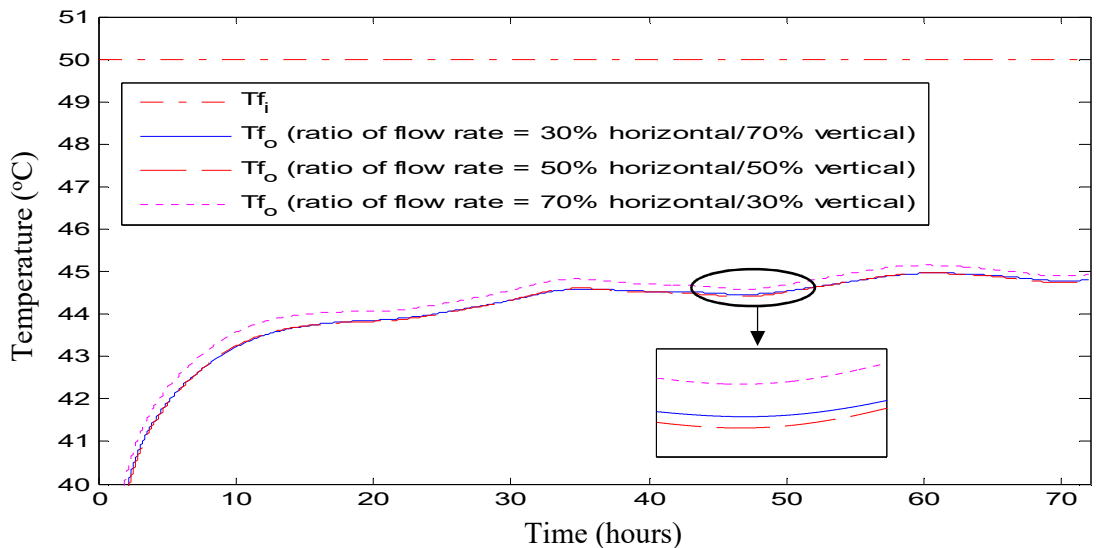
Figure 6.12: Profile of the outlet fluid temperature of the GHE (with a split flow operation mode) under different flow rate ratios (Adelaide case).

6.4.4 Climate condition

The performance of the GHE installed in a temperate climate corresponding to Adelaide is compared with that installed in a subtropical climate, such as near Brisbane. Figure 6.13 summarises the performance of the GHE, which is installed in two different regions, with different climate conditions. It is found that during 72 hours (3 days: 10-12 January) of the

continuous operation, the GHE installed in Adelaide's temperate climate can release 34.3% and 26.9% more energy compared with that installed in Brisbane, for the horizontal and vertical mode, respectively. While for the combined modes including horizontal to vertical, vertical to horizontal, and split flow are 31.7%, 31.8%, and 31% higher, respectively. It is observed that operating the vertical GHE only, in the temperate climate, Adelaide, can release an amount of energy that is almost the same as that released by the combined operation mode, in the sub-tropical climate. This tendency occurs because the climate condition influences the initial soil temperature in both regions. The initial soil temperature in Adelaide is lower than that in Brisbane, as seen in Figure 6.5. In addition, the difference in soil types in both locations contributes to the heat transfer capacity of the GHE. As a result, the GHE installed in a temperate climate, Adelaide, produces a lower outlet fluid temperature as demonstrated in Figure 6.14.
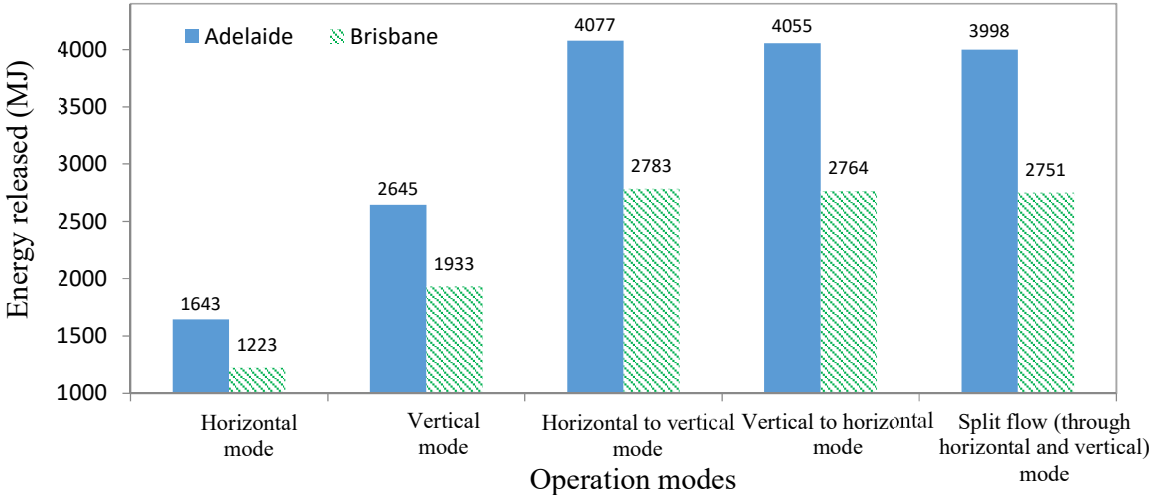
Figure 6.13: Energy released in 3 days (10-12 January) by the GHE under different climate conditions. The inlet fluid temperature = 50 °C, fluid mass flow rate = 0.6 kg/s, length of the horizontal GHE = 200 m, length of the vertical GHE = 200 m.
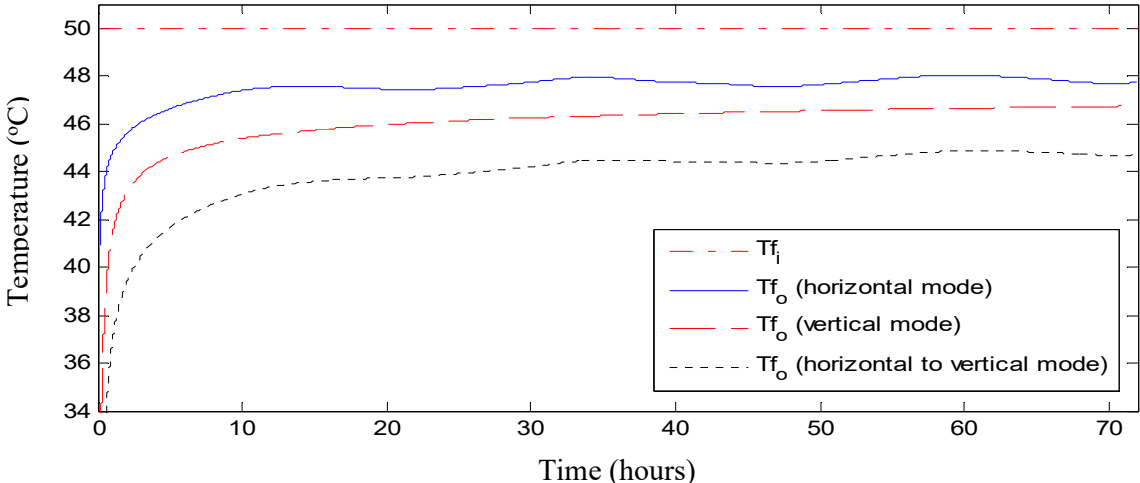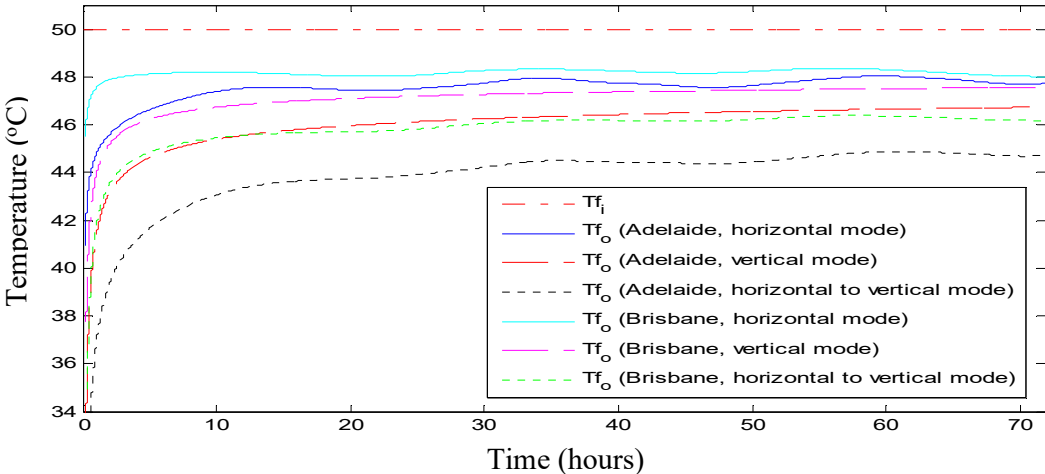

Figure 6.14: Profile of the outlet fluid temperatures of the GHE under different operation modes and climate conditions

6.4.5 Variations of the fluid mass flow rate

Figure 6.15 shows the effect of the fluid mass flow rate on the amount of energy released by the GHE in 3 summer days in Adelaide. The performance of the GHE under two different fluid mass flow rates namely, 0.6 kg/s and 1 kg/s, is compared. The results of the simulation indicate that the amount of energy released by the GHE increases as the fluid flow rate increases. This tendency occurs because the mass flow rate affects the convective heat transfer coefficient of the fluid inside the GHE. The higher the mass flow rate, the higher the coefficient convective heat transfer is attained [94]. As a result, it increases the heat transfer capacity and the amount of energy released by the GHE. As an example, Figure 6.16 shows the profile of the fluid temperature generated from the horizontal, vertical, and horizontal to vertical modes at two different mass flow rates namely, 0.6 kg/s and 1 kg/s. This figure shows that the outlet fluid temperature increases with the increase of fluid mass flow rate. This tendency occurs because at a higher mass flow rate, the time period during which the fluid makes contact with the pipe is shorter when compared to a relatively low flow rate. In addition, at a higher mass flow rate, the GHE releases more heat into the surrounding soil and leads to a quick increase in soil temperature, resulting in an increased outlet fluid temperature. Varying the mass flow rate from 0.6 kg/s to 1 kg/s has increased the amount of energy released by 2.4% for the horizontal mode and 3.3% for the vertical mode. The rate increases are 4.9%, 5.1%, and 5.6% for the horizontal to vertical, vertical to horizontal and split flow mode, respectively.
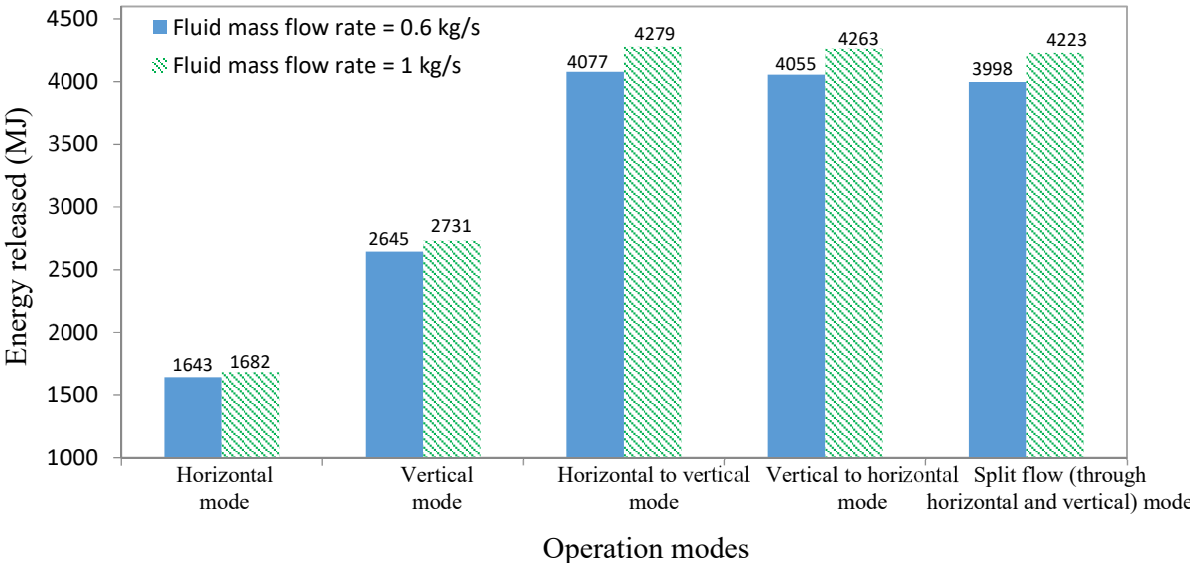
Figure 6.15: Energy released in 3 days (10-12 January) by the GHE with different mass flow rates (Adelaide case). The inlet fluid temperature = 50 °C, length of the horizontal GHE = 200 m, length of the vertical GHE = 200 m
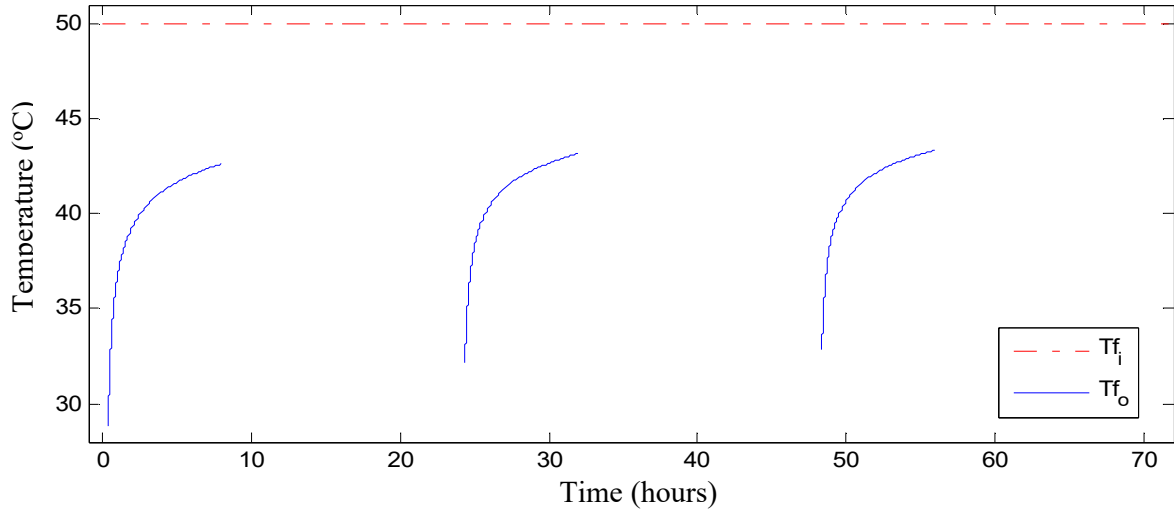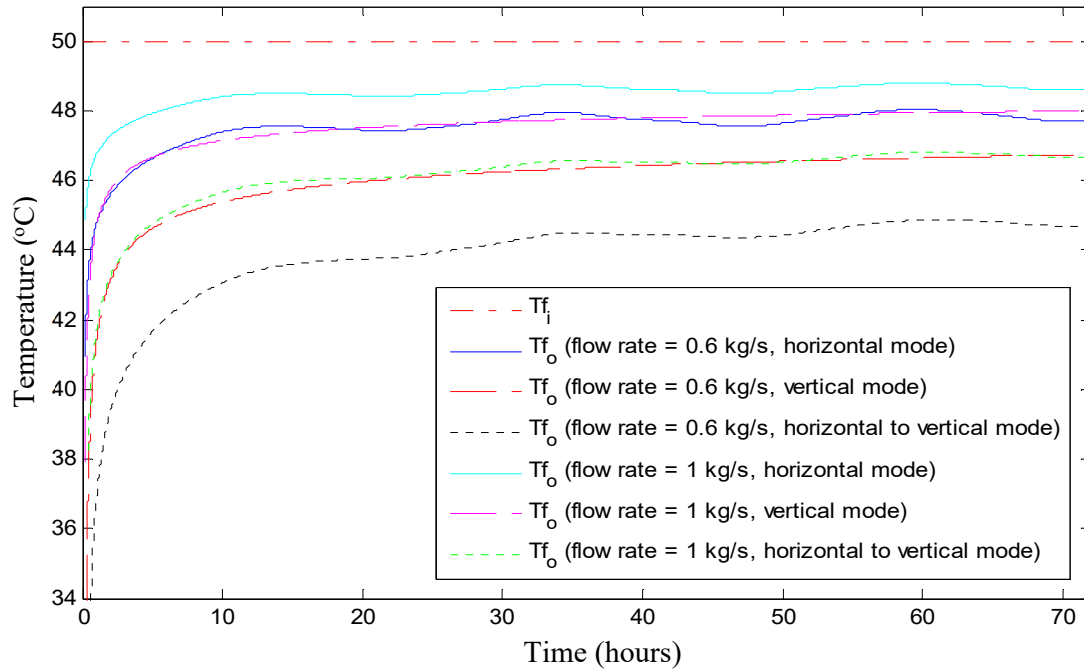
Figure 6.16: Profile of the outlet fluid temperature of the GHE under different operation modes and fluid mass flow rates (Adelaide case)

6.5 Summary

The performance of a combined horizontal-vertical GHE under five different operation modes, to deal with various demands and loading conditions, is studied. The effects of the continuous and intermittent operation conditions, the ratio of mass flow rate (for split flow mode only), and climate conditions are investigated in order to understand the factors that affect the performance of the combined GHE. It reveals the that the combined GHE's operation can have a significant advantage to be operated at peak loads or when heating/cooling demands are relatively high, while the horizontal or vertical GHE only, may be operated when the loading load is relatively low. In addition, operating the GHE continuously can release more heat than that the intermittent, however, the average of heat transfer rates of the continuously operated GHE decreases due to deterioration of the thermal soil condition around the GHE. It is found that during the continuous operation, the GHE installed in Adelaide's temperate climate can release more energy compared with that installed in Brisbane, as the initial soil temperature and climate conditions influence the performance of the GHE. The amount of heat rejected by the GHE may be enhanced if the mass flow rate of the working fluid is increased. It is observed that the ratio of the fluid flow in the split flow operation mode does not significantly affect the amount of energy released by the GHE.

CHAPTER 7
CASE STUDIES

This chapter aims to demonstrate the potential application of GHEs to assist the operation of air conditioning systems through two case studies. Case study I is based on Terminal 1 building, Adelaide airport. Whilst case study II is carried out on twenty units of residential building development also in Adelaide, South Australia. In this chapter, the combined horizontal-vertical GHE arrangement introduced in Chapter 6 is used to substitute the currently operating heat rejection devices, i.e. cooling tower for Case study I and air-cooled condenser for Case study II.

Chapter 7 is organised as follows. Section 7.1 presents a brief overview of Adelaide's weather conditions and soil temperature. Section 7.2 describes the case study I, including the building's floor map, the cooling load, and the reference chiller plant. In addition, three different scenarios on the reference chiller are proposed in order to investigate the energy and CO_2 savings. The case study II is presented in Section 7.3. This section describes the three-storey residential houses along with their heating and cooling loads. In addition, a brief overview of the reference air-cooled air conditioning systems (heat pumps) used to provide cooling (heating) for twenty units of residential houses is presented. The energy saving potential of the reference air-cooled air conditioning systems (heat pumps) is studied by modifying their air-cooled condenser to the water-cooled ones, in which, the cooling water is supplied by the GHEs. The total energy consumption and CO2 emission of both the air-cooled and water-cooled condenser air conditioning systems (heat pumps) in cooling and heating processes are then presented. Section 7.4 summaries the key findings of this chapter.

7.1 Adelaide weather conditions and soil temperature

The climate in Adelaide, South Australia, is mild, wet winters and warm, dry summers. The year can be divided into four seasons: summer (December-February), autumn (March-May), winter (June-August), and spring (September-November). The average maximum ambient temperature in summer is 29 °C. There are several days in a year in the daytime when the air temperature reaches 40 °C or slightly above. In winter, ambient temperature varies from 7 °C to 16 °C [98]. Figures 7.1 and 7.2 show examples of ambient air temperature profiles in Adelaide in the winter (June 1st-August 31st, 2006) and summer months (December 1st, 2006 - February 28th, 2007).

June	July	August
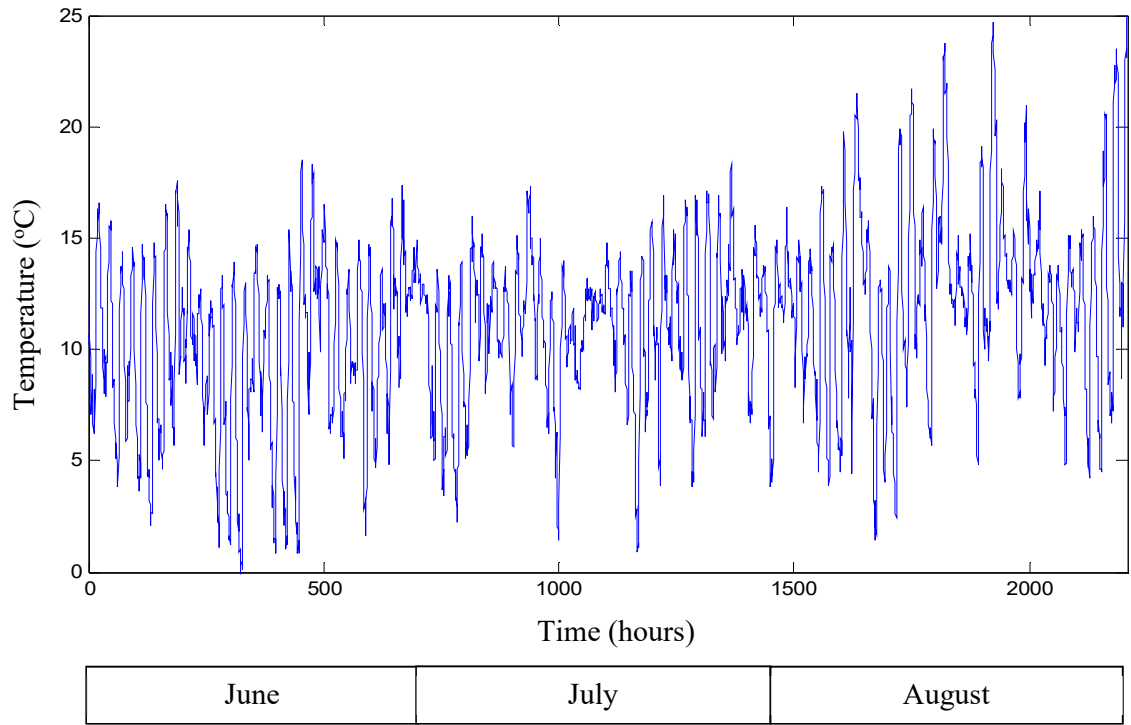
Figure 7.1: Profile of ambient temperature in Adelaide in 3 consecutive winter months (June 1st-August 31st, 2006)

December	January	February
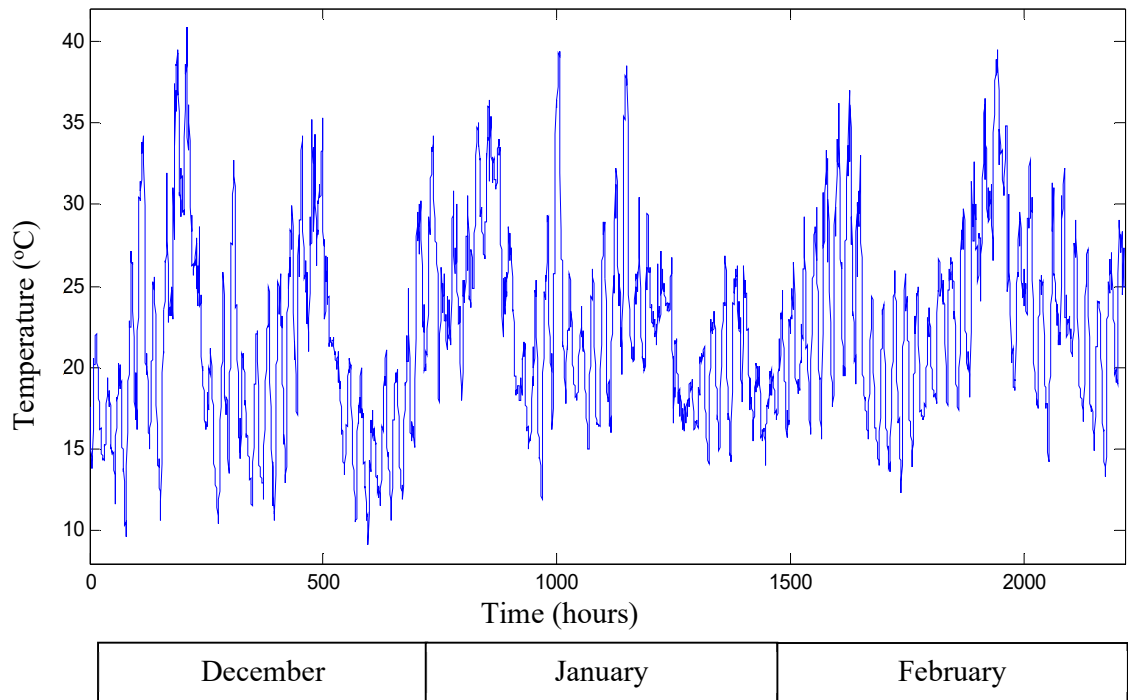
Figure 7.2: Profile of ambient temperature in Adelaide in 3 consecutive summer months (December 1st, 2006-February 28th, 2007)

Figure 7.3 shows the profile of soil temperature in Adelaide at the beginning of winter and summer generated by Baggs' Equation (i.e. Eq. 2.1) [20] with input parameters are summarised

in Tables 3.1 and 3.2. It is observed, at a shallow region up to 12 m below the surface, the ground temperature shifts significantly, as the ground continuously exchanges the heat (diurnally and seasonally) through its surface with the atmosphere. The changes in soil temperature are less and lag behind the changes in seasonal ambient air temperature since the soil has a relatively higher thermal conductivity than the air. In June, the surface ground temperature decreases up to 11 °C and shifts to 27 °C in December, as the ambient air temperature is being warmer. At a deeper region, the changes in soil temperature are less and lag than the shallower region. It shows, the ground temperature is relatively constant at a depth 12 m below the surface namely, 19 °C.
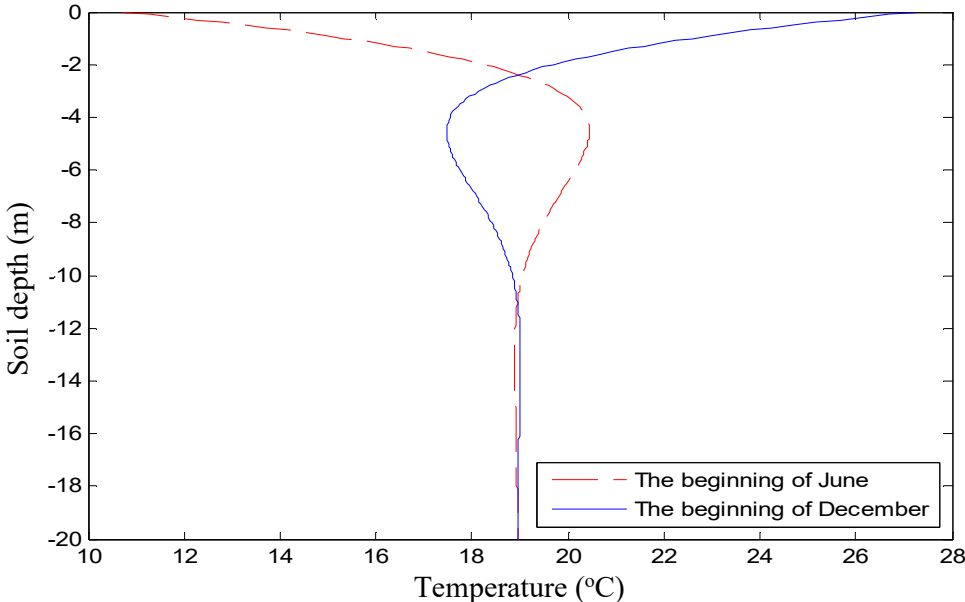
Figure 7.3: Soil temperature in Adelaide at the beginning of winter and summer

The soil internal heat source term values, as presented in Table 3.3, are used to take into account the effect of seasonal soil temperature changes in Adelaide. They are positive when the soil gets warmer (August to February in the southern hemisphere), and conversely are negative when the soil gets cooler (February to August). These internal heat source term values are used in the following case studies.

7.2 Case I: Terminal 1 building, Adelaide airport

This case study is to analyse and compare the energy consumptions of a chiller unit in Terminal 1 building as if it is equipped with GHEs instead of current cooling towers.

7.2.1 The terminal 1 building and chiller plant

Terminal I building, Adelaide airport, is a three-storey building with a total floor area of 75,000 m². The building has an approximated platform length of 750 m with its long axis is North-East

oriented. It is capable of processing 3000 passengers per hour. An extensive single glazing is installed along the gate lounges, as well as in the arrival and departures halls, yields a substantial solar heat gain to these areas and contributes to a major cooling load for the building. The building is opened to the public from 4.00 am to 11.00 pm. Figure 7.4 shows the floor map of Terminal 1 building, Adelaide airport.
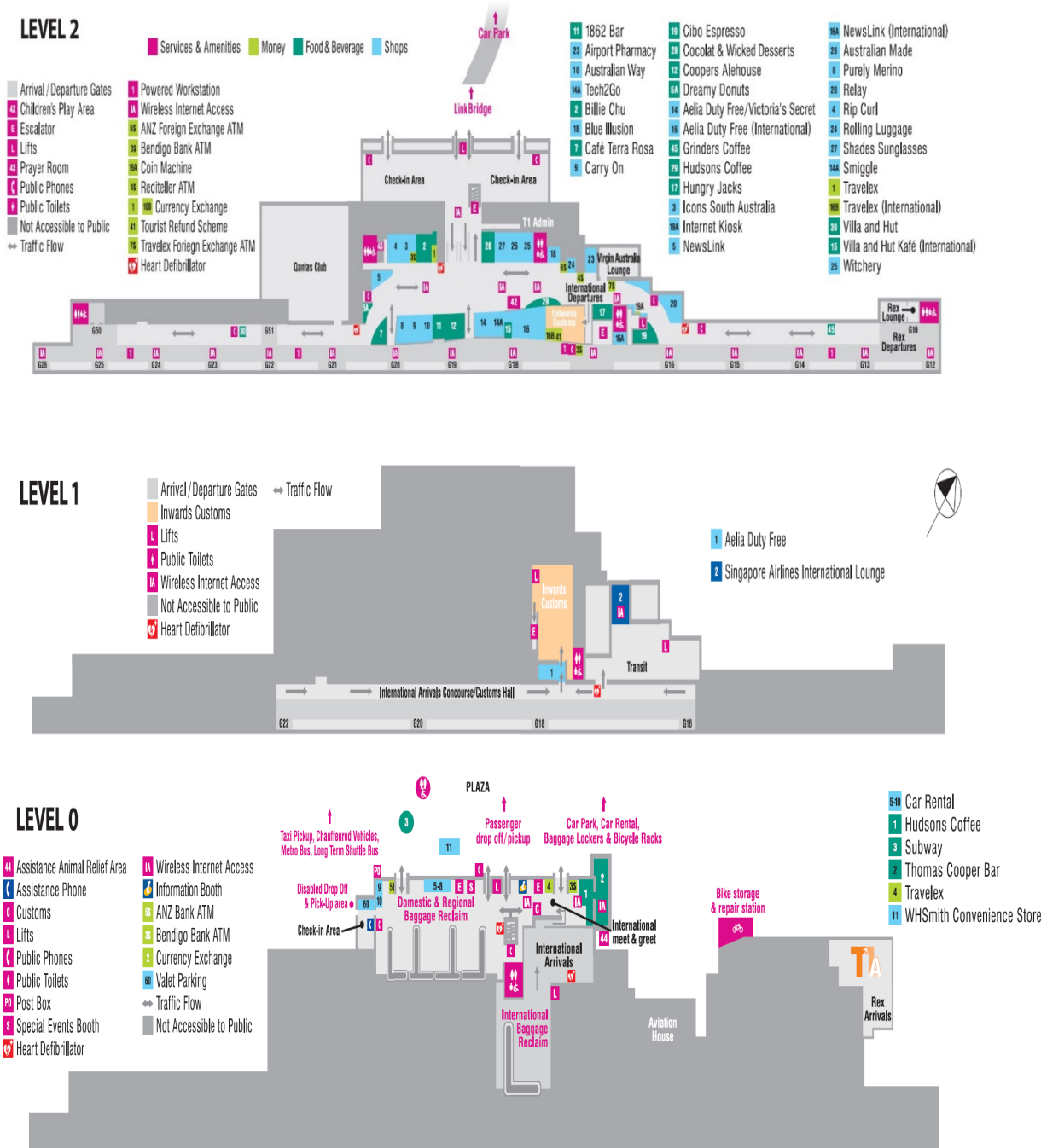
Figure 7.4: The floor map of Terminal 1 building, Adelaide Airport [100].

Figure 7.5 shows the typical hourly cooling load of Terminal 1 building in summer. As shown in the figure, during the summer months, the cooling load of Terminal 1 building varies from 4500 kW to 100 kW (at night).
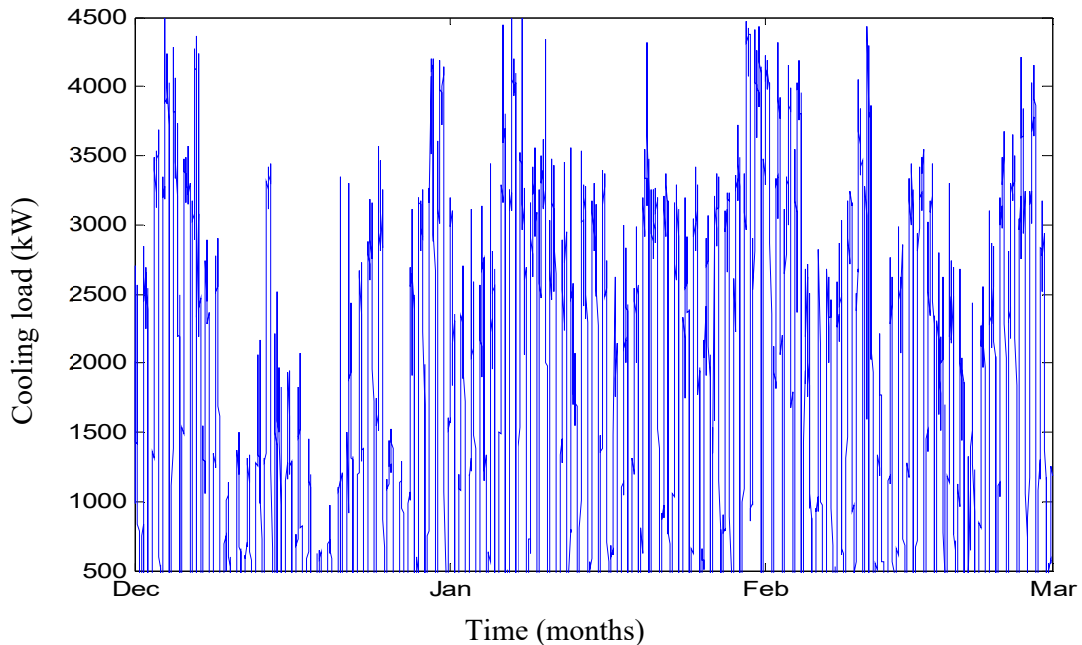
Figure 7.5: Profile of hourly cooling load in Terminal 1 building, Adelaide airport

Figures 7.6 shows the schematic of the chiller plant for terminal 1 building. The chiller plant consists of 3 chiller units in order to maintain the Terminal 1 building, at an indoor air temperature of 22 °C. Each chiller is rated at 1767 kW output and 320 kW electrical input at full load. They utilise R134a refrigerant as the cooling medium. The chillers are equipped with variable speed compressors, which enable the chillers to operate at 25% load or less. Two secondary chilled water pumps with a variable speed feature are used to circulate the chilled water from the chillers to 117 air handling units to provide cooling to the building. In the air-handling units, the air is cooled by passing it through cooling coils and then supplied to the local zones of Terminal 1 building. Three cooling towers are employed to dissipate the heat from the chillers to the atmosphere. The cooling towers each comprise modular counter flow draft construction with a vertical discharge. Each cooling tower works at an entering and leaving temperature of 36 °C and 28.5 °C, respectively and a flow rate of 66.6 L/s. Table 7.1 shows the chiller specification.
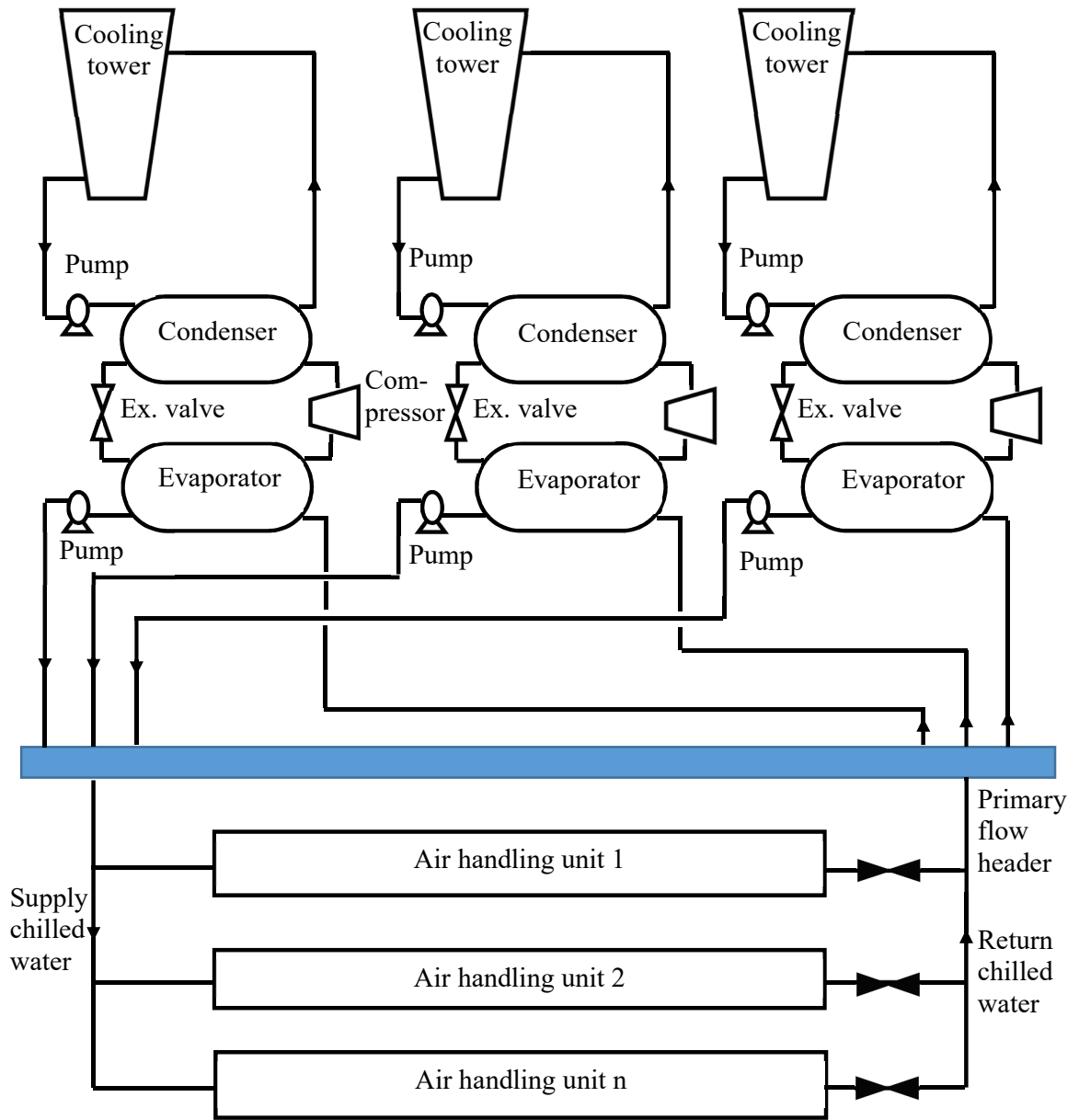
Figure 7.6: Schematic of the chiller plant

Table 7.1: Chiller specifications

Parameters	Value	Unit
Output capacity	1767	kW
Electrical input	320	kW
COP	5.52	-
Chilled water temperature entering air handling units	5	ºC
Chilled water temperature leaving air handling units	15	ºC
Cooling water temperature (at condenser)	28.5	ºC
Warm water temperature (at condenser)	36	ºC

7.2.2 The reference chiller and energy consumption

The chillers are controlled by the Building Management System (BMS) that enable them to operate based on the cooling load of the building. The BMS automatically activates another chiller once the cooling load increases, indicated by the rise in chilled water supply temperature above 12 °C, for more than five minutes. Whilst only a single unit chiller is operated at the nighttime when the ambient temperature drops. The existing chiller, which specification is given in Table 7.1, is set as the reference chiller for this study.

The thermodynamic analysis of the reference chiller is performed first in order to assess the required energy input to provide the required cooling. This analysis considers a single unit chiller only, operating at a full load capacity, i.e. 1767 kW, from 4:00 am to 11:00 pm. The chiller operates at a relatively low load fraction of 20%, from 11:00 pm to 4:00 am when the Terminal 1 is closed. In this study, this low load fraction is ignored and the analysis is conducted based on the following assumptions:

1. The expansion valve and compressor operate adiabatically;
2. The potential and kinetic energy effects are ignored;
3. The temperature difference between the cooling water and the condenser, ΔT_{cond}, is 5 °C;
4. Energy consumption by the circulation pump and pressure drop in GHEs is ignored;
5. Temperature difference between the evaporator and the chilled water, ΔT_{eva}, is 5 °C, and temperature difference between the chilled water and supply air is 10 °C;
6. The room temperature is set to 22 °C;
7. Isentropic efficiency of the chiller's compressor is 81.6%.

Based on the above assumptions, for the reference chiller (one of the chillers installed in Terminal 1 building), its condenser temperature T_{cond} is 33.5 °C and its evaporator temperature T_{eva} is 0 °C. Based on these two temperatures, its ideal cycle COP is 6.76. However, the actual COP of the chiller given by the manufacturer is 5.52. The difference of the two COPs indicates the isentropic efficiency of the compressor is 81.6%. The energy consumed by the chiller is calculated by multiplying the power input of the compressor with the period of operation. The total energy consumption of the chiller operated in 3 summer months, under intermittent operation (19 hours On and 5 hours Off daily), is equal to 547660 kWh.

7.2.3 Scenarios

This section is to set up different scenarios of the reference chiller system equipped with different cooling water supply systems. Three different scenarios are proposed and elaborated as follows:

➢ Scenario 1: Replacing the cooling tower with GHEs (Full load capacity)

The first scenario is to assume that the cooling tower used to supply the cooling water to the chiller unit was replaced by a GHE system and the chiller was operated at a full load (1767 kW cooling) for 19 hours and switched off for 5 hours every 24 hours, i.e from 4:00 am to 11:00 pm is On and from 11:00 pm to 4:00 am is Off.

The GHEs for this scenario are required to meet the specifications of the currently operated cooling tower. The amount of heat to be disposed by a single unit chiller through the GHEs is equal to the sum of the cooling capacity of the chiller and the compressor power.

$$\dot{Q}_{out} = \dot{Q}_{in} + \dot{W}_c \qquad (7.1)$$

where $\dot{Q}_{out}$ is the heat rejection rate of the condenser (kW), $\dot{Q}_{in}$ is the cooling capacity of the chiller (kW), and $\dot{W}_c$ is the compressor power (kW).

Since the chiller has a cooling capacity of 1767 kW and the compressor power of 320 kW, thus, the chiller needs to reject 2087 kW of the heat to the GHEs in the full load situation.

Based on the specification of the cooling tower, the mass flow rate of the cooling water required to dispose the chiller heat is 66.6 kg/s, with the temperature difference of 7.5 °C (i.e. 36→28.5 °C) as given in Table 7.1

In this scenario, each unit of the combined GHE structure (as illustrated in Figure 7.7) is assumed to be parallelly connected. Two manifolds are used to distribute/collect the warm/cool water to/from each unit of the combined GHE structure. In which, 0.2 kg/s of water is circulated in each unit of the combined GHE, in order to meet the condition of the cooling water temperature of the currently operated chiller. The combined GHE with a horizontal to vertical mode has been chosen as it can release more energy than other operation modes (refer to Chapter 6, Section 6.4). From the calculation, it requires 333 units of the combined GHE structure, which corresponds to a total pipe length of 266400 m, to dispose 2087 kW of heat at a total flow rate of the cooling water of 66.6 kg/s. Table 7.2 summarises the technical parameters of the combined GHE structure under the proposed scenario.
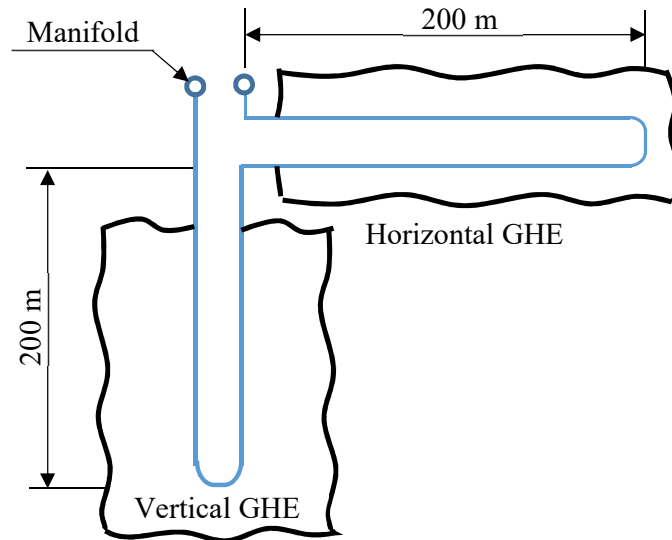
Figure 7.7: Schematic of a combined horizontal-vertical GHE unit

Table 7.2: The technical parameters of a combined horizontal-vertical GHE unit

Parameters	Value	Unit
Horizontal GHE		
Pipe length per each unit of the GHE	400	m
Burial depth	1	m
Pipe internal diameter	0.04	m
Pipe outer diameter	0.044	m
Centre distance between pipes	0.28	m
Soil domain span in x direction	0.14	m
Soil domain span in y direction	2	m
Vertical GHE		
Pipe length per each unit of the GHE	400	m
Borehole depth	200	m
Borehole diameter	0.15	m
Soil domain diameter	6	m
Pipe internal diameter	0.04	m
Pipe outer diameter	0.044	m
Centre distance between pipes	0.07	m

➢ Scenario 2: Installing half number of GHEs and a cooling tower

The second scenario is to install merely half number of GHEs as described in the first scenario, in the case of restriction of the land area and the capital budget. In this scenario, 50% of heat is disposed by GHEs and the rest is dissipated by a smaller cooling tower. Since the GHEs are designed using the same technical condition as that used for scenario 1, thus it requires 167 units GHEs, which is equal to 133600 m of the total pipe length, in order to dissipate the heat into the soil.

> Scenario 3: Installing half number of GHEs to dispose the chiller heat that operates at a full load capacity

The last scenario is to utilise the GHEs as installed in scenario 2 to dispose the heat of the chiller operating at a full load capacity. Namely, there is no cooling tower used in this scenario, which requires mass flow rate in each GHE unit to be increased from 0.2 kg/s to 0.4 kg/s. Table 7.3 summarises the proposed scenarios for case study I

Table 7.3: Scenarios for case study I

Operation and design conditions	Reference (existing system)	Scenario 1	Scenario 2	Scenario 3
Description	A cooling tower is used to dissipate the chiller heat to the atmosphere	Replacing the cooling tower with GHEs	Installing half number of GHEs and a small cooling tower	Installing half number of GHEs only
The amount of heat rejection rate of the chiller	2087 kW	2087 kW	2087 kW	2087 kW
Total units of the combined horizontal-vertical GHE required to be installed	-	333 units of GHE	167 units of GHE	167 units of GHE
Total length of the pipe	-	266400 m	133600 m	133600 m
Total mass flow rate of fluid in GHEs	-	66.6 kg/s	66.6 kg/s	66.6 kg/s
Mass flow rate in each unit of the GHE	-	0.2 kg/s	0.2 kg/s	0.4 kg/s
Heat rejection system	Cooling tower	GHEs	50% GHEs and 50% cooling tower	GHEs
Operation condition of the chiller	19 hours On and 5 hours Off daily	19 hours On and 5 hours Off daily	19 hours On and 5 hours Off daily	19 hours On and 5 hours Off daily

Table 7.4: Simulation parameters of the GHE

Parameters	Value	Unit
Circulation fluid (water)		
Inlet water temperature	36	ºC
Mass flow rate/ unit of the GHE	0.2	kg/s
Specific heat	4188	J/kg K
Density	980	kg/m^3
Soil type in Adelaide: layered old dune sands[91]		
Thermal conductivity	1.3	W/m K
Specific heat	1140	J/kg K
Density	1500	kg/m^3
Grout (vertical GHE)		
Thermal conductivity	2	W/m K
Specific heat	1140	J/kg K
Density	1500	kg/m^3
Wind speed (Adelaide)	4.9	m/s

7.2.4 Results and Discussions

Figures 7.8-7.10 show the simulation results of the outlet water temperature of the GHEs, in an intermittent mode (19 hours On and 5 hours Off daily), for three different scenarios of chiller systems operated in summer months (December, January, and February). The simulation is performed considering the weather and soil condition as illustrated in Figures 7.2 and 7.3 and the input parameters as summarised in Tables 7.2 and 7.4. In this simulation, the inlet water temperature of the GHEs is kept constant at 36 ºC in order to meet the specification of the cooling tower. The outlet water temperature of the GHEs under different scenarios is presented in 10 days for each summer month. As an example, Figure 7.8 presents the outlet water temperature of the GHEs in first ten days of operation. At the beginning of the operation, it shows that the GHEs with all proposed scenarios produce a relatively low outlet water temperature as the surrounding soil has a relatively low temperature. As the GHEs run, the temperature of the adjacent soil begins to increase due to the heat disposed by the GHEs flows through the soil domain. The relatively low thermal conductivity of the soil resists the heat flow in the soil domain and leads to the accumulation of heat in the adjacent soil. As a result, the heat transfer capacity of the GHEs gradually decreases, shown by the increase of the outlet water temperature over the period of operation.

As illustrated in Figure 7.8, at the beginning of the operation, the GHEs with scenario 1 produce the lowest outlet water temperature than other scenarios as they have a relatively lower mass flow rate which allows the working fluid to have a longer contact period with the inner surface of the pipe. In scenario 2, both GHEs and a cooling tower are used in order to dispose the chiller heat. In this scenario, it is only half numbers of GHEs as described in scenario 1 installed. In

which, 50% of the mass flow rate of the working fluid is circulated through the GHEs and the rest is passed to a cooling tower. The mixed water from both the GHEs and the cooling tower, at a certain temperature, is then fed into the condenser. As shown in Figure 7.8, the outlet water temperature with scenario 2 is relatively higher than that generated by scenario 1 during the first ten days of operation. This phenomenon is affected by a relatively higher temperature of water exits the cooling tower (28.5 °C) than that produced by the GHEs. As a result, it affects the final temperature of the mixed water from both GHEs and the cooling tower. It is shown in Figure 7.8 that the difference in the outlet fluid temperature between scenarios 1 and 2 decreases with increasing of operation period. The increase in soil temperature around the GHEs contributes to an increase of the outlet water temperature of the GHEs. This effect is significant for scenario 1 since it solely relies on the GHEs for heat dissipation, while scenario 2 benefits from the constant outlet water temperature of the cooling tower. It is noticed, the GHEs with scenario 3 produce a relatively lower outlet water temperature than scenario 2 only during the start-up of the GHEs (on a daily basis). As the GHEs run, the temperature of soil adjacent to the GHEs, for scenario 3, increases quicker than those yielded by other scenarios. This tendency is affected by a relatively higher mass flow rate in each unit of the GHE (in scenario 3), resulting in more heat dissipation to the surrounding soil. As a result, the outlet water temperature of the GHEs for scenario 3 increases quicker. Overall, the GHEs with scenario 3 produce the highest outlet water temperature as the mass flow rate in each unit of the GHE is increased in order to compensate the reduction in the number of the GHEs caused by the restriction of the land area and the capital costs.
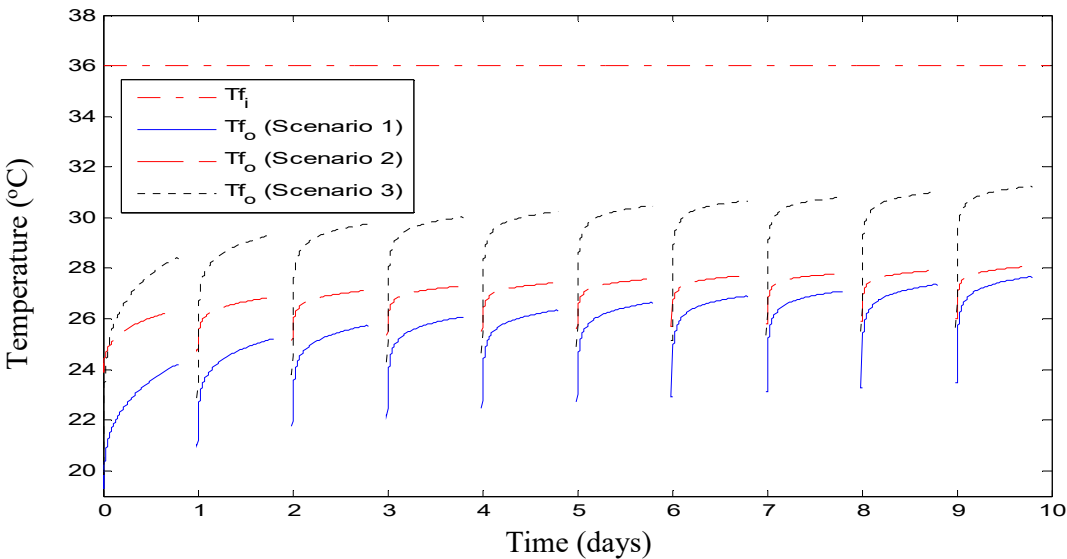
Figure 7.8 Profile of fluid temperature of the GHEs under three different scenarios, operated in 10 consecutive days of December, under an intermittent mode (19 hours On and 5 hours Off daily), where the inlet fluid temperature = 36 °C.

Figure 7.9 presents the outlet water temperature of the GHEs from day 40 to day 50 (mid of January). As shown in the figure, at the start up of the GHEs' operation (on a daily basis), the GHEs with the scenario 1 produce the lowest outlet water temperature than other scenarios. However, after a certain period of operation, the outlet water temperature of the GHEs with scenario 1 becomes higher than that generated by scenario 2, as the ground temperature around the GHE increases. While the outlet water temperature produced by the GHEs with scenario 3 is the highest among others. The relatively higher fluid mass flow rate circulated in the GHEs with scenario 3 deteriorates the soil temperature quicker than other scenarios and affects the heat transfer rate of the GHEs. Figure 7.10 shows the outlet water temperature of the GHEs from day 80 to day 90 (at the end of February). The results show the profile of the outlet water temperature of the GHEs for each scenario is almost identical in each day. The reason for this phenomenon is that the GHEs are close to the steady state condition. It is observed, at the end of summer, the difference in the outlet water temperature between scenarios 1 and 2 is being higher as the ground temperature keep increasing during the cooling operation. It is shown in Figures 7.8-7.10 that the outlet water temperature of the GHEs gradually increases with the operation period although the GHEs operate intermittently. The reason is because the soil temperature adjacent to the GHEs cannot fully recover to its initial condition within 5 hours of the system Off. In which, it agrees well with Dai et al.'s findings [68]. It is observed, even though scenario 1 generates the highest water temperature difference between inlet and outlet, during the first 10 days of operation, however, this water temperature difference decreases with operation time. It shows scenario 2 has a better performance for a long-term operation since it benefits from the stable performance of the cooling tower.
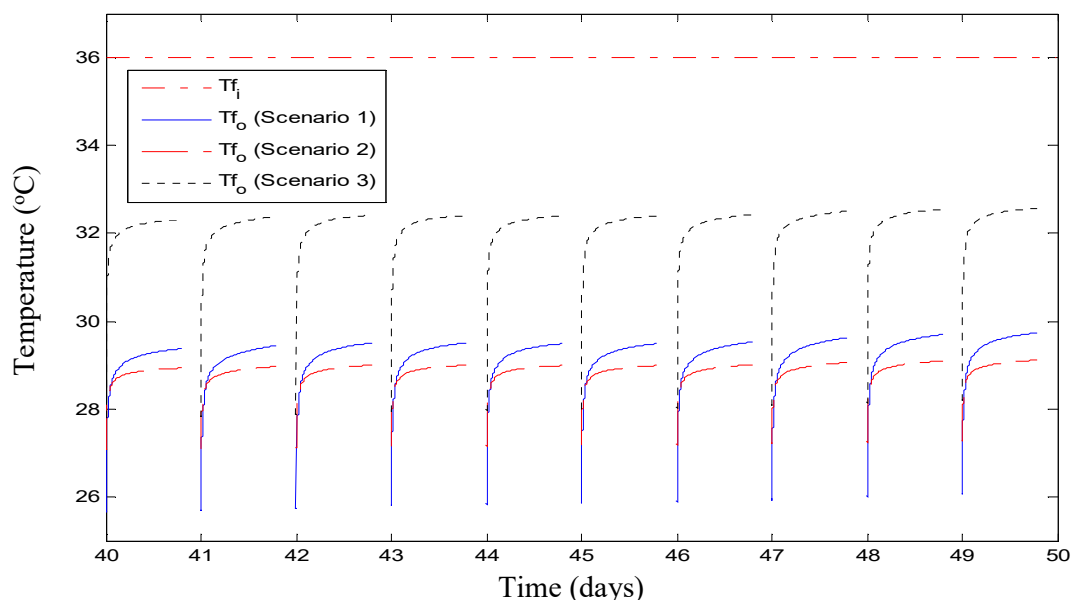
Figure 7.9 Profile of fluid temperature of the GHEs under three different scenarios, operated in 10 consecutive days of January, under an intermittent mode (19 hours On and 5 hours Off daily), where the inlet fluid temperature = 36 °C.
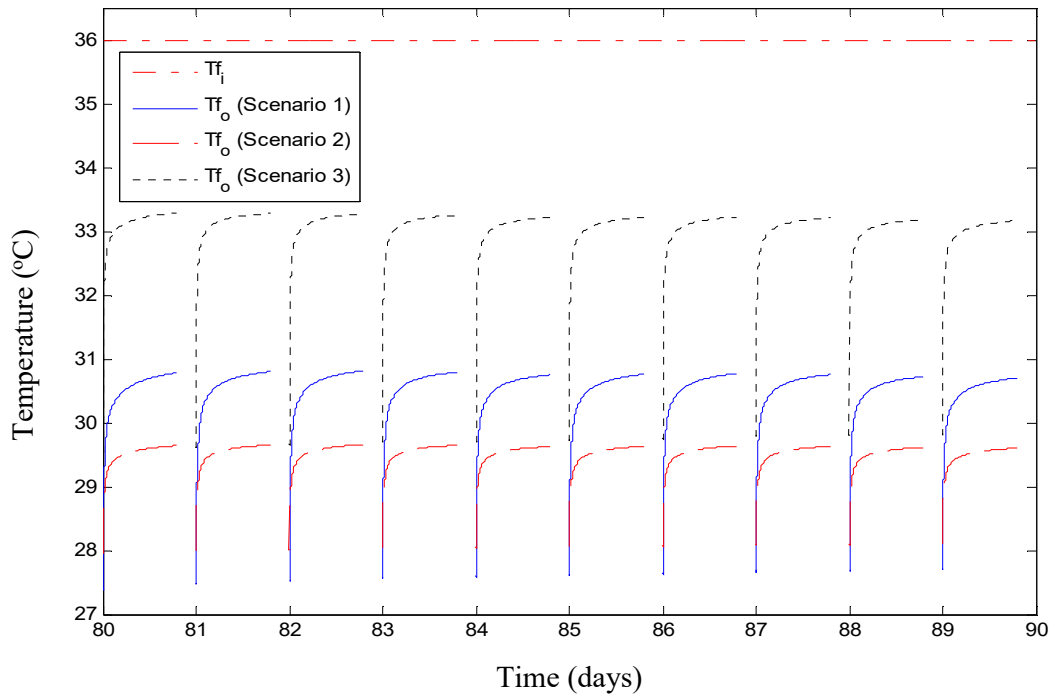
Figure 7.10 Profile of fluid temperature of the GHEs under three different scenarios, operated in 10 consecutive days of February, under an intermittent mode (19 hours On and 5 hours Off daily), where the inlet fluid temperature = 36 °C.

Figures 7.11 and 7.12 show the soil temperatures around the horizontal and vertical GHEs, respectively, during the cooling operation in the summer for 3 different scenarios of the chiller. It is observed, the soil temperatures subjected to scenarios 1 and 2 are lower than that scenario 3, since those scenarios (1 and 2) apply 50% less mass flow rate, for each unit of the GHE, than the other. At a relatively higher mass flow rate, the GHE rejects more heat to the soil domain, results in a quick increase in soil temperature. The soil temperature also varies with locations relative to the GHE. As the heat flows from a hot to a cold region, the soil that closer to the hot region has a relatively higher temperature than that at a further distance. The soil temperature is fluctuant under an intermittent load of the GHE. Figure 7.11 shows the soil temperature around the horizontal GHE significantly increases during the first ten days of operation as a response to the heat disposed by the GHE. When the soil temperature approaches the temperature of working fluid (at a temperature of 34 °C or above), the increase in soil temperature is not significant anymore, however, it swings following the pattern of ambient air temperature.

Figure 7.12 shows the soil temperature around the vertical GHE at a depth of 100 m below the surface. It is shown, even though the vertical GHE may benefit from the intermittent operation of the GHE, however, the soil temperature significantly increases with the increase of the operation period. The increase in soil temperature over the time is inevitable since the soil

cannot recover to its initial temperature within 5 hours of the system Off. From the simulation, it shows the vertical GHE benefits from the stable initial soil temperature at a specific depth below the surface. This condition enables the vertical GHE to exchange more heat with the surrounding soil than the horizontal loop buried in a shallow zone. The deterioration of soil temperature around the vertical GHE is hard to recover because of low soil thermal conductivity and soil's distance from the surface. While the horizontal GHE takes advantage of its shallow burial depth allowing the heat to reach the surface faster and transfer it to the atmosphere when the ambient air temperature drops (i.e. nighttime).
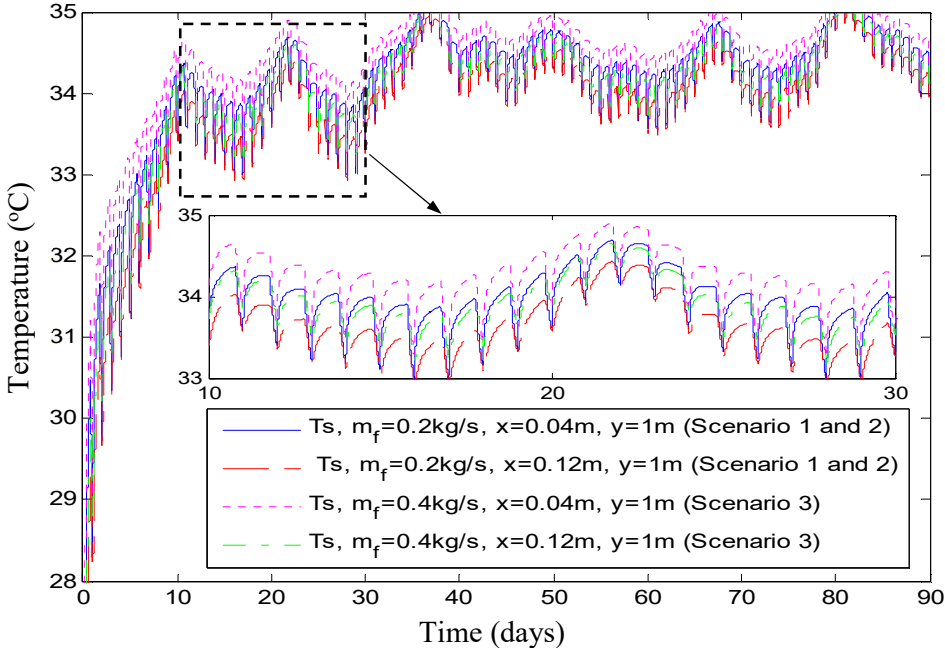
Figure 7.11: Soil temperature around the horizontal GHE
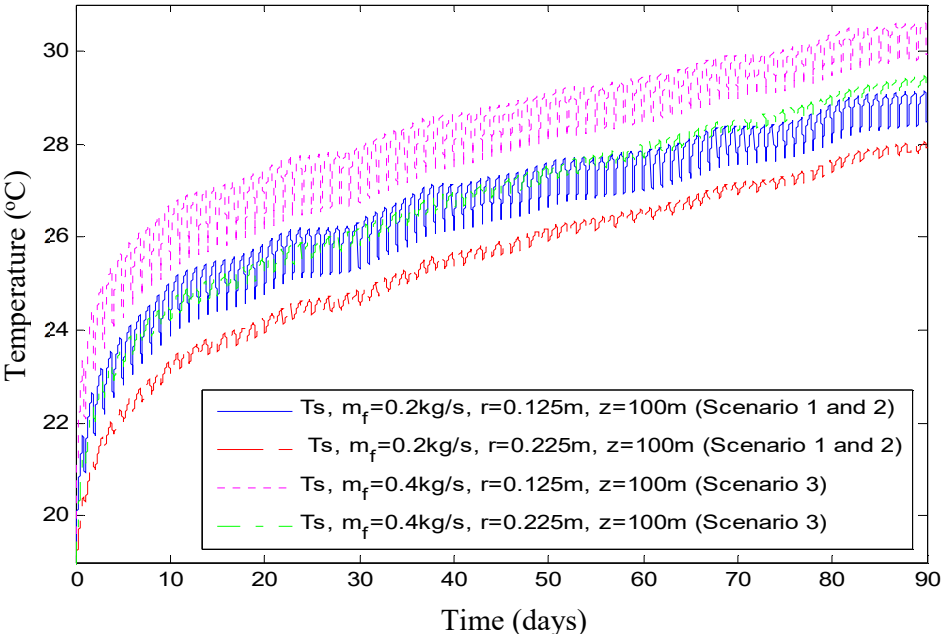
Figure7.12: Soil temperature around the vertical GHE

Figure 7.13 shows the modelling results of energy consumption of a chiller equipped with a variable speed compressor under different scenarios. The chiller is operated in an intermittent condition (19 hours On and 5 hours Off daily) during the summer months. The energy consumption is obtained based on the sum of every hour results. It is observed that the energy consumption of the chiller is affected by the temperature of water leaving the GHEs, as shown in Figures 7.8-7.10. It shows the chillers with scenarios 1 and 2 provide 12.9% and 6.5% of energy savings, respectively at the beginning of operation. However, these energy savings decrease with the increasing of operation period, as the soil temperature around the GHEs is deteriorated. Eventually, the energy consumed by the chillers with scenarios 1 and 2 become higher than that the reference cycle, when the operation time exceeds about 70 days. The scenario 3 is nonviable as the chiller consumes more energy than the reference cycle. For all proposed scenarios, it seems the GHE is difficult to compete with the cooling towers if the water consumption is not an issue under the current study conditions. In this case, the performance of the cooling tower is assumed constant. In fact, it depends on weather conditions [73]. The GHEs still have potential especially in a humid climate or if the length of the GHEs is increased. As shown in Figure 7.14, at the end of summer, all the proposed scenarios consume more energy than the reference cycle namely, 1.4%, 0.7% and 12.7% for scenario 1,2 and 3 respectively.
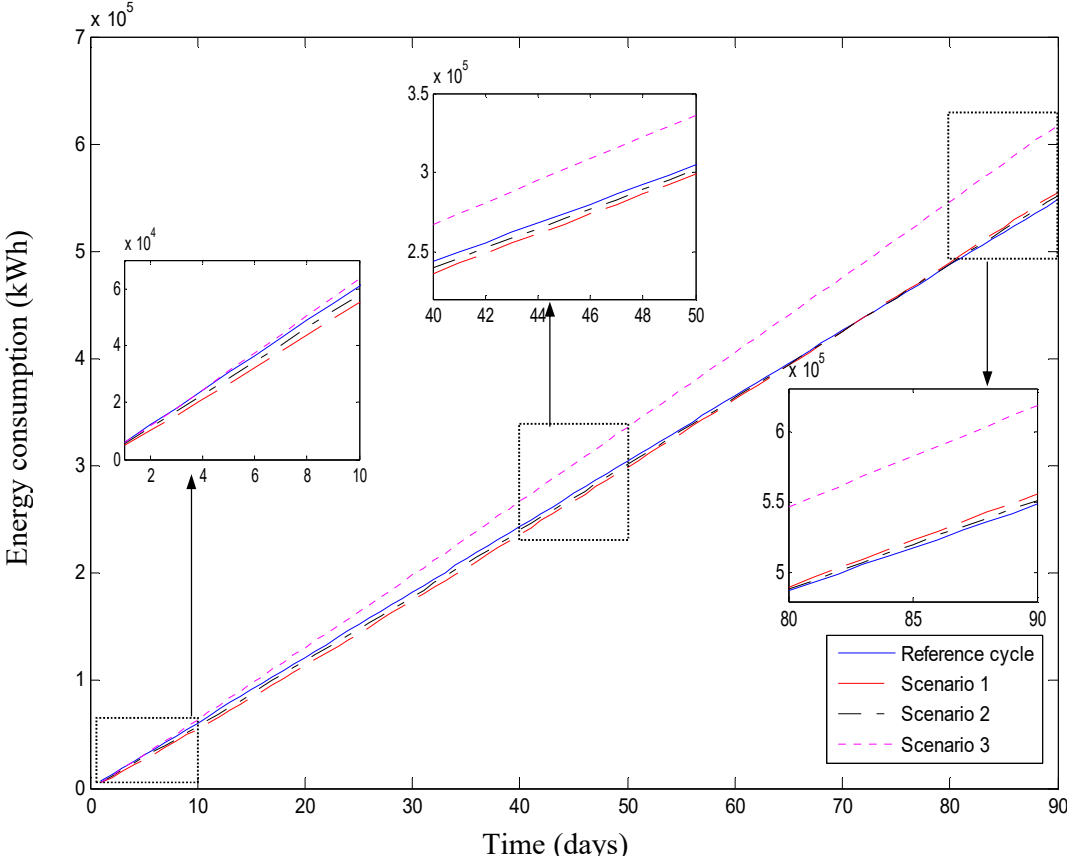
Figure 7.13: Comparison of energy consumption of the chiller under different scenarios

The carbon footprint of the chiller operated under different scenarios has been compared and presented in Figure 7.14. In Australia, the CO_2 emission per amount of electricity consumed is different amongst the states. According to the Australian government, department of environment, the emission factor of kg CO_2/kWhe in South Australia is equal to 0.72 [101]. As illustrated in Figure 7.14, the production of CO_2 emission depends on the electricity consumed by the chiller. The chiller with the lowest energy consumption produces less CO_2 emission. It shows, after fifty days of operation, the chillers with scenarios 1 and 2 produce 1.8% and 0.96% less CO_2 emission than the reference chiller, respectively. However, at the end of summer, these two scenarios cannot longer compete with the current cycle as they generate more CO_2 emission.
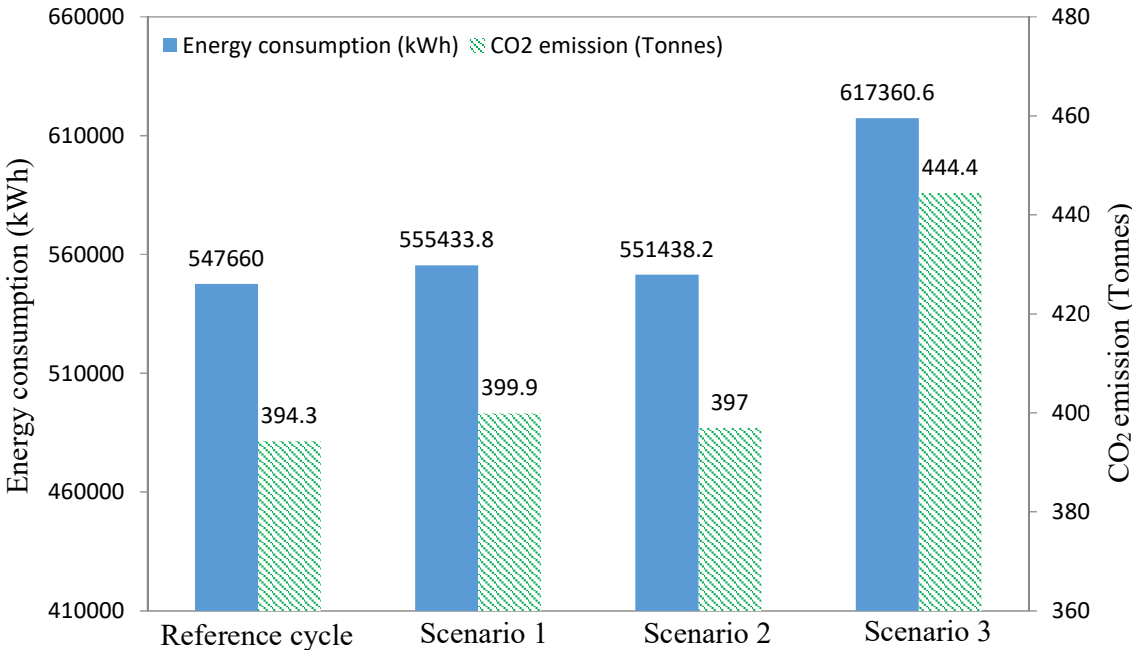
Figure 7.14: Energy consumption and CO_2 emission of the chiller system, over three summer months (December-February) under an intermittent mode (19 hours On and 5 hours Off daily).

7.3 Case II: Residential houses

The case study II is based on a real estate development of twenty three-storey residential houses in Adelaide. This case study is aimed to analyse and compare the energy consumption of the reference air-cooled air conditioning system with a water-cooled system under both heating and cooling.

7.3.1 The building and air conditioning system (heat pump)

The house has three levels and contains one garage, one living room, one dining room, one family room, two bedrooms and other activity areas, shown in Figure 7.15. The total floor area requires air conditioning is 137 m² (Table 7.5 summarises the construction data for a single unit house). The main active period in the house starts from 6:00 am to 10:00 pm every day in summer, and from 5:00 pm to 9:00 am in winter. Each unit of the house has 15 kW and 8 kW peak cooling and heating loads, respectively. These values correspond to 300 kW and 160 kW for twenty units of the house.
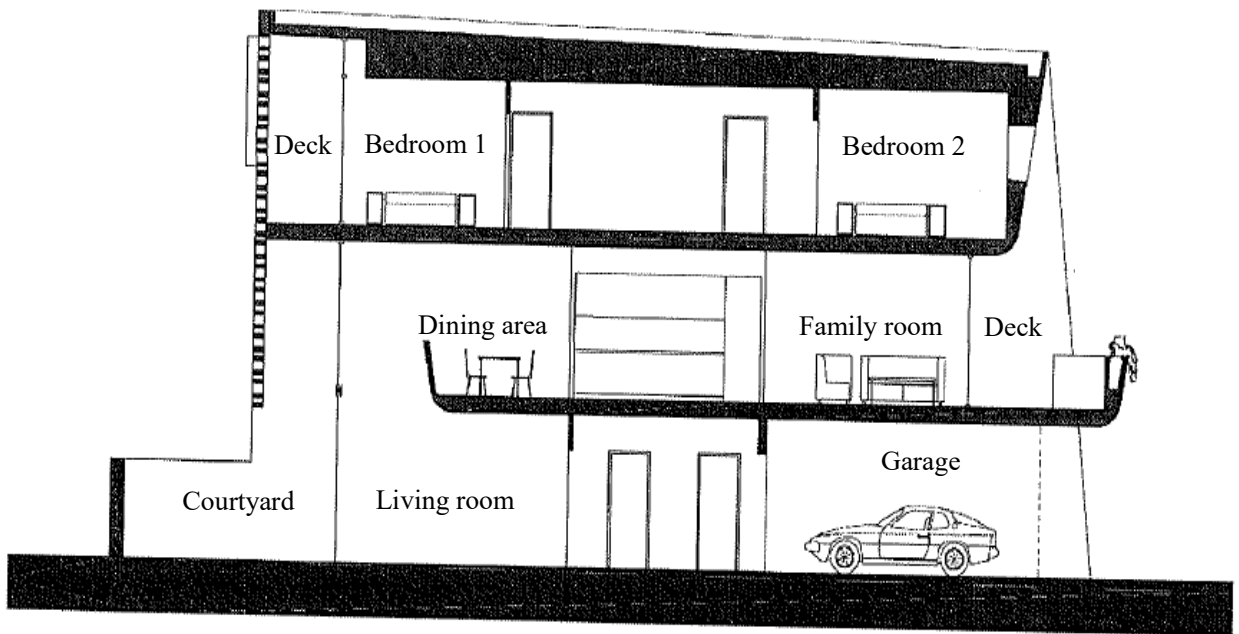
Figure 7.15: The blue print of the reference building.

Table 7.5: Construction data of the building

	Garage	Living room	Dining room	Family room	Bedroom 1	Bedroom 2	Other area
Height	2.8 m	2.8 m	2.8 m	2.8 m	2.8 m	2.8 m	2.8 m
Length	6 m	5 m	3 m	5 m	4 m	4 m	5 m
Width	5 m	5 m	5 m	5 m	5 m	5 m	5 m

Market research is conducted to find a suitable air conditioning system (heat pump), which has a cooling and heating capacity around 15 kW and 8 kW, respectively, to serve each unit of the residential house. Based on the market research, Daikin ducted-air conditioning system (heat pump), model: RZQ160LV1, with the cooling and heating capacity range 7.3-15.5 kW and 7.3-18 kW respectively, is selected. This variable speed compressor-air conditioning system (heat pump) uses refrigerant R-410A as a working fluid. Table 7.6 summarises the specification of Daikin air conditioning system.

Table 7.6: Specification of Daikin air conditioning system, model: RZQ160LV1.

Parameter		Value	Unit
Rated capacity	Cool	15.5	kW
	Heat	18	kW
Capacity range	Cool	7.3-15.5	kW
	Heat	7.3-18	kW
Power input (rated)	Cool	4.97	kW
	Heat	4.83	kW
COP	Cool	3.12	-
	Heat	3.73	-

7.3.2 Reference cycle air conditioning system (heat pump) and energy consumption

In order to provide the cooling and heating for 20 units of three-storey residential houses, which have total cooling and heating loads of 300 kW and 160 kW respectively, an air-cooled air conditioning system (heat pump) which its specification is given in Table 7.6, is assumed to be attached to each unit of the house and set as a reference air conditioning system for this study. A thermodynamic analysis is conducted to assess the energy consumed by the air conditioning system (heat pump) to provide the thermal comfort for occupants of the building. The analysis is performed based on the following assumptions:

1. The expansion valve and compressor operate adiabatically;
2. The potential and kinetic energy effects are ignored;
3. The reference air conditioning system (heat pump) is air-cooled (air-source). The temperature difference between outdoor air and the condenser, ΔT_{cond}, (the evaporator for the heat pump, ΔT_{eva}), is 10 °C;
4. Temperature difference between the room and the air conditioner's evaporator, ΔT_{eva}, (the condenser for the heat pump, ΔT_{cond}), is 10 °C;
5. The mean maximum outdoor air temperature in summer in Adelaide is 35 °C and the mean minimum outdoor temperature in winter is 6.5 °C;
6. The room temperature is set to 22 °C.

The thermodynamic analysis of the reference air conditioning system is performed based on an ideal vapour compression refrigeration cycle as shown in T-s diagram Figure 2.23, Section 2.4. Based on the previous assumptions, its condenser temperature T_{cond} is 45 °C and evaporator temperature T_{eva} is 12 °C for the air conditioning system. Based on these two temperatures, its ideal cycle COP for cooling is 6.1. While the air conditioner's COP given by the manufacturer is 3.12. Thus, based on the ratio of the actual COP to an ideal COP as given by the Equation 2.39, the isentropic efficiency of the compressor is 51%. Then, the input power of the air conditioning system is calculated using Equation 2.40. It requires 4.76 kW of electrical energy

to remove 15 kW of heat from each unit of the house. Total electrical energy consumed by the air conditioning system for three summer months is equal to 6866 kWh for a single house and 137316 kWh for twenty units of the house. Based on the same procedure, the energy consumed by the heat pump during heating in winter can be calculated. The COP of the heat pump is different from the air conditioning system. The COP of the heat pump is defined as a ratio of the heating effect to the input work. In which, the heating effect is corresponding to the sum of the heat transferred from the cold reservoir and input work. From the calculation, it requires 2.15 kW of electrical energy to provide 8 kW heating. Total energy consumed by the heat pump in winter for a single house is equal to 3096.6 kWh, which corresponds to 61932 kWh for twenty houses.

7.3.3 Scenario

In this case study, it is assumed that the air-cooled condenser of every air conditioning system (air heated evaporator for the heat pump) is modified to a water-cooled condenser (water-heated-evaporator) and the cooling (heating) water is supplied by a central GHE as shown in Figure 7.16. It is also assumed the twenty air conditioning systems (heat pumps), equipped with variable frequency compressors, are identical and turned On/Off for the same time every day. In summer, the air conditioning systems are operated from 6:00 am to 10:00 pm, while in winter the heat pumps are run from 5:00 pm to 9:00 am.
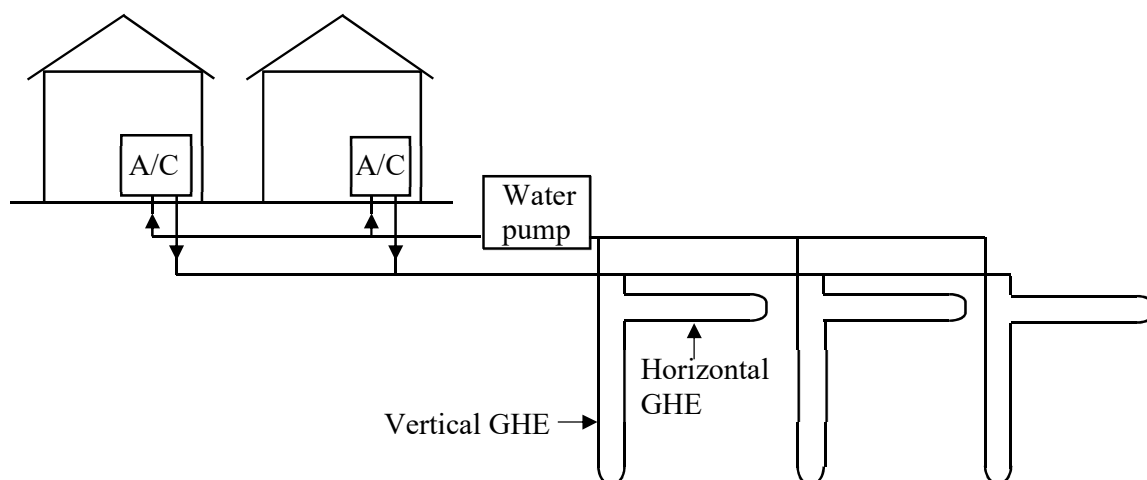
Figure 7.16: Schematic of residential houses with the combined horizontal-vertical ground source air conditioning systems (heat pumps)

The GHE is designed to have the same parameter as the Case I with the inlet and outlet fluid temperatures are 36 °C and 28.5 °C, respectively. Therefore, it requires 63 units of combined horizontal-vertical GHEs (as described in Figure 7.7 and Table 7.2) to be installed. Table 7.7 summarises scenario for case study II.

Table 7.7: Scenario for case study II

Operation and design conditions	Reference cycle	Scenario
Description	An air-cooled air conditioning system is used to provide the thermal comfort	Modify the air-cooled condenser of the reference air conditioning system to a water-cooled condenser in which the cooling water is supplied by a central GHE system
The amount of heat rejection rate of the air conditioning systems	395.2 kW	395.2 kW
Total units of the combined horizontal-vertical GHE required to be installed (refer to Figure 7.7)	-	63 units of GHE
Total length of the pipe	-	50400 m
Total mass flow rate of fluid in GHEs	-	12.6 kg/s
Mass flow rate in each unit of the GHE	-	0.2 kg/s
Operation condition	16 hours On and 8 hours Off daily	16 hours On and 8 hours Off daily

7.3.4 Results and Discussions

7.3.4.1 Cooling

Figures 7.17-7.19 show the simulation results of the outlet water temperature of the GHEs under intermittent condition (16 hours On and 8 hours Off daily) in three summer months (December, January, and February). The simulation is performed considering the weather and soil condition as illustrated in Figures 7.2 and 7.3 and the input parameters as summarised in Tables 7.2 and 7.4. The outlet water temperature is presented in 10 days for each summer month namely, early of December (Figure 7.17), mid of January (Figure 7.18) and the end of February (Figure 7.19). As shown in the figures that the outlet water temperature of the GHEs varies with the operation period. It is observed, the water temperature difference between the inlet and outlet is high at the beginning operation of the GHEs (see Figure 7.17). The relatively low soil temperature at the start up enables the GHEs to transfer more heat to surrounding soil. This temperature difference, however, decreases with increasing of the operation period. This tendency is affected by the accumulation of heat in the surrounding soil which contributes to a reduction in heat transfer rate of the GHEs. It is shown that the deterioration in the GHEs' performance is recovered during the system Off, shown by a relatively lower outlet water temperature generated on the next operation day. Since the GHE is turned off for 5 hours every day, its performance cannot fully recover to the initial condition, as it can take seasons to fully recover. As shown in Figure 7.18, the outlet water temperature of the GHEs is still increasing after forty

days of operation. The increase in outlet water temperature of the GHEs, however, is not as high as that generated during early operation of the GHEs, since the surrounding soil almost reaches steady state condition. It is shown, at end of summer, the outlet water temperature of the GHEs is almost identical from day to day (see Figure 7.18).

Figure 7.17: Fluid temperature of the GHEs in 10 consecutive days of December, under an intermittent mode (16 hours On and 8 hours Off daily), where the inlet fluid temperature = 36 ºC, fluid mass flow rate = 0.2 kg/s per unit of the GHE.

Figure 7.18: Fluid temperature of the GHEs in 10 consecutive days of January, under an intermittent mode (16 hours On and 8 hours Off daily), where the inlet fluid temperature = 36 ºC, fluid mass flow rate = 0.2 kg/s per unit of the GHE
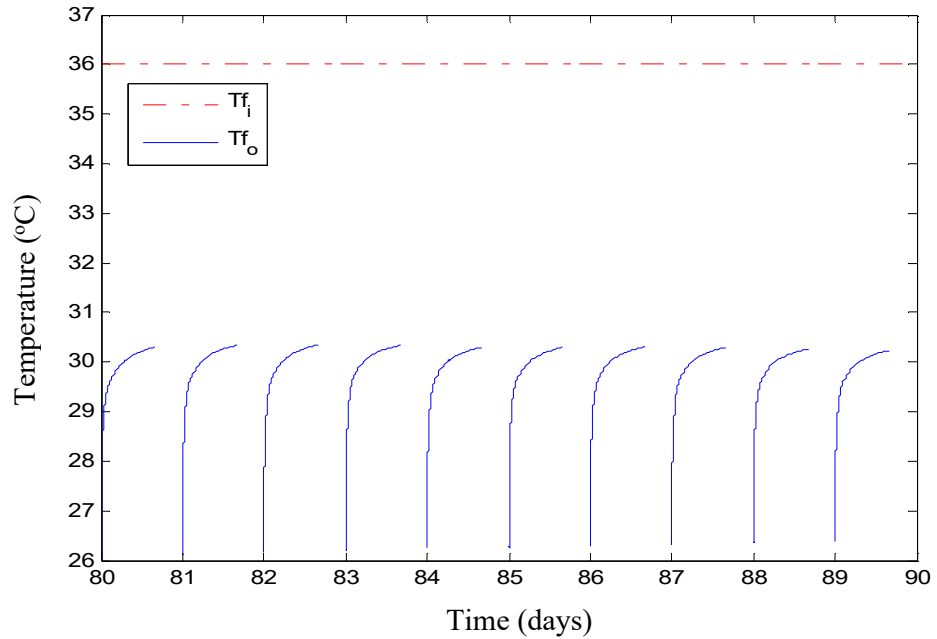
Figure 7.19: Fluid temperature of the GHEs in 10 consecutive days of February, under an intermittent mode (16 hours On and 8 hours Off daily), where the inlet fluid temperature = 36 ºC, fluid mass flow rate = 0.2 kg/s per unit of the GHE.

Figures 7.20 and 7.21 show the profile of soil temperature around the horizontal and vertical GHE, respectively, during the cooling operation in the summer. It shows, under the intermittent mode, the soil temperature is fluctuant. During the Off period, the heat accumulated in the surrounding soil, during the cooling, is diffused across the soil domain results in a temperature drop in the area adjacent to the GHE. It is observed that even though the recovery process occurs during the Off period, however, the soil cannot attain its initial temperature since the system is turned off for only 5 hours every day. This tendency causes the soil temperature to increase day by day. As shown in the figures that the soil temperature also varies with distances relative to the GHE. During the cooling, the indoor heat is delivered by the air conditioning system to the ground through the GHE causes the soil temperature to rise. As the heat flows from a high to a lower temperature, the soil that closer to the GHE has a relatively higher temperature than those at further distances. Different trends in soil temperature for both the horizontal and vertical GHE arrangement have been observed. Figure 7.20 illustrates the temperature of soil around the horizontal GHE at a depth of 1 m and distances of 0.04 m and 0.12 m from the centre of the pipe. It is noted, the soil temperature increased significantly in the first ten days of the cooling period. The soil with a low initial temperature absorbs the GHE's heat leads a quick increase in soil temperature. As the soil temperature approaches the temperature of working fluid (at a temperature above 33.5 ºC), the soil temperature begins to fluctuate as a response to ambient air temperature. It is noticed, the influence of atmospheric condition on the GHE performance is inevitably due to the burial depth of the horizontal GHE, as multiple modes of heat transfer

133

take place on the ground surface [33]. Figure 7.21 shows the soil temperature around the vertical GHE at a depth of 100 m and radius of 0.125 m and 0.225 m respectively. It shows, the soil temperature keeps increasing over the cooling period. The deterioration in soil temperature around the vertical GHE is hard to recover due to its burial depth. This condition is exacerbated with a relatively low soil thermal conductivity that resists the heat flow to the surface to take advantage of releasing heat to the atmosphere when the ambient temperature drops. In addition, the different observation points between the vertical and horizontal GHE also contributes to a different soil temperature response for both arrangements due to the distribution of temperature in the soil domain.

Figure7.20: Soil temperature around the horizontal GHE
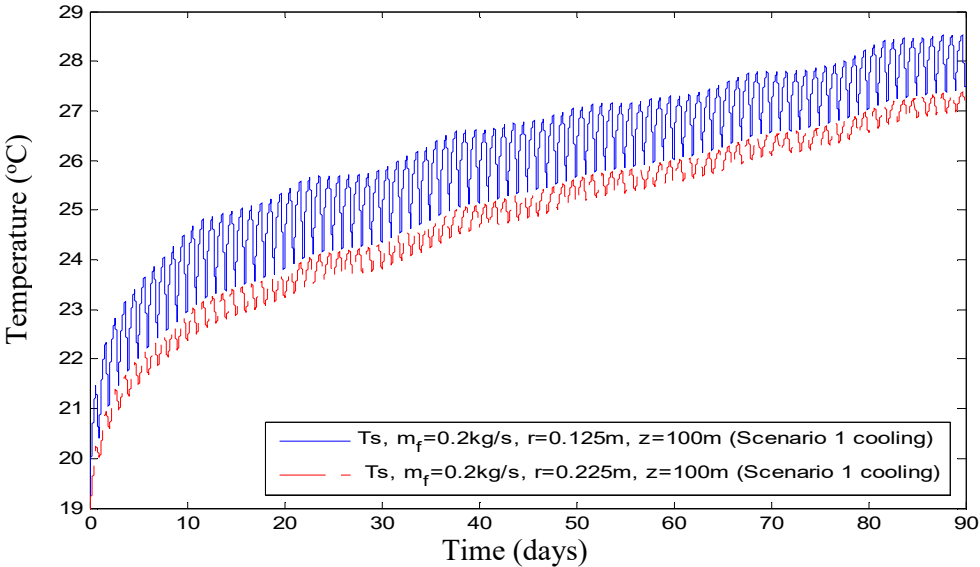
Figure7.21: Soil temperature around the vertical GHE

Figure 7.22 shows the energy consumption of the air conditioning systems of 20 units residential houses in Adelaide. The total energy consumed by the air conditioning systems under an intermittent mode, in three summer months, is estimated and presented in Figure 7.22. The energy consumption is obtained based on the sum of every hour results. It shows that the air-cooled condenser air conditioning systems (reference cycle) are less efficient than the water-cooled condenser air conditioning systems (the proposed scenario). The air-cooled air conditioning systems use the ambient air to carry the condenser's heat. As a result, substantial power is required by the air conditioners in order to remove the heat to the atmosphere, since the outdoor temperature is higher than that the indoor. As shown in Figure 7.22 that the water-cooled air conditioning systems (proposed scenario) consume 44% less energy than the reference air conditioning systems. In the proposed scenario, the reference air conditioning systems which are equipped with variable frequency compressors are modified to water-cooled condenser air conditioning systems and equipped with GHEs. The condenser's heat is carried by the working fluid of the GHEs and then transferred to the ground. The relatively lower temperature of the ground than the temperature of ambient air has contributed to a better performance of the air conditioning systems and a reduction in energy consumption. As shown in the figure that the CO_2 emission generated by the air conditioning systems is directly proportionate to the energy consumption. At an emission factor of 0.72 kg CO_2/kWhe [101], it yields a reduction in CO_2 emission corresponds to 44% for the proposed scenario during summer operation.
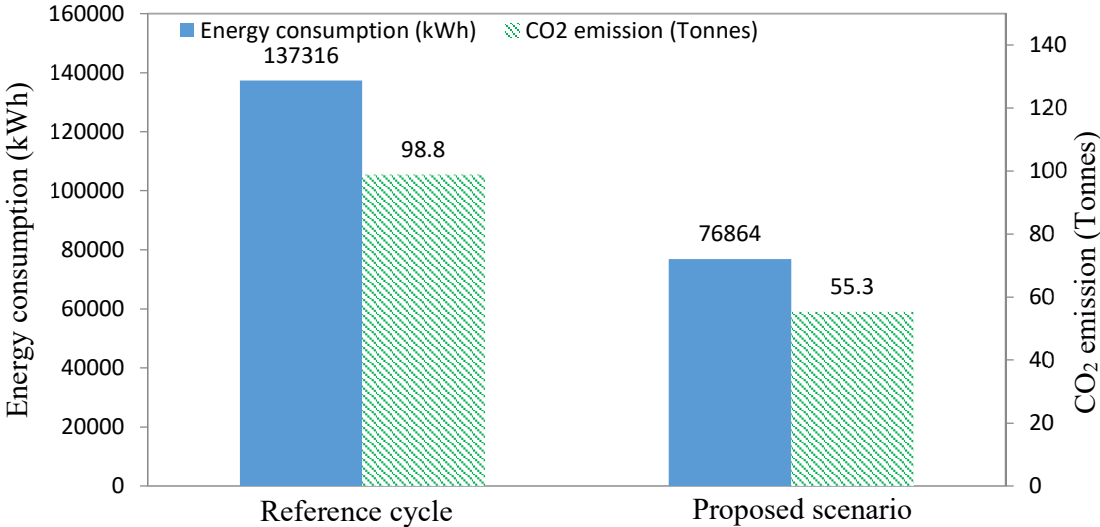
Figure 7.22: Energy consumption and CO_2 emission of twenty units of air conditioning systems, over three summer months, under an intermittent mode (16 hours On and 8 hours Off daily)

7.3.4.2 Heating

Figures 7.23-7.25 show the simulation results of the outlet water temperature of the GHEs in an intermittent mode (16 hours On and 8 hours Off daily) during heating period in winter (June-August). The simulation is performed considering the weather and soil condition as illustrated in Figures 7.1 and 7.3 and the input parameters as summarised in Tables 7.2 and 7.4. It is assumed, the deterioration of soil temperature during the cooling period has been fully recovered during the transition season when the heat pumps do not run. The outlet water temperature is presented in 10 days for each winter month namely, early of June (Figure 7.23), mid of July (Figure 7.24) and the end of August (Figure 7.25). During the heating, the working fluid at an inlet temperature of 6 °C enters the GHEs and extracts the soil heat, as the fluid flows along the GHEs, leads to a fluid temperature increase at the outlet. It is observed that the outlet water temperature drops deeply during early operation of the GHEs (see Figure 7.23). The relatively higher initial soil temperature enables the GHEs to extract more heat at the start up time. As the operation continues, the heat extraction rate of the GHEs decreases gradually due to a reduction in surrounding soil temperature. It is found that the performance of the GHEs declines over the operation period even though the GHEs operate in an intermittent mode. The relatively limited recovery period (5 hours of the system Off) hinders the GHEs to be completely recovered to its initial condition. As a result, the heat extraction capacity of the GHEs reduces day by day. Figure 7.24 shows that the decrease in outlet water temperature becomes tardy, at mid of winter, as the system nearly reaches the steady state. At the end of winter (see Figure 7.25), it is observed that the outlet water temperature of the GHEs drops to an approximated temperature of 10 °C, which corresponds to 4 °C water temperature difference at inlet and outlet
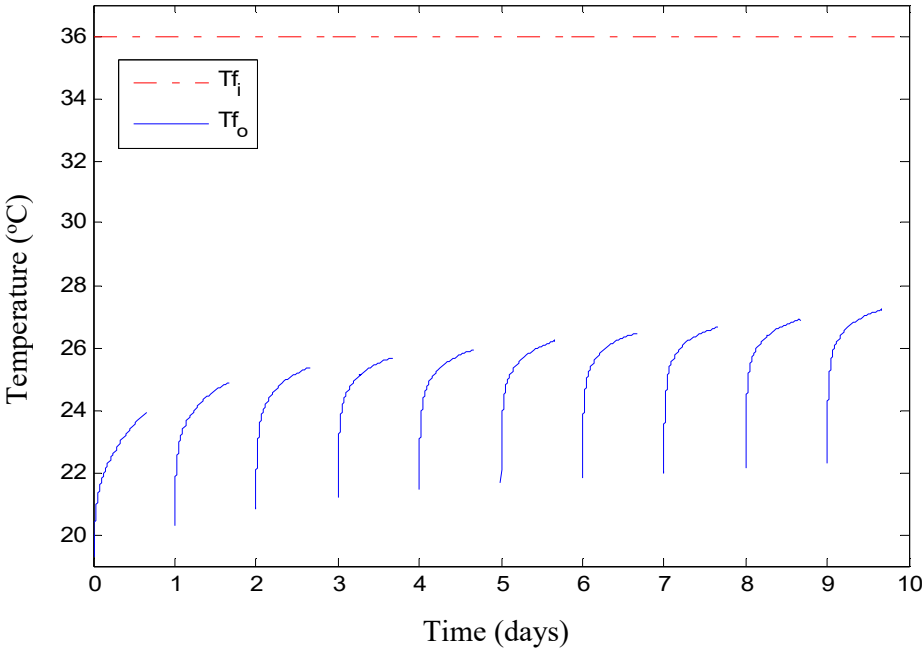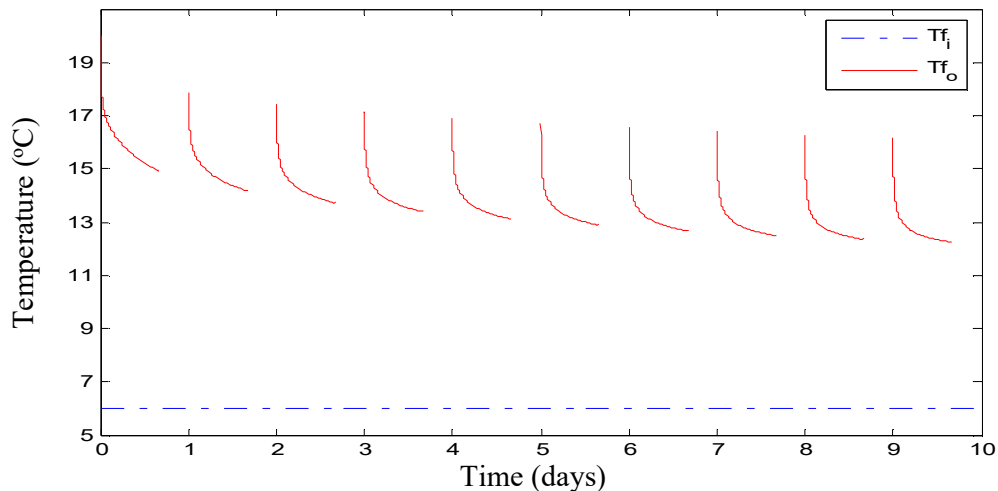

Figure 7.23: Fluid temperature of the GHEs in 10 consecutive days of June, under an intermittent mode (16 hours On and 5 hours Off every day), where the inlet fluid temperature = 6 °C, fluid mass flow rate = 0.2 kg/s per unit of the GHE
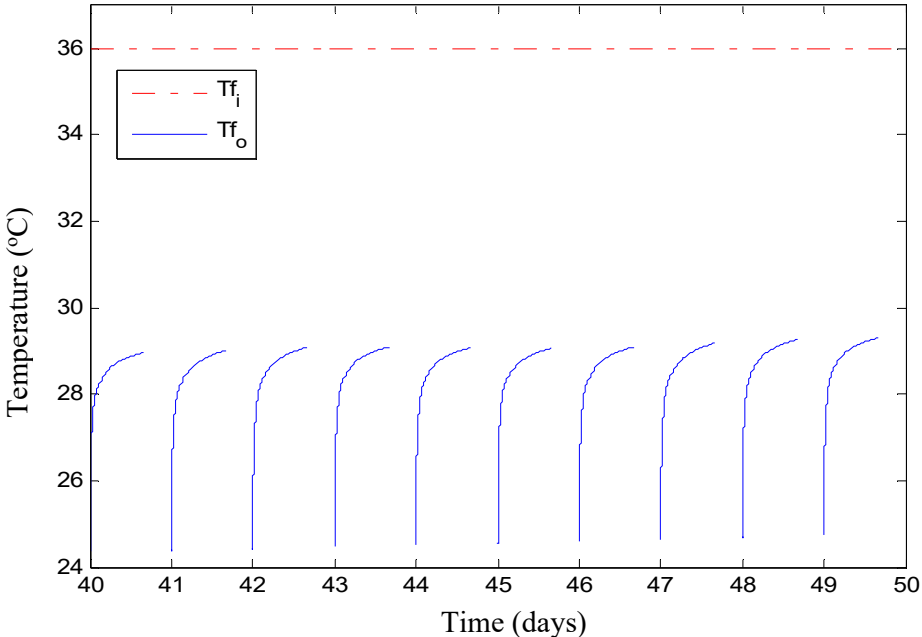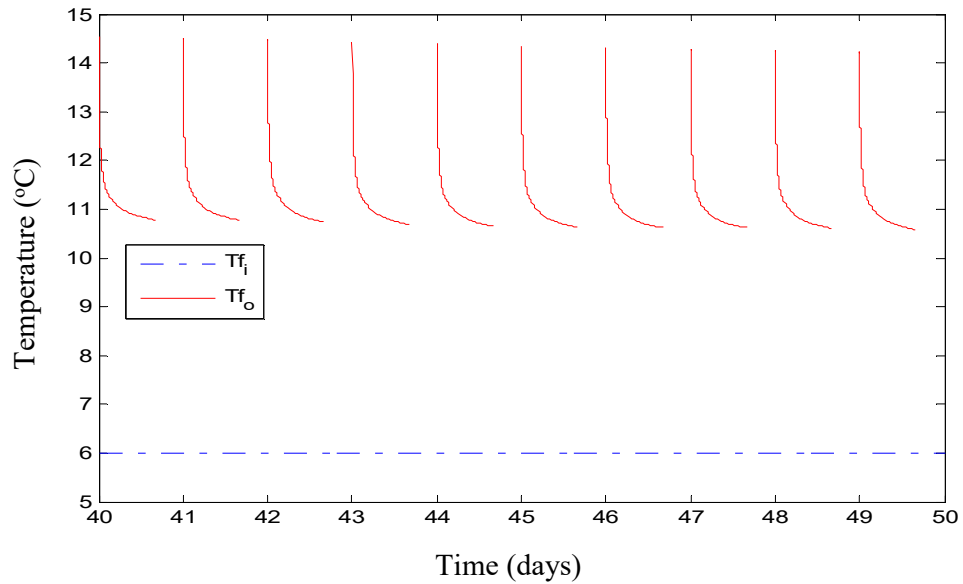
Figure 7.24: Fluid temperature of the GHEs in 10 consecutive days of July, under an intermittent mode (16 hours On and 5 hours Off daily), where the inlet fluid temperature = 6 ºC, fluid mass flow rate = 0.2 kg/s per unit of the GHE.
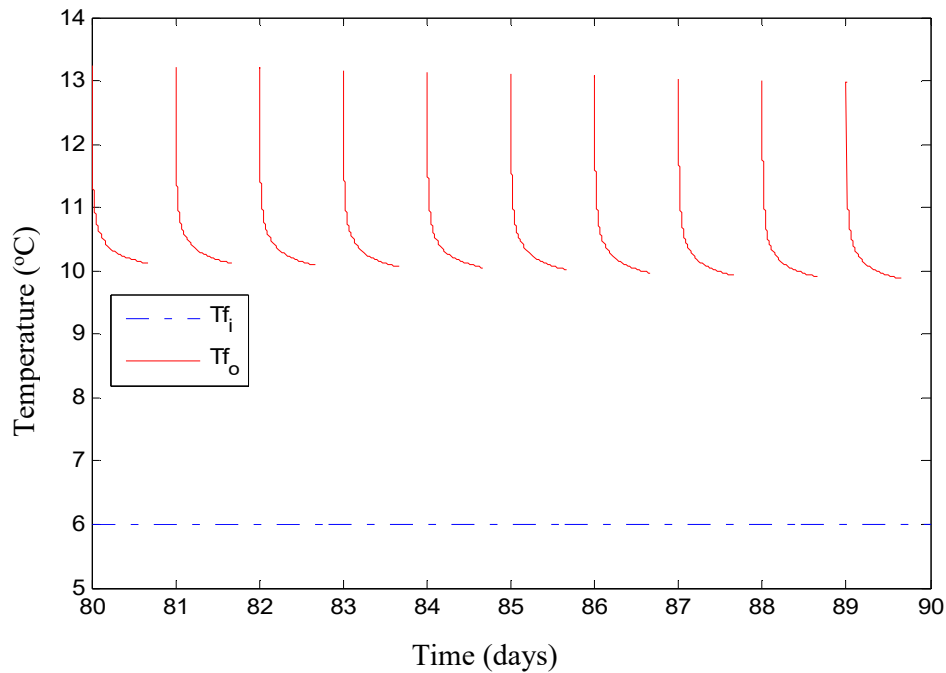
Figure 7.25: Fluid temperature of the GHEs in 10 consecutive days of August, under an intermittent mode (16 hours On and 5 hours Off daily), where the inlet fluid temperature = 6 ºC, fluid mass flow rate = 0.2 kg/s per unit of the GHE.

Figures 7.26 and 7.27 show the profile of soil temperature around the horizontal and vertical GHEs, respectively, subjected to the intermittent load of the heat pump in winter. During winter, the ground's heat is extracted by the GHE and then delivered by the heat pump into the room at a relatively higher temperature. As the process continues, the surrounding soil temperature decreases gradually. The closer to the GHE the greater the soil temperature drops. It is observed,

the soil temperature fluctuates under the intermittent mode. The soil temperature that deteriorates during the heating process is restored when the system Off, allowing the soil temperature to increase gradually as the heat at the far-field boundary is transferred to the area adjacent to the GHE. As pointed out in the figures, the soil temperature, however, declines over the time due to the cold accumulation in the surrounding soil cannot completely recover within 5 hours of the system Off. Figure 7.26 shows the temperature of soil around the horizontal GHE, at a depth of 1 m and distances of 0.04 m and 0.12 m, respectively, from the centre of the pipe. As illustrated in the figure, the soil temperature significantly decreases during early operation of the GHE as the soil, which initially has a relatively high temperature, exchanges its heat with the GHE. The soil temperature becomes relatively stable when the operation time exceeds about 21 days. It is observed, the influence of the ambient air is being significant when the soil temperature approaches the temperature of the working fluid. From the figure, it can be concluded that the soil around the horizontal GHE may relatively easy to lose its heat as the ground heat is not only extracted by the GHE but also exchanged with the atmosphere. Figure 7.27 shows the soil temperature around the vertical GHE at a depth of 100 m and radius of 0.125 m and 0.225 m respectively. Different from that the horizontal GHE, it shows that the soil temperature around the vertical GHE keeps decreasing until the end of summer. It seems taking longer time for the soil temperature to keep going down before reaching the steady state condition. This behaviour is affected by the relatively stable soil temperature deep down below the surface allows the vertical GHE to perform better than that the horizontal arrangement [3].
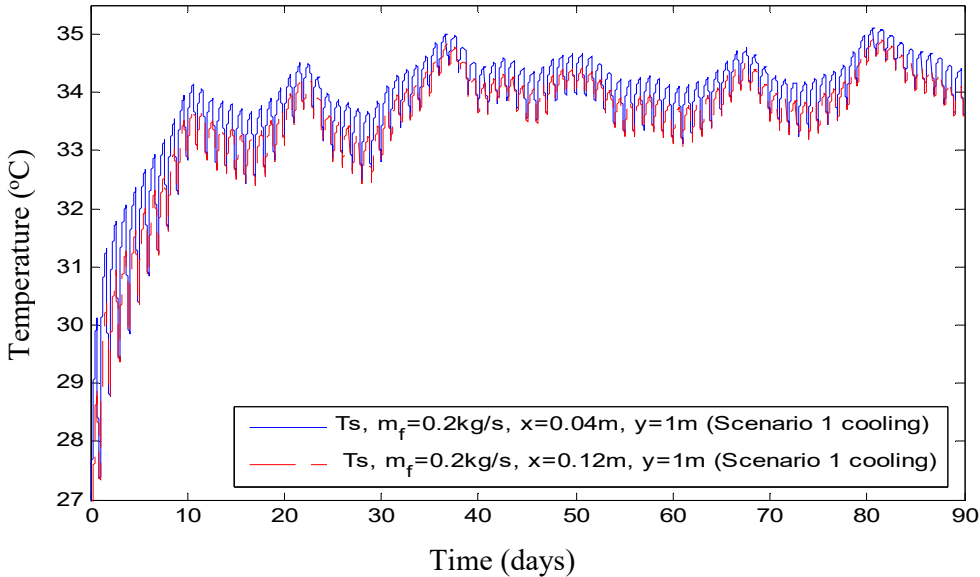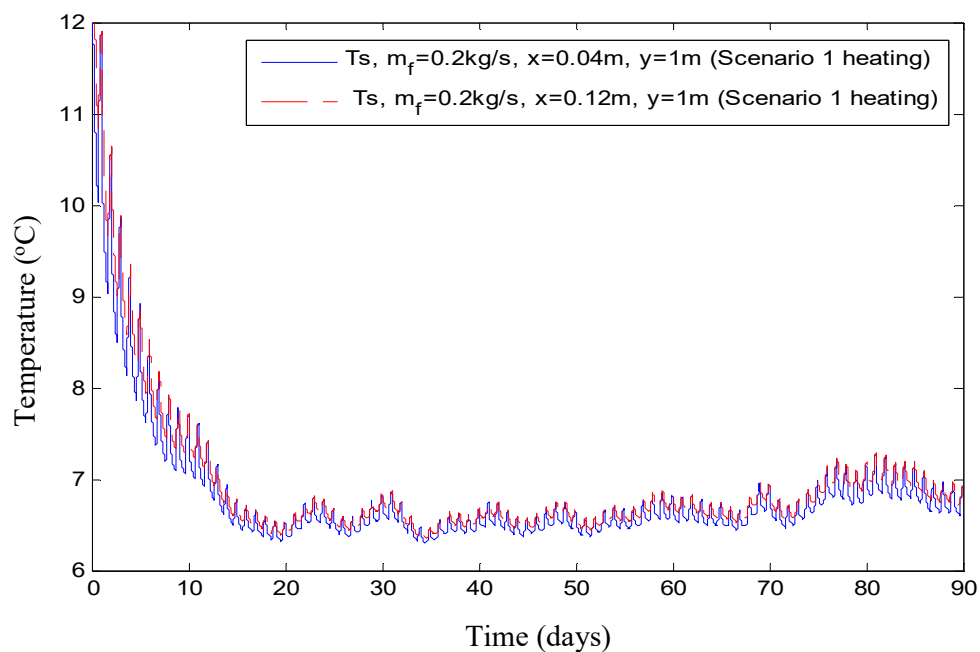

Figure7.26: Soil temperature around the horizontal GHE
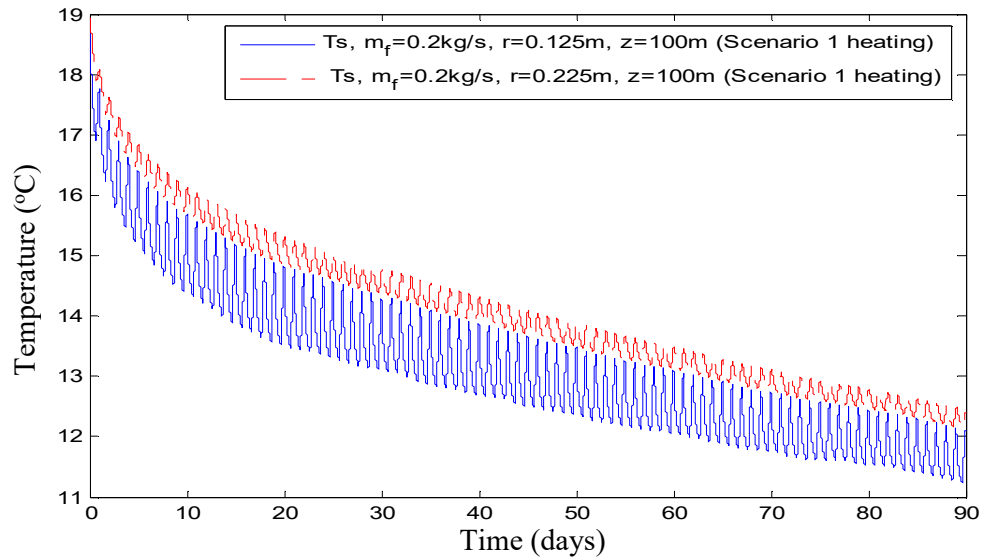
Figure7.27: Soil temperature around the vertical GHE

Figure 7.28 illustrates the energy consumption and CO_2 emission of the heat pumps used to provide heating for twenty unit residential houses, during winter (June-August), in Adelaide. The heat pumps are operated in an intermittent mode (16 hours On and 5 hours Off daily). As pointed out in the figure that the ground source heat pumps (proposed scenario) consume 29.3% less energy than the reference cycle. The ground source heat pumps owe its better performance on the relatively higher temperature of the ground than the atmosphere during winter. This relatively higher soil temperature permits the heat pumps to work efficiently. As a result, less electrical energy is needed by the heat pumps in order to satisfy the same condition of the heating load. It is found that operating the ground source heat pump has cut 13.1 tonnes of CO_2 emission, corresponds to a 29.3% reduction in CO_2 emission, at an emission factor of 0.72 kg CO_2/kWhe [101]. This study shows that for the same heating load, the use of the ground source heat pump leads to electricity and CO_2 savings.
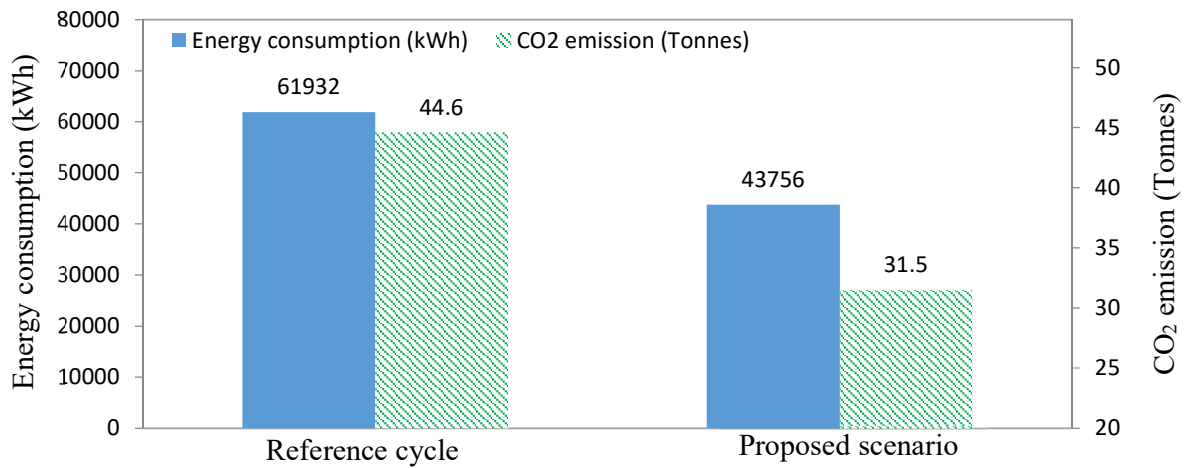
Figure 7.28: Energy consumption and CO_2 emission of twenty units of heat pumps, over three winter months, under an intermittent mode (16 hours On and 8 hours Off daily)

Figure 7.29 shows the total energy consumption and CO_2 emission of twenty units of air conditioning systems (heat pumps), operated intermittently (16 hours On and 8 hours Off daily) in winter (3 months) and summer (3 months). It shows the reference cycle air conditioning systems (heat pumps) consume 39.4% more electricity than the ground source air conditioning systems/heat pumps during both cooling and heating. It is observed, the energy consumed during the cooling is dominant than that during the heating. In which, 68.9% out of total energy is used for cooling while the rest is for heating. As shown in the figure, the total energy consumed by the ground source air conditioning systems (heat pumps) is significantly reduced, corresponding to a 39.4% of energy saving. The reduction in the energy consumption also gives a 39.4% saving of CO_2 emission. This result indicates that energy efficiency of the air conditioning systems (heat pumps) can significantly increase by coupling them with GHEs.
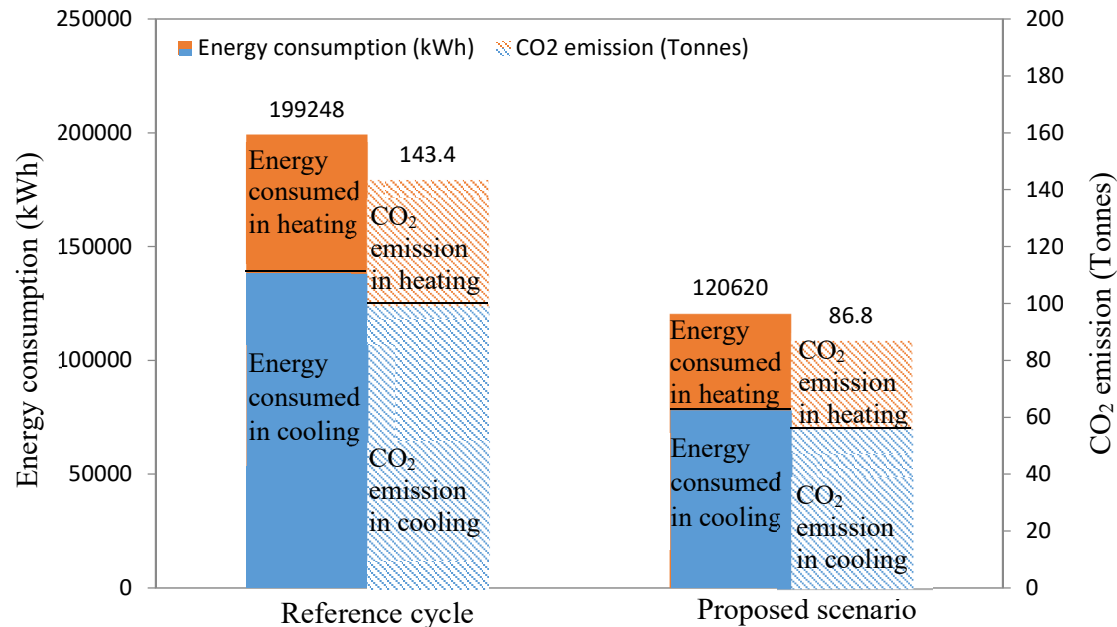
Figure 7.29: Total energy consumption and CO_2 emission of twenty units of air conditioning systems (heat pumps), over winter and summer months, under an intermittent mode (16 hours On and 8 hours Off daily)

7.4 Summary

The potential applications of GHEs in two hypothetical cases, i.e. Terminal 1 building, Adelaide airport and twenty residential houses in Adelaide have been presented. In case I, three scenarios are proposed for the existing/reference chiller which operates at Terminal 1 building including: (1) replacing the cooling tower with GHEs, (2) installing half number of GHEs and a small cooling tower, and (3) installing half numbers of GHEs only with increasing the fluid mass flow rate in each unit of GHE. The chiller is simulated under intermittent mode in three consecutive summer months, from December to February. The results show the chillers with scenarios 1 and 2 gain the energy savings significantly at the beginning operation of the chiller. These

energy savings, however, decrease over the time as the soil temperature around the GHEs is built up. It is noticed, the chillers with scenarios 1 and 2 cannot longer compete with the reference chiller when the operation time exceeds about 70 days. Overall, the chillers with scenarios 1 and 2 consume more energy than the reference cycle. The chiller with scenario 3 is nonviable, as it consumes more energy than the reference cycle even during the beginning operation of the chiller. It shows, the chillers with the proposed scenarios are difficult to compete with the reference chiller that is equipped with a cooling tower in energy term. Case study II is based on the air conditioning systems (heat pumps) installed in twenty units of residential houses in Adelaide. In this case study, the air-cooled condenser (air heated evaporator for the heat pump) of every air condition systems is modified to a water-cooled condenser (water heated evaporator) and the cooling (heating) water is supplied by a central GHE system. The performance of the heat pumps (in winter months) and air conditioning system (in summer months) under intermittent operation is presented. It shows that the ground source air conditioning systems (heat pumps) save 44% and 29.3 % of energy during cooling and heating, respectively. These correspond to a 39.4 % saving of total energy consumption and CO_2 emission during both processes.

CHAPTER 8

CONCLUSIONS

The main motivations of the present work are to introduce a combined horizontal-vertical GHE in order to synergy the benefits of the two configurations and negate their disadvantages. In addition, in order to optimise its design and operations, the thermo-dynamic performance of the combined GHE considering various loads and weather/soil conditions was studied using the separately validated horizontal and vertical GHE models as demonstrated in Chapters 4 and 5.

This chapter summarises the outcomes of the research works and the key findings with respect to the project aim and objectives. It concludes with the potential areas for further research to extend this study.

8.1 Outcomes

This thesis has developed new models for the horizontal, vertical, and combined structure GHEs. A new approach was developed and used to model soil temperature fluctuations during seasonal changes. It is based on an internal heat source term, which was incorporated into GHE models. The solutions of the GHE models were obtained using the explicit finite difference method. A computer program using MATLAB as a programming language was developed in order to provide numerical results of the performance of the GHEs. The models have also been validated using custom-built GHE test rigs. Based on the separately validated horizontal and vertical GHE models, the models then were integrated to perform the simulation of combined structure GHEs considering five operational modes. The sensitivity analysis for the horizontal, vertical and combined structure GHEs was carried out in order to understand the effect of technical parameters on the performance of the those GHE arrangements. Then, the potential application of the combined horizontal-vertical GHEs to assist the operation of air conditioning systems (heat pumps) was demonstrated through two case studies namely, based on Terminal 1 building Adelaide airport and twenty three-storey houses development in Adelaide.

8.2 Main findings

Through extensive simulations using the developed GHE models, the main findings of this study can be summarised as follows:

8.2.1 Development of the horizontal GHE model

The mathematical model of the horizontal GHE has been validated by comparing the theoretical and experimental results of both the soil and the outlet fluid temperatures. The results show that

the theoretical results are in a good agreement with the experimental data. It was observed, by introducing an internal heat source term, the accuracy of the soil temperature simulation has been improved by 1%. While, the accuracy of the outlet water temperature simulation has also been improved even though not significant. The sensitivity analysis was conducted using the validated model to investigate the effects of the pipe length, fluid flow rate, inlet fluid temperature and burial depth. The simulation results reveal that the pipe length of the GHE has the greatest impact on the performance of the GHE. Increasing the pipe length means expanding the heat transfer area, results in more heat to flow from the working fluid to the surrounding soil and vice versa. The inlet water temperature also has a significant effect on the performance of the GHE. The GHE with a higher inlet water temperature generates a higher water temperature difference between inlet and outlet. This tendency is due to the relatively higher the gradient temperature between the working fluid and surrounding soil, thus, it permits more heat to be exchanged. The performance of the GHE is also affected by the fluid mass flow rate. However, this effect is not as significant as those the pipe length and inlet water temperature, since the heat transfer rate of the GHE does not increase linearly with the increase of mass flow rate due to a quick increase in surrounding soil temperature. In addition, the burial depth has less effect on the GHE performance. The reason may be that the GHE was operated across a relatively short time period. The outcomes of this work were published in *Applied Energy* journal (see Appendix I).

8.2.2 Development of the vertical GHE model

It has been proved that the accuracy of the vertical GHE model could be improved by the introduction of the heat source term. This is reflected by the maximum relative error for the soil temperature generated by the model that incorporates and neglects the internal heat source term namely, 3.7% and 14%, respectively. The performance of the vertical GHE under different borehole thermal conductivity, borehole depth, fluid flow rate, type of carrier fluid, as well as continuous and intermittent operations, was investigated using the validated model. It is obtained that the borehole depth significantly affects the performance of the vertical GHE. A larger thermal contact enables the working fluid to exchange more heat with the surrounding soil. The performance of the GHE can be improved by using a grout material which has a relatively higher thermal conductivity, such as sand bentonite mixture. In addition, the nanofluid 3%TiO_2 could be used as the carrier fluid to enhance the thermal performance of the GHE. Besides, running the GHE intermittently might be an option as it can mitigate the deterioration of soil thermal condition.

8.2.3 Combined horizontal-vertical GHE

The main findings, which follow from the calculations, are summarised as follows:

a) With the same length of the pipe system, the vertical GHE can release more energy than the horizontal GHE, as the initial soil temperature (in summer) at a deeper layer is lower than that at a shallow region;

b) When the GHE operates in combined modes, the amount of energy released by the GHE is increased, as the contact area, where heat is exchanged with the surrounding soil, is increased;

c) The series operations (horizontal to vertical or vertical to horizontal) of the GHE can release more energy than can be done in the split mode. The difference in the fluid velocity in the split and series modes contributes to the difference of amount of energy released by the GHE;

d) The intermittent operation of the GHE may be conducted to cope with cyclic thermal loading. The intermittent operation can benefit the performance of the GHE as the degradation of the ground temperature during the operation of the GHE is largely recovered during the Off time of the system.

e) In the split flow mode, the ratio of the fluid mass flow rate does not significantly affect the amount of energy released by the GHE. The GHE with a ratio of mass flow rate of 40% horizontal and 60% vertical releases the highest amount of energy in the split flow operation mode.

f) Climate conditions have a significant effect on the GHE's performance. The GHE installed in a temperate climate, corresponding to Adelaide's conditions, can release more energy than the same installation located in a sub-tropical climate, such as Brisbane. This is due to the difference in the initial soil temperature and climate conditions.

g) Increasing the fluid mass flow rate can enhance the amount of energy released by the GHE as the fluid mass flow rate affects the coefficient of the convective heat transfer of the working fluid.

8.2.4 Case studies

Two case studies have been presented, one is based on Terminal 1 building Adelaide airport, and the other is based on twenty three-storey houses development in Adelaide. The findings from the case studies are summarised as follows:

a) Case I basically uses GHEs to replace a cooling tower. The study shows that the chillers with scenarios 1 and 2 save 12.9 % and 6.5% energy respectively, at the beginning

cooling operation. However, these energy savings gradually decrease due to the deterioration of soil temperature during the operation period, and all proposed scenarios are no longer technically viable at the end of summer as the chiller consumes more energy than the reference cycle.

b) Case II: Using water out of GHEs to replace air to cool the condensers of the split air conditioning systems for cooling (to heat the evaporator of the heat pumps for heating) has yielded significant energy and CO2 savings. In which, the air conditioning systems save 44% of energy during summer, while the heat pumps reduce 29.3% of the energy consumption during winter. These correspond to a 39.4% reduction in energy consumption and CO_2 emission for a whole year.

c) The results of the case studies indicate the GHEs are good for current air-cooled air condition systems (air source heat pumps). However, they are less attractive for the water-cooled systems, i.e. the system with the cooling tower.

8.3 Future work

As pointed out in Chapter 4 that the burial depth does not significantly affect the horizontal GHE performance in the short run. Since the subsurface temperature is influenced by both diurnal and seasonal climate conditions, a further study on the effect of burial depth of the GHE on its long-term operational performance is required. Therefore, an optimum burial depth can be specified. For instance, during the cooling period, when air conditioning systems are operated in summer and the GHE is heating up the surrounding soil. It is expected, an optimum depth of the GHE can mitigate the effect of the ambient air, on the performance of the GHE, in the daytime when the outdoor temperature is high. In addition, it allows the accumulated heat in the soil domain, during operation of the GHE, to be transferred to the atmosphere when the ambient temperature drop at nighttime. Furthermore, in the case study I, the performance of the cooling tower of the reference cycle was assumed constant. In fact, the cooling tower performance depends on weather conditions. Thus, further study is required to assess the energy consumption and CO_2 emission of the chiller considering the transient performance of the cooling tower. Moreover, the effect of groundwater on the performance of the combined horizontal-vertical GHE should be investigated. The existence of groundwater could improve the heat transfer in the soil domain. As a result, the GHE dimension can be minimised.

REFERENCES

[1] B. Sanner, C. Karytsas, D. Mendrinos, and L. Rybach, "Current status of ground source heat pumps and underground thermal energy storage in Europe," *Geothermics,* vol. 32, pp. 579-588, 2003.

[2] G. Florides and S. Kalogirou, "Ground heat exchangers—A review of systems, models and applications," *Renewable Energy,* vol. 32, pp. 2461-2478, 2007.

[3] R. Al-Khoury, *Computational modeling of shallow geothermal systems*. Leiden, Netherlands: Taylor & Francis, 2012.

[4] G. A. Florides, P. Christodoulides, and P. Pouloupatis, "Single and double U-tube ground heat exchangers in multiple-layer substrates," *Applied Energy,* vol. 102, pp. 364-373, 2013.

[5] S. K. Kim, G. O. Bae, K. K. Lee, and Y. Song, "Field-scale evaluation of the design of borehole heat exchangers for the use of shallow geothermal energy," *Energy,* vol. 35, pp. 491-500, 2010.

[6] Y. Wu, G. Gan, R. G. Gonzalez, A. Verhoef, and P. L. Vidale, "Prediction of the thermal performance of horizontal-coupled ground-source heat exchangers," *International Journal of Low-Carbon Technologies,* vol. 6, pp. 261-269, 2011.

[7] P. M. Congedo, G. Colangelo, and G. Starace, "CFD simulations of horizontal ground heat exchangers: A comparison among different configurations," *Applied Thermal Engineering,* vol. 33–34, pp. 24-32, 2012.

[8] M. de Moel, P. M. Bach, A. Bouazza, R. M. Singh, and J. O. Sun, "Technological advances and applications of geothermal energy pile foundations and their feasibility in Australia," *Renewable and Sustainable Energy Reviews,* vol. 14, pp. 2683-2696, 2010.

[9] H. J. G. Diersch, D. Bauer, W. Heidemann, W. Rühaak, and P. Schätzl, "Finite element modeling of borehole heat exchanger systems. Part 2. Numerical simulation," *Computers and Geosciences,* vol. 37, pp. 1136-1147, 2011.

[10] S. Gehlin, "Thermal response test: Method development and evaluation," Doctoral thesis, Environmental Engineering, Lulea University of Technology, Sweden, 2002.

[11] B. Dally and G. Nathan, "Shallow underground cooling for efficient thermal cycles: Experimental verification," The University of Adelaide, Final report TIG 6.2, 2011.

[12] H. Fujii, K. Nishi, Y. Komaniwa, and N. Chou, "Numerical modeling of slinky-coil horizontal ground heat exchangers," *Geothermics,* vol. 41, pp. 55-62, 2012.

[13] P. R. T. Ltd. (2016, 9 June 2016). *Ground source heat pumps*. Available: http://phoenixecoenergy.co.uk/products/ground-source-heat-pumps

[14] G. Florides and S. Kalogirou, "Ground heat exchangers - A review of systems, models and applications," *Renewable Energy,* vol. 32, pp. 2461-2478, Dec 2007.

[15] S. J. Self, B. V. Reddy, and M. A. Rosen, "Geothermal heat pump systems: Status review and comparison with other heating options," *Applied Energy,* vol. 101, pp. 341-348, 2013.

[16] A. Mustafa Omer, "Ground-source heat pumps systems and applications," *Renewable and Sustainable Energy Reviews,* vol. 12, pp. 344-371, 2008.

[17] M. M. Sorour, "Thermal-Conductivity and Diffusivity of Soil," *International Communications in Heat and Mass Transfer,* vol. 17, pp. 189-199, 1990.

[18] N. H. Abu-Hamdeh and R. C. Reeder, "Soil Thermal Conductivity Effects of Density, Moisture, Salt Concentration, and Organic Matter," *Soil Science Society of America Journal,* vol. 64, pp. 1285-1290, 2000.

[19] K. A. Alnefaie and N. H. Abu-Hamdeh, "Specific heat and volumetric heat capacity of some saudian soils as affected by moisture and density," in *International Conference on Mechanics, Fluids, Heat, Elasticity and Electromagnetic Fields*, 2013.

[20]   S. A. Baggs, "Remote prediction of ground temperature in australian soils and mapping its distribution," *Solar Energy,* vol. 30, pp. 351-366, 1983.

[21]   H. Esen, M. Inalli, and M. Esen, "Numerical and experimental analysis of a horizontal ground-coupled heat pump system," *Building and Environment,* vol. 42, pp. 1126-1134, 2007.

[22]   H. Demir, A. Koyun, and G. Temir, "Heat transfer of horizontal parallel pipe ground heat exchanger and experimental verification," *Applied Thermal Engineering,* vol. 29, pp. 224-233, 2009.

[23]   A. Rezaei-Bazkiaei, E. Dehghan-Niri, E. M. Kolahdouz, A. S. Weber, and G. F. Dargush, "A passive design strategy for a horizontal ground source heat pump pipe operation optimization with a non-homogeneous soil profile," *Energy and Buildings,* vol. 61, pp. 39-50, 2013.

[24]   A. Rezaei B, E. M. Kolahdouz, G. F. Dargush, and A. S. Weber, "Ground source heat pump pipe performance with Tire Derived Aggregate," *International Journal of Heat and Mass Transfer,* vol. 55, pp. 2844-2853, 2012.

[25]   C. Han, K.M. Ellett, S. Naylor, X. Yu, "Influence of local geological data on the performance of horizontal ground-coupled heat pump system integrated with building thermal loads," *Renewable Energy,* vol. 113, pp.1046-1055, 2017.

[26]   C. S. A. Chong, G. Gan, A. Verhoef, R. G. Garcia, and P. L. Vidale, "Simulation of thermal performance of horizontal slinky-loop heat exchangers for ground source heat pumps," *Applied Energy,* vol. 104, pp. 603-610, 2013.

[27]   H. Fujii, S. Yamasaki, T. Maehara, T. Ishikami, and N. Chou, "Numerical simulation and sensitivity study of double-layer Slinky-coil horizontal ground heat exchangers," *Geothermics,* vol. 47, pp. 61-68, 2013.

[28]   Z. Xiong, D. E. Fisher, and J. D. Spitler, "Development and validation of a Slinky™ ground heat exchanger model," *Applied Energy,* vol. 141, pp. 57-69, 2015.

[29]   G.-H. Go, S.-R. Lee, N. N.V, and S. Yoon, "A new performance evaluation algorithm for horizontal GCHPs (ground coupled heat pump systems) that considers rainfall infiltration," *Energy,* vol. 83, pp. 766-777, 2015.

[30]   L. Xing, J. R. Cullin, J. D. Spitler, P. Im, and D. E. Fisher, "Foundation heat exchangers for residential ground source heat pump systems-Numerical modeling and experimental validation," HVAC&R Research, vol. 17, pp. 1059-1074, 2011.

[31]   E. S. Lee, D. E. Fisher, and J. D. Spitler, "Efficient Horizontal Ground Heat Exchanger Simulation with Zone Heat Balance Integration," *HVAC&R Research,* vol. 19, pp. 307-323, 2013.

[32]   Y. Nam and H.-B. Chae, "Numerical simulation for the optimum design of ground source heat pump system using building foundation as horizontal heat exchanger," *Energy,* vol. 73, pp. 933-942, 2014.

[33]   G. Gan, "Dynamic thermal modelling of horizontal ground-source heat pumps," *International Journal of Low-Carbon Technologies,* vol.8, pp. 95-105, 2013.

[34]   K. Kupiec, B. Larwa, and M. Gwadera, "Heat transfer in horizontal ground heat exchangers," *Applied Thermal Engineering,* vol. 75, pp. 270-276, 2015.

[35]   G. Florides, E. Theofanous, I. Iosif-Stylianou, S. Tassou, P. Christodoulides, Z. Zomeni, E. Tsiolakis, S. Kalogirou, V. Messaritis, P. Pouloupatis, and G. Panayiotou, "Modeling and assessment of the efficiency of horizontal and vertical ground heat exchangers," *Energy,* vol. 58, pp. 655-663, 2013.

[36]   P. O. Fontaine, D. Marcotte, P. Pasquier, and D. Thibodeau, "Modeling of horizontal geoexchange systems for building heating and permafrost stabilization," *Geothermics,* vol. 40, pp. 211-220, 2011.

[37]   M. J. Kim, S. R. Lee, S. Yoon, J. S. Jeon, " An applicable design method for horizontal spiral-coil-type ground heat exchangers," *Geothermics,* vol. 72, pp. 338-347, 2018.

[38]   S. Kavanaugh and K. Rafferty, *Ground-source Heat Pumps: Design of Geothermal Systems for Commercial and Institutional Buildings*. USA: ASHRAE, 1997.

[39]   S. Sanaye and B. Niroomand, "Horizontal ground coupled heat pump: Thermal-economic modeling and optimization," *Energy Conversion and Management,* vol. 51, pp. 2600-2612, 2010.

[40]   N. Kayaci, and H. Demir, "Long time performance analysis of ground source heat pump for space heating and cooling applications based on thermo-economic optimization criteria," *Energy and Buildings,* vol. 163, pp. 121-139, 2018.

[41]   M. Bottarelli, M. Bortoloni, and Y. Su, "Heat transfer analysis of underground thermal energy storage in shallow trenches filled with encapsulated phase change materials," *Applied Thermal Engineering,* vol. 90, pp. 1044-1051, 2015.

[42]   M. Bottarelli, M. Bortoloni, Y. Su, C. Yousif, A. A. Aydın, and A. Georgiev, "Numerical analysis of a novel ground heat exchanger coupled with phase change materials," *Applied Thermal Engineering,* vol. 88, pp. 369-375, 2015.

[43]   M. Bortoloni and M. Bottarelli, "On the sizing of a flat-panel ground heat exchanger," *International Journal of Energy and Environmental Engineering,* vol. 6, pp. 55-63, 2015.

[44]   N. Pandey, K. Murugesan, H.R. Thomas, "Optimization of ground heat exchangers for space heating and cooling applications using Taguchi method and utility concept," *Applied Energy,* vol. 190, pp. 421-438, 2017.

[45]   Z. Li and M. Zheng, "Development of a numerical model for the simulation of vertical U-tube ground heat exchangers," *Applied Thermal Engineering,* vol. 29, pp. 920-924, 2009.

[46]   C. Han, and X. Yu, "Feasibility of geothermal heat exchanger pile-based bridge deck snow melting system: A simulation based analysis," *Renewable Energy,* vol. 101, pp.214-224, 2017.

[47]   C. Han, and X. Yu, "An innovative energy pile technology to expand the viability of geothermal bridge deck snow melting for different United States regions: Computational assisted feasibility analyses," *Renewable Energy,* vol. 123, pp.417-427, 2018.

[48]   S. Chen, J. Mao, F. Chen, P. Hou, Y. Li, "Development of ANN model for depth prediction of vertical ground heat exchanger," *International Journal of Heat and Mass Transfer,* vol. 117, pp.617-626, 2018.

[49]   R. Al-Khoury and P. G. Bonnier, "Efficient finite element formulation for geothermal heating systems. Part II: Transient," *International Journal for Numerical Methods in Engineering,* vol. 67, pp. 725-745, 2006.

[50]   C. K. Lee and H. N. Lam, "Computer simulation of borehole ground heat exchangers for geothermal heat pump systems," *Renewable Energy,* vol. 33, pp. 1286-1296, 2008.

[51]   C. K. Lee, "Effects of multiple ground layers on thermal response test analysis and ground-source heat pump simulation," *Applied Energy,* vol. 88, pp. 4405-4410, 2011.

[52]   C. K. Lee and H. N. Lam, "A modified multi-ground-layer model for borehole ground heat exchangers with an inhomogeneous groundwater flow," *Energy,* vol. 47, pp. 378-387, 2012.

[53]   E.-J. Kim, J.-J. Roux, M. A. Bernier, and O. Cauret, "Three-dimensional numerical modeling of vertical ground heat exchangers: Domain decomposition and state model reduction," *HVAC&R Research,* vol. 17, pp. 912-927, 2011.

[54]   S. J. Rees, "An extended two-dimensional borehole heat exchanger model for simulation of short and medium timescale thermal response," *Renewable Energy,* vol. 83, pp. 518-526, 2015.

[55]   J. Wang, E. Long, and W. Qin, "Numerical simulation of ground heat exchangers based on dynamic thermal boundary conditions in solid zone," *Applied Thermal Engineering,* vol. 59, pp. 106-115, 2013.

[56]   M. H. Sharqawy, E. M. Mokheimer, and H. M. Badr, "Effective pipe-to-borehole thermal resistance for vertical ground heat exchangers," *Geothermics,* vol. 38, pp. 271-277, 2009.

[57]   B. Bouhacina, R. Saim, and H. F. Oztop, "Numerical investigation of a novel tube design for the geothermal borehole heat exchanger," *Applied Thermal Engineering,* vol. 79, pp. 153-162, 2015.

[58]   Y. Shang, S. Li, and H. Li, "Analysis of geo-temperature recovery under intermittent operation of ground-source heat pump," *Energy and Buildings,* vol. 43, pp. 935-943, 2011.

[59]   M. De Carli, M. Tonon, A. Zarrella, and R. Zecchin, "A computational capacity resistance model (CaRM) for vertical ground-coupled heat exchangers," *Renewable Energy,* vol. 35, pp. 1537-1550, 2010.

[60]   A. Zarrella, M. Scarpa, and M. De Carli, "Short time step analysis of vertical ground-coupled heat exchangers: The approach of CaRM," *Renewable Energy,* vol. 36, pp. 2357-2367, 2011.

[61]   A. Zarrella and P. Pasquier, "Effect of axial heat transfer and atmospheric conditions on the energy performance of GSHP systems: A simulation-based analysis," *Applied Thermal Engineering,* vol. 78, pp. 591-604, 2015.

[62]   F. J. G. Gallero, I. R. Maestre, P. Á. Gómez, and J. L. F. Blázquez, "Numerical and experimental validation of a new hybrid model for vertical ground heat exchangers," *Energy Conversion and Management,* vol. 103, pp. 511-518, 2015.

[63]   F. Lei, P. Hu, N. Zhu, and T. Wu, "Periodic heat flux composite model for borehole heat exchanger and its application," *Applied Energy,* vol. 151, pp. 132-142, 2015.

[64]   J. A. Rivera, P. Blum, and P. Bayer, "Ground energy balance for borehole heat exchangers: Vertical fluxes, groundwater and storage," *Renewable Energy,* vol. 83, pp. 1341-1351, 2015.

[65]   J. A. Rivera, P. Blum, and P. Bayer, "Analytical simulation of groundwater flow and land surface effects on thermal plumes of borehole heat exchangers," *Applied Energy,* vol. 146, pp. 421-433, 2015.

[66]   W. Zhang, H. Yang, L. Lu, and Z. Fang, "Investigation on influential factors of engineering design of geothermal heat exchangers," *Applied Thermal Engineering,* vol. 84, pp. 310-319, 2015.

[67]   X. Q. Zhai, M. Qu, X. Yu, Y. Yang, and R. Z. Wang, "A review for the applications and integrated approaches of ground-coupled heat pump systems," *Renewable and Sustainable Energy Reviews,* vol. 15, pp. 3133-3140, 2011.

[68]   L. Dai, S. Li, L. DuanMu, X. Li, Y. Shang, and M. Dong, "Experimental performance analysis of a solar assisted ground source heat pump system under different heating operation modes," *Applied Thermal Engineering,* vol. 75, pp. 325-333, 2015.

[69]   E. Kjellsson, G. Hellström, and B. Perers, "Optimization of systems with the combination of ground-source heat pump and solar collectors in dwellings," *Energy,* vol. 35, pp. 2667-2673, 2010.

[70]   O. Ozgener and A. Hepbasli, "Experimental performance analysis of a solar assisted ground-source heat pump greenhouse heating system," *Energy and Buildings,* vol. 37, pp. 101-110, 2005.

[71]   W. Yang, L. Sun, and Y. Chen, "Experimental investigations of the performance of a solar-ground source heat pump system operated in heating modes," *Energy and Buildings,* vol. 89, pp. 97-111, 2015.

[72]   H. Park, J. S. Lee, W. Kim, and Y. Kim, "Performance optimization of a hybrid ground source heat pump with the parallel configuration of a ground heat exchanger and a supplemental heat rejecter in the cooling mode," *International Journal of Refrigeration,* vol. 35, pp. 1537-1546, 2012.

[73] Y. Man, H. Yang, and J. Wang, "Study on hybrid ground-coupled heat pump system for air-conditioning in hot-weather areas like Hong Kong," *Applied Energy,* vol. 87, pp. 2826-2833, 2010.

[74] S. Wang, X. Liu, and S. Gates, "Comparative study of control strategies for hybrid GSHP system in the cooling dominated climate," *Energy and Buildings,* vol. 89, pp. 222-230, 2015.

[75] Z. Sagia, C. Rakopoulos, and E. Kakaras, "Cooling dominated Hybrid Ground Source Heat Pump System application," *Applied Energy,* vol. 94, pp. 41-47, 2012.

[76] R. Fan, Y. Gao, L. Hua, X. Deng, and J. Shi, "Thermal performance and operation strategy optimization for a practical hybrid ground-source heat-pump system," *Energy and Buildings,* vol. 78, pp. 238-247, 2014.

[77] W. Gang, J. Wang, and S. Wang, "Performance analysis of hybrid ground source heat pump systems based on ANN predictive control," *Applied Energy,* vol. 136, pp. 1138-1144, 2014.

[78] M. Canelli, E. Entchev, M. Sasso, L. Yang, and M. Ghorab, "Dynamic simulations of hybrid energy systems in load sharing application," *Applied Thermal Engineering,* vol. 78, pp. 315-325, 2015.

[79] S. A. Putrayudha, E. C. Kang, E. Evgueniy, Y. Libing, and E. J. Lee, "A study of photovoltaic/thermal (PVT)-ground source heat pump hybrid system by using fuzzy logic control," *Applied Thermal Engineering,* vol. 89, pp. 578-586, 2015.

[80] B. Dehghan, "Performance assessment of ground source heat pump system integrated with micro gas turbine: Waste heat recovery," *Energy Conversion and Management,* vol. 152, pp. 328–341, 2017.

[81] W. Wu, X. Li, T. You, B. Wang, and W. Shi, "Combining ground source absorption heat pump with ground source electrical heat pump for thermal balance, higher efficiency and better economy in cold regions," *Renewable Energy,* vol. 84, pp. 74-88, 2015.

[82] T. You, W. Shi, B. Wang, W. Wu, and X. Li, "A new ground-coupled heat pump system integrated with a multi-mode air-source heat compensator to eliminate thermal imbalance in cold regions," *Energy and Buildings,* vol. 107, pp. 103-112, 2015.

[83] K. Allaerts, M. Coomans, and R. Salenbien, "Hybrid ground-source heat pump system with active air source regeneration," *Energy Conversion and Management,* vol. 90, pp. 230-237, 2015.

[84] A. D. Chiasson, J. D. Spitler, S. J. Rees, and M. D. Smith, "A model for simulating the performance of a pavement heating system as a supplemental heat rejecter with closed-loop ground-source heat pump systems," *Journal of Solar Energy Engineering-Transactions of the Asme,* vol. 122, pp. 183-191, Nov 2000.

[85] Y. A. Cengel and M. A. Boles, *Thermodynamics: an engineering approach*, Fifth edition ed. New York: McGraw-Hill Higher Education, 2006.

[86] S. A. R. I. Geoserver. (2014). *Soil association map*. Available: https://sarigbasis.pir.sa.gov.au/WebtopEw/ws/plans/sarig1/image/DDD/200471-235

[87] A. G. B. o. Meteorology. (2015). *Agricultural Observations Bulletin for South Australia*. Available: http://www.bom.gov.au/products/IDS65176.shtml

[88] D. R. Croft and D. G. Lilley, *Heat transfer calculations using finite difference equations*. England: Applied science publishers Ltd, 1977.

[89] Z. Wieslaw and D. Piotr, "Modelling of liquid flat-plate solar collector operation in transient states," in *Proceedings of the Institution of Mechanical Engineers Part A Journal of Power and Energy*, 2010, pp. 53-62.

[90] M. Bahrami. (18 June). Forced convection heat transfer. Available: http://www.sfu.ca/~mbahrami/ENSC%20388/Notes/Forced%20Convection.pdf

[91] A. G. B. o. Meteorology. (17 July). *Climate statistics for australian locations*. Available: http://www.bom.gov.au/climate/averages/tables/cw_023034.shtml

[92] Y. Gu and D. L. O'Neal, "Development of an equivalent diameter expression for vertical U-tube used in ground-coupled heat pumps," *ASHRAE Transactions,* vol. 104, pp. 347-355, 1998.

[93] J. R. Lloyd and W. R. Moran, "Natural Convection Adjacent to Horizontal Surface of Various Planforms," *Journal of Heat Transfer,* vol. 96, pp. 443-447, 1974.

[94] T. L. Bergman, A. S. Lavine, F. P. Incropera, and D. P. DeWitt, Fundamentals of heat and mass transfer, 7th Edition. New York, USA: Wiley, 2007.

[95] H. Wang, Y. Cui, and C. Qi, "Effects of Sand–Bentonite Backfill Materials on the Thermal Performance of Borehole Heat Exchangers," *Heat Transfer Engineering,* vol. 34, pp. 37-44, 2013/01/01 2013.

[96] R. S. Khedkar, S. S. Sonawane, and K. L. Wasewar, "Heat transfer study on concentric tube heat exchanger using TiO2–water based nanofluid," *International Communications in Heat and Mass Transfer,* vol. 57, pp. 163-169, 2014.

[97] J. Prangnell and G. McGowan, "Soil temperature calculation for burial site analysis," *Forensic Science International,* vol. 191, pp. 104-109, 2009.

[98] A. G. B. o. Meteorology. (2014). *Climate data online.* Available: http://www.bom.gov.au/climate/data/?ref=ftr

[99] S. E. Sofyan, E. Hu, and A. Kotousov, "A new approach to modelling of a horizontal geo-heat exchanger with an internal source term," *Applied Energy,* vol. 164, pp. 963-971, 2016.

[100] A. Airport. (2015). *Traveller's guide.* Available: https://www.adelaideairport.com.au/wp-content/uploads/2015/03/NJ00022-T1-FloorPlanMap.pdf

[101] A. G. D. o. t. Environment, "National greenhouse accounts factors," D. o. t. Environment, Ed., ed. Australia: Department of the Environment, 2014.

APPENDIX I

PUBLISHED JOURNAL
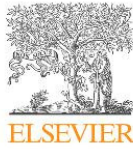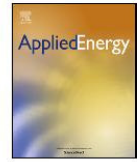
A new approach to modelling of a horizontal geo-heat exchanger with an internal source term ☆,☆☆

Sarwo Edhy Sofyan [a,b,*], Eric Hu [a,*], Andrei Kotousov [a]

[a] School of Mechanical Engineering, The University of Adelaide, Adelaide, SA 5005, Australia
[b] Department of Mechanical Engineering, Syiah Kuala University, Banda Aceh 2331, Indonesia

HIGHLIGHTS

- A new GHE model with an internal source term approach is presented.
- The theoretical results are in a good agreement with the experimental data.
- The effects of the technical parameters on the GHE's performance are investigated.

ABSTRACT

This paper presents a new approach to considering the effect of seasonal changes in soil temperature on the performance of a horizontal geo heat exchanger. It is different from extant models which consider the seasonal changes in soil temperature by applying a real energy balance on the ground surface. In the new model, the seasonal changes in soil temperature, which are affected by the thermal interaction between the ground and the atmosphere, are expressed as an internal source term. The value of the internal source term depends on the soil density, soil specific heat, soil temperature difference during summer and winter, and time period. The simulation results show that the new approach, which takes into account the effect of periodic soil temperature fluctuations on the performance of the horizontal geo heat exchanger, is valid. The validated model is then used to conduct a sensitivity analysis to investigate the effects of the pipe length, fluid flow rate, inlet fluid temperature, and burial depth on the thermal performance of the horizontal geo heat exchanger.

© 2015 Elsevier Ltd. All rights reserved.

1. Introduction

In recent years, geo heat exchangers (GHEs) have become attractive from a technical perspective in heating and cooling applications because of their renewable nature. GHEs use the ground/soil as a heat source or heat sink to harness the (renewable) thermal energy stored in the ground as the ground temperature is normally higher than the ambient air temperature during the winter and lower during the summer. Thus, the ground is a suitable medium to be used to extract/store the heat during the winter/summer. GHEs are usually coupled with heat pump and air conditioning systems to provide one of the most energy efficient ways of generating buildings' heating and cooling. There are two common configurations of GHEs, namely vertical and horizontal. Horizontal heat exchangers are relatively cheap to install, as they are only laid in a trench at a depth of up to 2 m below the surface. Their performance is affected by the continuous thermal interaction between the ground and the atmosphere. The diverse mechanisms of heat transfer occurring on the ground surface contribute to the thermal recovery of the ground conditions, especially when there is an imbalance between the heating and cooling operations [1].

There is much literature which discusses the theoretical study of horizontal GHEs, including the modelling of their linear [1–15], slinky [16–20], and flat-panel [21–23] arrangements. One of the key challenges associated with the theoretical study of the

performance of a horizontal heat exchanger is to take into account the effect of seasonal changes in soil temperature. Gan [1] developed a two dimensional transient finite volume model of a horizontal GHE. The heat transfer on the ground surface is calculated by taking into account the effects of ambient air temperature and convection heat transfer. Esen et al. [2] presented a two dimensional explicit finite difference model of a horizontal GHE. The model's domain is considered from the centre of the pipe to the mid span between the pipes. The adiabatic condition is applied at the right and left boundaries as the domain is divided symmetrically. The constant far field soil temperature is applied at the bottom boundary. At the surface boundary, only convection is taken into account. Benazza et al. [3] presented a transient quasi three dimensional finite volume model of a horizontal GHE. Three different boundary conditions are applied to the soil domain, namely: symmetry adiabatic at the left and the right boundaries, undisturbed far field soil temperature at the bottom boundary, and convection on the ground surface boundary, with consideration of the dynamic ambient air temperature. Wu et al. [4] developed a two dimensional transient model of a horizontal GHE. The model is used to investigate the effects of variation in the ambient air temperature, soil thermal conductivity, wind speed, and intermittent operation on the performance of the heat exchanger. This model ignores the effects of solar radiation and evaporation which occurs on the ground surface. A comprehensive two dimensional model of a horizontal GHE has been developed by Demir et al. [5]. The model is developed by taking into account the effects of the full energy balance on the ground surface including long radiation, convection, solar radiation, sensible and latent heat transfer, precipitation and surface cover. Rezaei-Bazkiaei et al. [6,7] introduced a new approach in order to optimize the design of a horizontal GHE by using a non-homogeneous layer in the soil domain to enhance the GHE's performance. The heat transfer behaviour of the GHE system is developed based on the previous work by Demir et al. with the exception only in the intermediate layer. A horizontal heat exchanger model considering one dimensional unsteady heat conduction has been presented by Kupiec et al. [8]. In this model, the soil domain is treated as the slabs, consisting of upper and lower layers. The temperature of the upper slab is affected by periodical ambient air temperature and the temperature of the lower slab is assumed to remain constant. A performance comparison between a vertical and a horizontal GHE has been presented by Florides et al. [9]. The result shows that, under the same conditions, the outlet temperature of the vertical GHE is lower than that for the horizontal GHE. Fontaine et al. [10] developed an analytical transient model of a horizontal GHE to be applied to the permafrost region. The model provides a new feature to estimate the profile of soil temperature in directions parallel to the pipe. Naili et al. [11] presented an energy and exergy analysis of a horizontal GHE operated in a hot climate: Tunisia. The results showed that the energy and exergy efficiency vary from 18% to 52% and 12% to 36%, respectively. A new model to predict the undisturbed ground temperature was developed, based on the simplified correlation of the ambient air temperature, and has been presented by Ouzzane et al. [12]. It has been shown that the simplified correlation model produces good estimation results, however the results are less accurate than the global correlation model.

Xing et al. [13], developed an explicit two dimensional finite volume model for the horizontal foundation heat exchanger. The model considers the effects of convection, evaporation, and radiation on the ground surface. Lee et al. [14] continued Xing et al.'s work by improving the simulation capabilities of the model, including integrating the model with the building simulation programs, developing a better grid generation technique which produces better accuracy and simulation efficiency. Nam and Chae [15] developed a numerical simulation model of a building

foundation horizontal GHE which is applied to an underground parking lot. The model considers the ground around the GHE as a porous medium comprising of gas, liquid, and solids. The fluctuation of the ground surface temperature is considered by applying the surface thermal energy balance to the surface boundary.

Chong et al. [16] developed a three dimensional numerical model of a horizontal slinky loop heat exchanger. The model is used to investigate the GHE's performance under variations of the loop pitch, loop diameter, and soil diffusivity. Xiong et al. [17], developed a slinky ground heat exchanger model which has better capability in its computational speed and could be integrated into building simulation programs. The model considers the variations of the ground surface's temperature by using a surface energy balance approach. Fujii et al. [18] conducted both experimental and numerical studies on a double layer-slinky coil horizontal heat exchanger. The results show that the double layer-slinky coil horizontal heat exchanger produces a remarkable heat transfer rate per unit of land area when compared with the single layer type. Adamovsky et al. [19] presented the thermal analysis for both the linear and the slinky types of horizontal GHEs. The results reveal that the linear type GHE produces better efficiency than the slinky type. Go et al. [20], investigated the effect of rainfall infiltration on the performance of a spiral coil horizontal heat exchanger. Under unsaturated soil conditions, the results obtained show that the GHE has a higher thermal efficiency when rainfall infiltration is considered.

Bortoloni and Bottarelli [21] presented an analytical line source model of a new configuration of the horizontal GHE, called a flat-panel ground heat exchanger. In this study, the new shape of the heat exchanger is treated as an equivalent to a slinky-coil, which has the same heat transfer surface. The soil domain is assumed to be isentropic and the surface's boundary condition is determined based on the sinusoidal analytical function of the soil temperature. Bottarelli et al. [22] developed a novel two dimensional flat-panel model of a horizontal GHE which uses the encapsulated phase change materials (PCMs) as the trench's filling material. The model considers groundwater in porous media. In addition, the model applies the dynamic surface energy balance, with an hourly scale, at the ground's surface. The effectiveness of the PCMs as the backfill material is compared with the use of the coarse gravel. The results show that the GHE with PCMs as backfill material has a lower performance than that with the coarse gravel. Bottarelli et al. [23] continued their work to investigate the effect of using the mixture of soil and PCMs as backfill materials. The results show that the GHE with the mixture of soil and encapsulated PCMs has a relatively higher surface temperature than that without PCMs during the winter, and, conversely, lower during the summer.

A review of the literature [1–23] shows that the existing models use traditional approaches to consider the periodic soil temperature fluctuations during seasonal changes. Some of the models use a simplified function of the ambient air temperature to consider the soil's fluctuations in temperature due to seasonal changes. The simplified approach produces less accurate results. Others apply the ground surface's dynamic energy balance in which the inputs are spatially and temporally difficult to collect, thereby making the model complicated and inefficient in terms of computational time.

This paper presents a novel three dimensional unsteady heat transfer model for a horizontal GHE. In the model, seasonal changes in soil temperature, caused by external factors such as solar radiation, evaporation, and vegetation cover, are presented as a single internal source term for the first time. This approach, in which the value of the internal source term depends on soil density, soil specific heat, soil temperature differences during summer and winter, and a specified time period, is more practical to use and it is expected to generate more precise outcomes. The

validated model is used to conduct a sensitivity analysis to investigate the effects of the pipe length, fluid flow rate, inlet fluid temperature and burial depth on the thermal performance of the horizontal GHE.

2. Development model of the horizontal GHE

2.1. Physical model

The physical model of the horizontal GHE consists of a multi-U-shaped pipe, which has a certain diameter, d length L and thickness t. It is buried at a specific depth, h, horizontally and has a centre to centre distance of the pipe, S. When an air conditioning system is working, the GHE fluid, which passes through a system of heat exchangers, absorbs the heat from the air conditioning system's condenser. The working fluid then enters the inlet pipe of the GHE at a certain temperature T_{fi}. Inside the pipe, the heat is exchanged by the fluid to the pipe's surface by convection and then passes through the pipe wall to the soil through conduction. Half of this heat flows down to a deeper soil layer. The rest of this heat flows up to the soil surface and then into the atmosphere. The heat transfer process causes the working fluid temperature to drop and, at the same time, it raises the soil temperature. The working fluid then exits the pipe at a lower temperature T_{fo}. Fig. 1 illustrates a schematic of the horizontal GHE.

2.2. Mathematical model

In this section, the mathematical model of the horizontal GHE is presented. The model is developed by considering the transient heat transfer of the soil, pipe, and circulating fluid. In this model, it is assumed the mechanism of heat transfer in the soil domain is pure heat conduction. The three dimensional profile of the soil temperature is modelled by dividing the soil and pipe into small segments. In each segment, it is considered that the working fluid transfers the heat to the soil in two dimensions. The transient temperatures of the working fluid, pipe and soil are evaluated iteratively by using the explicit finite different method. The governing equations for the soil, pipe and working fluid are derived from the equations of the energy balance. The governing equation for the soil is given as:

(a) Soil

$$\frac{1}{\alpha_s}\frac{\partial T_s}{\partial t} = \frac{\partial^2 T_s}{\partial x^2} + \frac{\partial^2 T_s}{\partial y^2} + \frac{H_s}{k_s} \tag{1}$$
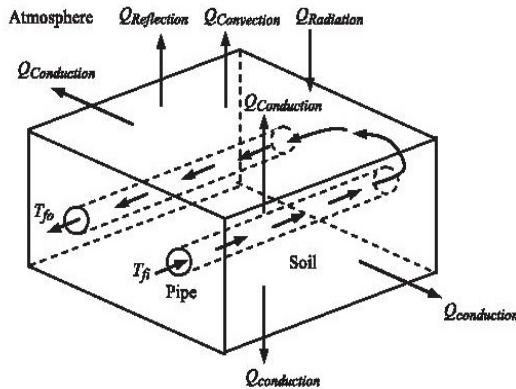
Fig. 1. Schematic of the horizontal GHE.

where α_s is the soil diffusivity (m^2/s), T_s is the soil temperature (K), t is the time period (s), H_s is the soil source term (W/m^3), k_s is the soil conductivity (W/m K), x and y are the distance in the x and y direction (m).

In this model, the seasonal changes in soil temperature are calculated by using an internal source term approach. This approach is more practical to use, as the internal source term is calculated based on the differences in soil temperature during summer and winter. Since the soil temperature varies with depth from the surface, the different depths of soil have different source term values. For instance, a source term value at a depth of 1 m below the ground surface is higher than a source term value at a depth of 2 m below the ground surface. The differences in source term values are affected by different ground temperature amplitudes during winter and summer. At a depth of more than 10 m below the ground surface, the temperature of the ground is relatively constant [24]. The internal source term model can be used once the value of the annual periodic soil temperature fluctuations caused by the seasonal climate changes is known from the testing or estimations. The model can cover different types of climate conditions such as tropical, sub-tropical and temperate. Fig. 2a shows the typical profile of the soil temperature during summer and winter. Fig. 2b shows the computational domain of the horizontal GHE, to which different source term values are applied for the different soil layers. The internal source term H_s is calculated as:

$$H_s = \rho_s c_s \frac{\Delta T_s}{\Delta t} \tag{2}$$

where H_s is the source term (W/m^3), ρ_s is the soil density (kg/m^3), c_s is the soil specific heat (J/kg K), Δt is the time period (s), and ΔT_s is the soil temperature difference during summer and winter (K).

The values of the soil temperature differences during summer and winter can either be obtained from the measurement results or predicted using the equation given by Baggs [25]. The equation is given as:

$$T(x,t) = (T_m \pm \Delta T_m) + 1.07 k_v A_s \ \exp\left(-0.00316x\left(\frac{1}{\alpha}\right)^{0.5}\right)$$

$$\times \cos\left[\frac{2\pi}{365}\left(t - t_0 - 0.1834x\left(\frac{1}{\alpha}\right)^{0.5}\right)\right] \tag{3}$$

in which, $T(x,t)$ is the ground temperature at a given depth x on calendar day t (°C), x is the soil depth (cm), t is the calendar day where 1 January = 1 and so forth, T_m is the average annual air temperature (°C), ΔT_m is the local site variable for the ground temperature (K), k_v is the vegetation coefficient (k_v = 1 for bare ground, k_v = 0.22 for year round full vegetation cover), A_s is the amplitude of the annual air temperature (K), α is the average soil thermal diffusivity (10^{-2} cm^2 s^{-1}), and t_0 is the phase of air temperature wave (day).

(b) Pipe

The governing equation for the pipe is given as:

$$c_p \rho_p V_p \frac{\partial T_p}{\partial t} = A h_f (T_f - T_p) + \frac{k_s A}{0.5\Delta x}(T_s - T_p) \tag{4}$$

where c_p is the pipe specific heat (J/kg K), ρ_p is the pipe density (kg/m^3), V_p is the volume of the pipe wall (m^3), T_p is the pipe temperature (K), t is the time period (s), A is the heat transfer area of the pipe (m^2), h_f is the convection heat transfer (W/m^2 K), T_f is the fluid temperature (K), k_s is the soil conductivity (W/m K), Δx is the distance in the x direction (m), and T_s is the soil temperature (K).

(c) Working fluid

The governing equation for the fluid is given as:

$$c_f \rho_f A \frac{\partial T_f}{\partial t} = \pi d_{in} h_f (T_p - T_f) - \dot{m}_f c_f \frac{\partial T_f}{\partial z} \tag{5}$$
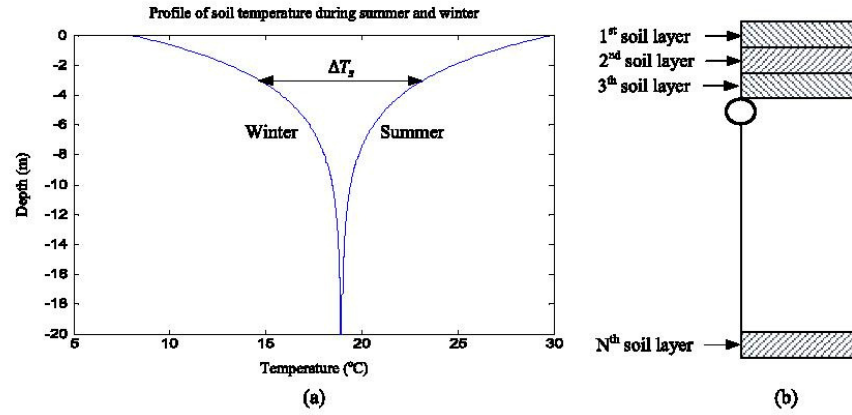
Fig. 2. (a) Typical profile of soil temperature during summer and winter. (b) The computational domain of the horizontal GHE to which different source term values are applied for the different soil layers.

where c_f is the fluid specific heat (J/kg K), ρ_f is the fluid density (kg/m^3), A is the heat transfer area of the pipe (m^2), T_f is the fluid temperature (K), t is the time period (s), d_{in} is the inner pipe diameter (m), h_f is the convection heat transfer (W/m^2 K), T_p is the pipe temperature (K), T_f is the fluid temperature (K), $\dot{m}_f$ is the fluid mass flow rate (kg/s), z is the distance in direction parallel to the pipe (m).

The solutions in the differential Eqs. (1), (4) and (5) are solved by using the explicit finite different method and given as:

(a) Soil temperature

$$T_{s(i,j)}^{t+\Delta t} = F_o\left(T_{s(i+1,j)}^t + T_{s(i-1,j)}^t + T_{s(i,j+1)}^t + T_{s(i,j-1)}^t + \frac{H(\Delta x)^2}{k_s}\right) + (1 - 4F_o)T_{s(i,j)}^t \tag{6}$$

where

$$F_o = \frac{\alpha_s \Delta t}{(\Delta x)^2} \tag{7}$$

in which $T_s^{t+\Delta t}$ is the soil temperature at the new time step (K), T_s^t is the soil temperature at the current time step (K), and i and j are indices in the x and y directions, respectively. Other parameters are the same as those elaborated in Eq. (1).

(b) Pipe temperature

$$T_{p(k)}^{t+\Delta t} = \frac{\Delta t}{c_p \rho_p V_p}\left[Ah_f(T_{f(k)}^t - T_{p(k)}^t) + \frac{k_s A}{0.5\Delta x}(T_{s(k)}^t - T_{p(k)}^t)\right] + T_{p(k)}^t \tag{8}$$

where $T_p^{t+\Delta t}$ is the pipe temperature at the new step (K), T_p^t is the pipe temperature at the current time step (K), k is the index in the direction parallel to the pipe. The other parameters are the same as those elaborated in Eq. (4).

(c) Fluid temperature

$$T_{f(k)}^{t+\Delta t} = \frac{\Delta t}{c_f \rho_f A}\left[\pi d_{in} h_f\left(T_{p(k)}^t - T_{f(k)}^t\right) - \dot{m}_f c_f \frac{T_{fo(k)}^t - T_{fi(k)}^t}{\Delta z}\right] + T_{f(k)}^t \tag{9}$$

where $T_f^{t+\Delta t}$ is the fluid temperature at the new time step (K), T_f^t is the fluid temperature at the current time step (K), k is the index in the direction parallel to the pipe. The other parameters are the same as those elaborated in Eq. (5).

Using the explicit finite different method, the partial differential equations can be solved relatively simply. The unknown nodal temperature at an entity and the new time step are approximated by using the already known temperature values from the adjacent nodes. The drawback of the explicit method is that it is conditionally stable. To satisfy the stability criterion, the time step Δt must be within the Courant–Friedrichs–Lewy stability condition, given as follows:

$$|\psi| \leqslant 1, \ \Delta t \leqslant \frac{\Delta z}{v_f} \tag{10}$$

in which, $\psi = (v_f \Delta t / \Delta z)$ is the Courant number, Δt is the time step (s), Δz is the distance in the direction parallel to the pipe (m), and v_f is the velocity of the working fluid (m/s).

Fig. 3 shows the computational domain of the horizontal GHE. In this paper, the serpentine pipe of the horizontal GHE is analysed by applying symmetry analysis. The computational domain of the GHE is considered from the centre of the pipe to the mid span distance between the pipes. The soil domain is discretised by using the structured rectangular mesh which has an equal distance in the x and y directions. Different boundary conditions are applied for the computational domain. Convective heat transfer is considered on the soil surface. The other external effects such as radiation, precipitation, evaporation, and vegetation cover, are considered by applying an internal source term value for each soil layer. In addition, the adiabatic condition is applied at both the symmetry and bottom boundaries.

3. Validation of the proposed model

The theoretical results of the proposed model are validated against the experimental data obtained from a reduced scale experimental rig system. Validation using a reduced scale rig system has been chosen because it enables us to simulate the seasonal changes in soil temperature in a relatively short period of time by using the lamps' ON/OFF operation. In addition, due to the time and financial constraints, it is not feasible to conduct full scale tests. The scaled down experiment is believed to be sufficient for the purpose of model validation in this paper. The experimental apparatus consists of a single U-shaped pipe laid in a sandy loam-filled box. The box is made up of 19 mm plywood which is reinforced with 70×30 mm^2 of structural pine. It is lined with a layer of construction lining plastic. The box's dimensions are
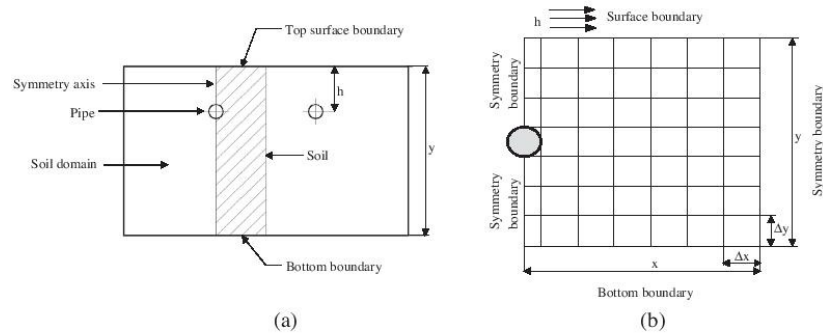
Fig. 3. (a) A horizontal GHE buried in the soil domain. (b) A computational domain of the horizontal GHE.
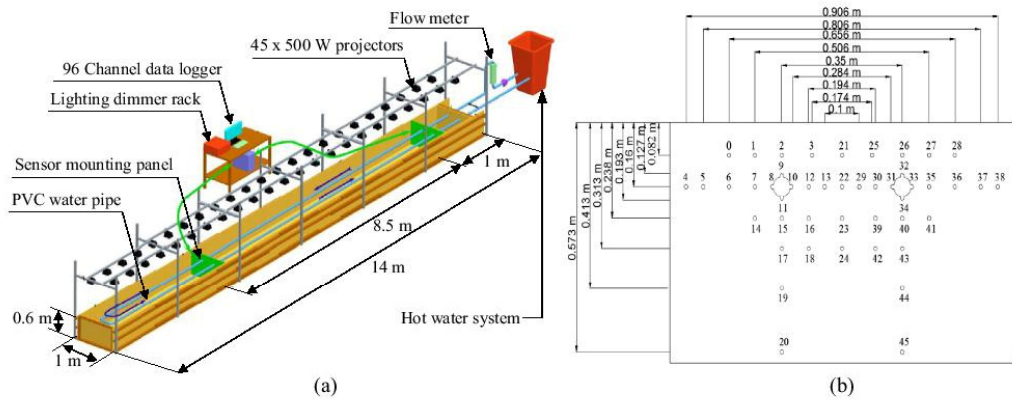
Fig. 4. (a) The experimental set up of the horizontal GHE. (b) The cross section of the sand bed showing the location of the thermal sensors.

14 m in length, 1 m width, and 0.6 m height. The 0.05 m diameter and 27.5 m length of PVC pipe are set to a depth of 0.16 m from the sand surface. The pipe has a 0.35 m centre-to-centre distance and it is connected to a hot water system. Forty-five halogen lamps, which have a power of 500 W each, are installed 1 m above the sand bed to heat up and simulate the seasonal changes in soil temperature. Fig. 4a and b shows the schematics of the test rig and cross section of the sand bed, showing the location of the thermal sensors, respectively.

Two sets of experiments were carried out to validate the horizontal GHE model. The first experiment was conducted to determine the internal heat source term and validate the soil temperature model of the horizontal GHE when there is no hot water being circulated inside the pipe. In this experiment, the change of soil temperature was caused by the lamps' being on/off and the interaction between the soil and the atmosphere. The soil temperature's seasonal changes were simulated by running the experiment with 3 h of on-light heating and 10 h of off-light cooling, without water circulation. A lighting dimmer rack, which was controlled by Sunlight 2004 software, was used to regulate the radiation output released by the halogen lamps. It was set to 700 W/m². The changes in the temperature of the sand bed during the heating and cooling period at six different depths, namely, 0.082 m, 0.16 m, 0.238 m, 0.313 m, 0.413 m, and 0.573 m, were measured using the LM 35 temperature sensors which were

installed at two different locations along the pipe, namely, 1 m and 9.5 m from the edge of the box. The temperature was recorded using a data logger, connected to a computer, at 1 min intervals. In addition, the ambient indoor air temperature in the laboratory was measured as it contributes to heat dissipation by natural convection and it was considered in the simulation. Then the value of internal source term was calculated by using the measurement values of the changes in soil temperature during the heating and cooling process. The results will be used to create input values in the simulation. The second experiment was conducted to validate the model of the horizontal GHE when there is hot water being circulated inside the pipe. The second experiment was conducted by repeating the first experiment and considering the circulating fluid during the first 3 h before turning it off for the next 10 h. In this experiment, the inlet temperature and flow rate were set to 66 °C and 0.66 kg/s, respectively. Table 1 shows the thermal properties of the GHE materials.

Table 1
Thermal properties of the GHE materials.

Thermal properties	Soil	Pipe	Water
Thermal conductivity (W/m K)	0.5	0.15	0.66
Thermal diffusivity (m²/s)	2.5×10^{-7}	–	–
Specific heat (J/kg K)	1100	1046	4188
Density (kg/m³)	1777	1400	980

As an example, Fig. 5 shows the profile of the soil temperature measured at a depth of 0.16 m during 3 h of on-light heating and 10 h of off-light cooling. From Fig. 5 it can be seen that the changes in the soil temperature can be divided into 4 distinctive periods over the 13 h, according to the gradients of the changes. Each period refers to a value of the internal heat source term. Table 2 shows the calculated values of the internal source term for each soil layer for a certain period of time. In order to increase accuracy, the internal source term at each soil layer is calculated over a short period of time.

The simulations of the performance of the horizontal GHE are conducted by using the above parameter values. The initial condition of the pipe and working fluid of the horizontal GHE is assumed to be the same as a steady state soil temperature before the heating or cooling operation.

3.1. Validation of the soil temperature model

Fig. 6a and b shows a comparison of the simulated and the measured soil temperatures at a depth of 0.082 m and 0.16 m, respectively, when there is no water being circulated inside the horizontal GHE. The simulation results show that the simulated soil temperature with the source term approach is in good agreement with the measured soil temperature, for which, the highest temperature discrepancy between the calculated and the measured result is 0.3 °C. The simulated soil temperature without the source term approach fails to approximate the experimental results because it is only natural convection is applied on the ground surface. Thus, it can be concluded that a new method which expresses the seasonal changes in soil temperature as an internal source term is valid.

3.2. Validation of horizontal GHE model

The validation of the dynamic model of the horizontal GHE is conducted by comparing the measured with the simulated soil and water outlet temperatures of the GHE when the hot water is being circulated inside the pipe. Fig. 7a shows the comparison of the measured and simulated soil temperatures, where sensor number 2 is installed (refer to Fig. 4b). The results show that the simulated soil temperatures with the source term approach produce more accurate results than those without the source term. Fig. 7b shows the profile of the outlet fluid temperature. It is shown that the theoretical result is relatively higher than the measured outlet fluid temperature. This phenomenon could have been affected by the fluctuation of the inlet fluid temperature during the experiment. In the simulation, it is assumed that the inlet fluid temperature is constant. In addition, it is shown that the outlet fluid temperatures generated by the model with and without source term are identical. The reason could be that the fluctuations in soil

Fig. 5. Profile of the soil temperature at the second soil layer.

Table 2
Values of the internal heat source term for each soil layer obtained in the experiment.

Layer 1 (0–0.082 m)		Layer 2 (0.082–0.16 m)		Layer 3 (0.016–0.238 m)		Layer 4 (0.238–0.313 m)		Layer 5 (0.313–0.413 m)		Layer 6 (0.413–0.6 m)	
Time (h)	Source term (W/m³)	Time (h)	Source term (W/m³)	Time (h)	Source term (W/m³)	Time (h)	Source term (W/m³)	Time (h)	Source term (W/m³)	Time (h)	Source term (W/m³)
0–3	326.5 (H_s1)	0–3	254.6 (H_s1)	0–3	118.1 (H_s1)	0–3	69.1 (H_s1)	0–3	35.6 (H_s1)	0–3	25.3 (H_s1)
3–4	45.2 (H_s2)	3–5.5	91.6 (H_s2)	3–8	88 (H_s2)	3–8.5	75.1 (H_s2)	3–6	35 (H_s2)	3–6.5	14.8 (H_s2)
4–10.5	−159.8 (H_s3)	5.5–9.5	−51.5 (H_s3)	8–13	−23.4 (H_s3)	8.5–13	−1 (H_s3)	6–8.5	81.4 (H_s3)	6.5–13	15.5 (H_s3)
10.5–13	−80.1 (H_s4)	9.5–13	−80.7 (H_s4)					8.5–13	12 (H_s4)		

Fig. 6. (a) Profile of the soil temperature at a depth of 0.082 m. (b) Profile of the soil temperature at a depth of 0.16 m.

Fig. 7. (a) Profile of the soil temperature at sensor 2. (b) Profile of the outlet fluid temperature (where the inlet fluid temperature = 66 °C, fluid mass flow rate = 0.66 kg/s, and initial soil temperature = 18 °C).

temperature over a short time had no significant effect on the performance of the GHE when the fluid flow rate is relatively high.

4. Sensitivity analysis

In this section, the sensitivity analysis is conducted by using the validated model. The sensitivity analysis is performed based on the soil and climate conditions at Adelaide Airport, Australia. In this section, the distribution of the soil temperature along the depth of the soil is determined by using Baggs' equation [25]. The values of the average annual air temperature and the amplitude of the annual air temperature can be obtained from the Australian Bureau of Meteorology [26]: they are 16.45 C and 10.2 C, respectively. The local site variable for the ground temperature is based on data given by Baggs [25], namely 2.5 °C. The k_v vegetation coefficient is taken as one, as it is assumed there is no vegetation cover on the ground surface.

The thermal properties of the soil at Adelaide Airport are determined, based on the existing literature data. The soil type at Adelaide Airport is layered old dune sands, generally compact and normally brown in colour [27]. Al-khoury [24], gives a different range of values for the thermal conductivity, density and specific heat of the sand. They range from 0.15 to 4 W/m K for the thermal conductivity, 1280–2150 kg/m³ for the density, and 0.8–1.48 kJ/kg K for the specific heat. Taking a conservative approach, the mean of those values is considered, namely 2 W/m K for the thermal conductivity, 1715 kg/m³ for the density and 1.140 kJ/kg K for specific heat.

Table 3
The parameters of the reference case.

Parameters	Value
Pipe length (m)	100
Burial depth (m)	0.175
Pipe internal diameter (m)	0.05
Pipe outer diameter (m)	0.054
Centre distance between pipes (m)	0.35
Distance of soil domain in the *x* direction (m)	0.175
Distance of soil domain in the *y* direction (m)	1.5
Inlet fluid temperature (°C)	60
Flow rate (kg/s)	0.5
Initial soil temperature (°C)	25

The sensitivity analysis is carried out by simulating the performance of the horizontal GHE at Adelaide Airport under variations of the pipe length, fluid flow rate, inlet fluid temperature, and burial depth. The parameters of the reference case are given in Table 3.

The value of the internal source term for this analysis is calculated based on the soil temperature difference between summer and winter, soil density, soil specific heat, and the period of soil temperature changes at Adelaide Airport. Table 4 gives the values of the internal heat source terms at various depths.

The convection heat transfer is considered by taking into account the average of wind speeds of 4.9 m/s at the surface of the soil domain and the average ambient air temperature of 24 °C [28]. The initial temperature of the system, namely the soil, pipe, and circulating water is assumed the same, namely 25 °C. The thermal properties of the pipe and water are the same as those given in Table 1.

4.1. Pipe length

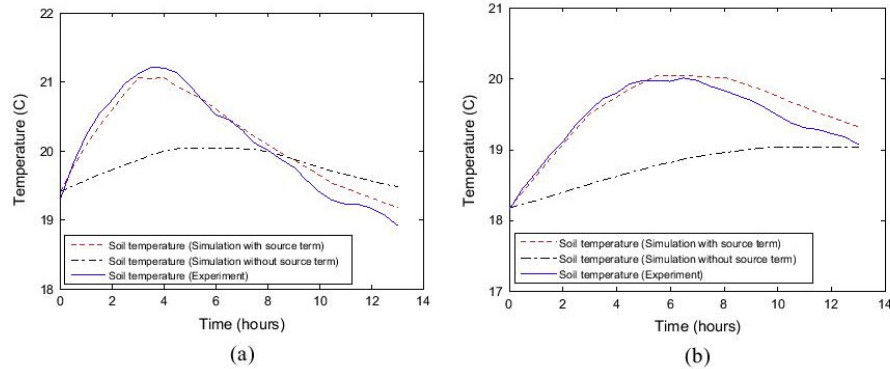One of the technical factors affecting the thermal performance of the heat exchanger is the pipe length. The longer pipe means that there is a larger area in which the heat may be exchanged. In this study, the thermal performance of the horizontal heat

Table 4
The value of the internal heat source for each soil layer at Adelaide Airport.

Soil layer	Soil temperature difference between summer and winter (°C)	Time period	Source term value (W/m³)
1st soil layer (0–0.1 m depth)	21.15	6 months	2.62
2nd soil layer (0.1–0.2 m depth)	20.50	6 months	2.54
3th soil layer (0.2–0.3 m depth)	19.87	6 months	2.46
4th soil layer (0.3–0.4 m depth)	19.26	6 months	2.38
5th soil layer (0.4–0.5 m depth)	18.67	6 months	2.31
6th soil layer (0.5–0.6 m depth)	18.09	6 months	2.24
7th soil layer (0.6–0.7 m depth)	17.53	6 months	2.17
8th soil layer (0.7–0.8 m depth)	17	6 months	2.10
9th soil layer (0.8–0.9 m depth)	16.47	6 months	2.04
10th soil layer (0.9–1 m depth)	15.97	6 months	1.98
11th soil layer (1–1.1 m depth)	15.47	6 months	1.91
12th soil layer (1.1–1.2 m depth)	15	6 months	1.86
13th soil layer (1.2–1.3 m depth)	14.54	6 months	1.80
14th soil layer (13–14 m depth)	14.09	6 months	1.74
15th soil layer (1.4–1.5 m depth)	13.66	6 months	1.69

Fig. 8. The effect of the pipe length on the performance of the GHE (where the inlet fluid temperature = 60 °C, fluid mass flow rate = 0.5 kg/s, burial depth = 0.175 m and initial soil temperature = 25 °C).

exchanger for seven different pipe lengths, from 50 m to 200 m with an increment of 25 m, is investigated. Fig. 8 illustrates the effect of the pipe length on the performance of the GHE at six different periods, namely 1–6 h of operation. It is shown that the outlet fluid temperatures of the horizontal GHE decrease with the increase in pipe length. The longer the pipe, the higher heat can be transferred to the soil as a result of the larger contact area of the fluid, pipe and soil. The outlet fluid temperatures increase with the increase in the operation time. This phenomenon occurs because, with the increase in the operation time, the ground temperature around the GHE becomes higher than it was in its initial condition, as the ground absorbs the heat transferred from the circulating fluid. Thus, the amount of heat transferred to the ground becomes lower. As a result, the outlet fluid temperature of the GHE is higher after a certain period of operation. Although increasing the pipe length can increase the heat transfer rate, the heat transfer rate per pipe length decreases. This phenomenon occurs

because the outlet fluid temperature decreases in a non-linear trend with the increase in pipe length. For instance, incrementing the pipe length from 75 m to 100 m leads to a drop in the outlet fluid temperature of 1.3 °C. In addition, it drops to 1.2 °C when the pipe length is increased from 100 m to 125 m.

4.2. Flow rate

The fluid flow rate is another technical factor affecting the performance of the heat exchanger. Fig. 9 shows the effect of flow rates on the outlet temperatures of the horizontal GHE at six different periods, namely 1–6 h of operation. The flow rate is varied from 0.3 kg/s to 0.7 kg/s, with an increment of 0.1 kg/s. It is shown that the higher flow rates lead to a higher fluid outlet temperature. At the lower flow rate, the changes in the outlet fluid temperature over the period of operation are relatively higher. For instance, the difference in the outlet fluid temperature of the GHE with a flow rate of 0.3 kg/s, from 1 to 6 h of operation, is 4.6 °C. Meanwhile it is 2.2 °C for a flow rate of 0.7 kg/s. This phenomenon occurs because the GHE with a higher fluid flow rate releases more heat to the surrounding soil. As a result, the soil temperature around the GHE increases relatively quickly. This degradation of the soil's thermal condition affects the heat exchange capacity of the GHE and results in an increased outlet fluid temperature.

4.3. Inlet fluid temperature

The inlet temperature of the GHE may vary, depending on the loading conditions. In this section, the effect of the inlet temperature on the performance of the GHE is presented. Fig. 10 shows that the outlet fluid temperature is affected by the inlet input temperature and the period of the operation. The temperature difference between the inlet and outlet fluid temperatures is higher when the inlet input temperature is higher. The GHE with the higher inlet fluid temperature can release more heat into the ground as the temperature difference between the working fluid and the ground is relatively higher. It is shown that during the first hours of operation, the temperature difference between inlet and outlet temperatures rises from 6 °C to 10.7 °C, for the GHE with the lowest and the highest inlet fluid temperatures respectively. However, these values decrease with the increase of the operation period, namely 3.7 °C and 6.7 °C respectively.

Fig. 9. The effect of the fluid flow rate on the performance of the GHE (where the inlet fluid temperature = 60 °C, pipe length = 100 m, burial depth = 0.175 m and initial soil temperature = 25 °C).

Fig. 10. The effect of the inlet temperature on the performance of the GHE (where the fluid mass flow rate = 0.5 kg/s, pipe length = 100 m, burial depth = 0.175 m and initial soil temperature = 25 °C).
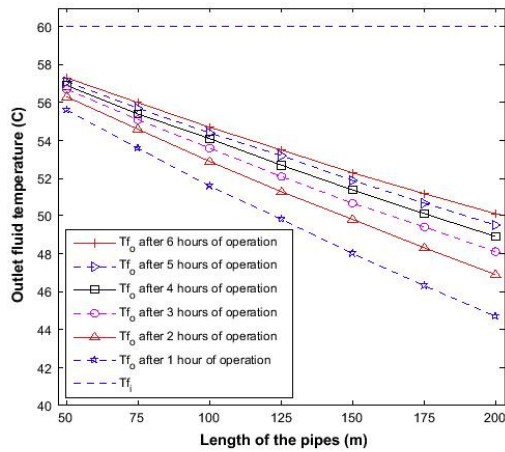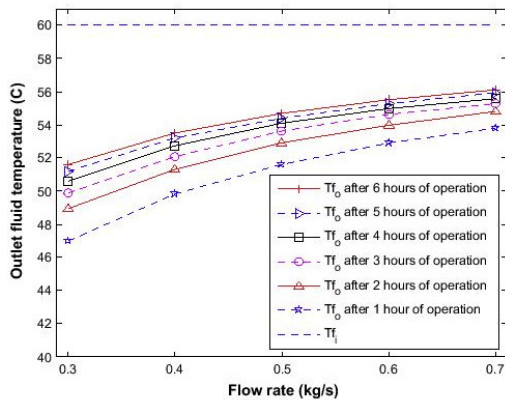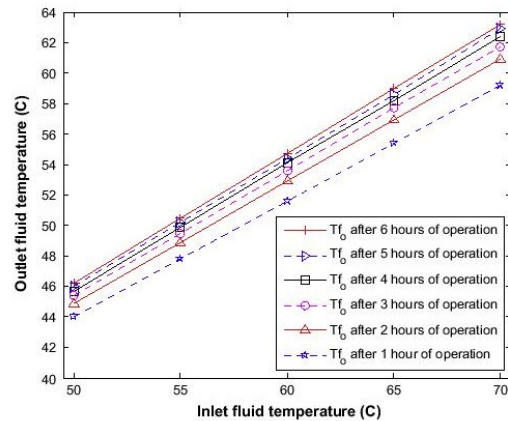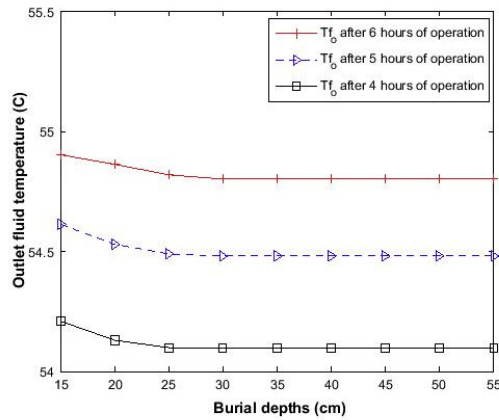
Fig. 11. The effect of burial depth on the performance of the GHE (where the inlet fluid temperature = 60 °C, fluid mass flow rate = 0.5 kg/s, pipe length = 100 m and initial soil temperature = 25 °C).

4.4. Burial depth

The thermal performance of the horizontal heat exchanger with different burial depths, from 15 to 55 cm with an increment of 5 cm, is investigated. Fig. 11 shows the outlet fluid temperature of the GHE at three different periods, namely 4, 5 and 6 h of operation. Overall, it is shown that the burial depth does not significantly affect the outlet fluid temperature. The pipe which is buried at a depth relatively close to the ground surface has a slightly higher outlet fluid temperature. This indicates that the performance of the GHE is affected by the seasonal changes in soil temperature. Although the effect of burial depth is insignificant across a short time period, for long term operations, this effect should be taken into account since diverse heat transfer mechanisms take place on the ground surface. For instance, if the pipe is buried relatively close to the ground surface, the degradation of the soil conditions during operation may be recovered relatively quickly since heat gains/losses takes places on the ground surface.

5. Conclusion

In conclusion, a new model of the horizontal GHE, which uses an internal source term to consider the fluctuation in soil temperature during seasonal changes, has been presented. The model has been validated by comparing the theoretical and experimental results of both the soil and the outlet fluid temperatures. The results show that the theoretical results are in a good agreement with the experimental data. The sensitivity analysis is conducted by using the validated model to investigate the effects of the pipe length, fluid flow rate, inlet fluid temperature and burial depth. These technical parameters affect the thermal performances of the horizontal GHE. The burial depth has less effect on the performance of the GHE. The reason may be because the GHE is operated across a relatively short time period. Future work to investigate the effect of burial depths on the performance of the GHE under a long-term operation period is required as diverse heat transfer mechanisms occur on the ground surface.

References

[1] Gan G. Dynamic thermal modelling of horizontal ground-source heat pumps. Int J Low-Carbon Technol 2013:ctt012.
[2] Esen H, Inalli M, Esen M. Numerical and experimental analysis of a horizontal ground-coupled heat pump system. Build Environ 2007;42:1126–34.
[3] Benazza A, Blanco E, Aichouba M, Río JL, Laouedj S. Numerical investigation of horizontal ground coupled heat exchanger. Beirut 2011:29–35.
[4] Wu Y, Gan G, Verhoef A, Vidale PL, Gonzalez RG. Experimental measurement and numerical simulation of horizontal-coupled slinky ground source heat exchangers. Appl Therm Eng 2010;30:2574–83.
[5] Demir H, Koyun A, Temir G. Heat transfer of horizontal parallel pipe ground heat exchanger and experimental verification. Appl Therm Eng 2009;29:224–33.
[6] Rezaei-Bazkiaei A, Dehghan-Niri E, Kolahdouz EM, Weber AS, Dargush GF. A passive design strategy for a horizontal ground source heat pump pipe operation optimization with a non-homogeneous soil profile. Energy Build 2013;61:39–50.
[7] Rezaei-Bazkiaei A, Kolahdouz EM, Dargush GF, Weber AS. Ground source heat pump pipe performance with tire derived aggregate. Int J Heat Mass Transfer 2012;55:2844–53.
[8] Kupiec K, Larwa B, Gwadera M. Heat transfer in horizontal ground heat exchangers. Appl Therm Eng 2015;75:270–6.
[9] Florides G, Theofanous E, Iosif-Stylianou I, Tassou S, Christodoulides P, Zomeni Z, et al. Modeling and assessment of the efficiency of horizontal and vertical ground heat exchangers. Energy 2013;58:655–63.
[10] Fontaine PO, Marcotte D, Pasquier P, Thibodeau D. Modeling of horizontal geoexchange systems for building heating and permafrost stabilization. Geothermics 2011;40:211–20.
[11] Naili N, Hazami M, Kooli S, Farhat A. Energy and exergy analysis of horizontal ground heat exchanger for hot climatic condition of northern Tunisia. Geothermics 2015;53:270–80.
[12] Ouzzane M, Eslami-Nejad P, Badache M, Aidoun Z. New correlations for the prediction of the undisturbed ground temperature. Geothermics 2015;53:379–84.
[13] Xing L, Cullin JR, Spitler JD, Im P, Fisher DE. Foundation heat exchangers for residential ground source heat pump systems—numerical modeling and experimental validation. HVAC&R Res 2011;17:1059–74.
[14] Lee ES, Fisher DE, Spitler JD. Efficient horizontal ground heat exchanger simulation with zone heat balance integration. HVAC&R Res 2013;19:307–23.
[15] Nam Y, Chae H-B. Numerical simulation for the optimum design of ground source heat pump system using building foundation as horizontal heat exchanger. Energy 2014;73:933–42.
[16] Chong CSA, Gan G, Verhoef A, Garcia RG, Vidale PL. Simulation of thermal performance of horizontal slinky-loop heat exchangers for ground source heat pumps. Appl Energy 2013;104:603–10.
[17] Xiong Z, Fisher DE, Spitler JD. Development and validation of a Slinky™ ground heat exchanger model. Appl Energy 2015;141:57–69.
[18] Fujii H, Yamasaki S, Maehara T, Ishikami T, Chou N. Numerical simulation and sensitivity study of double-layer slinky-coil horizontal ground heat exchangers. Geothermics 2013;47:61–8.
[19] Adamovsky D, Neuberger P, Adamovsky R. Changes in energy and temperature in the ground mass with horizontal heat exchangers—the energy source for heat pumps. Energy Build 2015;92:107–15.
[20] Go GH, Lee SR, Nikhil NV, Yoon S. A new performance evaluation algorithm for horizontal GCHPs (ground coupled heat pump systems) that considers rainfall infiltration. Energy 2015;83:766–77.
[21] Bortoloni M, Bottarelli M. On the sizing of a flat-panel ground heat exchanger. Int J Energy Environ Eng 2015;6:55–63.
[22] Bottarelli M, Bortoloni M, Su Y. Heat transfer analysis of underground thermal energy storage in shallow trenches filled with encapsulated phase change materials. Appl Therm Eng 2015:1–8. in press.
[23] Bottarelli M, Bortoloni M, Su Y, Yousif C, Aydın AA, Georgiev A. Numerical analysis of a novel ground heat exchanger coupled with phase change materials. Appl Therm Eng 2014:1–7. in press.
[24] Al-Khoury R. Computational modeling of shallow geothermal systems. Leiden, Netherlands: Taylor & Francis; 2012.
[25] Baggs SA. Remote prediction of ground temperature in Australian soils and mapping its distribution. Sol Energy 1983;30:351–66.
[26] A.G.B.o. Meteorology. Climate data online, 15 July <http://www.bom.gov.au/climate/data/?ref=ftr>.
[27] S.A.R.I. Geoserver, Soil association map, 16 June <https://sarigbasis.pir.sa.gov.au/WebtopEw/ws/plans/sarig1/image/DDD/200471-235>.
[28] A.G.B.o. Meteorology. Climate statistics for Australian locations, 17 July <http://www.bom.gov.au/climate/averages/tables/cw_023034.shtml>.

APPENDIX II

COMPUTER CODE FOR GEO HEAT EXCHANGER SIMULATIONS

A. Horizontal GHE

The horizontal GHE model developed in Section 4.2 is saved as a model m-file. The computer program for the horizontal GHE model is shown below.

```matlab
%---------------------- INPUT PARAMETERS--------------------------------%
clear all;
% WORKING FLUID (water)
Tfi=65+273.15; % Inlet fluid temperature(K)
mf=0.5; %Fluid mass flow rate(kg/s)
rhof=980; %Fluid density(kg/m^3)
kf=0.66; %Fluid thermal conductivity(W/mK)
cf=4188; %Fluid specific heat(W/mK)
v_kin=0.4435e-6; %Kinematic viscosity of fluid %(m^2/s)
Prf=2.66; %Prandtl number

% Pipe (PVC)
d_out=0.054; %Outer diameter of the pipe(m)
d_in=0.05; %Inner diameter of the pipe(m)
Lp=100; %Pipe length(m)
kp=0.28; %Pipe thermal conductivity(W/mK)
rhop=1400; %Pipe density(kg/m^3)
th_p=0.002; %Pipe thickness(m)
cp=1046; %Pipe specific heat(J/kgK)
Z=Lp; %A distance in the z direction(m)
dz=0.5; %Finite increment in the z direction(m)

% Soil (sand)
rhos=1715; %Soil density(kg/m^3)
ks=2; %Soil thermal conductivity(W/mK)
cs=1140; %Soil specific heat (J/kgK)
alfas=ks/(rhos*cs); %Soil thermal diffusivity(m^2/s)
Ts=25+273.15; %Soil temperature(K)

%Internal heat source term
H=2.6232; % Internal heat source term value (W/m^3)

% Dimensions of soil domain
X=0.175; %Soil domain span in x direction(m)
dx=0.05; %Finite increment in x direction(m)
Y=1.5; %Soil domain span in y direction(m)
dy=0.05; %Finite increment in y direction(m)

% Generate the mesh
m=X/dx; %Number of grid columns
m=ceil(m);
n=Y/dy; %Number of grid rows
n=ceil(n);
p=Z/dz; %Number of grid in the z direction

%Grid number in the z direction at a distance of 9.5 m
Pz=9.5/dz;
Pz=ceil(Pz);
```

```matlab
%Initial fluid temperature at each control volume (inside pipe)
Tf=20+273.15; %K
Tf_old=Tf*ones(1,p); %Fluid temperature in the control volume at the
current time step (K)
Tf_new=Tf*ones(1,p); %Fluid temperature in the control volume at the new
time step (K)

%Initial pipe temperature at each control volume
Tp=Tf;
Tp_old=Tp*ones(1,p); %Pipe temperature at each control volume at the
current time step (K)
Tp_new=Tp*ones(1,p); %Pipe temperature at each control volume at the new
time step (K)

%Soil temperature
Ts_old=Ts*ones(n,m,p);%Soil temperature at each control volume at the
current time step (K)
Ts_new=Ts*ones(n,m,p);%Soil temperature at each control volume at the new
time step (K)

%Determine pipe's area
Ap=(pi*d_in^2)/4; %Cross section area of the pipe(m^2)
Aps=pi*d_in*dz; %Surface area of the pipe(m^2)

% Determine pipe's volume
Vp=(d_out^2 - d_in^2)*(pi*dz)/4; %Volume of the pipe wall (m^3)

% Determine the convective heat transfer coefficient of fluid circulated
% inside the pipe
vf=mf/(rhof*Ap); %Fluid velocity(m/s)
Re=(vf*d_in)/v_kin; %Reynold Number
if Re <=2000
Nu=4.36; %Nusselt Number for laminar flow
else
nn=0.3; %nn=0.3 for cooling and nn=0.4 for heating
Nu=0.023*(Re^(4/5))*Prf^nn; %Nusselt Number for turbulent flow
end
hf=Nu*kf/d_in; %Convective heat transfer of working fluid(W/m^2K)

% Determine the convective heat transfer coefficient of air in contact with
% soil surface
Ta=24.25+273.15; %The average air temperature in Adelaide in January (K)
Va=4.9; %Annual average wind speed in Adelaide (m/s)
va=15.89e-6; %Kinematic viscosity of air (m^2/s)
ka=26.3e-3; %Thermal conductivity of air (W/mK)
Pra=0.707; %Prandtl Number
L=X; %Unit length (m)
Rea=Va*L/va; %Reynold Number
if Rea>=5e5
    Nua=0.037*(Rea^0.8)*Pra^(1/3); %Nusselt Number for laminar flow
else
    Nua=0.664*(Rea^0.5)*Pra^(1/3); %Nusselt Number for turbulent flow
end
ha=Nua*ka/L; %Convective heat transfer of air in contact with soil surface
(W/m^2.K)

Rconv=1/ha; %The thermal resistance for the convection heat transfer
Rcond=(5e-2/2)/ks; %The thermal resistance for the conduction heat transfer
Uas=1/(Rconv+Rcond); %Overall heat transfer coefficient of air in contact
with soil surface (W/m^2.K)

% Time discretization
T=6*3600; %Maximum simulation time (s)
```

```matlab
% Courant-Friedrichs-Lewy condition
dt=dz/vf; %Time step (s)
mu=vf*dt/dz; %The Courant number
if mu>1 %make sure dt satisfy stability condition
    error('mu should <1')
end
tt=T/dt; %Number of time steps
tt=ceil(tt);
t=0:dt:T; %Temporal discretisation (s)
th=t/3600; %Temporal discretisation (h)

% Calculate Fourier number
Fo=alfas*dt/dx^2;

%Constants in fluid temperature equation
cf1=pi*d_in*hf;
cf2=mf*cf/dz;
cf3=cf*rhof*Ap/dt;
cf4=dt/(rhof*Ap*dz*cf);

%Constants in pipe temperature equation
cp1=dt/(cp*rhop*Vp);
cp2=Aps*hf;
cp3=(ks*Aps)/(0.5*dx);
cp4=kp*Aps/th_p;

%Store the outlet fluid temperature at various time step
Tfluid_outlet=zeros(1,tt);

%Store the pipe temperature at various time step
Tpipe=zeros(tt,p);

%Stored soil temperature at various time step at a distance 9.5 m from
%pipe's inlet
Tsoil=zeros(n,m,tt);

for l=1:tt
for k=1:p
    %Calculation of the fluid temperature (Eq.4.4)
    if k==1
    Tf_new(k)=(((cf1*(Tp_old(k)-Tf_old(k)))-(cf2*(Tf_old(k)-
Tfi)))/cf3)+Tf_old(k);
    elseif k>1
    Tf_new(k)=(((cf1*(Tp_old(k)-Tf_old(k)))-(cf2*(Tf_old(k)-Tf_old(k-
1))))/cf3)+Tf_old(k);
    end
    %Determine the average soil temperature around the pipe
    Ts_aveold=(Ts_old(3,1,k)+ Ts_old(5,1,k)+ 2*Ts_old(4,2,k))/4;
    %Calculation pf the pipe temperature (Eq.4.5)
    Tp_new(k)=(cp1*((cp2*(Tf_new(k)-Tp_old(k)))+(cp3*(Ts_aveold-
Tp_old(k)))))+Tp_old(k);
 end
%-----------------------------------------------------------------------
% Surface boundary
%Ts next to soil boundary
% Corner left hand side (i=1 and j=1)Eq.4.8
    for j=1
        for i=1
            for k=1:p

Ts_new(j,i,k)=(Fo*(2*Ts_old(j,i+1,k)+Ts_old(j+1,i,k)+((Uas*dx*Ta)/ks)+((H*d
x^2)/ks)))+(1-(3+((Uas*dx)/ks))*Fo)*Ts_old(j,i,k);
            end
```

```matlab
                end
            end
% Middle nodes(i=2,3,4....m-1 and j=1)Eq.4.9
      for j=1
            for i=2:m-1
                for k=1:p
                Ts_new(j,i,k)=(Fo*(Ts_old(j,i-
1,k)+Ts_old(j,i+1,k)+Ts_old(j+1,i,k)+((Uas*dx*Ta)/ks)+((H*dx^2)/ks)))+(1-
(3+((Uas*dx)/ks))*Fo)*Ts_old(j,i,k);
                end
            end
      end
% Corner right hand side (i=m and j=1)Eq.4.10
     for j=1
        for i=m
            for k=1:p
             Ts_new(j,i,k)=(Fo*(Ts_old(j,i-
1,k)+Ts_old(j+1,i,k)+((Uas*dx*Ta)/ks)+((H*dx^2)/ks)))+(1-
(2+((Uas*dx)/ks))*Fo)*Ts_old(j,i,k);
            end
        end
     end


%Ts next to soil boundary
% Bottom boundary
% Corner left hand side (i=1 and j=n) Eq.4.11
      for j=n
            for i=1
                for k=1:p
                Ts_new(j,i,k)=(Fo*(2*Ts_old(j,i+1,k)+Ts_old(j-
1,i,k)+((H*dx^2)/ks)))+(1-3*Fo)*Ts_old(j,i,k);
                end
            end
      end
% Middle nodes(i=2,3,4....m-1 and j=n) Eq.4.12
      for j=n
            for i=2:m-1
                for k=1:p
                 Ts_new(j,i,k)=(Fo*(Ts_old(j,i-1,k)+Ts_old(j,i+1,k)+Ts_old(j-
1,i,k)+((H*dx^2)/ks)))+(1-3*Fo)*Ts_old(j,i,k);
                end
            end
      end
% Corner right hand side (i=m and j=n) Eq.4.13
     for j=n
        for i=m
            for k=1:p
             Ts_new(j,i,k)=(Fo*(Ts_old(j,i-1,k)+Ts_old(j-
1,i,k)+((H*dx^2)/ks)))+(1-2*Fo)*Ts_old(j,i,k);
            end
        end
     end


% Symmetry boundary
%Middle nodes(i=m and j=2,3,4....n-1) Eq.4.14
    for j=2:n-1
        for i=m
            for k=1:p
             Ts_new(j,i,k)=(Fo*(Ts_old(j,i-1,k)+Ts_old(j+1,i,k)+Ts_old(j-
1,i,k)+((H*dx^2)/ks)))+(1-3*Fo)*Ts_old(j,i,k);
            end
        end
    end
%Middle nodes(i=1 and j=2,3,4....n-1) Eq.4.15
```

```matlab
for j=2
        for i=1
            for k=1:p
             Ts_new(j,i,k)=(Fo*(Ts_old(j,i+1,k)+Ts_old(j+1,i,k)+Ts_old(j-
1,i,k)+((H*dx^2)/ks)))+(1-3*Fo)*Ts_old(j,i,k);
            end
        end
end
for j=6:n-1
        for i=1
            for k=1:p
            Ts_new(j,i,k)=(Fo*(Ts_old(j,i+1,k)+Ts_old(j+1,i,k)+Ts_old(j-
1,i,k)+((H*dx^2)/ks)))+(1-3*Fo)*Ts_old(j,i,k);
            end
        end
end
%Ts for node situated above the pipe Eq.4.16
for j=3
        for i=1
            for k=1:p
            Ts_new(j,i,k)=(Fo*(2*Tp_new(k)+2*Ts_old(j,i+1,k)+Ts_old(j-
1,i,k)+((H*dx^2)/ks)))+(1 - 5*Fo)*Ts_old(j,i,k);
            end
        end
end
%Ts for node situated below the pipe Eq.4.17
    for j=5
        for i=1
            for k=1:p

Ts_new(j,i,k)=(Fo*(2*Tp_new(k)+2*Ts_old(j,i+1,k)+Ts_old(j+1,i,k)+((H*dx^2)/
ks)))+(1 - 5*Fo)*Ts_old(j,i,k);
            end
        end
    end
%Ts for node situated on the right handside of the pipe Eq.4.18
    for j=4
        for i=2
         for k=1:p

Ts_new(j,i,k)=(Fo*(2*Tp_new(k)+Ts_old(j,i+1,k)+Ts_old(j+1,i,k)+Ts_old(j-
1,i,k)+((H*dx^2)/ks)))+(1 - 5*Fo)*Ts_old(j,i,k);
          end
         end
    end

% Ts Interior nodes Eq.4.6
for j=2:3
        for i=2:m-1
            for k=1:p
             Ts_new(j,i,k)=(Fo*(Ts_old(j,i+1,k)+Ts_old(j,i-
1,k)+Ts_old(j+1,i,k)+Ts_old(j-1,i,k)+((H*dx^2)/ks))) + (1 -
4*Fo)*Ts_old(j,i,k);
            end
        end
end
for j=4
        for i=3:m-1
            for k=1:p
             Ts_new(j,i,k)=(Fo*(Ts_old(j,i+1,k)+Ts_old(j,i-
1,k)+Ts_old(j+1,i,k)+Ts_old(j-1,i,k)+((H*dx^2)/ks))) + (1 -
4*Fo)*Ts_old(j,i,k);
            end
        end
```

```
end
for j=5:n-1
        for i=2:m-1
            for k=1:p
            Ts_new(j,i,k)=(Fo*(Ts_old(j,i+1,k)+Ts_old(j,i-
1,k)+Ts_old(j+1,i,k)+Ts_old(j-1,i,k)+((H*dx^2)/ks))) + (1 -
4*Fo)*Ts_old(j,i,k);
                end
        end
end

Tf_old=Tf_new;
Tp_old=Tp_new;
Ts_old=Ts_new;

% soil temperature at a distance 9.5 m from the pipe's inlet
Ts_new9p5=Ts_new(:,:,Pz);

%Save fluid outlet temperature
Tfoutlet_cel=Tf_new(p)-273.15;%Outlet fluid temperature
Tfluid_outlet(l)=Tfoutlet_cel;%Store the outlet fluid temperature at
various time step

%Save pipe temperature
Tpipe(l,:)=Tp_new-273.15;%Pipe temperature

%Save soil temperature
Tsoil(:,:,l)=Ts_new9p5-273.15;%Soil temperature at a distance 9.5 m from
the pipe's inlet
End
```

B. Vertical GHE

The vertical GHE model developed in Section 5.2 is saved as a model m-file. The computer program for the vertical GHE model is shown below.

```matlab
%----------------------- INPUT PARAMETERS------------------------------%
clear all
% Working Fluid
Tfi=60+273.15; %Inlet fluid temperature(K)
mf=0.3; %Fluid mass flow rate(kg/s)
rhof=980; %Fluid density(kg/m^3)
kf=0.66; %(Fluid thermal conductivity(W/mK)
cf=4188; %Fluid specific heat(W/mK)
v_kin=0.4435e-6; %Kinematic viscosity of fluid %(m^2/s)
Prf=2.66; %Prandtl number

% Pipe (PVC)
d_out=0.029; %Outer diameter of the pipe(m)
d_in=0.025; %Inner diameter of the pipe(m)
kp=0.147; %Pipe thermal conductivity(W/mK)
rhop=1400; %Pipe density(kg/m^3)
th_p=(d_out-d_in)/2; %Pipe thickness(m)
cp=1046.5; %Pipe specific heat(J/kgK)

% Grout
rhog=1500; %Grout density(kg/m^3)
kg=2; %Grout thermal conductivity(W/mK)
cg=1140; %Grout specific heat(J/kgK)
alfag=kg/(rhog*cg); %Grout thermal diffusivity(m^2/s)

% Soil (sand)#1st soil layer
rhos_1=1500; %Soil density of 1st soil layer(kg/m^3)
ks_1=1.3; %Soil thermal conductivity of 1st soil layer(W/mK)
cs_1=1140; %Soil specific heat of 1st soil layer(J/kgK)
alfas_1=ks_1/(rhos_1*cs_1); %Soil thermal diffusivity of 1st soil
layer(m^2/s)

% Soil (sandyloam)#2nd soil layer
rhos_2=1500; %Soil density of 2nd soil layer(kg/m^3)
ks_2=0.37; %Soil thermal conductivity of 2nd soil layer(W/mK)
cs_2=1264.7; %Soil specific heat of 2nd soil layer(J/kgK)
alfas_2=ks_2/(rhos_2*cs_2); %Soil thermal diffusivity of 2nd soil
layer(m^2/s)

% Soil (loam)#3th soil layer
rhos_3=1650; %Soil density of 3rd soil layer(kg/m^3)
ks_3=0.42; %Soil thermal conductivity of 3rd soil layer(W/mK)
cs_3=1450; %Soil specific heat of 3rd soil layer(J/kgK)
alfas_3=ks_3/(rhos_3*cs_3); %Soil thermal diffusivity of 3rd soil
layer(m^2/s)

%Borehole
d_bhe=0.15; %Borehole diameter(m)
Z=60; %Borehole depth(m)
L_s=0.07; %Pipe spacing(m)
D_f=6; %Far field diameter boundary(m)
R_f=D_f/2; %Far field radius boundary(m)
Ab=(pi*D_f^2)/4; %Area of far field diameter boundary(m)
Pb=pi*D_f; %Perimeter of far field diameter boundary(m)
```

167

```matlab
%Calculate the equivalent diameter
d_eqin=sqrt(2*d_in*L_s);
d_eqout=sqrt(2*d_out*L_s);

%Discretization of the grout
drg=(d_bhe-d_eqin)/2; %Finite increment of the grout in radius direction(m)
dzg=0.2; %Finite increment of the grout in axial direction(m)

%Discretization of the soil domain
Ths=(D_f-d_bhe)/2;% The soil thickness (from the outer radius of the grout
to outer radius of soil boundary)
drs=0.04; %Finite increment of the soil in axial direction(m)
dzs=dzg; %%Finite increment of the soil in axial direction(m)

% Generate the mesh
m=Ths/drs; %Number of grid columns
m=round(m);
n=Z/dzs; %Number of grid rows
n=round(n);
z=(dzs/2):dzs:Z; %Discretisation of soil depth (m)


rg=(d_eqin/2)+(drg/2); %Distance from the centre of the pipe to centre
nodal of the grout control volume (m)
rs_1=(d_bhe/2)+(drs/2); %Radius from the centre of the BHE to the nodal of
first soil domain(m)
rs=rs_1:drs:R_f; %Radius from the centre of the BHE to each soil's control
volume nodal (m)

% Bottom depth of ground layer
z_1=20; %Depth1: From the surface to the bottom of 1st soil layer (m)
z_2=40; %Depth2: From the surface to the bottom 2nd soil layer (m)
z_3=Z; %m Depth3: From the surface to the bottom 3rd soil layer (m)

z_1_1=z_1-(dzs+(dzs*0.5)); %The depth from the surface to the n-1 nodal of
1st soil layer (m)
z_1_2=z_1-(dzs*0.5); %The depth from the surface to the n nodal of 1st soil
layer (m)

z_2_1=z_1+(dzs*0.5); %The depth from the surface to the 1st nodal of 2nd
soil layer (m)
z_2_2=z_2-(dzs+(dzs*0.5)); %The depth from the surface to the n-1 nodal of
2nd soil layer (m)
z_2_3=z_2-(dzs*0.5); %The depth from the surface to the n nodal of 2nd soil
layer (m)

z_3_1=z_2+(dzs*0.5); %The depth from the surface to the 1st nodal of 3rd
soil layer (m)
z_3_2=z_3-(dzs+(dzs*0.5)); %The depth from the surface to the n-1 nodal of
3rd soil layer (m)

%Internal heat source term
H1=1.64; %Internal heat source term value to a depth of 1 m (W/m^3)
H2=1.14; %Internal heat source term value to a depth of 2 m (W/m^3)
H3=0.79; %Internal heat source term value to a depth of 3 m (W/m^3)
H4=0.55; %Internal heat source term value to a depth of 4 m (W/m^3)
H5=0.38; %Internal heat source term value to a depth of 5 m (W/m^3)
H6=0.26; %Internal heat source term value to a depth of 6 m (W/m^3)
H7=0.18; %Internal heat source term value to a depth of 7 m (W/m^3)
H8=0.13; %Internal heat source term value to a depth of 8 m (W/m^3)
H9=0.09; %Internal heat source term value to a depth of 9 m (W/m^3)
H10=0.06; %Internal heat source term value to a depth of 10 m (W/m^3)
H11=0.04; %Internal heat source term value to a depth of 11 m (W/m^3)
```

```matlab
H12=0.03; %Internal heat source term value to a depth of 12 m (W/m^3)
H13=0; %Internal heat source term value to a depth more than 12 m (W/m^3)


%Initial fluid temperature at each control volume (inside the pipe)
Tf=20+273.15; %K
Tf_old=Tf*ones(1,n); %Fluid temperature in the control volume at the
current time step (K)
Tf_new=Tf*ones(1,n); %Fluid temperature in the control volume at the new
time step (K)

%Initial pipe temperature at each control volume
Tp=Tf;
Tp_old=Tp*ones(1,n); %Pipe temperature at each control volume at the
current time step (K)
Tp_new=Tp*ones(1,n); %Pipe temperature at each control volume at the new
time step (K)

%Soil temperature
load('Ts.mat'); %Load the soil temperature at various depth
Ts=Ts+273.15; %The soil temperature is converted from Celsius to Kelvin
Ts_old=repmat(Ts,1,m); %Soil temperature at each control volume at the
current time step (K)
Ts_new=zeros(n,m); %Soil temperature at each control volume at the new time
step (K)

%Grout temperature
%The initial grout temperature is assumed the same as initial soil
temperature
Tg_old=Ts;
Tg_new=Ts;

%Determine pipe's area
Ap=(pi*d_eqin^2)/4; %%Cross section area of the pipe(m^2)
Aps=pi*d_eqin*dzs; %Surface area of the pipe(m^2)

%Determine pipe's volume
Vp=(d_eqout^2 - d_eqin^2)*(pi*dzs)/4; %Volume of pipe wall (m^3)

% Determine the convective heat transfer coefficient of fluid circulated
vf=mf/(rhof*Ap); %Fluid velocity(m/s)
Re=(vf*d_eqin)/v_kin; %Reynold Number
if Re <=2000
Nu=4.36; %Nusselt Number for laminar flow
else
nn=0.3; %nn=0.3 for cooling and nn=0.4 for heating
Nu=0.023*(Re^(4/5))*Prf^nn; %Nusselt Number for turbulent flow
end
hf=Nu*kf/d_eqin; %Convective heat transfer of working fluid(W/m^2K)

% Determine the convective heat transfer coefficient of air in contact with
% soil surface
Ta=29+273.15; %The average air temperature in Adelaide in January (K)
Va=4.9; %Annual average wind speed in Adelaide (m/s)
va=15.89e-6; %Kinematic viscosity of air (m^2/s)
ka=26.3e-3; %Thermal conductivity of air (W/mK)
Pra=0.707; %Prandtl Number
L=Ab/Pb; %Unit length (m)
Rea=Va*L/va; %Reynold Number
if Rea>=5e5
    Nua=0.037*(Rea^0.8)*Pra^(1/3); %Nusselt Number for laminar flow
else
    Nua=0.664*(Rea^0.5)*Pra^(1/3); %Nusselt Number for turbulent flow
```

```matlab
end
ha=Nua*ka/L; %Convective heat transfer of air in contact with soil surface
(W/m^2K)


%Time discretization
T=10*3600; %Maximum simulation time (s)
% Courant-Friedrichs-Lewy condition
dt=dzs/vf; %Time step (s)
mu=vf*dt/dzs; %The Courant number
if mu>1 %make sure dt satisfy stability condition
    error('mu should <1')
end
tt=T/dt; %Number of time steps
tt=ceil(tt);
t=0:dt:T; %Temporal discretisation (s)
t_hour=t/3600; %Temporal discretisation (h)

%Calculate Fourier number
Fos_1=alfas_1*dt/drs^2; %For the 1st soil layer
Fos_2=alfas_2*dt/drs^2; %For the 2nd soil layer
Fos_3=alfas_3*dt/drs^2; %For the 3rd soil layer


Fog=alfag*dt/drg^2;


%Constants in fluid temperature equation
cf1=pi*d_eqin*hf;
cf2=mf*cf/dzs;
cf3=cf*rhof*Ap/dt;
cf4=dt/(rhof*Ap*dzs*cf);

%Constants in pipe temperature equation
cp1=dt/(cp*rhop*Vp);
cp2=Aps*hf;
cp3=(kg*Aps)/(0.5*drg);
cp4=kp*Aps/th_p;

%Constant in grout temperature equation
Cg1=dzg/drg; %Coefficient if drg is not equal to drs
Cag=drg/((kg*Cg1/ha)+ (drg*Cg1^2)/2);
Csg_s_1=0.5/(1+(drg/(2*rg))) +
((drs/(2*drg))/((ks_1/kg)*(1+(drg/(2*rg)))));
Csg_s_2=0.5/(1+(drg/(2*rg))) +
((drs/(2*drg))/((ks_2/kg)*(1+(drg/(2*rg)))));
Csg_s_3=0.5/(1+(drg/(2*rg))) +
((drs/(2*drg))/((ks_3/kg)*(1+(drg/(2*rg)))));

%Constant in soil temperature equation
Cs1=dzs/drs;%coefficient if drs is not equalto drs
Cas=drs/((ks_1*Cs1/ha)+ ((Cs1^2)*drs)/2);

%Stored outlet fluid temperature
Tfluid_outlet=ones(1,tt);

 for l=1:tt
%Calculation of the fluid temperature Eq.5.6
  for j=1:n
      if j==1
      Tf_new(j)=(((cf1*(Tp_old(j)-Tf_old(j)))-(cf2*(Tf_old(j)-
Tfi)))/cf3)+Tf_old(j);
      elseif j>1
      Tf_new(j)=(((cf1*(Tp_old(j)-Tf_old(j)))-(cf2*(Tf_old(j)-Tf_old(j-
1))))/cf3)+Tf_old(j);
      end
```

```matlab
  %Calculation of the pipe temperature Eq.5.7
  Tp_new(j)=(cp1*((cp2*(Tf_new(j)-Tp_old(j)))+(cp3*(Tg_old(j)-
Tp_old(j))))))+Tp_old(j);
   end
%Grout temperature calculation
%The grout temperature next to surface boundary (j = 1) Eq.5.11
for j=1
   for i=1
     Tg_new(j,i)=Fog*(2*Tp_new(j)*(1-(drg/(2*rg)))+ Ts_old(j,i)/Csg_s_1 +
Ta*Cag + Tg_old(j+1,i)/Cg1^2) + (1-(2*(1-(drg/(2*rg))) + 1/Csg_s_1 + Cag +
1/Cg1^2)*Fog)*Tg_old(j,i);
   end
end
%The grout temperature for the internal nodes (j = 2,3,4….n-1)Eq.5.10
for j=2:n-1
    for i=1
        if z(j)<=z_1
        Csg=Csg_s_1;
        elseif z(j)<=z_2
        Csg=Csg_s_2;
        elseif z(j)<=z_3
        Csg=Csg_s_3;
        end
    Tg_new(j,i)=Fog*(2*Tp_new(j)*(1-(drg/(2*rg)))+ Ts_old(j,i)/Csg +
Tg_old(j-1,i)/Cg1^2 + Tg_old(j+1,i)/Cg1^2) + (1-(2*(1-(drg/(2*rg))) + 1/Csg
+ 2/Cg1^2)*Fog)*Tg_old(j,i);
    end
end
%The grout temperature next to bottom boundary (j = n) Eq.5.12
 for j=n
    for i=1
    Tg_new(j,i)=Fog*(2*Tp_new(j)*(1-(drg/(2*rg)))+ Ts_old(j,i)/Csg_s_3 +
Tg_old(j-1,i)/Cg1^2)+(1-(2*(1-(drg/(2*rg))) + 1/Csg_s_3 +
1/Cg1^2)*Fog)*Tg_old(j,i);
    end
 end
%Surface boundary
%Corner left hand side (i=1 and j=1)Eq.5.15
for j=1
    for i=1
        if z(j)<=1
        H=H1;
        elseif z(j)<=2
        H=H2;
        elseif z(j)<=3
        H=H3;
        elseif z(j)<=4
        H=H4;
        elseif z(j)<=5
        H=H5;
        elseif z(j)<=6
        H=H6;
        elseif z(j)<=7
        H=H7;
        elseif z(j)<=8
        H=H8;
        elseif z(j)<=9
        H=H9;
        elseif z(j)<=10
        H=H10;
        elseif z(j)<=11
        H=H11;
        elseif z(j)<=12
        H=H12;
        else
```

```
                H=H13;
            end
        Fos=Fos_1;
        ks=ks_1;
        Cgs=((drg/(2*drs))/((1-(drs/(2*rs(i))))*kg/ks))+(0.5/(1-
(drs/(2*rs(i))))));
        Ts_new(j,i)=Fos*(Tg_old(j,i)/Cgs + (1+(drs/(2*rs(i))))*Ts_old(j,i+1)+
Ta*Cas + Ts_old(j+1,i)/Cs1^2 + ((H*drs^2)/ks)) + (1-(1/Cgs +
(1+(drs/(2*rs(i)))) + Cas + 1/Cs1^2)*Fos)*Ts_old(j,i);
        end
end
% Middle nodes(i=2,3,4....m-1 and j=1)Eq.5.18
for j=1
    for i=2:m-1
        if z(j)<=1
        H=H1;
        elseif z(j)<=2
        H=H2;
        elseif z(j)<=3
        H=H3;
        elseif z(j)<=4
        H=H4;
        elseif z(j)<=5
        H=H5;
        elseif z(j)<=6
        H=H6;
        elseif z(j)<=7
        H=H7;
        elseif z(j)<=8
        H=H8;
        elseif z(j)<=9
        H=H9;
        elseif z(j)<=10
        H=H10;
        elseif z(j)<=11
        H=H11;
        elseif z(j)<=12
        H=H12;
        else
        H=H13;
        end
        Fos=Fos_1;
        ks=ks_1;
      Ts_new(j,i)=Fos*((1-(drs/(2*rs(i))))*Ts_old(j,i-1) +
(1+(drs/(2*rs(i))))*Ts_old(j,i+1)+ Ta*Cas + Ts_old(j+1,i)/Cs1^2 +
((H*drs^2)/ks)) + (1-((1-(drs/(2*rs(i)))) + (1+(drs/(2*rs(i)))) + Cas +
1/Cs1^2)*Fos)*Ts_old(j,i);
        end
end
% Corner right hand side (i=m and j=1)Eq.5.19
for j=1
    for i=m
        if z(j)<=1
        H=H1;
        elseif z(j)<=2
        H=H2;
        elseif z(j)<=3
        H=H3;
        elseif z(j)<=4
        H=H4;
        elseif z(j)<=5
        H=H5;
        elseif z(j)<=6
        H=H6;
        elseif z(j)<=7
```

```matlab
            H=H7;
            elseif z(j)<=8
            H=H8;
            elseif z(j)<=9
            H=H9;
            elseif z(j)<=10
            H=H10;
            elseif z(j)<=11
            H=H11;
            elseif z(j)<=12
            H=H12;
            else
            H=H13;
            end
        Fos=Fos_1;
        ks=ks_1;
        Ts_new(j,i)=Fos*((1-(drs/(2*rs(i))))*Ts_old(j,i-1) + Ta*Cas +
Ts_old(j+1,i)/Cs1^2 + ((H*drs^2)/ks)) + (1-((1-(drs/(2*rs(i)))) + Cas +
1/Cs1^2)*Fos)*Ts_old(j,i);
        end
end
%Bottom boundary
% Corner left hand side (i=1 and j=n) Eq.5.20
for j=n
    for i=1
        if z(j)<=1
        H=H1;
        elseif z(j)<=2
        H=H2;
        elseif z(j)<=3
        H=H3;
        elseif z(j)<=4
        H=H4;
        elseif z(j)<=5
        H=H5;
        elseif z(j)<=6
        H=H6;
        elseif z(j)<=7
        H=H7;
        elseif z(j)<=8
        H=H8;
        elseif z(j)<=9
        H=H9;
        elseif z(j)<=10
        H=H10;
        elseif z(j)<=11
        H=H11;
        elseif z(j)<=12
        H=H12;
        else
        H=H13;
        end
    Fos=Fos_3;
    ks=ks_3;
    Cgs=((drg/(2*drs))/((1-(drs/(2*rs(i))))*kg/ks))+(0.5/(1-
(drs/(2*rs(i)))));
    Ts_new(j,i)=Fos*(Tg_old(j,i)/Cgs + (1+(drs/(2*rs(i))))*Ts_old(j,i+1)+
Ts_old(j-1,i)/Cs1^2 + ((H*drs^2)/ks)) + (1-(1/Cgs + (1+(drs/(2*rs(i)))) +
1/Cs1^2)*Fos)*Ts_old(j,i);
        end
end
% Middle nodes(i=2,3,4....m-1 and j=n) Eq.5.21
for j=n
    for i=2:m-1
        if z(j)<=1
```

173

```matlab
        H=H1;
        elseif z(j)<=2
        H=H2;
        elseif z(j)<=3
        H=H3;
        elseif z(j)<=4
        H=H4;
        elseif z(j)<=5
        H=H5;
        elseif z(j)<=6
        H=H6;
        elseif z(j)<=7
        H=H7;
        elseif z(j)<=8
        H=H8;
        elseif z(j)<=9
        H=H9;
        elseif z(j)<=10
        H=H10;
        elseif z(j)<=11
        H=H11;
        elseif z(j)<=12
        H=H12;
        else
        H=H13;
        end
    Fos=Fos_3;
    ks=ks_3;
    Ts_new(j,i)=Fos*((1-(drs/(2*rs(i))))*Ts_old(j,i-1) +
(1+(drs/(2*rs(i))))*Ts_old(j,i+1)+ Ts_old(j-1,i)/Cs1^2 + ((H*drs^2)/ks))+
(1-((1-(drs/(2*rs(i)))) + (1+(drs/(2*rs(i)))) + 1/Cs1^2)*Fos)*Ts_old(j,i);
    end
end
% Corner right hand side (i=m and j=n) Eq.5.22
for j=n
    for i=m
        if z(j)<=1
        H=H1;
        elseif z(j)<=2
        H=H2;
        elseif z(j)<=3
        H=H3;
        elseif z(j)<=4
        H=H4;
        elseif z(j)<=5
        H=H5;
        elseif z(j)<=6
        H=H6;
        elseif z(j)<=7
        H=H7;
        elseif z(j)<=8
        H=H8;
        elseif z(j)<=9
        H=H9;
        elseif z(j)<=10
        H=H10;
        elseif z(j)<=11
        H=H11;
        elseif z(j)<=12
        H=H12;
        else
        H=H13;
        end
    Fos=Fos_3;
    ks=ks_3;
```

```matlab
        Ts_new(j,i)=Fos*((1-(drs/(2*rs(i))))*Ts_old(j,i-1) + Ts_old(j-
1,i)/Cs1^2 + ((H*drs^2)/ks))+ (1-((1-(drs/(2*rs(i)))) +
1/Cs1^2)*Fos)*Ts_old(j,i);
    end
end
%Lateral boundary
%Middle nodes(i=1 and j=2,3,4....n-1) Eq.5.23
for j=2:n-1
    for i=1
        if z(j)<=1
        H=H1;
        elseif z(j)<=2
        H=H2;
        elseif z(j)<=3
        H=H3;
        elseif z(j)<=4
        H=H4;
        elseif z(j)<=5
        H=H5;
        elseif z(j)<=6
        H=H6;
        elseif z(j)<=7
        H=H7;
        elseif z(j)<=8
        H=H8;
        elseif z(j)<=9
        H=H9;
        elseif z(j)<=10
        H=H10;
        elseif z(j)<=11
        H=H11;
        elseif z(j)<=12
        H=H12;
        else
        H=H13;
        end
if z(j)<=z_1_1
        Fos=Fos_1;
        ks=ks_1;
        Cgs=((drg/(2*drs))/((1-(drs/(2*rs(i))))*kg/ks))+(0.5/(1-
(drs/(2*rs(i))))));
        Ts_new(j,i)=Fos*(Tg_old(j,i)/Cgs +
(1+(drs/(2*rs(i))))*Ts_old(j,i+1) + Ts_old(j-1,i)/Cs1^2 +
Ts_old(j+1,i)/Cs1^2 +((H*drs^2)/ks)) + (1-(1/Cgs + (1+(drs/(2*rs(i)))) +
2/Cs1^2)*Fos)*Ts_old(j,i);
        elseif z(j)<=z_1_2
        Fos=Fos_1;
        ks=ks_1;
        Cgs=((drg/(2*drs))/((1-(drs/(2*rs(i))))*kg/ks))+(0.5/(1-
(drs/(2*rs(i))))));
        Ts_new(j,i)=Fos*(Tg_old(j,i)/Cgs +
(1+(drs/(2*rs(i))))*Ts_old(j,i+1) + Ts_old(j-1,i)/Cs1^2 +
(1+(ks_2/ks))*0.5*Ts_old(j+1,i)/Cs1^2 +((H*drs^2)/ks)) + (1-(1/Cgs +
(1+(drs/(2*rs(i)))) + ((1+(ks_2/ks))*0.5 + 1)/Cs1^2)*Fos)*Ts_old(j,i);
         elseif z(j)<=z_2_1
        Fos=Fos_2;
        ks=ks_2;
        Cgs=((drg/(2*drs))/((1-(drs/(2*rs(i))))*kg/ks))+(0.5/(1-
(drs/(2*rs(i))))));
        Ts_new(j,i)=Fos*(Tg_old(j,i)/Cgs +
(1+(drs/(2*rs(i))))*Ts_old(j,i+1) + (1+(ks_1/ks))*0.5*Ts_old(j-1,i)/Cs1^2 +
Ts_old(j+1,i)/Cs1^2 +((H*drs^2)/ks)) + (1-(1/Cgs + (1+(drs/(2*rs(i)))) +
((1+(ks_1/ks))*0.5 + 1)/Cs1^2)*Fos)*Ts_old(j,i);
        elseif z(j)<=z_2_2
        Fos=Fos_2;
```

```matlab
            ks=ks_2;
            Cgs=((drg/(2*drs))/((1-(drs/(2*rs(i))))*kg/ks))+(0.5/(1-
(drs/(2*rs(i))))));
            Ts_new(j,i)=Fos*(Tg_old(j,i)/Cgs +
(1+(drs/(2*rs(i))))*Ts_old(j,i+1) + Ts_old(j-1,i)/Cs1^2 +
Ts_old(j+1,i)/Cs1^2 +((H*drs^2)/ks)) + (1-(1/Cgs + (1+(drs/(2*rs(i)))) +
2/Cs1^2)*Fos)*Ts_old(j,i);
        elseif z(j)<=z_2_3
            Fos=Fos_2;
            ks=ks_2;
            Cgs=((drg/(2*drs))/((1-(drs/(2*rs(i))))*kg/ks))+(0.5/(1-
(drs/(2*rs(i))))));
            Ts_new(j,i)=Fos*(Tg_old(j,i)/Cgs +
(1+(drs/(2*rs(i))))*Ts_old(j,i+1) + Ts_old(j-1,i)/Cs1^2 +
(1+(ks_3/ks))*0.5*Ts_old(j+1,i)/Cs1^2 +((H*drs^2)/ks)) + (1-(1/Cgs +
(1+(drs/(2*rs(i)))) + ((1+(ks_3/ks))*0.5 + 1)/Cs1^2)*Fos)*Ts_old(j,i);
        elseif z(j)<=z_3_1
            Fos=Fos_3;
            ks=ks_3;
            Cgs=((drg/(2*drs))/((1-(drs/(2*rs(i))))*kg/ks))+(0.5/(1-
(drs/(2*rs(i))))));
            Ts_new(j,i)=Fos*(Tg_old(j,i)/Cgs +
(1+(drs/(2*rs(i))))*Ts_old(j,i+1) + (1+(ks_2/ks))*0.5*Ts_old(j-1,i)/Cs1^2 +
Ts_old(j+1,i)/Cs1^2 +((H*drs^2)/ks)) + (1-(1/Cgs + (1+(drs/(2*rs(i)))) +
((1+(ks_2/ks))*0.5 + 1)/Cs1^2)*Fos)*Ts_old(j,i);
        elseif z(j)<=z_3_2
            Fos=Fos_3;
            ks=ks_3;
            Cgs=((drg/(2*drs))/((1-(drs/(2*rs(i))))*kg/ks))+(0.5/(1-
(drs/(2*rs(i))))));
            Ts_new(j,i)=Fos*(Tg_old(j,i)/Cgs +
(1+(drs/(2*rs(i))))*Ts_old(j,i+1) + Ts_old(j-1,i)/Cs1^2 +
Ts_old(j+1,i)/Cs1^2 +((H*drs^2)/ks)) + (1-(1/Cgs + (1+(drs/(2*rs(i)))) +
2/Cs1^2)*Fos)*Ts_old(j,i);
end
    end
end
%Lateral boundary
%Middle nodes(i=m and j=2,3,4....n-1) Eq.5.24
for j=2:n-1
    for i=m
        if z(j)<=1
        H=H1;
        elseif z(j)<=2
        H=H2;
        elseif z(j)<=3
        H=H3;
        elseif z(j)<=4
        H=H4;
        elseif z(j)<=5
        H=H5;
        elseif z(j)<=6
        H=H6;
        elseif z(j)<=7
        H=H7;
        elseif z(j)<=8
        H=H8;
        elseif z(j)<=9
        H=H9;
        elseif z(j)<=10
        H=H10;
        elseif z(j)<=11
        H=H11;
        elseif z(j)<=12
        H=H12;
```

```matlab
            else
            H=H13;
            end
            if z(j)<=z_1_1
            Fos=Fos_1;
            ks=ks_1;
             Ts_new(j,i)=Fos*((1-(drs/(2*rs(i))))*Ts_old(j,i-1) + Ts_old(j-
1,i)/Cs1^2 + Ts_old(j+1,i)/Cs1^2 + ((H*drs^2)/ks)) + (1-((1-
(drs/(2*rs(i)))) + 2/Cs1^2)*Fos)*Ts_old(j,i);
            elseif z(j)<=z_1_2
            Fos=Fos_1;
            ks=ks_1;
            Ts_new(j,i)=Fos*((1-(drs/(2*rs(i))))*Ts_old(j,i-1) + Ts_old(j-
1,i)/Cs1^2 + (1+(ks_2/ks))*0.5*Ts_old(j+1,i)/Cs1^2 + ((H*drs^2)/ks)) + (1-
((1-(drs/(2*rs(i)))) + ((1+(ks_2/ks))*0.5 + 1)/Cs1^2)*Fos)*Ts_old(j,i);
            elseif z(j)<=z_2_1
            Fos=Fos_2;
            ks=ks_2;
            Ts_new(j,i)=Fos*((1-(drs/(2*rs(i))))*Ts_old(j,i-1) +
(1+(ks_1/ks))*0.5*Ts_old(j-1,i)/Cs1^2 + Ts_old(j+1,i)/Cs1^2
+((H*drs^2)/ks)) + (1-((1-(drs/(2*rs(i)))) + ((1+(ks_1/ks))*0.5 +
1)/Cs1^2)*Fos)*Ts_old(j,i);
             elseif z(j)<=z_2_2
            Fos=Fos_2;
            ks=ks_2;
            Ts_new(j,i)=Fos*((1-(drs/(2*rs(i))))*Ts_old(j,i-1) + Ts_old(j-
1,i)/Cs1^2 + Ts_old(j+1,i)/Cs1^2 + ((H*drs^2)/ks)) + (1-((1-
(drs/(2*rs(i)))) + 2/Cs1^2)*Fos)*Ts_old(j,i);
            elseif z(j)<=z_2_3
            Fos=Fos_2;
            ks=ks_2;
            Ts_new(j,i)=Fos*((1-(drs/(2*rs(i))))*Ts_old(j,i-1) + Ts_old(j-
1,i)/Cs1^2+ (1+(ks_3/ks))*0.5*Ts_old(j+1,i)/Cs1^2 + ((H*drs^2)/ks)) + (1-
((1-(drs/(2*rs(i)))) + ((1+(ks_3/ks))*0.5 + 1)/Cs1^2)*Fos)*Ts_old(j,i);
            elseif z(j)<=z_3_1
            Fos=Fos_3;
            ks=ks_3;
            Ts_new(j,i)=Fos*((1-(drs/(2*rs(i))))*Ts_old(j,i-1) +
(1+(ks_2/ks))*0.5*Ts_old(j-1,i)/Cs1^2 + Ts_old(j+1,i)/Cs1^2 +
((H*drs^2)/ks)) + (1-((1-(drs/(2*rs(i)))) + ((1+(ks_2/ks))*0.5 +
1)/Cs1^2)*Fos)*Ts_old(j,i);
            elseif z(j)<=z_3_2
            Fos=Fos_3;
            ks=ks_3;
            Ts_new(j,i)=Fos*((1-(drs/(2*rs(i))))*Ts_old(j,i-1) + Ts_old(j-
1,i)/Cs1^2 + Ts_old(j+1,i)/Cs1^2 + ((H*drs^2)/ks)) + (1-((1-
(drs/(2*rs(i)))) + 2/Cs1^2)*Fos)*Ts_old(j,i);
            end
        end
end
%Internal nodes Eq.5.13
for j=2:n-1
    for i=2:m-1
        if z(j)<=1
        H=H1;
        elseif z(j)<=2
        H=H2;
        elseif z(j)<=3
        H=H3;
        elseif z(j)<=4
        H=H4;
        elseif z(j)<=5
        H=H5;
        elseif z(j)<=6
        H=H6;
```

```matlab
        elseif z(j)<=7
        H=H7;
        elseif z(j)<=8
        H=H8;
        elseif z(j)<=9
        H=H9;
        elseif z(j)<=10
        H=H10;
        elseif z(j)<=11
        H=H11;
        elseif z(j)<=12
        H=H12;
        else
        H=H13;
        end
        if z(j)<=z_1_1
        Fos=Fos_1;
        ks=ks_1;
         Ts_new(j,i)=Fos*((1-(drs/(2*rs(i))))*Ts_old(j,i-1)+
(1+(drs/(2*rs(i))))*Ts_old(j,i+1) + Ts_old(j-1,i)/Cs1^2 +
Ts_old(j+1,i)/Cs1^2 + ((H*drs^2)/ks)) + (1-((1-(drs/(2*rs(i)))) +
(1+(drs/(2*rs(i)))) + 2/Cs1^2)*Fos)*Ts_old(j,i);
        elseif z(j)<=z_1_2
            Fos=Fos_1;
            ks=ks_1;
            Ts_new(j,i)=Fos*((1-(drs/(2*rs(i))))*Ts_old(j,i-1)+
(1+(drs/(2*rs(i))))*Ts_old(j,i+1) + Ts_old(j-1,i)/Cs1^2 +
(1+(ks_2/ks))*0.5*Ts_old(j+1,i)/Cs1^2 + ((H*drs^2)/ks)) + (1-((1-
(drs/(2*rs(i)))) + (1+(drs/(2*rs(i)))) + ((1+(ks_2/ks))*0.5 +
1)/Cs1^2)*Fos)*Ts_old(j,i);
        elseif z(j)<=z_2_1
            Fos=Fos_2;
            ks=ks_2;
            Ts_new(j,i)=Fos*((1-(drs/(2*rs(i))))*Ts_old(j,i-1)+
(1+(drs/(2*rs(i))))*Ts_old(j,i+1) + (1+(ks_1/ks))*0.5*Ts_old(j-1,i)/Cs1^2 +
Ts_old(j+1,i)/Cs1^2 + ((H*drs^2)/ks)) + (1-((1-(drs/(2*rs(i)))) +
(1+(drs/(2*rs(i)))) + ((1+(ks_1/ks))*0.5 + 1)/Cs1^2)*Fos)*Ts_old(j,i);
        elseif z(j)<=z_2_2
            Fos=Fos_2;
            ks=ks_2;
            Ts_new(j,i)=Fos*((1-(drs/(2*rs(i))))*Ts_old(j,i-1)+
(1+(drs/(2*rs(i))))*Ts_old(j,i+1) + Ts_old(j-1,i)/Cs1^2 +
Ts_old(j+1,i)/Cs1^2 + ((H*drs^2)/ks)) + (1-((1-(drs/(2*rs(i)))) +
(1+(drs/(2*rs(i)))) + 2/Cs1^2)*Fos)*Ts_old(j,i);
        elseif z(j)<=z_2_3
            Fos=Fos_2;
            ks=ks_2;
             Ts_new(j,i)=Fos*((1-(drs/(2*rs(i))))*Ts_old(j,i-1)+
(1+(drs/(2*rs(i))))*Ts_old(j,i+1) + Ts_old(j-1,i)/Cs1^2 +
(1+(ks_3/ks))*0.5*Ts_old(j+1,i)/Cs1^2 + ((H*drs^2)/ks)) + (1-((1-
(drs/(2*rs(i))))+ (1+(drs/(2*rs(i)))) + ((1+(ks_3/ks))*0.5 +
1)/Cs1^2)*Fos)*Ts_old(j,i);
        elseif z(j)<=z_3_1
          Fos=Fos_3;
          ks=ks_3;
          Ts_new(j,i)=Fos*((1-(drs/(2*rs(i))))*Ts_old(j,i-1) +
(1+(drs/(2*rs(i))))*Ts_old(j,i+1) + (1+(ks_2/ks))*0.5*Ts_old(j-1,i)/Cs1^2 +
Ts_old(j+1,i)/Cs1^2 + ((H*drs^2)/ks)) + (1-((1-(drs/(2*rs(i))))+
(1+(drs/(2*rs(i)))) + ((1+(ks_2/ks))*0.5 + 1)/Cs1^2)*Fos)*Ts_old(j,i);
            elseif z(j)<=z_3_2
            Fos=Fos_3;
            ks=ks_3;
            Ts_new(j,i)=Fos*((1-(drs/(2*rs(i))))*Ts_old(j,i-1)+
(1+(drs/(2*rs(i))))*Ts_old(j,i+1) + Ts_old(j-1,i)/Cs1^2 +
```

```matlab
Ts_old(j+1,i)/Cs1^2 + ((H*drs^2)/ks)) + (1-((1-(drs/(2*rs(i)))) +
(1+(drs/(2*rs(i)))) + 2/Cs1^2)*Fos)*Ts_old(j,i);
        end
    end
end
%-------------------------------------------------------------------------
Tf_old=Tf_new;
Tp_old=Tp_new;
Tg_old=Tg_new;
Ts_old=Ts_new;
%-------------------------------------------------------------------------
%Save fluid outlet temperature
Tfoutlet_cel=Tf_new(n)-273.15;
Tfluid_outlet(l)=Tfoutlet_cel;
end
```

C. Combined horizontal-vertical GHE

The computer program for the combined horizontal-vertical GHE model is shown below.

```
%----------------------- INPUT PARAMETERS--------------------------------%
 clear all;
% WORKING FLUID (water)
Tfi=36+273.15; %Inlet fluid temperature(K)
mf=0.2; %Fluid mass flow rate(kg/s)
rhof=995.7; %Fluid density(kg/m^3)
kf=0.66; %Fluid thermal conductivity(W/mK)
cf=4178; %Fluid specific heat(W/mK)
v_kin=0.801e-6; %Kinematic viscosity of fluid %(m^2/s)
Prf=5.43; %Prandtl number

%Pipe (PVC)
% Horizontal Pipe (PVC)
d_out_h=0.044; %Outer diameter of the pipe(m)
d_in_h=0.04; %Inner diameter of the pipe(m)
Lp_h=400; %Pipe length(m)
kp_h=0.147; %Pipe thermal conductivity(W/mK)
rhop_h=1400; %Pipe density(kg/m^3)
th_ph=(d_out_h-d_in_h)/2; %Pipe thickness(m)
cp_h=1046; %Pipe specific heat(J/kgK)
Z_h=Lp_h; %Distance in z direction(m)
dz_h=5; %Finite increment in the z direction(m)

% Vertical pipe
d_out_v=0.044; %Outer diameter of the pipe(m)
d_in_v=0.04; %Inner diameter of the pipe(m)
kp_v=0.147; %Pipe thermal conductivity(W/mK)
rhop_v=1400; %Pipe density(kg/m^3)
th_pv=(d_out_v-d_in_v)/2; %Pipe thickness(m)
cp_v=1046.5; %Pipe specific heat(J/kgK)

% Grout
rhog_v=1500; %Grout density(kg/m^3)
kg_v=2; %Grout thermal conductivity(W/mK)
cg_v=1140; %Grout specific heat(J/kgK)
alfag_v=kg_v/(rhog_v*cg_v); %Grout thermal diffusivity(m^2/s)

% Soil
rhos=1500; %Soil density(kg/m^3)
ks=1.3; %Soil thermal conductivity(W/mK)
cs=1140; %Soil specific heat (J/kgK)
alfas=ks/(rhos*cs); %Grout thermal diffusivity(m^2/s)

%Borehole
d_bhe_v=0.15; %Borehole diameter(m)
Z_v=200; %Borehole depth(m)
L_s_v=0.07; %Pipe spacing(m)
D_f_v=4; %Far field diameter boundary(m)
R_f_v=D_f_v/2; %Far field radius boundary(m)
Ab_v=(pi*D_f_v^2)/4; %Area of far field diameter boundary(m)
Pb_v=pi*D_f_v; %Perimeter of far field diameter boundary(m)

%Calculate the equivalent diameter for the vertical GHE
d_eqin_v=sqrt(2*d_in_v*L_s_v);
d_eqout_v=sqrt(2*d_out_v*L_s_v);

%Internal heat source term
H1=1.64; %Internal heat source term value to a depth of 1 m (W/m^3)
```

180

```matlab
H2=1.14; %Internal heat source term value to a depth of 2 m (W/m^3)
H3=0.79; %Internal heat source term value to a depth of 3 m (W/m^3)
H4=0.55; %Internal heat source term value to a depth of 4 m (W/m^3)
H5=0.38; %Internal heat source term value to a depth of 5 m (W/m^3)
H6=0.26; %Internal heat source term value to a depth of 6 m (W/m^3)
H7=0.18; %Internal heat source term value to a depth of 7 m (W/m^3)
H8=0.13; %Internal heat source term value to a depth of 8 m (W/m^3)
H9=0.09; %Internal heat source term value to a depth of 9 m (W/m^3)
H10=0.06; %Internal heat source term value to a depth of 10 m (W/m^3)
H11=0.04; %Internal heat source term value to a depth of 11 m (W/m^3)
H12=0.03; %Internal heat source term value to a depth of 12 m (W/m^3)
H13=0; %Internal heat source term value to a depth more than 12 m (W/m^3)


% Dimension of soil domain for horizontal GHE
X_h=0.14; % Soil domain span in x direction(m)
dx_h=0.04; %Finite increment in x direction(m)
Y_h=2; %Soil domain span in y direction(m)
dy_h=0.04; %Finite increment in y direction(m)


% Generate the mesh of the computational domain of the horizontal GHE
m_h=X_h/dx_h; %Number of grid columns
m_h=ceil(m_h);
n_h=Y_h/dy_h; %Number of grid rows
n_h=ceil(n_h);
y_h=(dy_h/2):dy_h:Y_h;
p_h=Z_h/dz_h; %Number of grid in z direction
z_h=dz_h:dz_h:Z_h;


%Grid number in z direction at a distance of 100 m
Pz_h=100/dz_h;
Pz_h=ceil(Pz_h);


%Initial fluid temperature at each control volume (inside pipe) of the
%horizontal GHE
Tf=20+273.15; %K
Tf_old_h=Tf*ones(1,p_h); %Fluid temperature in the control volume at the
current time step (K)
Tf_new_h=Tf*ones(1,p_h); %Fluid temperature in the control volume at the
new time step (K)


%Initial pipe temperature at each control volume of the horizontal GHE
Tp=Tf;
Tp_old_h=Tp*ones(1,p_h); %Pipe temperature at each control volume at the
current time step (K)
Tp_new_h=Tp*ones(1,p_h); %Pipe temperature at each control volume at the
new time step (K)


%Initial soil temperature around the horizontal GHE
load('Ts_h.mat'); %Load the soil temperature around the horizontal GHE
Ts_h=Ts_h+273.15; %Convert the unit of soil temperature from Celsius to
Kelvin (K)
Ts_h=repmat(Ts_h,1,m_h);
Ts_old_h=repmat(Ts_h,[1 1 p_h]); %Soil temperature at the current time step
(K)
Ts_new_h=zeros(n_h,m_h,p_h); %Soil temperature at each control volume at
the new time step (K)


% Determine pipe's area of the horizontal GHE
Ap_h=(pi*d_in_h^2)/4; %Cross section area of the pipe(m^2)
Aps_h=pi*d_in_h*dz_h; %Surface area of the pipe(m^2)


% Determine pipe's volume of the horizontal GHE
Vp_h=(d_out_h^2 - d_in_h^2)*(pi*dz_h)/4; %Volume of pipe wall (m^3)
```

```matlab
% Determine the convective heat transfer coefficient of fluid circulated
% inside the pipe for the horizontal GHE
vf_h=mf/(rhof*Ap_h); %(m/s)
vf_v=(vf_h*d_in_h^2)/d_eqin_v^2; %Fluid velocity(m/s)
Re_h=(vf_h*d_in_h)/v_kin; %Reynold Number
if Re_h>=2000
nn=0.3; % nn=0.3 for cooling and nn=0.4 for heating
Nu_h=0.023*(Re_h^(4/5))*Prf^nn; %Nusselt Number for turbulent flow
else
Nu=4.36; %Nusselt Number for laminar flow
end
hf_h=Nu_h*kf/d_in_h; %Convective heat transfer of working fluid(W/m^2.K)

% Determine the convective heat transfer coefficient of fluid circulated
% for the vertical GHE
Re_v=(vf_v*d_eqin_v)/v_kin; %Reynold Number
if Re_v>=2000
nn=0.3; %nn=0.3 for cooling and nn=0.4 for heating
Nu_v=0.023*(Re_v^(4/5))*Prf^nn; %Nusselt Number for turbulent flow
else
Nu_v=4.36; %Nusselt Number for laminar flow
end
hf_v=Nu_v*kf/d_eqin_v; %Convective heat transfer of working fluid(W/m^2.K)

%Time discretization
T=5*24*3600; %Maximum simulation time (s)
% Courant-Friedrichs-Lewy condition
dt_h=dz_h/vf_h; %Time step (s)
mu=vf_h*dt_h/dzs_h; %The Courant number
if mu>1 %make sure dt satisfy stability condition
error('mu should <1')
end
tt_h=T/dt_h; %Number of time steps
tt_h=ceil(tt_h);
t_h=0:dt_h:T; %Temporal discretisation (s)
th=t_h/3600; %Temporal discretisation (h)
ttt=1:length(t_h);
t_store=3600/dt_h; % Convert the unit of time step from second (s) to
hour(h)
dt_v=dt_h;

%Discretization of the grout of the vertical GHE
drg_v=(d_bhe_v-d_eqin_v)/2; %Finite increment of the grout in radius
direction(m)
dzg_v=dt_v*vf_v; %Finite increment of the grout in axial direction(m)

%Discretization of the soil domain of vertical GHE
Ths_v=(D_f_v-d_bhe_v)/2; % The soil thickness (from the outer radius of the
grout to outer radius of soil boundary)
drs_v=0.1; %Finite increment of the soil in radial direction(m)
dzs_v=dzg_v; %Finite increment of the soil in axial direction(m)

% Generate the mesh of the vertical GHE
m_v=Ths_v/drs_v; %Number of grid coloumns
m_v=round(m_v);
n_v=Z_v/dzs_v; %Number of grid rows
n_v=round(n_v);
z_v=(dzs_v/2):dzs_v:Z_v; %Discretisation of soil depth (m)

rg_v=(d_eqin_v/2)+(drg_v/2); %Distance from the centre of the pipe to
centre nodal of the grout control volume (m)
c1_v=dzg_v/drg_v; %coefficient if drg is not equalto drs
```

```matlab
Cs1_v=dzs_v/drs_v; %coefficient if drs is not equalto drs
rs_1_v=(d_bhe_v/2)+(drs_v/2); %Radius from the centre of the BHE to the
nodal of first soil domain(m)
rs_v=rs_1_v:drs_v:R_f_v; % Radius from the centre of the BHE to each soil's
control volume nodal (m)

%Determine pipe's area of the vertical GHE
Ap_v=(pi*d_eqin_v^2)/4; %Cross section area of the pipe(m^2)
Aps_v=pi*d_eqin_v*dzs_v; %Surface area of the pipe(m^2)

%Determine pipe's volume of the vertical GHE
Vp_v=(d_eqout_v^2 - d_eqin_v^2)*(pi*dzs_v)/4; %Volume of pipe wall (m^3)

%Initial fluid temperature at each control volume (inside the pipe) of the
%vertical GHE
Tf_old_v=Tf*ones(1,n_v); %Fluid temperature in the control volume at the
current time step (K)
Tf_new_v=Tf*ones(1,n_v); %Fluid temperature in the control volume at the
new time step (K)

%INITIAL PIPE TEMPERATURE AT EACH CONTROL VOLUME OF THE VERTICAL GHE
Tp=Tf;
Tp_old_v=Tp*ones(1,n_v); %Pipe temperature at each control volume at the
current time step (K)
Tp_new_v=Tp*ones(1,n_v); %Pipe temperature at each control volume at the
new time step (K)

%Initial soil temperature
load('Ts_v.mat'); %Load the soil temperature at various depth
Ts_v=Ts_v+273.15; %The soil temperature is converted from Celsius to Kelvin
Ts_old_v=repmat(Ts_v,1,m_v); %Soil temperature at each control volume at
the current time step (K)
Ts_new_v=zeros(n_v,m_v); %Soil temperature at each control volume at the
new time step (K)

%Grout temperature
%The initial grout temperature is assumed the same as initial soil
%temperature
Tg_old_v=Ts_v;%Grout temperature at each control volume at the current time
step (K)
Tg_new_v=Ts_v;%Grout temperature at each control volume at the new time
step (K)

% Calculate Fourier number for the horizontal GHE
Fo_h=alfas*dt_h/dx_h^2;

%Calculate Fourier number for the vertical GHE
Fos_v=alfas*dt_v/drs_v^2;
Fog_v=alfag_v*dt_v/drg_v^2;

%Constants for fluid temperature equation for the horizontal GHE
cf1_h=pi*d_in_h*hf_h;
cf2_h=mf*cf/dz_h;
cf3_h=cf*rhof*Ap_h/dt_h;
cf4_h=dt_h/(rhof*Ap_h*dz_h*cf);
Rwp_h=(0.5*d_in_h/(Aps_h*kf))+(th_ph/(Aps_h*kp_h));

%Constants for fluid temperature equation for the vertical GHE
cf1_v=pi*d_eqin_v*hf_v;
cf2_v=mf*cf/dzs_v;
cf3_v=cf*rhof*Ap_v/dt_v;
cf4_v=dt_v/(rhof*Ap_v*dzs_v*cf);
Rwp_v=(0.5*d_eqin_v/(Aps_v*kf))+(th_pv/(Aps_v*kp_v));
```
183

```matlab
%Constants for pipe temperature equation for the horizontal GHE
cp1_h=dt_h/(cp_h*rhop_h*Vp_h);
cp2_h=Aps_h*hf_h;
cp3_h=(ks*Aps_h)/(0.5*dx_h);
cp4_h=kp_h*Aps_h/th_ph;


%Constants for pipe temperature equation for the vertical GHE
cp1_v=dt_v/(cp_v*rhop_v*Vp_v);
cp2_v=Aps_v*hf_v;
cp3_v=(kg_v*Aps_v)/(0.5*drg_v);
cp4_v=kp_v*Aps_v/th_pv;


%Constant for grout temperature equation
Csg_s=0.5/(1+(drg_v/(2*rg_v))) +
((drs_v/(2*drg_v))/((ks/kg_v)*(1+(drg_v/(2*rg_v)))));


%Stored outlet fluid temperature for the horizontal GHE
Tfluid_outlet_h=zeros(1,tt_h);

%Stored outlet fluid temperature for the vertical GHE
 Tfluid_outlet_v=zeros(1,tt_h);

%Stored soil temperature for the horizontal GHE at a specific x,y,z
Ts_Y98cmX4cmZ100m_h=zeros(1,tt_h);% Soil temperature at x=4cm, y=98 cm,
z=100m
Ts_Y98cmX8cmZ100m_h=zeros(1,tt_h);% Soil temperature at x=8cm, y=98 cm,
z=100m
Ts_Y98cmX12cmZ100m_h=zeros(1,tt_h);% Soil temperature at x=12cm, y=98 cm,
z=100m
Ts_Y22cmX12cmZ100m_h=zeros(1,tt_h);% Soil temperature at x=12cm, y=22 cm,
z=100m
Ts_Y46cmX12cmZ100m_h=zeros(1,tt_h);% Soil temperature at x=12cm, y=46 cm,
z=100m
Ts_Y70cmX12cmZ100m_h=zeros(1,tt_h);% Soil temperature at x=12cm, y=70 cm,
z=100m


%Stored soil temperature for the vertical GHE at a specific rand z
Ts_Z25md0525m=zeros(1,tt_h);% Soil temperature at r=0.525m, z=25m
Ts_Z50md0525m=zeros(1,tt_h);% Soil temperature at r=0.525m, z=50m
Ts_Z75md0525m=zeros(1,tt_h);% Soil temperature at r=0.525m, z=75m
Ts_Z100md0525m=zeros(1,tt_h);% Soil temperature at r=0.525m, z=100m
Ts_Z125md0525m=zeros(1,tt_h);% Soil temperature at r=0.525m, z=125m
Ts_Z100md0425m=zeros(1,tt_h);% Soil temperature at r=0.425m, z=100m
Ts_Z100md0325m=zeros(1,tt_h);% Soil temperature at r=0.325m, z=100m
Ts_Z100md0225m=zeros(1,tt_h);% Soil temperature at r=0.225m, z=100m
Ts_Z100md0125m=zeros(1,tt_h);% Soil temperature at r=0.125m, z=100m

 B_h=((1/hf_h)+(th_ph/kp_h))*(1/Aps_h);
 E_h=ks*(((1/hf_h)+(th_ph/kp_h)))/(0.5*dx_h);
 F_h=ks*Aps_h/(0.5*dx_h);


 B_v=((1/hf_v)+(th_pv/kp_v))*(1/Aps_v);
 E_v=kg_v*(((1/hf_v)+(th_pv/kp_v)))/(0.5*drg_v);


for l=1:tt_h
% Determine the convective heat transfer coefficient of air in contact with
% soil surface
load('Tamb.mat')% Load the ambient air temperature during winter or summer
Ta=Tamb(t_h(l))+273.15; %Convert the unit of soil temperature from Celsius
to Kelvin
Va=4.9; %Annual average wind speed in Adelaide (m/s)
va=15.89e-6; %Kinematic viscosity of air (m^2/s)
```

```matlab
ka=26.3e-3; %Thermal conductivity of air (W/m.K)
Pra=0.707; %Prandtl Number
L_h=X_h; %Unit length (m) of soil in contact with air for the horizontal
GHE
L_v=Ab_v/Pb_v; %Unit length (m) of soil in contact with air for the
vertical GHE
Rea_h=Va*L_h/va; %Reynold Number
Rea_v=Va*L_v/va; %Reynold Number


if Rea_h>=5e5
    Nua_h=0.037*(Rea_h^0.8)*Pra^(1/3); %Nusselt Number for laminar flow
else
    Nua_h=0.664*(Rea_h^0.5)*Pra^(1/3); %Nusselt Number for turbulent flow
end


if Rea_v>=5e5
    Nua_v=0.037*(Rea_v^0.8)*Pra^(1/3); %Nusselt Number for laminar flow
else
    Nua_v=0.664*(Rea_v^0.5)*Pra^(1/3); %Nusselt Number for turbulent flow
end


ha_h=Nua_h*ka/L_h; %Convective heat transfer of air in contact with soil
surface (W/m^2K)
Rconv_h=1/ha_h;
Rcond_h=(dy_h/2)/ks;
Uas_h=1/(Rconv_h+Rcond_h);


ha_v=Nua_v*ka/L_v; %Convective heat transfer of air in contact with soil
surface (W/m^2K)
Cag=drg_v/((kg_v*c1_v/ha_v)+ (drg_v*c1_v^2)/2);
Cas=drs_v/((ks*Cs1_v/ha_v)+ ((Cs1_v^2)*drs_v)/2);


%Calculation of the fluid and pipe temperatures (Eq.4.4)
  for k=1:p_h
      Ts_aveold_h=(Ts_old_h(25,1,k)+ Ts_old_h(27,1,k)+
2*Ts_old_h(26,2,k))/4;% Determine the average soil temperature around the
pipe (K)
      if and(k==1,t_h(l)<=19*3600)
      Tf_new_h(k)=(Tfi*(2*mf*cf*B_h - 1) + 2*Tp_new_h(k))/(1 +
2*mf*cf*B_h);
      Tp_new_h(k)=(Tf_new_h(k)/2 + Tfi/2 + (E_h*Ts_aveold_h))/(E_h+1);
      elseif and(k>1,t_h(l)<=19*3600)
      Tf_new_h(k)=(Tf_new_h(k-1)*(2*mf*cf*B_h - 1) + 2*Tp_new_h(k))/(1 +
2*mf*cf*B_h);
      Tp_new_h(k)=(Tf_new_h(k)/2 + Tf_new_h(k-1)/2 +
(E_h*Ts_aveold_h))/(E_h+1);
      elseif and(k>=1,t_h(l)<=24*3600)
      Tf_new_h(k)=cf4_h*((Tp_old_h(k)-Tf_old_h(k))/Rwp_h) + Tf_old_h(k);
      Tp_new_h(k)=cp1_h*(((Tf_new_h(k)-
Tp_old_h(k))/Rwp_h)+(cp3_h*(Ts_aveold_h-Tp_old_h(k))))+Tp_old_h(k);

      elseif and(k==1,t_h(l)<=43*3600)
      Tf_new_h(k)=(Tf_in*(2*mf_flow*cf*B_h - 1) + 2*Tp_new_h(k))/(1 +
2*mf_flow*cf*B_h);
      Tp_new_h(k)=(Tf_new_h(k)/2 + Tf_in/2 + (E_h*Ts_aveold_h))/(E_h+1);
      elseif and(k>1,t_h(l)<=43*3600)
      Tf_new_h(k)=(Tf_new_h(k-1)*(2*mf_flow*cf*B_h - 1) + 2*Tp_new_h(k))/(1
+ 2*mf_flow*cf*B_h);
      Tp_new_h(k)=(Tf_new_h(k)/2 + Tf_new_h(k-1)/2 +
(E_h*Ts_aveold_h))/(E_h+1);
      elseif and(k>=1,t_h(l)<=48*3600)
      Tf_new_h(k)=cf4_h*((Tp_old_h(k)-Tf_old_h(k))/Rwp_h) + Tf_old_h(k);
```

```
    Tp_new_h(k)=cp1_h*(((Tf_new_h(k)-
Tp_old_h(k)))/Rwp_h)+(cp3_h*(Ts_aveold_h-Tp_old_h(k))))+Tp_old_h(k);


        elseif and(k==1,t_h(l)<=67*3600)
        Tf_new_h(k)=(Tf_in*(2*mf_flow*cf*B_h - 1) + 2*Tp_new_h(k))/(1 +
2*mf_flow*cf*B_h);
        Tp_new_h(k)=(Tf_new_h(k)/2 + Tf_in/2 + (E_h*Ts_aveold_h))/(E_h+1);
        elseif and(k>1,t_h(l)<=67*3600)
        Tf_new_h(k)=(Tf_new_h(k-1)*(2*mf_flow*cf*B_h - 1) + 2*Tp_new_h(k))/(1
+ 2*mf_flow*cf*B_h);
        Tp_new_h(k)=(Tf_new_h(k)/2 + Tf_new_h(k-1)/2 +
(E_h*Ts_aveold_h))/(E_h+1);
        elseif and(k>=1,t_h(l)<=72*3600)
        Tf_new_h(k)=cf4_h*((Tp_old_h(k)-Tf_old_h(k))/Rwp_h) + Tf_old_h(k);
        Tp_new_h(k)=cp1_h*(((Tf_new_h(k)-
Tp_old_h(k))/Rwp_h)+(cp3_h*(Ts_aveold_h-Tp_old_h(k))))+Tp_old_h(k);


        elseif and(k==1,t_h(l)<=91*3600)
        Tf_new_h(k)=(Tf_in*(2*mf_flow*cf*B_h - 1) + 2*Tp_new_h(k))/(1 +
2*mf_flow*cf*B_h);
        Tp_new_h(k)=(Tf_new_h(k)/2 + Tf_in/2 + (E_h*Ts_aveold_h))/(E_h+1);
        elseif and(k>1,t_h(l)<=91*3600)
        Tf_new_h(k)=(Tf_new_h(k-1)*(2*mf_flow*cf*B_h - 1) + 2*Tp_new_h(k))/(1
+ 2*mf_flow*cf*B_h);
        Tp_new_h(k)=(Tf_new_h(k)/2 + Tf_new_h(k-1)/2 +
(E_h*Ts_aveold_h))/(E_h+1);
        elseif and(k>=1,t_h(l)<=96*3600)
        Tf_new_h(k)=cf4_h*((Tp_old_h(k)-Tf_old_h(k))/Rwp_h) + Tf_old_h(k);
        Tp_new_h(k)=cp1_h*(((Tf_new_h(k)-
Tp_old_h(k))/Rwp_h)+(cp3_h*(Ts_aveold_h-Tp_old_h(k))))+Tp_old_h(k);


        elseif and(k==1,t_h(l)<=115*3600)
        Tf_new_h(k)=(Tf_in*(2*mf_flow*cf*B_h - 1) + 2*Tp_new_h(k))/(1 +
2*mf_flow*cf*B_h);
        Tp_new_h(k)=(Tf_new_h(k)/2 + Tf_in/2 + (E_h*Ts_aveold_h))/(E_h+1);
        elseif and(k>1,t_h(l)<=115*3600)
        Tf_new_h(k)=(Tf_new_h(k-1)*(2*mf_flow*cf*B_h - 1) + 2*Tp_new_h(k))/(1
+ 2*mf_flow*cf*B_h);
        Tp_new_h(k)=(Tf_new_h(k)/2 + T_new_h(k-1)/2 +
(E_h*Ts_aveold_h))/(E_h+1);
        elseif and(k>=1,t_h(l)<=120*3600)
        Tf_new_h(k)=cf4_h*((Tp_old_h(k)-T_old_h(k))/Rwp_h) + Tf_old_h(k);
        Tp_new_h(k)=cp1_h*(((Tf_new_h(k)-
Tp_old_h(k))/Rwp_h)+(cp3_h*(Ts_aveold_h-Tp_old_h(k))))+Tp_old_h(k);


        elseif and(k==1,t_h(l)<=139*3600)
        Tf_new_h(k)=(Tf_in*(2*mf_flow*cf*B_h - 1) + 2*Tp_new_h(k))/(1 +
2*mf_flow*cf*B_h);
        Tp_new_h(k)=(Tf_new_h(k)/2 + Tf_in/2 + (E_h*Ts_aveold_h))/(E_h+1);
        elseif and(k>1,t_h(l)<=139*3600)
        Tf_new_h(k)=(Tf_new_h(k-1)*(2*mf_flow*cf*B_h - 1) + 2*Tp_new_h(k))/(1
+ 2*mf_flow*cf*B_h);
        Tp_new_h(k)=(Tf_new_h(k)/2 + Tf_new_h(k-1)/2 +
(E_h*Ts_aveold_h))/(E_h+1);
        elseif and(k>=1,t_h(l)<=144*3600)
        Tf_new_h(k)=cf4_h*((Tp_old_h(k)-Tf_old_h(k))/Rwp_h) + Tf_old_h(k);
        Tp_new_h(k)=cp1_h*(((Tf_new_h(k)-
Tp_old_h(k))/Rwp_h)+(cp3_h*(Ts_aveold_h-Tp_old_h(k))))+Tp_old_h(k);


        elseif and(k==1,t_h(l)<=163*3600)
        Tf_new_h(k)=(Tf_in*(2*mf_flow*cf*B_h - 1) + 2*Tp_new_h(k))/(1 +
2*mf_flow*cf*B_h);
        Tp_new_h(k)=(Tf_new_h(k)/2 + Tf_in/2 + (E_h*Ts_aveold_h))/(E_h+1);
        elseif and(k>1,t_h(l)<=163*3600)
```

```
        Tf_new_h(k)=(Tf_new_h(k-1)*(2*mf_flow*cf*B_h - 1) + 2*Tp_new_h(k))/(1
+ 2*mf_flow*cf*B_h);
        Tp_new_h(k)=(Tf_new_h(k)/2 + Tf_new_h(k-1)/2 +
(E_h*Ts_aveold_h))/(E_h+1);
        elseif and(k>=1,t_h(l)<=168*3600)
        Tf_new_h(k)=cf4_h*((Tp_old_h(k)-Tf_old_h(k))/Rwp_h) + Tf_old_h(k);
        Tp_new_h(k)=cp1_h*(((Tf_new_h(k)-
Tp_old_h(k))/Rwp_h)+(cp3_h*(Ts_aveold_h-Tp_old_h(k))))+Tp_old_h(k);


        elseif and(k==1,t_h(l)<=187*3600)
        Tf_new_h(k)=(Tf_in*(2*mf_flow*cf*B_h - 1) + 2*Tp_new_h(k))/(1 +
2*mf_flow*cf*B_h);
        Tp_new_h(k)=(Tf_new_h(k)/2 + Tf_in/2 + (E_h*Ts_aveold_h))/(E_h+1);
        elseif and(k>1,t_h(l)<=187*3600)
        Tf_new_h(k)=(Tf_new_h(k-1)*(2*mf_flow*cf*B_h - 1) + 2*Tp_new_h(k))/(1
+ 2*mf_flow*cf*B_h);
        Tp_new_h(k)=(Tf_new_h(k)/2 + Tf_new_h(k-1)/2 +
(E_h*Ts_aveold_h))/(E_h+1);
        elseif and(k>=1,t_h(l)<=192*3600)
        Tf_new_h(k)=cf4_h*((Tp_old_h(k)-Tf_old_h(k))/Rwp_h) + Tf_old_h(k);
        Tp_new_h(k)=cp1_h*(((Tf_new_h(k)-
Tp_old_h(k))/Rwp_h)+(cp3_h*(Ts_aveold_h-Tp_old_h(k))))+Tp_old_h(k);


        elseif and(k==1,t_h(l)<=211*3600)
        Tf_new_h(k)=(Tf_in*(2*mf_flow*cf*B_h - 1) + 2*Tp_new_h(k))/(1 +
2*mf_flow*cf*B_h);
        Tp_new_h(k)=(Tf_new_h(k)/2 + Tf_in/2 + (E_h*Ts_aveold_h))/(E_h+1);
        elseif and(k>1,t_h(l)<=211*3600)
        Tf_new_h(k)=(Tf_new_h(k-1)*(2*mf_flow*cf*B_h - 1) + 2*Tp_new_h(k))/(1
+ 2*mf_flow*cf*B_h);
        Tp_new_h(k)=(Tf_new_h(k)/2 + Tf_new_h(k-1)/2 +
(E_h*Ts_aveold_h))/(E_h+1);
        elseif and(k>=1,t_h(l)<=216*3600)
        Tf_new_h(k)=cf4_h*((Tp_old_h(k)-Tf_old_h(k))/Rwp_h) + Tf_old_h(k);
        Tp_new_h(k)=cp1_h*(((Tf_new_h(k)-
Tp_old_h(k))/Rwp_h)+(cp3_h*(Ts_aveold_h-Tp_old_h(k))))+Tp_old_h(k);


        elseif and(k==1,t_h(l)<=235*3600)
        Tf_new_h(k)=(Tf_in*(2*mf_flow*cf*B_h - 1) + 2*Tp_new_h(k))/(1 +
2*mf_flow*cf*B_h);
        Tp_new_h(k)=(Tf_new_h(k)/2 + Tf_in/2 + (E_h*Ts_aveold_h))/(E_h+1);
        elseif and(k>1,t_h(l)<=235*3600)
        Tf_new_h(k)=(Tf_new_h(k-1)*(2*mf_flow*cf*B_h - 1) + 2*Tp_new_h(k))/(1
+ 2*mf_flow*cf*B_h);
        Tp_new_h(k)=(Tf_new_h(k)/2 + Tf_new_h(k-1)/2 +
(E_h*Ts_aveold_h))/(E_h+1);
        elseif and(k>=1,t_h(l)<=240*3600)
        Tf_new_h(k)=cf4_h*((Tp_old_h(k)-Tf_old_h(k))/Rwp_h) + Tf_old_h(k);
        Tp_new_h(k)=cp1_h*(((Tf_new_h(k)-
Tp_old_h(k))/Rwp_h)+(cp3_h*(Ts_aveold_h-Tp_old_h(k))))+Tp_old_h(k);


        elseif and(k==1,t_h(l)<=259*3600)
        Tf_new_h(k)=(Tf_in*(2*mf_flow*cf*B_h - 1) + 2*Tp_new_h(k))/(1 +
2*mf_flow*cf*B_h);
        Tp_new_h(k)=(Tf_new_h(k)/2 + Tf_in/2 + (E_h*Ts_aveold_h))/(E_h+1);
        elseif and(k>1,t_h(l)<=259*3600)
        Tf_new_h(k)=(Tf_new_h(k-1)*(2*mf_flow*cf*B_h - 1) + 2*Tp_new_h(k))/(1
+ 2*mf_flow*cf*B_h);
        Tp_new_h(k)=(Tf_new_h(k)/2 + Tf_new_h(k-1)/2 +
(E_h*Ts_aveold_h))/(E_h+1);
        elseif and(k>=1,t_h(l)<=264*3600)
        Tf_new_h(k)=cf4_h*((Tp_old_h(k)-Tf_old_h(k))/Rwp_h) + Tf_old_h(k);
        Tp_new_h(k)=cp1_h*(((Tf_new_h(k)-
Tp_old_h(k))/Rwp_h)+(cp3_h*(Ts_aveold_h-Tp_old_h(k))))+Tp_old_h(k);
```

```
    elseif and(k==1,t_h(l)<=283*3600)
    Tf_new_h(k)=(Tf_in*(2*mf_flow*cf*B_h - 1) + 2*Tp_new_h(k))/(1 +
2*mf_flow*cf*B_h);
    Tp_new_h(k)=(Tf_new_h(k)/2 + Tf_in/2 + (E_h*Ts_aveold_h))/(E_h+1);
    elseif and(k>1,t_h(l)<=283*3600)
    Tf_new_h(k)=(Tf_new_h(k-1)*(2*mf_flow*cf*B_h - 1) + 2*Tp_new_h(k))/(1
+ 2*mf_flow*cf*B_h);
    Tp_new_h(k)=(Tf_new_h(k)/2 + Tf_new_h(k-1)/2 +
(E_h*Ts_aveold_h))/(E_h+1);
    elseif and(k>=1,t_h(l)<=288*3600)
    Tf_new_h(k)=cf4_h*((Tp_old_h(k)-Tf_old_h(k))/Rwp_h) + Tf_old_h(k);
    Tp_new_h(k)=cp1_h*(((Tf_new_h(k)-
Tp_old_h(k))/Rwp_h)+(cp3_h*(Ts_aveold_h-Tp_old_h(k))))+Tp_old_h(k);


    elseif and(k==1,t_h(l)<=307*3600)
    Tf_new_h(k)=(Tf_in*(2*mf_flow*cf*B_h - 1) + 2*Tp_new_h(k))/(1 +
2*mf_flow*cf*B_h);
    Tp_new_h(k)=(Tf_new_h(k)/2 + Tf_in/2 + (E_h*Ts_aveold_h))/(E_h+1);
    elseif and(k>1,t_h(l)<=307*3600)
    Tf_new_h(k)=(Tf_new_h(k-1)*(2*mf_flow*cf*B_h - 1) + 2*Tp_new_h(k))/(1
+ 2*mf_flow*cf*B_h);
    Tp_new_h(k)=(Tf_new_h(k)/2 + Tf_new_h(k-1)/2 +
(E_h*Ts_aveold_h))/(E_h+1);
    elseif and(k>=1,t_h(l)<=312*3600)
    Tf_new_h(k)=cf4_h*((Tp_old_h(k)-Tf_old_h(k))/Rwp_h) + Tf_old_h(k);
    Tp_new_h(k)=cp1_h*(((Tf_new_h(k)-
Tp_old_h(k))/Rwp_h)+(cp3_h*(Ts_aveold_h-Tp_old_h(k))))+Tp_old_h(k);


    elseif and(k==1,t_h(l)<=331*3600)
    Tf_new_h(k)=(Tf_in*(2*mf_flow*cf*B_h - 1) + 2*Tp_new_h(k))/(1 +
2*mf_flow*cf*B_h);
    Tp_new_h(k)=(Tf_new_h(k)/2 + Tf_in/2 + (E_h*Ts_aveold_h))/(E_h+1);
    elseif and(k>1,t_h(l)<=331*3600)
    Tf_new_h(k)=(Tf_new_h(k-1)*(2*mf_flow*cf*B_h - 1) + 2*Tp_new_h(k))/(1
+ 2*mf_flow*cf*B_h);
    Tp_new_h(k)=(Tf_new_h(k)/2 + Tf_new_h(k-1)/2 +
(E_h*Ts_aveold_h))/(E_h+1);
    elseif and(k>=1,t_h(l)<=336*3600)
    Tf_new_h(k)=cf4_h*((Tp_old_h(k)-Tf_old_h(k))/Rwp_h) + Tf_old_h(k);
    Tp_new_h(k)=cp1_h*(((Tf_new_h(k)-
Tp_old_h(k))/Rwp_h)+(cp3_h*(Ts_aveold_h-Tp_old_h(k))))+Tp_old_h(k);


    elseif and(k==1,t_h(l)<=355*3600)
    Tf_new_h(k)=(Tf_in*(2*mf_flow*cf*B_h - 1) + 2*Tp_new_h(k))/(1 +
2*mf_flow*cf*B_h);
    Tp_new_h(k)=(Tf_new_h(k)/2 + Tf_in/2 + (E_h*Ts_aveold_h))/(E_h+1);
    elseif and(k>1,t_h(l)<=355*3600)
    Tf_new_h(k)=(Tf_new_h(k-1)*(2*mf_flow*cf*B_h - 1) + 2*Tp_new_h(k))/(1
+ 2*mf_flow*cf*B_h);
    Tp_new_h(k)=(Tf_new_h(k)/2 + Tf_new_h(k-1)/2 +
(E_h*Ts_aveold_h))/(E_h+1);
    elseif and(k>=1,t_h(l)<=360*3600)
    Tf_new_h(k)=cf4_h*((Tp_old_h(k)-Tf_old_h(k))/Rwp_h) + Tf_old_h(k);
    Tp_new_h(k)=cp1_h*(((Tf_new_h(k)-
Tp_old_h(k))/Rwp_h)+(cp3_h*(Ts_aveold_h-Tp_old_h(k))))+Tp_old_h(k);


    elseif and(k==1,t_h(l)<=379*3600)
    Tf_new_h(k)=(Tf_in*(2*mf_flow*cf*B_h - 1) + 2*Tp_new_h(k))/(1 +
2*mf_flow*cf*B_h);
    Tp_new_h(k)=(Tf_new_h(k)/2 + Tf_in/2 + (E_h*Ts_aveold_h))/(E_h+1);
    elseif and(k>1,t_h(l)<=379*3600)
    Tf_new_h(k)=(Tf_new_h(k-1)*(2*mf_flow*cf*B_h - 1) + 2*Tp_new_h(k))/(1
+ 2*mf_flow*cf*B_h);
```

```
        Tp_new_h(k)=(Tf_new_h(k)/2 + Tf_new_h(k-1)/2 +
(E_h*Ts_aveold_h))/(E_h+1);
        elseif and(k>=1,t_h(l)<=384*3600)
        Tf_new_h(k)=cf4_h*((Tp_old_h(k)-Tf_old_h(k))/Rwp_h) + Tf_old_h(k);
        Tp_new_h(k)=cp1_h*(((Tf_new_h(k)-
Tp_old_h(k))/Rwp_h)+(cp3_h*(Ts_aveold_h-Tp_old_h(k))))+Tp_old_h(k);


        elseif and(k==1,t_h(l)<=403*3600)
        Tf_new_h(k)=(Tf_in*(2*mf_flow*cf*B_h - 1) + 2*Tp_new_h(k))/(1 +
2*mf_flow*cf*B_h);
        Tp_new_h(k)=(Tf_new_h(k)/2 + Tf_in/2 + (E_h*Ts_aveold_h))/(E_h+1);
        elseif and(k>1,t_h(l)<=403*3600)
        Tf_new_h(k)=(Tf_new_h(k-1)*(2*mf_flow*cf*B_h - 1) + 2*Tp_new_h(k))/(1
+ 2*mf_flow*cf*B_h);
        Tp_new_h(k)=(Tf_new_h(k)/2 + Tf_new_h(k-1)/2 +
(E_h*Ts_aveold_h))/(E_h+1);
        elseif and(k>=1,t_h(l)<=408*3600)
        Tf_new_h(k)=cf4_h*((Tp_old_h(k)-Tf_old_h(k))/Rwp_h) + Tf_old_h(k);
        Tp_new_h(k)=cp1_h*(((Tf_new_h(k)-
Tp_old_h(k))/Rwp_h)+(cp3_h*(Ts_aveold_h-Tp_old_h(k))))+Tp_old_h(k);


        elseif and(k==1,t_h(l)<=427*3600)
        Tf_new_h(k)=(Tf_in*(2*mf_flow*cf*B_h - 1) + 2*Tp_new_h(k))/(1 +
2*mf_flow*cf*B_h);
        Tp_new_h(k)=(Tf_new_h(k)/2 + Tf_in/2 + (E_h*Ts_aveold_h))/(E_h+1);
        elseif and(k>1,t_h(l)<=427*3600)
        Tf_new_h(k)=(Tf_new_h(k-1)*(2*mf_flow*cf*B_h - 1) + 2*Tp_new_h(k))/(1
+ 2*mf_flow*cf*B_h);
        Tp_new_h(k)=(Tf_new_h(k)/2 + Tf_new_h(k-1)/2 +
(E_h*Ts_aveold_h))/(E_h+1);
        elseif and(k>=1,t_h(l)<=432*3600)
        Tf_new_h(k)=cf4_h*((Tp_old_h(k)-Tf_old_h(k))/Rwp_h) + Tf_old_h(k);
        Tp_new_h(k)=cp1_h*(((Tf_new_h(k)-
Tp_old_h(k))/Rwp_h)+(cp3_h*(Ts_aveold_h-Tp_old_h(k))))+Tp_old_h(k);


        elseif and(k==1,t_h(l)<=451*3600)
        Tf_new_h(k)=(Tf_in*(2*mf_flow*cf*B_h - 1) + 2*Tp_new_h(k))/(1 +
2*mf_flow*cf*B_h);
        Tp_new_h(k)=(Tf_new_h(k)/2 + Tf_in/2 + (E_h*Ts_aveold_h))/(E_h+1);
        elseif and(k>1,t_h(l)<=451*3600)
        Tf_new_h(k)=(Tf_new_h(k-1)*(2*mf_flow*cf*B_h - 1) + 2*Tp_new_h(k))/(1
+ 2*mf_flow*cf*B_h);
        Tp_new_h(k)=(Tf_new_h(k)/2 + Tf_new_h(k-1)/2 +
(E_h*Ts_aveold_h))/(E_h+1);
        elseif and(k>=1,t_h(l)<=456*3600)
        Tf_new_h(k)=cf4_h*((Tp_old_h(k)-Tf_old_h(k))/Rwp_h) + Tf_old_h(k);
        Tp_new_h(k)=cp1_h*(((Tf_new_h(k)-
Tp_old_h(k))/Rwp_h)+(cp3_h*(Ts_aveold_h-Tp_old_h(k))))+Tp_old_h(k);


        elseif and(k==1,t_h(l)<=475*3600)
        Tf_new_h(k)=(Tf_in*(2*mf_flow*cf*B_h - 1) + 2*Tp_new_h(k))/(1 +
2*mf_flow*cf*B_h);
        Tp_new_h(k)=(Tf_new_h(k)/2 + Tf_in/2 + (E_h*Ts_aveold_h))/(E_h+1);
        elseif and(k>1,t_h(l)<=475*3600)
        Tf_new_h(k)=(Tf_new_h(k-1)*(2*mf_flow*cf*B_h - 1) + 2*Tp_new_h(k))/(1
+ 2*mf_flow*cf*B_h);
        Tp_new_h(k)=(Tf_new_h(k)/2 + Tf_new_h(k-1)/2 +
(E_h*Ts_aveold_h))/(E_h+1);
        elseif and(k>=1,t_h(l)<=480*3600)
        Tf_new_h(k)=cf4_h*((Tp_old_h(k)-Tf_old_h(k))/Rwp_h) + Tf_old_h(k);
        Tp_new_h(k)=cp1_h*(((Tf_new_h(k)-
Tp_old_h(k))/Rwp_h)+(cp3_h*(Ts_aveold_h-Tp_old_h(k))))+Tp_old_h(k);


        elseif and(k==1,t_h(l)<=499*3600)
```

```
        Tf_new_h(k)=(Tf_in*(2*mf_flow*cf*B_h - 1) + 2*Tp_new_h(k))/(1 +
2*mf_flow*cf*B_h);
        Tp_new_h(k)=(Tf_new_h(k)/2 + Tf_in/2 + (E_h*Ts_aveold_h))/(E_h+1);
        elseif and(k>1,t_h(l)<=499*3600)
        Tf_new_h(k)=(Tf_new_h(k-1)*(2*mf_flow*cf*B_h - 1) + 2*Tp_new_h(k))/(1
+ 2*mf_flow*cf*B_h);
        Tp_new_h(k)=(Tf_new_h(k)/2 + Tf_new_h(k-1)/2 +
(E_h*Ts_aveold_h))/(E_h+1);
        elseif and(k>=1,t_h(l)<=504*3600)
        Tf_new_h(k)=cf4_h*((Tp_old_h(k)-Tf_old_h(k))/Rwp_h) + Tf_old_h(k);
        Tp_new_h(k)=cp1_h*(((Tf_new_h(k)-
Tp_old_h(k))/Rwp_h)+(cp3_h*(Ts_aveold_h-Tp_old_h(k))))+Tp_old_h(k);

        elseif and(k==1,t_h(l)<=523*3600)
        Tf_new_h(k)=(Tf_in*(2*mf_flow*cf*B_h - 1) + 2*Tp_new_h(k))/(1 +
2*mf_flow*cf*B_h);
        Tp_new_h(k)=(Tf_new_h(k)/2 + Tf_in/2 + (E_h*Ts_aveold_h))/(E_h+1);
        elseif and(k>1,t_h(l)<=523*3600)
        Tf_new_h(k)=(Tf_new_h(k-1)*(2*mf_flow*cf*B_h - 1) + 2*Tp_new_h(k))/(1
+ 2*mf_flow*cf*B_h);
        Tp_new_h(k)=(Tf_new_h(k)/2 + Tf_new_h(k-1)/2 +
(E_h*Ts_aveold_h))/(E_h+1);
        elseif and(k>=1,t_h(l)<=528*3600)
        Tf_new_h(k)=cf4_h*((Tp_old_h(k)-Tf_old_h(k))/Rwp_h) + Tf_old_h(k);
        Tp_new_h(k)=cp1_h*(((Tf_new_h(k)-
Tp_old_h(k))/Rwp_h)+(cp3_h*(Ts_aveold_h-Tp_old_h(k))))+Tp_old_h(k);

        elseif and(k==1,t_h(l)<=547*3600)
        Tf_new_h(k)=(Tf_in*(2*mf_flow*cf*B_h - 1) + 2*Tp_new_h(k))/(1 +
2*mf_flow*cf*B_h);
        Tp_new_h(k)=(Tf_new_h(k)/2 + Tf_in/2 + (E_h*Ts_aveold_h))/(E_h+1);
        elseif and(k>1,t_h(l)<=547*3600)
        Tf_new_h(k)=(Tf_new_h(k-1)*(2*mf_flow*cf*B_h - 1) + 2*Tp_new_h(k))/(1
+ 2*mf_flow*cf*B_h);
        Tp_new_h(k)=(Tf_new_h(k)/2 + Tf_new_h(k-1)/2 +
(E_h*Ts_aveold_h))/(E_h+1);
        elseif and(k>=1,t_h(l)<=552*3600)
        Tf_new_h(k)=cf4_h*((Tp_old_h(k)-Tf_old_h(k))/Rwp_h) + Tf_old_h(k);
        Tp_new_h(k)=cp1_h*(((Tf_new_h(k)-
Tp_old_h(k))/Rwp_h)+(cp3_h*(Ts_aveold_h-Tp_old_h(k))))+Tp_old_h(k);

        elseif and(k==1,t_h(l)<=571*3600)
        Tf_new_h(k)=(Tf_in*(2*mf_flow*cf*B_h - 1) + 2*Tp_new_h(k))/(1 +
2*mf_flow*cf*B_h);
        Tp_new_h(k)=(Tf_new_h(k)/2 + Tf_in/2 + (E_h*Ts_aveold_h))/(E_h+1);
        elseif and(k>1,t_h(l)<=571*3600)
        Tf_new_h(k)=(Tf_new_h(k-1)*(2*mf_flow*cf*B_h - 1) + 2*Tp_new_h(k))/(1
+ 2*mf_flow*cf*B_h);
        Tp_new_h(k)=(Tf_new_h(k)/2 + Tf_new_h(k-1)/2 +
(E_h*Ts_aveold_h))/(E_h+1);
        elseif and(k>=1,t_h(l)<=576*3600)
        Tf_new_h(k)=cf4_h*((Tp_old_h(k)-Tf_old_h(k))/Rwp_h) + Tf_old_h(k);
        Tp_new_h(k)=cp1_h*(((Tf_new_h(k)-
Tp_old_h(k))/Rwp_h)+(cp3_h*(Ts_aveold_h-Tp_old_h(k))))+Tp_old_h(k);

        elseif and(k==1,t_h(l)<=595*3600)
        Tf_new_h(k)=(Tf_in*(2*mf_flow*cf*B_h - 1) + 2*Tp_new_h(k))/(1 +
2*mf_flow*cf*B_h);
        Tp_new_h(k)=(Tf_new_h(k)/2 + Tf_in/2 + (E_h*Ts_aveold_h))/(E_h+1);
        elseif and(k>1,t_h(l)<=595*3600)
        Tf_new_h(k)=(Tf_new_h(k-1)*(2*mf_flow*cf*B_h - 1) + 2*Tp_new_h(k))/(1
+ 2*mf_flow*cf*B_h);
        Tp_new_h(k)=(Tf_new_h(k)/2 + Tf_new_h(k-1)/2 +
(E_h*Ts_aveold_h))/(E_h+1);
```

```
      elseif and(k>=1,t_h(l)<=600*3600)
      Tf_new_h(k)=cf4_h*((Tp_old_h(k)-Tf_old_h(k))/Rwp_h) + Tf_old_h(k);
      Tp_new_h(k)=cp1_h*(((Tf_new_h(k)-
Tp_old_h(k))/Rwp_h)+(cp3_h*(Ts_aveold_h-Tp_old_h(k))))+Tp_old_h(k);


      elseif and(k==1,t_h(l)<=619*3600)
      Tf_new_h(k)=(Tf_in*(2*mf_flow*cf*B_h - 1) + 2*Tp_new_h(k))/(1 +
2*mf_flow*cf*B_h);
      Tp_new_h(k)=(Tf_new_h(k)/2 + Tf_in/2 + (E_h*Ts_aveold_h))/(E_h+1);
      elseif and(k>1,t_h(l)<=619*3600)
      Tf_new_h(k)=(Tf_new_h(k-1)*(2*mf_flow*cf*B_h - 1) + 2*Tp_new_h(k))/(1
+ 2*mf_flow*cf*B_h);
      Tp_new_h(k)=(Tf_new_h(k)/2 + Tf_new_h(k-1)/2 +
(E_h*Ts_aveold_h))/(E_h+1);
      elseif and(k>=1,t_h(l)<=624*3600)
      Tf_new_h(k)=cf4_h*((Tp_old_h(k)-Tf_old_h(k))/Rwp_h) + Tf_old_h(k);
      Tp_new_h(k)=cp1_h*(((Tf_new_h(k)-
Tp_old_h(k))/Rwp_h)+(cp3_h*(Ts_aveold_h-Tp_old_h(k))))+Tp_old_h(k);


      elseif and(k==1,t_h(l)<=643*3600)
      Tf_new_h(k)=(Tf_in*(2*mf_flow*cf*B_h - 1) + 2*Tp_new_h(k))/(1 +
2*mf_flow*cf*B_h);
      Tp_new_h(k)=(Tf_new_h(k)/2 + Tf_in/2 + (E_h*Ts_aveold_h))/(E_h+1);
      elseif and(k>1,t_h(l)<=643*3600)
      Tf_new_h(k)=(Tf_new_h(k-1)*(2*mf_flow*cf*B_h - 1) + 2*Tp_new_h(k))/(1
+ 2*mf_flow*cf*B_h);
      Tp_new_h(k)=(Tf_new_h(k)/2 + Tf_new_h(k-1)/2 +
(E_h*Ts_aveold_h))/(E_h+1);
      elseif and(k>=1,t_h(l)<=648*3600)
      Tf_new_h(k)=cf4_h*((Tp_old_h(k)-Tf_old_h(k))/Rwp_h) + Tf_old_h(k);
      Tp_new_h(k)=cp1_h*(((Tf_new_h(k)-
Tp_old_h(k))/Rwp_h)+(cp3_h*(Ts_aveold_h-Tp_old_h(k))))+Tp_old_h(k);


      elseif and(k==1,t_h(l)<=667*3600)
      Tf_new_h(k)=(Tf_in*(2*mf_flow*cf*B_h - 1) + 2*Tp_new_h(k))/(1 +
2*mf_flow*cf*B_h);
      Tp_new_h(k)=(Tf_new_h(k)/2 + Tf_in/2 + (E_h*Ts_aveold_h))/(E_h+1);
      elseif and(k>1,t_h(l)<=667*3600)
      Tf_new_h(k)=(Tf_new_h(k-1)*(2*mf_flow*cf*B_h - 1) + 2*Tp_new_h(k))/(1
+ 2*mf_flow*cf*B_h);
      Tp_new_h(k)=(Tf_new_h(k)/2 + Tf_new_h(k-1)/2 +
(E_h*Ts_aveold_h))/(E_h+1);
      elseif and(k>=1,t_h(l)<=672*3600)
      Tf_new_h(k)=cf4_h*((Tp_old_h(k)-Tf_old_h(k))/Rwp_h) + Tf_old_h(k);
      Tp_new_h(k)=cp1_h*(((Tf_new_h(k)-
Tp_old_h(k))/Rwp_h)+(cp3_h*(Ts_aveold_h-Tp_old_h(k))))+Tp_old_h(k);


      elseif and(k==1,t_h(l)<=691*3600)
      Tf_new_h(k)=(Tf_in*(2*mf_flow*cf*B_h - 1) + 2*Tp_new_h(k))/(1 +
2*mf_flow*cf*B_h);
      Tp_new_h(k)=(Tf_new_h(k)/2 + Tf_in/2 + (E_h*Ts_aveold_h))/(E_h+1);
      elseif and(k>1,t_h(l)<=691*3600)
      Tf_new_h(k)=(Tf_new_h(k-1)*(2*mf_flow*cf*B_h - 1) + 2*Tp_new_h(k))/(1
+ 2*mf_flow*cf*B_h);
      Tp_new_h(k)=(Tf_new_h(k)/2 + Tf_new_h(k-1)/2 +
(E_h*Ts_aveold_h))/(E_h+1);
      elseif and(k>=1,t_h(l)<=696*3600)
      Tf_new_h(k)=cf4_h*((Tp_old_h(k)-Tf_old_h(k))/Rwp_h) + Tf_old_h(k);
      Tp_new_h(k)=cp1_h*(((Tf_new_h(k)-
Tp_old_h(k))/Rwp_h)+(cp3_h*(Ts_aveold_h-Tp_old_h(k))))+Tp_old_h(k);


      elseif and(k==1,t_h(l)<=715*3600)
      Tf_new_h(k)=(Tf_in*(2*mf_flow*cf*B_h - 1) + 2*Tp_new_h(k))/(1 +
2*mf_flow*cf*B_h);
```

```matlab
        Tp_new_h(k)=(Tf_new_h(k)/2 + Tf_in/2 + (E_h*Ts_aveold_h))/(E_h+1);
        elseif and(k>1,t_h(l)<=715*3600)
        Tf_new_h(k)=(Tf_new_h(k-1)*(2*mf_flow*cf*B_h - 1) + 2*Tp_new_h(k))/(1
+ 2*mf_flow*cf*B_h);
        Tp_new_h(k)=(Tf_new_h(k)/2 + Tf_new_h(k-1)/2 +
(E_h*Ts_aveold_h))/(E_h+1);
        elseif and(k>=1,t_h(l)<=720*3600)
        Tf_new_h(k)=cf4_h*((Tp_old_h(k)-Tf_old_h(k))/Rwp_h) + Tf_old_h(k);
        Tp_new_h(k)=cp1_h*(((Tf_new_h(k)-
Tp_old_h(k))/Rwp_h)+(cp3_h*(Ts_aveold_h-Tp_old_h(k))))+Tp_old_h(k);

        elseif and(k==1,t_h(l)<=739*3600)
        Tf_new_h(k)=(Tf_in*(2*mf_flow*cf*B_h - 1) + 2*Tp_new_h(k))/(1 +
2*mf_flow*cf*B_h);
        Tp_new_h(k)=(Tf_new_h(k)/2 + Tf_in/2 + (E_h*Ts_aveold_h))/(E_h+1);
        elseif and(k>1,t_h(l)<=739*3600)
        Tf_new_h(k)=(Tf_new_h(k-1)*(2*mf_flow*cf*B_h - 1) + 2*Tp_new_h(k))/(1
+ 2*mf_flow*cf*B_h);
        Tp_new_h(k)=(Tf_new_h(k)/2 + Tf_new_h(k-1)/2 +
(E_h*Ts_aveold_h))/(E_h+1);
        elseif and(k>=1,t_h(l)<=744*3600)
        Tf_new_h(k)=cf4_h*((Tp_old_h(k)-Tf_old_h(k))/Rwp_h) + Tf_old_h(k);
        Tp_new_h(k)=cp1_h*(((Tf_new_h(k)-
Tp_old_h(k))/Rwp_h)+(cp3_h*(Ts_aveold_h-Tp_old_h(k))))+Tp_old_h(k);
        end
  end
%Calculation of the fluid temperature Eq.5.6
%Calculation of the pipe temperature Eq.5.7
  for j=1:n_v
        if and(j==1,t_h(l)<=19*3600)
        Tf_new_v(j)=(Tf_new_h(p_h)*(2*mf*cf*B_v - 1) + 2*Tp_new_v(j))/(1 +
2*mf*cf*B_v);
        Tp_new_v(j)=(Tf_new_v(j)/2 + Tf_new_h(p_h)/2 +
(E_v*Tg_old_v(j)))/(E_v+1);
        elseif and(j>1,t_h(l)<=19*3600)
        Tf_new_v(j)=(Tf_new_v(j-1)*(2*mf*cf*B_v - 1) + 2*Tp_new_v(j))/(1 +
2*mf*cf*B_v);
        Tp_new_v(j)=(Tf_new_v(j)/2 + Tf_new_v(j-1)/2 +
(E_v*Tg_old_v(j)))/(E_v+1);
        elseif and(j>=1,t_h(l)<=24*3600)
        Tf_new_v(j)=cf4_v*((Tp_old_v(j)-Tf_old_v(j))/Rwp_v) + Tf_old_v(j);
        Tp_new_v(j)=cp1_v*(((Tf_new_v(j)-
Tp_old_v(j))/Rwp_v)+(cp3_v*(Tg_old_v(j)-Tp_old_v(j))))+Tp_old_v(j);

        elseif and(j==1,t_h(l)<=43*3600)
        Tf_new_v(j)=(Tf_new_h(p_h)*(2*mf_flow*cf*B_v - 1) + 2*Tp_new_v(j))/(1
+ 2*mf_flow*cf*B_v);
        Tp_new_v(j)=(Tf_new_v(j)/2 + Tf_new_h(p_h)/2 +
(E_v*Tg_old_v(j)))/(E_v+1);
        elseif and(j>1,t_h(l)<=43*3600)
        Tf_new_v(j)=(Tf_new_v(j-1)*(2*mf_flow*cf*B_v - 1) + 2*Tp_new_v(j))/(1
+ 2*mf_flow*cf*B_v);
        Tp_new_v(j)=(Tf_new_v(j)/2 + Tf_new_v(j-1)/2 +
(E_v*Tg_old_v(j)))/(E_v+1);
        elseif and(j>=1,t_h(l)<=48*3600)
        Tf_new_v(j)=cf4_v*((Tp_old_v(j)-Tf_old_v(j))/Rwp_v) + Tf_old_v(j);
        Tp_new_v(j)=cp1_v*(((Tf_new_v(j)-
Tp_old_v(j))/Rwp_v)+(cp3_v*(Tg_old_v(j)-Tp_old_v(j))))+Tp_old_v(j);

        elseif and(j==1,t_h(l)<=67*3600)
        Tf_new_v(j)=(Tf_new_h(p_h)*(2*mf_flow*cf*B_v - 1) + 2*Tp_new_v(j))/(1
+ 2*mf_flow*cf*B_v);
        Tp_new_v(j)=(Tf_new_v(j)/2 + Tf_new_h(p_h)/2 +
(E_v*Tg_old_v(j)))/(E_v+1);
```

```
        elseif and(j>1,t_h(l)<=67*3600)
        Tf_new_v(j)=(Tf_new_v(j-1)*(2*mf_flow*cf*B_v - 1) + 2*Tp_new_v(j))/(1
+ 2*mf_flow*cf*B_v);
        Tp_new_v(j)=(Tf_new_v(j)/2 + Tf_new_v(j-1)/2 +
(E_v*Tg_old_v(j)))/(E_v+1);
        elseif and(j>=1,t_h(l)<=72*3600)
        Tf_new_v(j)=cf4_v*((Tp_old_v(j)-Tf_old_v(j))/Rwp_v) + Tf_old_v(j);
        Tp_new_v(j)=cp1_v*(((Tf_new_v(j)-
Tp_old_v(j))/Rwp_v)+(cp3_v*(Tg_old_v(j)-Tp_old_v(j))))+Tp_old_v(j);


        elseif and(j==1,t_h(l)<=91*3600)
        Tf_new_v(j)=(Tf_new_h(p_h)*(2*mf_flow*cf*B_v - 1) + 2*Tp_new_v(j))/(1
+ 2*mf_flow*cf*B_v);
        Tp_new_v(j)=(Tf_new_v(j)/2 + Tf_new_h(p_h)/2 +
(E_v*Tg_old_v(j)))/(E_v+1);
        elseif and(j>1,t_h(l)<=91*3600)
        Tf_new_v(j)=(Tf_new_v(j-1)*(2*mf_flow*cf*B_v - 1) + 2*Tp_new_v(j))/(1
+ 2*mf_flow*cf*B_v);
        Tp_new_v(j)=(Tf_new_v(j)/2 + Tf_new_v(j-1)/2 +
(E_v*Tg_old_v(j)))/(E_v+1);
        elseif and(j>=1,t_h(l)<=96*3600)
        Tf_new_v(j)=cf4_v*((Tp_old_v(j)-Tf_old_v(j))/Rwp_v) + Tf_old_v(j);
        Tp_new_v(j)=cp1_v*(((Tf_new_v(j)-
Tp_old_v(j))/Rwp_v)+(cp3_v*(Tg_old_v(j)-Tp_old_v(j))))+Tp_old_v(j);


        elseif and(j==1,t_h(l)<=115*3600)
        Tf_new_v(j)=(Tf_new_h(p_h)*(2*mf_flow*cf*B_v - 1) + 2*Tp_new_v(j))/(1
+ 2*mf_flow*cf*B_v);
        Tp_new_v(j)=(Tf_new_v(j)/2 + Tf_new_h(p_h)/2 +
(E_v*Tg_old_v(j)))/(E_v+1);
        elseif and(j>1,t_h(l)<=115*3600)
        Tf_new_v(j)=(Tf_new_v(j-1)*(2*mf_flow*cf*B_v - 1) + 2*Tp_new_v(j))/(1
+ 2*mf_flow*cf*B_v);
        Tp_new_v(j)=(Tf_new_v(j)/2 + Tf_new_v(j-1)/2 +
(E_v*Tg_old_v(j)))/(E_v+1);
        elseif and(j>=1,t_h(l)<=120*3600)
        Tf_new_v(j)=cf4_v*((Tp_old_v(j)-Tf_old_v(j))/Rwp_v) + Tf_old_v(j);
        Tp_new_v(j)=cp1_v*(((Tf_new_v(j)-
Tp_old_v(j))/Rwp_v)+(cp3_v*(Tg_old_v(j)-Tp_old_v(j))))+Tp_old_v(j);


        elseif and(j==1,t_h(l)<=139*3600)
        Tf_new_v(j)=(Tf_new_h(p_h)*(2*mf_flow*cf*B_v - 1) + 2*Tp_new_v(j))/(1
+ 2*mf_flow*cf*B_v);
        Tp_new_v(j)=(Tf_new_v(j)/2 + Tf_new_h(p_h)/2 +
(E_v*Tg_old_v(j)))/(E_v+1);
        elseif and(j>1,t_h(l)<=139*3600)
        Tf_new_v(j)=(Tf_new_v(j-1)*(2*mf_flow*cf*B_v - 1) + 2*Tp_new_v(j))/(1
+ 2*mf_flow*cf*B_v);
        Tp_new_v(j)=(Tf_new_v(j)/2 + Tf_new_v(j-1)/2 +
(E_v*Tg_old_v(j)))/(E_v+1);
        elseif and(j>=1,t_h(l)<=144*3600)
        Tf_new_v(j)=cf4_v*((Tp_old_v(j)-Tf_old_v(j))/Rwp_v) + Tf_old_v(j);
        Tp_new_v(j)=cp1_v*(((Tf_new_v(j)-
Tp_old_v(j))/Rwp_v)+(cp3_v*(Tg_old_v(j)-Tp_old_v(j))))+Tp_old_v(j);


        elseif and(j==1,t_h(l)<=163*3600)
        Tf_new_v(j)=(Tf_new_h(p_h)*(2*mf_flow*cf*B_v - 1) + 2*Tp_new_v(j))/(1
+ 2*mf_flow*cf*B_v);
        Tp_new_v(j)=(Tf_new_v(j)/2 + Tf_new_h(p_h)/2 +
(E_v*Tg_old_v(j)))/(E_v+1);
        elseif and(j>1,t_h(l)<=163*3600)
        Tf_new_v(j)=(Tf_new_v(j-1)*(2*mf_flow*cf*B_v - 1) + 2*Tp_new_v(j))/(1
+ 2*mf_flow*cf*B_v);
```

```matlab
    Tp_new_v(j)=(Tf_new_v(j)/2 + Tf_new_v(j-1)/2 +
(E_v*Tg_old_v(j)))/(E_v+1);
    elseif and(j>=1,t_h(l)<=168*3600)
    Tf_new_v(j)=cf4_v*((Tp_old_v(j)-Tf_old_v(j))/Rwp_v) + Tf_old_v(j);
    Tp_new_v(j)=cp1_v*(((Tf_new_v(j)-
Tp_old_v(j))/Rwp_v)+(cp3_v*(Tg_old_v(j)-Tp_old_v(j))))+Tp_old_v(j);


    elseif and(j==1,t_h(l)<=187*3600)
    Tf_new_v(j)=(Tf_new_h(p_h)*(2*mf_flow*cf*B_v - 1) + 2*Tp_new_v(j))/(1
+ 2*mf_flow*cf*B_v);
    Tp_new_v(j)=(Tf_new_v(j)/2 + Tf_new_h(p_h)/2 +
(E_v*Tg_old_v(j)))/(E_v+1);
    elseif and(j>1,t_h(l)<=187*3600)
    Tf_new_v(j)=(Tf_new_v(j-1)*(2*mf_flow*cf*B_v - 1) + 2*Tp_new_v(j))/(1
+ 2*mf_flow*cf*B_v);
    Tp_new_v(j)=(Tf_new_v(j)/2 + Tf_new_v(j-1)/2 +
(E_v*Tg_old_v(j)))/(E_v+1);
    elseif and(j>=1,t_h(l)<=192*3600)
    Tf_new_v(j)=cf4_v*((Tp_old_v(j)-Tf_old_v(j))/Rwp_v) + Tf_old_v(j);
    Tp_new_v(j)=cp1_v*(((Tf_new_v(j)-
Tp_old_v(j))/Rwp_v)+(cp3_v*(Tg_old_v(j)-Tp_old_v(j))))+Tp_old_v(j);


    elseif and(j==1,t_h(l)<=211*3600)
    Tf_new_v(j)=(Tf_new_h(p_h)*(2*mf_flow*cf*B_v - 1) + 2*Tp_new_v(j))/(1
+ 2*mf_flow*cf*B_v);
    Tp_new_v(j)=(Tf_new_v(j)/2 + Tf_new_h(p_h)/2 +
(E_v*Tg_old_v(j)))/(E_v+1);
    elseif and(j>1,t_h(l)<=211*3600)
    Tf_new_v(j)=(Tf_new_v(j-1)*(2*mf_flow*cf*B_v - 1) + 2*Tp_new_v(j))/(1
+ 2*mf_flow*cf*B_v);
    Tp_new_v(j)=(Tf_new_v(j)/2 + Tf_new_v(j-1)/2 +
(E_v*Tg_old_v(j)))/(E_v+1);
    elseif and(j>=1,t_h(l)<=216*3600)
    Tf_new_v(j)=cf4_v*((Tp_old_v(j)-Tf_old_v(j))/Rwp_v) + Tf_old_v(j);
    Tp_new_v(j)=cp1_v*(((Tf_new_v(j)-
Tp_old_v(j))/Rwp_v)+(cp3_v*(Tg_old_v(j)-Tp_old_v(j))))+Tp_old_v(j);


    elseif and(j==1,t_h(l)<=235*3600)
    Tf_new_v(j)=(Tf_new_h(p_h)*(2*mf_flow*cf*B_v - 1) + 2*Tp_new_v(j))/(1
+ 2*mf_flow*cf*B_v);
    Tp_new_v(j)=(Tf_new_v(j)/2 + Tf_new_h(p_h)/2 +
(E_v*Tg_old_v(j)))/(E_v+1);
    elseif and(j>1,t_h(l)<=235*3600)
    Tf_new_v(j)=(Tf_new_v(j-1)*(2*mf_flow*cf*B_v - 1) + 2*Tp_new_v(j))/(1
+ 2*mf_flow*cf*B_v);
    Tp_new_v(j)=(Tf_new_v(j)/2 + Tf_new_v(j-1)/2 +
(E_v*Tg_old_v(j)))/(E_v+1);
    elseif and(j>=1,t_h(l)<=240*3600)
    Tf_new_v(j)=cf4_v*((Tp_old_v(j)-Tf_old_v(j))/Rwp_v) + Tf_old_v(j);
    Tp_new_v(j)=cp1_v*(((Tf_new_v(j)-
Tp_old_v(j))/Rwp_v)+(cp3_v*(Tg_old_v(j)-Tp_old_v(j))))+Tp_old_v(j);


    elseif and(j==1,t_h(l)<=259*3600)
    Tf_new_v(j)=(Tf_new_h(p_h)*(2*mf_flow*cf*B_v - 1) + 2*Tp_new_v(j))/(1
+ 2*mf_flow*cf*B_v);
    Tp_new_v(j)=(Tf_new_v(j)/2 + Tf_new_h(p_h)/2 +
(E_v*Tg_old_v(j)))/(E_v+1);
    elseif and(j>1,t_h(l)<=259*3600)
    Tf_new_v(j)=(Tf_new_v(j-1)*(2*mf_flow*cf*B_v - 1) + 2*Tp_new_v(j))/(1
+ 2*mf_flow*cf*B_v);
    Tp_new_v(j)=(Tf_new_v(j)/2 + Tf_new_v(j-1)/2 +
(E_v*Tg_old_v(j)))/(E_v+1);
    elseif and(j>=1,t_h(l)<=264*3600)
    Tf_new_v(j)=cf4_v*((Tp_old_v(j)-Tf_old_v(j))/Rwp_v) + Tf_old_v(j);
```

```
        Tp_new_v(j)=cp1_v*(((Tf_new_v(j)-
Tp_old_v(j))/Rwp_v)+(cp3_v*(Tg_old_v(j)-Tp_old_v(j))))+Tp_old_v(j);


         elseif and(j==1,t_h(l)<=283*3600)
        Tf_new_v(j)=(Tf_new_h(p_h)*(2*mf_flow*cf*B_v - 1) + 2*Tp_new_v(j))/(1
+ 2*mf_flow*cf*B_v);
        Tp_new_v(j)=(Tf_new_v(j)/2 + Tf_new_h(p_h)/2 +
(E_v*Tg_old_v(j)))/(E_v+1);
         elseif and(j>1,t_h(l)<=283*3600)
        Tf_new_v(j)=(Tf_new_v(j-1)*(2*mf_flow*cf*B_v - 1) + 2*Tp_new_v(j))/(1
+ 2*mf_flow*cf*B_v);
        Tp_new_v(j)=(Tf_new_v(j)/2 + Tf_new_v(j-1)/2 +
(E_v*Tg_old_v(j)))/(E_v+1);
         elseif and(j>=1,t_h(l)<=288*3600)
        Tf_new_v(j)=cf4_v*((Tp_old_v(j)-Tf_old_v(j))/Rwp_v) + Tf_old_v(j);
        Tp_new_v(j)=cp1_v*(((Tf_new_v(j)-
Tp_old_v(j))/Rwp_v)+(cp3_v*(Tg_old_v(j)-Tp_old_v(j))))+Tp_old_v(j);


         elseif and(j==1,t_h(l)<=307*3600)
        Tf_new_v(j)=(Tf_new_h(p_h)*(2*mf_flow*cf*B_v - 1) + 2*Tp_new_v(j))/(1
+ 2*mf_flow*cf*B_v);
        Tp_new_v(j)=(Tf_new_v(j)/2 + Tf_new_h(p_h)/2 +
(E_v*Tg_old_v(j)))/(E_v+1);
         elseif and(j>1,t_h(l)<=307*3600)
        Tf_new_v(j)=(Tf_new_v(j-1)*(2*mf_flow*cf*B_v - 1) + 2*Tp_new_v(j))/(1
+ 2*mf_flow*cf*B_v);
        Tp_new_v(j)=(Tf_new_v(j)/2 + Tf_new_v(j-1)/2 +
(E_v*Tg_old_v(j)))/(E_v+1);
         elseif and(j>=1,t_h(l)<=312*3600)
        Tf_new_v(j)=cf4_v*((Tp_old_v(j)-Tf_old_v(j))/Rwp_v) + Tf_old_v(j);
        Tp_new_v(j)=cp1_v*(((Tf_new_v(j)-
Tp_old_v(j))/Rwp_v)+(cp3_v*(Tg_old_v(j)-Tp_old_v(j))))+Tp_old_v(j);


         elseif and(j==1,t_h(l)<=331*3600)
        Tf_new_v(j)=(Tf_new_h(p_h)*(2*mf_flow*cf*B_v - 1) + 2*Tp_new_v(j))/(1
+ 2*mf_flow*cf*B_v);
        Tp_new_v(j)=(Tf_new_v(j)/2 + Tf_new_h(p_h)/2 +
(E_v*Tg_old_v(j)))/(E_v+1);
         elseif and(j>1,t_h(l)<=331*3600)
        Tf_new_v(j)=(Tf_new_v(j-1)*(2*mf_flow*cf*B_v - 1) + 2*Tp_new_v(j))/(1
+ 2*mf_flow*cf*B_v);
        Tp_new_v(j)=(Tf_new_v(j)/2 + Tf_new_v(j-1)/2 +
(E_v*Tg_old_v(j)))/(E_v+1);
         elseif and(j>=1,t_h(l)<=336*3600)
        Tf_new_v(j)=cf4_v*((Tp_old_v(j)-Tf_old_v(j))/Rwp_v) + Tf_old_v(j);
        Tp_new_v(j)=cp1_v*(((Tf_new_v(j)-
Tp_old_v(j))/Rwp_v)+(cp3_v*(Tg_old_v(j)-Tp_old_v(j))))+Tp_old_v(j);


         elseif and(j==1,t_h(l)<=355*3600)
        Tf_new_v(j)=(Tf_new_h(p_h)*(2*mf_flow*cf*B_v - 1) + 2*Tp_new_v(j))/(1
+ 2*mf_flow*cf*B_v);
        Tp_new_v(j)=(Tf_new_v(j)/2 + Tf_new_h(p_h)/2 +
(E_v*Tg_old_v(j)))/(E_v+1);
         elseif and(j>1,t_h(l)<=355*3600)
        Tf_new_v(j)=(Tf_new_v(j-1)*(2*mf_flow*cf*B_v - 1) + 2*Tp_new_v(j))/(1
+ 2*mf_flow*cf*B_v);
        Tp_new_v(j)=(Tf_new_v(j)/2 + Tf_new_v(j-1)/2 +
(E_v*Tg_old_v(j)))/(E_v+1);
         elseif and(j>=1,t_h(l)<=360*3600)
        Tf_new_v(j)=cf4_v*((Tp_old_v(j)-Tf_old_v(j))/Rwp_v) + Tf_old_v(j);
        Tp_new_v(j)=cp1_v*(((Tf_new_v(j)-
Tp_old_v(j))/Rwp_v)+(cp3_v*(Tg_old_v(j)-Tp_old_v(j))))+Tp_old_v(j);


         elseif and(j==1,t_h(l)<=379*3600)
```

```
      Tf_new_v(j)=(Tf_new_h(p_h)*(2*mf_flow*cf*B_v - 1) + 2*Tp_new_v(j))/(1
+ 2*mf_flow*cf*B_v);
      Tp_new_v(j)=(Tf_new_v(j)/2 + Tf_new_h(p_h)/2 +
(E_v*Tg_old_v(j)))/(E_v+1);
      elseif and(j>1,t_h(l)<=379*3600)
      Tf_new_v(j)=(Tf_new_v(j-1)*(2*mf_flow*cf*B_v - 1) + 2*Tp_new_v(j))/(1
+ 2*mf_flow*cf*B_v);
      Tp_new_v(j)=(Tf_new_v(j)/2 + Tf_new_v(j-1)/2 +
(E_v*Tg_old_v(j)))/(E_v+1);
      elseif and(j>=1,t_h(l)<=384*3600)
      Tf_new_v(j)=cf4_v*((Tp_old_v(j)-Tf_old_v(j))/Rwp_v) + Tf_old_v(j);
      Tp_new_v(j)=cp1_v*(((Tf_new_v(j)-
Tp_old_v(j))/Rwp_v)+(cp3_v*(Tg_old_v(j)-Tp_old_v(j))))+Tp_old_v(j);


      elseif and(j==1,t_h(l)<=403*3600)
      Tf_new_v(j)=(Tf_new_h(p_h)*(2*mf_flow*cf*B_v - 1) + 2*Tp_new_v(j))/(1
+ 2*mf_flow*cf*B_v);
      Tp_new_v(j)=(Tf_new_v(j)/2 + Tf_new_h(p_h)/2 +
(E_v*Tg_old_v(j)))/(E_v+1);
      elseif and(j>1,t_h(l)<=403*3600)
      Tf_new_v(j)=(Tf_new_v(j-1)*(2*mf_flow*cf*B_v - 1) + 2*Tp_new_v(j))/(1
+ 2*mf_flow*cf*B_v);
      Tp_new_v(j)=(Tf_new_v(j)/2 + Tf_new_v(j-1)/2 +
(E_v*Tg_old_v(j)))/(E_v+1);
      elseif and(j>=1,t_h(l)<=408*3600)
      Tf_new_v(j)=cf4_v*((Tp_old_v(j)-Tf_old_v(j))/Rwp_v) + Tf_old_v(j);
      Tp_new_v(j)=cp1_v*(((Tf_new_v(j)-
Tp_old_v(j))/Rwp_v)+(cp3_v*(Tg_old_v(j)-Tp_old_v(j))))+Tp_old_v(j);


      elseif and(j==1,t_h(l)<=427*3600)
      Tf_new_v(j)=(Tf_new_h(p_h)*(2*mf_flow*cf*B_v - 1) + 2*Tp_new_v(j))/(1
+ 2*mf_flow*cf*B_v);
      Tp_new_v(j)=(Tf_new_v(j)/2 + Tf_new_h(p_h)/2 +
(E_v*Tg_old_v(j)))/(E_v+1);
      elseif and(j>1,t_h(l)<=427*3600)
      Tf_new_v(j)=(Tf_new_v(j-1)*(2*mf_flow*cf*B_v - 1) + 2*Tp_new_v(j))/(1
+ 2*mf_flow*cf*B_v);
      Tp_new_v(j)=(Tf_new_v(j)/2 + Tf_new_v(j-1)/2 +
(E_v*Tg_old_v(j)))/(E_v+1);
      elseif and(j>=1,t_h(l)<=432*3600)
      Tf_new_v(j)=cf4_v*((Tp_old_v(j)-Tf_old_v(j))/Rwp_v) + Tf_old_v(j);
      Tp_new_v(j)=cp1_v*(((Tf_new_v(j)-
Tp_old_v(j))/Rwp_v)+(cp3_v*(Tg_old_v(j)-Tp_old_v(j))))+Tp_old_v(j);


      elseif and(j==1,t_h(l)<=451*3600)
      Tf_new_v(j)=(Tf_new_h(p_h)*(2*mf_flow*cf*B_v - 1) + 2*Tp_new_v(j))/(1
+ 2*mf_flow*cf*B_v);
      Tp_new_v(j)=(Tf_new_v(j)/2 + Tf_new_h(p_h)/2 +
(E_v*Tg_old_v(j)))/(E_v+1);
      elseif and(j>1,t_h(l)<=451*3600)
      Tf_new_v(j)=(Tf_new_v(j-1)*(2*mf_flow*cf*B_v - 1) + 2*Tp_new_v(j))/(1
+ 2*mf_flow*cf*B_v);
      Tp_new_v(j)=(Tf_new_v(j)/2 + Tf_new_v(j-1)/2 +
(E_v*Tg_old_v(j)))/(E_v+1);
      elseif and(j>=1,t_h(l)<=456*3600)
      Tf_new_v(j)=cf4_v*((Tp_old_v(j)-Tf_old_v(j))/Rwp_v) + Tf_old_v(j);
      Tp_new_v(j)=cp1_v*(((Tf_new_v(j)-
Tp_old_v(j))/Rwp_v)+(cp3_v*(Tg_old_v(j)-Tp_old_v(j))))+Tp_old_v(j);


      elseif and(j==1,t_h(l)<=475*3600)
      Tf_new_v(j)=(Tf_new_h(p_h)*(2*mf_flow*cf*B_v - 1) + 2*Tp_new_v(j))/(1
+ 2*mf_flow*cf*B_v);
      Tp_new_v(j)=(Tf_new_v(j)/2 + Tf_new_h(p_h)/2 +
(E_v*Tg_old_v(j)))/(E_v+1);
```

```
    elseif and(j>1,t_h(l)<=475*3600)
    Tf_new_v(j)=(Tf_new_v(j-1)*(2*mf_flow*cf*B_v - 1) + 2*Tp_new_v(j))/(1
+ 2*mf_flow*cf*B_v);
    Tp_new_v(j)=(Tf_new_v(j)/2 + Tf_new_v(j-1)/2 +
(E_v*Tg_old_v(j)))/(E_v+1);
    elseif and(j>=1,t_h(l)<=480*3600)
    Tf_new_v(j)=cf4_v*((Tp_old_v(j)-Tf_old_v(j))/Rwp_v) + Tf_old_v(j);
    Tp_new_v(j)=cp1_v*(((Tf_new_v(j)-
Tp_old_v(j))/Rwp_v)+(cp3_v*(Tg_old_v(j)-Tp_old_v(j))))+Tp_old_v(j);


     elseif and(j==1,t_h(l)<=499*3600)
    Tf_new_v(j)=(Tf_new_h(p_h)*(2*mf_flow*cf*B_v - 1) + 2*Tp_new_v(j))/(1
+ 2*mf_flow*cf*B_v);
    Tp_new_v(j)=(Tf_new_v(j)/2 + Tf_new_h(p_h)/2 +
(E_v*Tg_old_v(j)))/(E_v+1);
    elseif and(j>1,t_h(l)<=499*3600)
    Tf_new_v(j)=(Tf_new_v(j-1)*(2*mf_flow*cf*B_v - 1) + 2*Tp_new_v(j))/(1
+ 2*mf_flow*cf*B_v);
    Tp_new_v(j)=(Tf_new_v(j)/2 + Tf_new_v(j-1)/2 +
(E_v*Tg_old_v(j)))/(E_v+1);
    elseif and(j>=1,t_h(l)<=504*3600)
    Tf_new_v(j)=cf4_v*((Tp_old_v(j)-Tf_old_v(j))/Rwp_v) + Tf_old_v(j);
    Tp_new_v(j)=cp1_v*(((Tf_new_v(j)-
Tp_old_v(j))/Rwp_v)+(cp3_v*(Tg_old_v(j)-Tp_old_v(j))))+Tp_old_v(j);


     elseif and(j==1,t_h(l)<=523*3600)
    Tf_new_v(j)=(Tf_new_h(p_h)*(2*mf_flow*cf*B_v - 1) + 2*Tp_new_v(j))/(1
+ 2*mf_flow*cf*B_v);
    Tp_new_v(j)=(Tf_new_v(j)/2 + Tf_new_h(p_h)/2 +
(E_v*Tg_old_v(j)))/(E_v+1);
    elseif and(j>1,t_h(l)<=523*3600)
    Tf_new_v(j)=(Tf_new_v(j-1)*(2*mf_flow*cf*B_v - 1) + 2*Tp_new_v(j))/(1
+ 2*mf_flow*cf*B_v);
    Tp_new_v(j)=(Tf_new_v(j)/2 + Tf_new_v(j-1)/2 +
(E_v*Tg_old_v(j)))/(E_v+1);
    elseif and(j>=1,t_h(l)<=528*3600)
    Tf_new_v(j)=cf4_v*((Tp_old_v(j)-Tf_old_v(j))/Rwp_v) + Tf_old_v(j);
    Tp_new_v(j)=cp1_v*(((Tf_new_v(j)-
Tp_old_v(j))/Rwp_v)+(cp3_v*(Tg_old_v(j)-Tp_old_v(j))))+Tp_old_v(j);


     elseif and(j==1,t_h(l)<=547*3600)
    Tf_new_v(j)=(Tf_new_h(p_h)*(2*mf_flow*cf*B_v - 1) + 2*Tp_new_v(j))/(1
+ 2*mf_flow*cf*B_v);
    Tp_new_v(j)=(Tf_new_v(j)/2 + Tf_new_h(p_h)/2 +
(E_v*Tg_old_v(j)))/(E_v+1);
    elseif and(j>1,t_h(l)<=547*3600)
    Tf_new_v(j)=(Tf_new_v(j-1)*(2*mf_flow*cf*B_v - 1) + 2*Tp_new_v(j))/(1
+ 2*mf_flow*cf*B_v);
    Tp_new_v(j)=(Tf_new_v(j)/2 + Tf_new_v(j-1)/2 +
(E_v*Tg_old_v(j)))/(E_v+1);
    elseif and(j>=1,t_h(l)<=552*3600)
    Tf_new_v(j)=cf4_v*((Tp_old_v(j)-Tf_old_v(j))/Rwp_v) + Tf_old_v(j);
    Tp_new_v(j)=cp1_v*(((Tf_new_v(j)-
Tp_old_v(j))/Rwp_v)+(cp3_v*(Tg_old_v(j)-Tp_old_v(j))))+Tp_old_v(j);


     elseif and(j==1,t_h(l)<=571*3600)
    Tf_new_v(j)=(Tf_new_h(p_h)*(2*mf_flow*cf*B_v - 1) + 2*Tp_new_v(j))/(1
+ 2*mf_flow*cf*B_v);
    Tp_new_v(j)=(Tf_new_v(j)/2 + Tf_new_h(p_h)/2 +
(E_v*Tg_old_v(j)))/(E_v+1);
    elseif and(j>1,t_h(l)<=571*3600)
    Tf_new_v(j)=(Tf_new_v(j-1)*(2*mf_flow*cf*B_v - 1) + 2*Tp_new_v(j))/(1
+ 2*mf_flow*cf*B_v);
```

```matlab
        Tp_new_v(j)=(Tf_new_v(j)/2 + Tf_new_v(j-1)/2 +
(E_v*Tg_old_v(j)))/(E_v+1);
        elseif and(j>=1,t_h(l)<=576*3600)
        Tf_new_v(j)=cf4_v*((Tp_old_v(j)-Tf_old_v(j))/Rwp_v) + Tf_old_v(j);
        Tp_new_v(j)=cp1_v*(((Tf_new_v(j)-
Tp_old_v(j))/Rwp_v)+(cp3_v*(Tg_old_v(j)-Tp_old_v(j))))+Tp_old_v(j);


        elseif and(j==1,t_h(l)<=595*3600)
        Tf_new_v(j)=(Tf_new_h(p_h)*(2*mf_flow*cf*B_v - 1) + 2*Tp_new_v(j))/(1
+ 2*mf_flow*cf*B_v);
        Tp_new_v(j)=(Tf_new_v(j)/2 + Tf_new_h(p_h)/2 +
(E_v*Tg_old_v(j)))/(E_v+1);
        elseif and(j>1,t_h(l)<=595*3600)
        Tf_new_v(j)=(Tf_new_v(j-1)*(2*mf_flow*cf*B_v - 1) + 2*Tp_new_v(j))/(1
+ 2*mf_flow*cf*B_v);
        Tp_new_v(j)=(Tf_new_v(j)/2 + Tf_new_v(j-1)/2 +
(E_v*Tg_old_v(j)))/(E_v+1);
        elseif and(j>=1,t_h(l)<=600*3600)
        Tf_new_v(j)=cf4_v*((Tp_old_v(j)-Tf_old_v(j))/Rwp_v) + Tf_old_v(j);
        Tp_new_v(j)=cp1_v*(((Tf_new_v(j)-
Tp_old_v(j))/Rwp_v)+(cp3_v*(Tg_old_v(j)-Tp_old_v(j))))+Tp_old_v(j);


        elseif and(j==1,t_h(l)<=619*3600)
        Tf_new_v(j)=(Tf_new_h(p_h)*(2*mf_flow*cf*B_v - 1) + 2*Tp_new_v(j))/(1
+ 2*mf_flow*cf*B_v);
        Tp_new_v(j)=(Tf_new_v(j)/2 + Tf_new_h(p_h)/2 +
(E_v*Tg_old_v(j)))/(E_v+1);
        elseif and(j>1,t_h(l)<=619*3600)
        Tf_new_v(j)=(Tf_new_v(j-1)*(2*mf_flow*cf*B_v - 1) + 2*Tp_new_v(j))/(1
+ 2*mf_flow*cf*B_v);
        Tp_new_v(j)=(Tf_new_v(j)/2 + Tf_new_v(j-1)/2 +
(E_v*Tg_old_v(j)))/(E_v+1);
        elseif and(j>=1,t_h(l)<=624*3600)
        Tf_new_v(j)=cf4_v*((Tp_old_v(j)-Tf_old_v(j))/Rwp_v) + Tf_old_v(j);
        Tp_new_v(j)=cp1_v*(((Tf_new_v(j)-
Tp_old_v(j))/Rwp_v)+(cp3_v*(Tg_old_v(j)-Tp_old_v(j))))+Tp_old_v(j);


        elseif and(j==1,t_h(l)<=643*3600)
        Tf_new_v(j)=(Tf_new_h(p_h)*(2*mf_flow*cf*B_v - 1) + 2*Tp_new_v(j))/(1
+ 2*mf_flow*cf*B_v);
        Tp_new_v(j)=(Tf_new_v(j)/2 + Tf_new_h(p_h)/2 +
(E_v*Tg_old_v(j)))/(E_v+1);
        elseif and(j>1,t_h(l)<=643*3600)
        Tf_new_v(j)=(Tf_new_v(j-1)*(2*mf_flow*cf*B_v - 1) + 2*Tp_new_v(j))/(1
+ 2*mf_flow*cf*B_v);
        Tp_new_v(j)=(Tf_new_v(j)/2 + Tf_new_v(j-1)/2 +
(E_v*Tg_old_v(j)))/(E_v+1);
        elseif and(j>=1,t_h(l)<=648*3600)
        Tf_new_v(j)=cf4_v*((Tp_old_v(j)-Tf_old_v(j))/Rwp_v) + Tf_old_v(j);
        Tp_new_v(j)=cp1_v*(((Tf_new_v(j)-
Tp_old_v(j))/Rwp_v)+(cp3_v*(Tg_old_v(j)-Tp_old_v(j))))+Tp_old_v(j);


        elseif and(j==1,t_h(l)<=667*3600)
        Tf_new_v(j)=(Tf_new_h(p_h)*(2*mf_flow*cf*B_v - 1) + 2*Tp_new_v(j))/(1
+ 2*mf_flow*cf*B_v);
        Tp_new_v(j)=(Tf_new_v(j)/2 + Tf_new_h(p_h)/2 +
(E_v*Tg_old_v(j)))/(E_v+1);
        elseif and(j>1,t_h(l)<=667*3600)
        Tf_new_v(j)=(Tf_new_v(j-1)*(2*mf_flow*cf*B_v - 1) + 2*Tp_new_v(j))/(1
+ 2*mf_flow*cf*B_v);
        Tp_new_v(j)=(Tf_new_v(j)/2 + Tf_new_v(j-1)/2 +
(E_v*Tg_old_v(j)))/(E_v+1);
        elseif and(j>=1,t_h(l)<=672*3600)
        Tf_new_v(j)=cf4_v*((Tp_old_v(j)-Tf_old_v(j))/Rwp_v) + Tf_old_v(j);
```

```matlab
            Tp_new_v(j)=cp1_v*(((Tf_new_v(j)-
Tp_old_v(j))/Rwp_v)+(cp3_v*(Tg_old_v(j)-Tp_old_v(j))))+Tp_old_v(j);


        elseif and(j==1,t_h(l)<=691*3600)
        Tf_new_v(j)=(Tf_new_h(p_h)*(2*mf_flow*cf*B_v - 1) + 2*Tp_new_v(j))/(1
+ 2*mf_flow*cf*B_v);
        Tp_new_v(j)=(Tf_new_v(j)/2 + Tf_new_h(p_h)/2 +
(E_v*Tg_old_v(j)))/(E_v+1);
        elseif and(j>1,t_h(l)<=691*3600)
        Tf_new_v(j)=(Tf_new_v(j-1)*(2*mf_flow*cf*B_v - 1) + 2*Tp_new_v(j))/(1
+ 2*mf_flow*cf*B_v);
        Tp_new_v(j)=(Tf_new_v(j)/2 + Tf_new_v(j-1)/2 +
(E_v*Tg_old_v(j)))/(E_v+1);
        elseif and(j>=1,t_h(l)<=696*3600)
        Tf_new_v(j)=cf4_v*((Tp_old_v(j)-Tf_old_v(j))/Rwp_v) + Tf_old_v(j);
        Tp_new_v(j)=cp1_v*(((Tf_new_v(j)-
Tp_old_v(j))/Rwp_v)+(cp3_v*(Tg_old_v(j)-Tp_old_v(j))))+Tp_old_v(j);


        elseif and(j==1,t_h(l)<=715*3600)
        Tf_new_v(j)=(Tf_new_h(p_h)*(2*mf_flow*cf*B_v - 1) + 2*Tp_new_v(j))/(1
+ 2*mf_flow*cf*B_v);
        Tp_new_v(j)=(Tf_new_v(j)/2 + Tf_new_h(p_h)/2 +
(E_v*Tg_old_v(j)))/(E_v+1);
        elseif and(j>1,t_h(l)<=715*3600)
        Tf_new_v(j)=(Tf_new_v(j-1)*(2*mf_flow*cf*B_v - 1) + 2*Tp_new_v(j))/(1
+ 2*mf_flow*cf*B_v);
        Tp_new_v(j)=(Tf_new_v(j)/2 + Tf_new_v(j-1)/2 +
(E_v*Tg_old_v(j)))/(E_v+1);
        elseif and(j>=1,t_h(l)<=720*3600)
        Tf_new_v(j)=cf4_v*((Tp_old_v(j)-Tf_old_v(j))/Rwp_v) + Tf_old_v(j);
        Tp_new_v(j)=cp1_v*(((Tf_new_v(j)-
Tp_old_v(j))/Rwp_v)+(cp3_v*(Tg_old_v(j)-Tp_old_v(j))))+Tp_old_v(j);


        elseif and(j==1,t_h(l)<=739*3600)
        Tf_new_v(j)=(Tf_new_h(p_h)*(2*mf_flow*cf*B_v - 1) + 2*Tp_new_v(j))/(1
+ 2*mf_flow*cf*B_v);
        Tp_new_v(j)=(Tf_new_v(j)/2 + Tf_new_h(p_h)/2 +
(E_v*Tg_old_v(j)))/(E_v+1);
        elseif and(j>1,t_h(l)<=739*3600)
        Tf_new_v(j)=(Tf_new_v(j-1)*(2*mf_flow*cf*B_v - 1) + 2*Tp_new_v(j))/(1
+ 2*mf_flow*cf*B_v);
        Tp_new_v(j)=(Tf_new_v(j)/2 + Tf_new_v(j-1)/2 +
(E_v*Tg_old_v(j)))/(E_v+1);
        elseif and(j>=1,t_h(l)<=744*3600)
        Tf_new_v(j)=cf4_v*((Tp_old_v(j)-Tf_old_v(j))/Rwp_v) + Tf_old_v(j);
        Tp_new_v(j)=cp1_v*(((Tf_new_v(j)-
Tp_old_v(j))/Rwp_v)+(cp3_v*(Tg_old_v(j)-Tp_old_v(j))))+Tp_old_v(j);
        end

 end

% Surface boundary
%Ts next to soil boundary
% Corner left hand side (i=1 and j=1)Eq.4.8
    for j=1
        for i=1
            for k=1:p_h
            if y_h(j)<=1
                H=H1;
            else
                H=H2;
            end
```

```
Ts_new_h(j,i,k)=(Fo_h*(2*Ts_old_h(j,i+1,k)+Ts_old_h(j+1,i,k)+((Uas_h*dx_h*T
a)/ks)+((H*dx_h^2)/ks)))+(1-(3+((Uas_h*dx_h)/ks))*Fo_h)*Ts_old_h(j,i,k);
            end
        end
    end
 % Middle nodes(i=2,3,4....m-1 and j=1)Eq.4.9
    for j=1
        for i=2:m_h-1
            for k=1:p_h
            if y_h(j)<=1
                H=H1;
            else
                H=H2;
            end
            Ts_new_h(j,i,k)=(Fo_h*(Ts_old_h(j,i-
1,k)+Ts_old_h(j,i+1,k)+Ts_old_h(j+1,i,k)+((Uas_h*dx_h*Ta)/ks)+((H*dx_h^2)/k
s)))+(1-(3+((Uas_h*dx_h)/ks))*Fo_h)*Ts_old_h(j,i,k);
            end
        end
    end
  % Corner right hand side (i=m and j=1)Eq.4.10
    for j=1
        for i=m_h
            for k=1:p_h
            if y_h(j)<=1
                H=H1;
            else
                H=H2;
            end
            Ts_new_h(j,i,k)=(Fo_h*(Ts_old_h(j,i-
1,k)+Ts_old_h(j+1,i,k)+((Uas_h*dx_h*Ta)/ks)+((H*dx_h^2)/ks)))+(1-
(2+((Uas_h*dx_h)/ks))*Fo_h)*Ts_old_h(j,i,k);
            end
        end
    end

%Ts next to soil boundary
% Bottom boundary
% Corner left hand side (i=1 and j=n) Eq.4.11
    for j=n_h
        for i=1
            for k=1:p_h
            if y_h(j)<=1
                H=H1;
            else
                H=H2;
            end
            Ts_new_h(j,i,k)=(Fo_h*(2*Ts_old_h(j,i+1,k)+Ts_old_h(j-
1,i,k)+((H*dx_h^2)/ks)))+(1-3*Fo_h)*Ts_old_h(j,i,k);
            end
        end
    end
% Middle nodes(i=2,3,4....m-1 and j=n) Eq.4.12
    for j=n_h
        for i=2:m_h-1
            for k=1:p_h
            if y_h(j)<=1
                H=H1;
            else
                H=H2;
            end
```

```matlab
            Ts_new_h(j,i,k)=(Fo_h*(Ts_old_h(j,i-
1,k)+Ts_old_h(j,i+1,k)+Ts_old_h(j-1,i,k)+((H*dx_h^2)/ks)))+(1-
3*Fo_h)*Ts_old_h(j,i,k);
            end
        end
    end
  %Corner right hand side (i=m and j=n) Eq.4.13
    for j=n_h
        for i=m_h
            for k=1:p_h
                if y_h(j)<=1
                    H=H1;
                else
                    H=H2;
                end
                Ts_new_h(j,i,k)=(Fo_h*(Ts_old_h(j,i-1,k)+Ts_old_h(j-
1,i,k)+((H*dx_h^2)/ks)))+(1-2*Fo_h)*Ts_old_h(j,i,k);
            end
        end
    end


% Symmetry boundary
%Middle nodes(i=m and j=2,3,4....n-1) Eq.4.14
    for j=2:n_h-1
        for i=m_h
            for k=1:p_h
                if y_h(j)<=1
                    H=H1;
                else
                    H=H2;
                end
                Ts_new_h(j,i,k)=(Fo_h*(Ts_old_h(j,i-
1,k)+Ts_old_h(j+1,i,k)+Ts_old_h(j-1,i,k)+((H*dx_h^2)/ks)))+(1-
3*Fo_h)*Ts_old_h(j,i,k);
            end
        end
    end
%Middle nodes(i=1 and j=2,3,4....n-1) Eq.4.15
for j=2:24
        for i=1
            for k=1:p_h
                if y_h(j)<=1
                    H=H1;
                else
                    H=H2;
                end

Ts_new_h(j,i,k)=(Fo_h*(2*Ts_old_h(j,i+1,k)+Ts_old_h(j+1,i,k)+Ts_old_h(j-
1,i,k)+((H*dx_h^2)/ks)))+(1-4*Fo_h)*Ts_old_h(j,i,k);
            end
        end
end
for j=28:n_h-1
        for i=1
            for k=1:p_h
                if y_h(j)<=1
                    H=H1;
                else
                    H=H2;
                end

Ts_new_h(j,i,k)=(Fo_h*(2*Ts_old_h(j,i+1,k)+Ts_old_h(j+1,i,k)+Ts_old_h(j-
1,i,k)+((H*dx_h^2)/ks)))+(1-4*Fo_h)*Ts_old_h(j,i,k);
            end
```

```matlab
        end
end
%Ts for node situated above the pipe Eq.4.16
for j=25
        for i=1
            for k=1:p_h
            if y_h(j)<=1
                H=H1;
            else
                H=H2;
            end

Ts_new_h(j,i,k)=(Fo_h*(2*Tp_new_h(k)+2*Ts_old_h(j,i+1,k)+Ts_old_h(j-
1,i,k)+((H*dx_h^2)/ks)))+(1 - 5*Fo_h)*Ts_old_h(j,i,k);
            end
        end
end
 %Ts for node situated below the pipe Eq.4.17
    for j=27
        for i=1
            for k=1:p_h
            if y_h(j)<=1
                H=H1;
            else
                H=H2;
            end

Ts_new_h(j,i,k)=(Fo_h*(2*Tp_new_h(k)+2*Ts_old_h(j,i+1,k)+Ts_old_h(j+1,i,k)+
((H*dx_h^2)/ks)))+(1 - 5*Fo_h)*Ts_old_h(j,i,k);
            end
        end
    end
 %Ts for node situated on the right handside of the pipe Eq.4.18
    for j=26
        for i=2
         for k=1:p_h
            if y_h(j)<=1
                H=H1;
            else
                H=H2;
            end

Ts_new_h(j,i,k)=(Fo_h*(2*Tp_new_h(k)+Ts_old_h(j,i+1,k)+Ts_old_h(j+1,i,k)+Ts
_old_h(j-1,i,k)+((H*dx_h^2)/ks)))+(1 - 5*Fo_h)*Ts_old_h(j,i,k);
          end
        end
    end

% Ts Interior nodes Eq.4.6
for j=2:25
        for i=2:m_h-1
            for k=1:p_h
            if y_h(j)<=1
                H=H1;
            else
                H=H2;
            end
            Ts_new_h(j,i,k)=(Fo_h*(Ts_old_h(j,i+1,k)+Ts_old_h(j,i-
1,k)+Ts_old_h(j+1,i,k)+Ts_old_h(j-1,i,k)+((H*dx_h^2)/ks))) + (1 -
4*Fo_h)*Ts_old_h(j,i,k);
            end
        end
end
for j=26
```

```
        for i=3:m_h-1
            for k=1:p_h
            if y_h(j)<=1
                H=H1;
            else
                H=H2;
            end
            Ts_new_h(j,i,k)=(Fo_h*(Ts_old_h(j,i+1,k)+Ts_old_h(j,i-
1,k)+Ts_old_h(j+1,i,k)+Ts_old_h(j-1,i,k)+((H*dx_h^2)/ks))) + (1 -
4*Fo_h)*Ts_old_h(j,i,k);
                end
            end
end
for j=27:n_h-1
        for i=2:m_h-1
            for k=1:p_h
            if y_h(j)<=1
                H=H1;
            else
                H=H2;
            end
            Ts_new_h(j,i,k)=(Fo_h*(Ts_old_h(j,i+1,k)+Ts_old_h(j,i-
1,k)+Ts_old_h(j+1,i,k)+Ts_old_h(j-1,i,k)+((H*dx_h^2)/ks))) + (1 -
4*Fo_h)*Ts_old_h(j,i,k);
                end
            end
end


Tf_old_h=Tf_new_h;
Tp_old_h=Tp_new_h;
Ts_old_h=Ts_new_h;

%Save fluid outlet temperature
Tf_cel_h=Tf_new_h(p_h)-273.15;
Tfluid_outlet_h(l)=Tf_cel_h;

 %Save the soil temperature at certain depth and distance
Ts_cel_Y98cmX4cmZ100m_h=Ts_new_h(25,2,Pz_h)-273.15;
Ts_Y98cmX4cmZ100m_h(l)=Ts_cel_Y98cmX4cmZ100m_h;

Ts_cel_Y98cmX8cmZ100m_h=Ts_new_h(25,3,Pz_h)-273.15;
Ts_Y98cmX8cmZ100m_h(l)=Ts_cel_Y98cmX8cmZ100m_h;

Ts_cel_Y98cmX12cmZ100m_h=Ts_new_h(25,4,Pz_h)-273.15;
Ts_Y98cmX12cmZ100m_h(l)=Ts_cel_Y98cmX12cmZ100m_h;

Ts_cel_Y22cmX12cmZ100m_h=Ts_new_h(6,4,Pz_h)-273.15;
Ts_Y22cmX12cmZ100m_h(l)=Ts_cel_Y22cmX12cmZ100m_h;

Ts_cel_Y46cmX12cmZ100m_h=Ts_new_h(12,4,Pz_h)-273.15;
Ts_Y46cmX12cmZ100m_h(l)=Ts_cel_Y46cmX12cmZ100m_h;

Ts_cel_Y70cmX12cmZ100m_h=Ts_new_h(18,4,Pz_h)-273.15;
Ts_Y70cmX12cmZ100m_h(l)=Ts_cel_Y70cmX12cmZ100m_h;

% soil temperature at a distance 100m from the box's edge
Ts_new_h100m=Ts_new_h(:,:,Pz_h);

%Grout temperature calculation
%The grout temperature next to surface boundary (j = 1) Eq.5.11
for j=1
  for i=1
```

```matlab
        Tg_new_v(j,i)=Fog_v*(2*Tp_new_v(j)*(1-(drg_v/(2*rg_v)))+
Ts_old_v(j,i)/Csg_s + Ta*Cag + Tg_old_v(j+1,i)/c1_v^2) + (1-(2*(1-
(drg_v/(2*rg_v))) + 1/Csg_s + Cag + 1/c1_v^2)*Fog_v)*Tg_old_v(j,i);
    end
end
%The grout temperature for the internal nodes (j = 2,3,4….n-1)Eq.5.10
for j=2:n_v-1
    for i=1
        Tg_new_v(j,i)=Fog_v*(2*Tp_new_v(j)*(1-(drg_v/(2*rg_v)))+
Ts_old_v(j,i)/Csg_s + Tg_old_v(j-1,i)/c1_v^2 + Tg_old_v(j+1,i)/c1_v^2) +
(1-(2*(1-(drg_v/(2*rg_v))) + 1/Csg_s + 2/c1_v^2)*Fog_v)*Tg_old_v(j,i);
    end
end
%The grout temperature next to bottom boundary (j = n) Eq.5.12
 for j=n_v
    for i=1
        Tg_new_v(j,i)=Fog_v*(2*Tp_new_v(j)*(1-(drg_v/(2*rg_v)))+
Ts_old_v(j,i)/Csg_s + Tg_old_v(j-1,i)/c1_v^2)+(1-(2*(1-(drg_v/(2*rg_v))) +
1/Csg_s + 1/c1_v^2)*Fog_v)*Tg_old_v(j,i);
    end
 end

%Surface boundary
%Corner left hand side (i=1 and j=1)Eq.5.15
for j=1
    for i=1
        if z_v(j)<=1
        H=H1;
        elseif z_v(j)<=2
        H=H2;
        elseif z_v(j)<=3
        H=H3;
        elseif z_v(j)<=4
        H=H4;
        elseif z_v(j)<=5
        H=H5;
        elseif z_v(j)<=6
        H=H6;
        elseif z_v(j)<=7
        H=H7;
        elseif z_v(j)<=8
        H=H8;
        elseif z_v(j)<=9
        H=H9;
        elseif z_v(j)<=10
        H=H10;
        elseif z_v(j)<=11
        H=H11;
        elseif z_v(j)<=12
        H=H12;
        else
        H=H13;
        end
    Fos=Fos_v;
    Cgs=((drg_v/(2*drs_v))/((1-(drs_v/(2*rs_v(i))))*kg_v/ks))+(0.5/(1-
(drs_v/(2*rs_v(i)))));
    Ts_new_v(j,i)=Fos*(Tg_old_v(j,i)/Cgs +
(1+(drs_v/(2*rs_v(i))))*Ts_old_v(j,i+1)+ Ta*Cas + Ts_old_v(j+1,i)/Cs1_v^2 +
((H*drs_v^2)/ks)) + (1-(1/Cgs + (1+(drs_v/(2*rs_v(i)))) + Cas +
1/Cs1_v^2)*Fos)*Ts_old_v(j,i);
    end
end
% Middle nodes(i=2,3,4....m-1 and j=1)Eq.5.18
for j=1
```

```matlab
    for i=2:m_v-1
        if z_v(j)<=1
         H=H1;
         elseif z_v(j)<=2
         H=H2;
         elseif z_v(j)<=3
         H=H3;
         elseif z_v(j)<=4
         H=H4;
         elseif z_v(j)<=5
         H=H5;
         elseif z_v(j)<=6
         H=H6;
         elseif z_v(j)<=7
         H=H7;
         elseif z_v(j)<=8
         H=H8;
         elseif z_v(j)<=9
         H=H9;
         elseif z_v(j)<=10
         H=H10;
         elseif z_v(j)<=11
         H=H11;
         elseif z_v(j)<=12
         H=H12;
         else
         H=H13;
         end
    Fos=Fos_v;
    Ts_new_v(j,i)=Fos*((1-(drs_v/(2*rs_v(i))))*Ts_old_v(j,i-1) +
(1+(drs_v/(2*rs_v(i))))*Ts_old_v(j,i+1)+ Ta*Cas + Ts_old_v(j+1,i)/Cs1_v^2 +
((H*drs_v^2)/ks)) + (1-((1-(drs_v/(2*rs_v(i)))) + (1+(drs_v/(2*rs_v(i)))) +
Cas + 1/Cs1_v^2)*Fos)*Ts_old_v(j,i);
    end
end
% Corner right hand side (i=m and j=1)Eq.5.19
for j=1
    for i=m_v
        if z_v(j)<=1
        H=H1;
        elseif z_v(j)<=2
        H=H2;
        elseif z_v(j)<=3
        H=H3;
        elseif z_v(j)<=4
        H=H4;
        elseif z_v(j)<=5
        H=H5;
        elseif z_v(j)<=6
        H=H6;
        elseif z_v(j)<=7
        H=H7;
        elseif z_v(j)<=8
        H=H8;
        elseif z_v(j)<=9
        H=H9;
        elseif z_v(j)<=10
        H=H10;
        elseif z_v(j)<=11
        H=H11;
        elseif z_v(j)<=12
        H=H12;
        else
        H=H13;
        end
```
205

```matlab
        Fos=Fos_v;
        Ts_new_v(j,i)=Fos*((1-(drs_v/(2*rs_v(i))))*Ts_old_v(j,i-1) + Ta*Cas +
Ts_old_v(j+1,i)/Cs1_v^2 + ((H*drs_v^2)/ks)) + (1-((1-(drs_v/(2*rs_v(i)))) +
Cas + 1/Cs1_v^2)*Fos)*Ts_old_v(j,i);
    end
end

%Bottom boundary
% Corner left hand side (i=1 and j=n) Eq.5.20
for j=n_v
    for i=1
        if z_v(j)<=1
        H=H1;
        elseif z_v(j)<=2
        H=H2;
        elseif z_v(j)<=3
        H=H3;
        elseif z_v(j)<=4
        H=H4;
        elseif z_v(j)<=5
        H=H5;
        elseif z_v(j)<=6
        H=H6;
        elseif z_v(j)<=7
        H=H7;
        elseif z_v(j)<=8
        H=H8;
        elseif z_v(j)<=9
        H=H9;
        elseif z_v(j)<=10
        H=H10;
        elseif z_v(j)<=11
        H=H11;
        elseif z_v(j)<=12
        H=H12;
        else
        H=H13;
        end
    Fos=Fos_v;
    Cgs=((drg_v/(2*drs_v))/((1-(drs_v/(2*rs_v(i))))*kg_v/ks))+(0.5/(1-
(drs_v/(2*rs_v(i)))));
    Ts_new_v(j,i)=Fos*(Tg_old_v(j,i)/Cgs +
(1+(drs_v/(2*rs_v(i))))*Ts_old_v(j,i+1)+ Ts_old_v(j-1,i)/Cs1_v^2
+((H*drs_v^2)/ks)) + (1-(1/Cgs + (1+(drs_v/(2*rs_v(i)))) +
1/Cs1_v^2)*Fos)*Ts_old_v(j,i);
    end
end
% Middle nodes(i=2,3,4....m-1 and j=n) Eq.5.21
for j=n_v
    for i=2:m_v-1
        if z_v(j)<=1
        H=H1;
        elseif z_v(j)<=2
        H=H2;
        elseif z_v(j)<=3
        H=H3;
        elseif z_v(j)<=4
        H=H4;
        elseif z_v(j)<=5
        H=H5;
        elseif z_v(j)<=6
        H=H6;
        elseif z_v(j)<=7
        H=H7;
```

```
            elseif z_v(j)<=8
            H=H8;
            elseif z_v(j)<=9
            H=H9;
            elseif z_v(j)<=10
            H=H10;
            elseif z_v(j)<=11
            H=H11;
            elseif z_v(j)<=12
            H=H12;
            else
            H=H13;
            end
        Fos=Fos_v;
        Ts_new_v(j,i)=Fos*((1-(drs_v/(2*rs_v(i))))*Ts_old_v(j,i-1) +
(1+(drs_v/(2*rs_v(i))))*Ts_old_v(j,i+1)+ Ts_old_v(j-1,i)/Cs1_v^2 +
((H*drs_v^2)/ks))+ (1-((1-(drs_v/(2*rs_v(i)))) + (1+(drs_v/(2*rs_v(i)))) +
1/Cs1_v^2)*Fos)*Ts_old_v(j,i);
        end
end
% Corner right hand side (i=m and j=n) Eq.5.22
for j=n_v
    for i=m_v
        if z_v(j)<=1
        H=H1;
        elseif z_v(j)<=2
        H=H2;
        elseif z_v(j)<=3
        H=H3;
        elseif z_v(j)<=4
        H=H4;
        elseif z_v(j)<=5
        H=H5;
        elseif z_v(j)<=6
        H=H6;
        elseif z_v(j)<=7
        H=H7;
        elseif z_v(j)<=8
        H=H8;
        elseif z_v(j)<=9
        H=H9;
        elseif z_v(j)<=10
        H=H10;
        elseif z_v(j)<=11
        H=H11;
        elseif z_v(j)<=12
        H=H12;
        else
        H=H13;
        end
    Fos=Fos_v;
    Ts_new_v(j,i)=Fos*((1-(drs_v/(2*rs_v(i))))*Ts_old_v(j,i-1) +
Ts_old_v(j-1,i)/Cs1_v^2 + ((H*drs_v^2)/ks))+ (1-((1-(drs_v/(2*rs_v(i)))) +
1/Cs1_v^2)*Fos)*Ts_old_v(j,i);
        end
end

%Lateral boundary
%Middle nodes(i=1 and j=2,3,4....n-1) Eq.5.23
for j=2:n_v-1
    for i=1
        if z_v(j)<=1
        H=H1;
        elseif z_v(j)<=2
```

```matlab
        H=H2;
        elseif z_v(j)<=3
        H=H3;
        elseif z_v(j)<=4
        H=H4;
        elseif z_v(j)<=5
        H=H5;
        elseif z_v(j)<=6
        H=H6;
        elseif z_v(j)<=7
        H=H7;
        elseif z_v(j)<=8
        H=H8;
        elseif z_v(j)<=9
        H=H9;
        elseif z_v(j)<=10
        H=H10;
        elseif z_v(j)<=11
        H=H11;
        elseif z_v(j)<=12
        H=H12;
        else
        H=H13;
        end
        Fos=Fos_v;
        Cgs=((drg_v/(2*drs_v))/((1-(drs_v/(2*rs_v(i))))*kg_v/ks))+(0.5/(1-
(drs_v/(2*rs_v(i)))));
        Ts_new_v(j,i)=Fos*(Tg_old_v(j,i)/Cgs +
(1+(drs_v/(2*rs_v(i))))*Ts_old_v(j,i+1) + Ts_old_v(j-1,i)/Cs1_v^2 +
Ts_old_v(j+1,i)/Cs1_v^2 + ((H*drs_v^2)/ks)) + (1-(1/Cgs +
(1+(drs_v/(2*rs_v(i)))) + 2/Cs1_v^2)*Fos)*Ts_old_v(j,i);
    end
end
%Middle nodes(i=m and j=2,3,4....n-1) Eq.5.24
for j=2:n_v-1
    for i=m_v
        if z_v(j)<=1
        H=H1;
        elseif z_v(j)<=2
        H=H2;
        elseif z_v(j)<=3
        H=H3;
        elseif z_v(j)<=4
        H=H4;
        elseif z_v(j)<=5
        H=H5;
        elseif z_v(j)<=6
        H=H6;
        elseif z_v(j)<=7
        H=H7;
        elseif z_v(j)<=8
        H=H8;
        elseif z_v(j)<=9
        H=H9;
        elseif z_v(j)<=10
        H=H10;
        elseif z_v(j)<=11
        H=H11;
        elseif z_v(j)<=12
        H=H12;
        else
        H=H13;
        end
        Fos=Fos_v;
```

```matlab
            Ts_new_v(j,i)=Fos*((1-(drs_v/(2*rs_v(i))))*Ts_old_v(j,i-1) +
Ts_old_v(j-1,i)/Cs1_v^2 + Ts_old_v(j+1,i)/Cs1_v^2 + ((H*drs_v^2)/ks)) + (1-
((1-(drs_v/(2*rs_v(i)))) + 2/Cs1_v^2)*Fos)*Ts_old_v(j,i);
        end
end
%Internal nodes
for j=2:n_v-1
    for i=2:m_v-1
        if z_v(j)<=1
        H=H1;
        elseif z_v(j)<=2
        H=H2;
        elseif z_v(j)<=3
        H=H3;
        elseif z_v(j)<=4
        H=H4;
        elseif z_v(j)<=5
        H=H5;
        elseif z_v(j)<=6
        H=H6;
        elseif z_v(j)<=7
        H=H7;
        elseif z_v(j)<=8
        H=H8;
        elseif z_v(j)<=9
        H=H9;
        elseif z_v(j)<=10
        H=H10;
        elseif z_v(j)<=11
        H=H11;
        elseif z_v(j)<=12
        H=H12;
        else
        H=H13;
        end
         Fos=Fos_v;
         Ts_new_v(j,i)=Fos*((1-(drs_v/(2*rs_v(i))))*Ts_old_v(j,i-1)+
(1+(drs_v/(2*rs_v(i))))*Ts_old_v(j,i+1) + Ts_old_v(j-1,i)/Cs1_v^2 +
Ts_old_v(j+1,i)/Cs1_v^2 + ((H*drs_v^2)/ks)) + (1-((1-(drs_v/(2*rs_v(i)))) +
(1+(drs_v/(2*rs_v(i)))) + 2/Cs1_v^2)*Fos)*Ts_old_v(j,i);
        end
end
Tf_old_v=Tf_new_v;
Tp_old_v=Tp_new_v;
Tg_old_v=Tg_new_v;
Ts_old_v=Ts_new_v;

%Save fluid outlet temperature
Tfout_cel_v=Tf_new_v(n_v)-273.15;
Tfluid_outlet_v(l)=Tfout_cel_v;


Ts_cel_Z25md0525m_v=Ts_new_v(18,5)-273.15;
Ts_Z25md0525m(l)=Ts_cel_Z25md0525m_v;


Ts_cel_Z50md0525m_v=Ts_new_v(35,5)-273.15;
Ts_Z50md0525m(l)=Ts_cel_Z50md0525m_v;


Ts_cel_Z75md0525m_v=Ts_new_v(53,5)-273.15;
Ts_Z75md0525m(l)=Ts_cel_Z75md0525m_v;


Ts_cel_Z100md0525m_v=Ts_new_v(70,5)-273.15;
Ts_Z100md0525m(l)=Ts_cel_Z100md0525m_v;
```

```
Ts_cel_Z125md0525m_v=Ts_new_v(88,5)-273.15;
Ts_Z125md0525m(l)=Ts_cel_Z125md0525m_v;

Ts_cel_Z100md0425m_v=Ts_new_v(70,4)-273.15;
Ts_Z100md0425m(l)=Ts_cel_Z100md0425m_v;

Ts_cel_Z100md0325m_v=Ts_new_v(70,3)-273.15;
Ts_Z100md0325m(l)=Ts_cel_Z100md0325m_v;

Ts_cel_Z100md0225m_v=Ts_new_v(70,2)-273.15;
Ts_Z100md0225m(l)=Ts_cel_Z100md0225m_v;

Ts_cel_Z100md0125m_v=Ts_new_v(70,1)-273.15;
Ts_Z100md0125m(l)=Ts_cel_Z100md0125m_v;
end
```

D. Air conditioning system (heat pump) computer program

The computer program for the ground source air conditioning system (heat pump) is shown below.

```
 clear all
% Table properties R134a
M = dlmread('TempR134a saturated.txt'); %Read the saturated properties data
of R134a
MM0 = dlmread('R134asuperheated0.txt'); %Read the superheated properties
data of R134a at pressures of 0.6 MPa and 0.7 MPa
MM1 = dlmread('R134asuperheated1.txt'); %Read the superheated properties
data of R134a at pressures of 0.8 MPa, 0.9 MPa and 1 MPa
MM2 = dlmread('R134asuperheated2.txt'); %Read the superheated properties
data of R134a at pressures of 0.8 MPa, 0.9 MPa and 1 MPa
T=M(:,1); %Saturated temperature of refrigerant R134a (C)
P=M(:,2); %Saturated pressure of refrigerant R134a (kPa)
h_f=M(:,8); %Enthalpy of saturated liquid of refrigerant R134a (kJ/kg)
h_g=M(:,10); %Enthalpy of saturated vapour of refrigerant R134a (kJ/kg)
s_g=M(:,13); %Entropy of saturated vapour of refrigerant R134a (kJ/kg K)

%Cooling capacity
Q_dot_in=1767; %Cooling capacity of the chiller (kW)
Comp_effi=0.816; %Isentropic efficiency of the compressor

%Operation period
dt=1; %Time step used to calculate the energy consumed by the chiller (h)
dt_GHE=31.2808; %Time step used in the simulation of the GHE's performance
(s)
t=[0.5:1:19 24.5:1:43 48.5:1:67 72.5:1:91 96.5:1:120]*3600; %Temporal
discretisation of the energy consumed by the GHE is calculated hourly per
120h of operation (s)
tt=t/dt_GHE; %Number of time step (s)
tt=round(tt);

%Evaporator (Point 1)
T_cw=5; %Chilled water temperature leacing the chiller (C)
dTeva=5; %Temperature difference between the evaporator and the chiller (C)
T_1=T_cw-dTeva; %Temperature at point 1 of T-s diagram of vapour
compression refrigeration cycle (C)
poly_h_g=polyfit(T,h_g,4);
h_1=polyval(poly_h_g,T_1); %Enthalpy of saturated vapour of refrigerant
R134a at point 1 (kJ/kg)
poly_s_g=polyfit(T,s_g,4);
s_1=polyval(poly_s_g,T_1); %Entropy of saturated vapour of refrigerant
R134a at point 1 (kJ/kgK)
s_2=s_1; %Entropy refrigerant R134a at point 2 (kJ/kgK)

load('Tfluid_outlet_v.mat') %Load the water temperature exits the GHE
Tf_in=Tfluid_outlet_v(tt); %Cooling water temperature entering the
condenser (C)
Tf_out=36; %warm water temperature leaving the condenser

%stored the COP of chiller at a given time step
COP_s=zeros(1,length(Tf_in));

%stored the compressor power at a given time step
W_dot_s=zeros(1,length(Tf_in));

%stored the energy consumed by the chiller at a given time step
E_s=zeros(1,length(Tf_in));
```

```matlab
for t=1:length(Tf_in)
Tf=Tf_in(t); %Cooling water temperature entering the condenser at a given
time step (C)
dTcond=5; %The temperature difference between the cooling water and the
condenser (C)
T_3=Tf+dTcond; %Temperature at point 3 of T-s diagram of vapour compression
refrigeration cycle (C)
poly_h_f=polyfit(T,h_f,4);
h_3=polyval(poly_h_f,T_3); %Enthalpy of saturated liquid of refrigerant
R134a at point 3 (kJ/kg)
h_4=h_3; %Enthalpy of refrigerant R134a at point 4 (kJ/kg)
poly_P=polyfit(T,P,3);
P_3=polyval(poly_P,T_3); %Pressure at point 3 of T-s diagram of vapour
compression refrigeration cycle (kPa)
P_2=P_3; %Pressure at point 2 of T-s diagram of vapour compression
refrigeration cycle (kPa)
P_2=P_2/1000; %Conver the pressure unit form kPa to Mpa

%Point 2
if P_2==0.6 %MPa
s=MM0(:,9);
h=MM0(:,8);
poly_h=polyfit(s,h,3);
h_2=polyval(poly_h,s_2); %Enthalpy at point 2 (kJ/kg)

elseif P_2==0.7 %MPa
s=MM0(:,13);
h=MM0(:,12);
poly_h=polyfit(s,h,3);
h_2=polyval(poly_h,s_2); %Enthalpy at point 2 (kJ/kg)

elseif P_2==0.8 %MPa
s=MM1(:,5);
h=MM1(:,4);
poly_h=polyfit(s,h,3);
h_2=polyval(poly_h,s_2); %Enthalpy at point 2 (kJ/kg)

elseif P_2==0.9 %MPa
s=MM1(:,9);
h=MM1(:,8);
poly_h=polyfit(s,h,3);
h_2=polyval(poly_h,s_2); %Enthalpy at point 2 (kJ/kg)

elseif P_2==1 %MPa
s=MM1(:,13);
h=MM1(:,12);
poly_h=polyfit(s,h,3);
h_2=polyval(poly_h,s_2); %Enthalpy at point 2 (kJ/kg)

elseif P_2==1.2 %MPa
s=MM2(:,5);
h=MM2(:,4);
poly_h=polyfit(s,h,3);
h_2=polyval(poly_h,s_2); %Enthalpy at point 2 (kJ/kg)

elseif and(P_2>0.6,P_2<0.7)
s_p6=MM0(:,9);
h_p6=MM0(:,8);
poly_h_p6=polyfit(s_p6,h_p6,3);
h_2_p6=polyval(poly_h_p6,s_2);
```

```matlab
s_p7=MM0(:,13);
h_p7=MM0(:,12);
poly_h_p7=polyfit(s_p7,h_p7,3);
h_2_p7=polyval(poly_h_p7,s_2);

P_2_p6=0.6;
P_2_p7=0.7;
h_2=h_2_p6+((h_2_p7-h_2_p6)*((P_2-P_2_p6)/(P_2_p7-P_2_p6))); %Enthalpy at
point 2 (kJ/kg)

elseif and(P_2>0.7,P_2<0.8)
s_p7=MM0(:,13);
h_p7=MM0(:,12);
poly_h_p7=polyfit(s_p7,h_p7,3);
h_2_p7=polyval(poly_h_p7,s_2);

s_p8=MM1(:,5);
h_p8=MM1(:,4);
poly_h_p8=polyfit(s_p8,h_p8,3);
h_2_p8=polyval(poly_h_p8,s_2);

P_2_p7=0.7;
P_2_p8=0.8;

h_2=h_2_p7+((h_2_p8-h_2_p7)*((P_2-P_2_p7)/(P_2_p8-P_2_p7))); %Enthalpy at
point 2 (kJ/kg)

elseif and(P_2>0.8,P_2<0.9)
s_p8=MM1(:,5);
h_p8=MM1(:,4);
poly_h_p8=polyfit(s_p8,h_p8,3);
h_2_p8=polyval(poly_h_p8,s_2);

s_p9=MM1(:,9);
h_p9=MM1(:,8);
poly_h_p9=polyfit(s_p9,h_p9,3);
h_2_p9=polyval(poly_h_p9,s_2);

P_2_p8=0.8;
P_2_p9=0.9;

h_2=h_2_p8+((h_2_p9-h_2_p8)*((P_2-P_2_p8)/(P_2_p9-P_2_p8))); %Enthalpy at
point 2 (kJ/kg)

elseif and(P_2>0.9,P_2<1)
s_p9=MM1(:,9);
h_p9=MM1(:,8);
poly_h_p9=polyfit(s_p9,h_p9,3);
h_2_p9=polyval(poly_h_p9,s_2);

s_1p0=MM1(:,13);
h_1p0=MM1(:,12);
poly_h_1p0=polyfit(s_1p0,h_1p0,3);
h_2_1p0=polyval(poly_h_1p0,s_2);

P_2_p9=0.9;
P_2_1p0=1;

h_2=h_2_p9+((h_2_1p0-h_2_p9)*((P_2-P_2_p9)/(P_2_1p0-P_2_p9)));%Enthalpy at
point 2 (kJ/kg)
```

```matlab
elseif and(P_2>1,P_2<1.2)
s_1p0=MM1(:,13);
h_1p0=MM1(:,12);
poly_h_1p0=polyfit(s_1p0,h_1p0,3);
h_2_1p0=polyval(poly_h_1p0,s_2);

s_1p2=MM2(:,5);
h_1p2=MM2(:,4);
poly_h_1p2=polyfit(s_1p2,h_1p2,3);
h_2_1p2=polyval(poly_h_1p2,s_2);

P_2_1p0=1;
P_2_1p2=1.2;

h_2=h_2_1p0+((h_2_1p2-h_2_1p0)*((P_2-P_2_1p0)/(P_2_1p2-P_2_1p0)));
%Enthalpy at point 2 (kJ/kg)
end
COP=(h_1-h_4)/(h_2-h_1); %Ideal COP
COPa=COP*Comp_effi; %Actual COP
W_dot=Q_dot_in/COPa; %Compressor power (kW)
E=W_dot*dt; %Energy consumed by the chiller (kWh)
%stored COP, W_dot, E
COP_s(t)=COP;
W_dot_s(t)=W_dot;
E_s(t)=E;
end
E_tot=sum(E_s) %Total energy consumption under intermittent mode/5 days of
operation (kWh)
```